Program

Lunar and Planetary Institute 3600 Bay Area Boulevard Houston TX 77058-1113

Mercury:
Current and Future Science of the Innermost Planet

May 1–3, 2018 • Columbia, Maryland

Institutional Support

Lunar and Planetary Institute

Universities Space Research Association

Convener

Nancy Chabot
Johns Hopkins Applied Physics Laboratory

Organizing Committee

Caleb Fassett
NASA Marshall Space Flight Center

Masaki Fujimoto
JAXA Institute of Space and Astronautical Science

Catherine Johnson
University of British Columbia

Erwan Mazarico
NASA Goddard Space Flight Center

Valeria Mangano
INAF/Istituto di Astrofisica e Planetologia Spaziali

Anna Milillo
INAF/Istituto di Astrofisica e Planetologia Spaziali

Larry Nittler
Carnegie Institution of Washington

Jim Raines
University of Michigan

David Rothery
The Open University

Kathleen Vander Kaaden
Jacobs, JETS Contract, NASA Johnson Space Center

Ron Vervack
Johns Hopkins Applied Physics Laboratory

Lunar and Planetary Institute
Travel Award Recipients

Brendan Anzures
Brown University, Rhode Island, U.S.A.

Jurrien Sebastiaan Knibbe
VU University, Amsterdam, Netherlands

David Pegg
The Open University, United Kingdom

Austin N. Glass
University of Michigan, U.S.A.

Lior Rubanenko
University of California, U.S.A.

Indhu Varatharajan
German Aerospace Center, Germany

Ryan Dewey
University of Michigan, U.S.A.

Christopher Malliband
The Open University, United Kingdom

Ariel N. Deutsch
Brown University, Rhode Island, U.S.A.

Chuanfei Dong
Princeton University, New Jersey, U.S.A.

Abstracts for this meeting are available via the meeting website at
https://www.hou.usra.edu/meetings/mercury2018/
Abstracts can be cited as
Author A. B. and Author C. D. (2018) Title of abstract. In *Mercury: Current and Future Science of the Innermost Planet,* Abstract #XXXX.
LPI Contribution No. 2047, Lunar and Planetary Institute, Houston.

Guide to Sessions

Tuesday, May 1, 2018

8:00 a.m.	USRA Education Gallery	Registration
8:45 a.m.	USRA Conference Center	Welcome and Introduction
10:00 a.m.	USRA Conference Center	Solar-Wind Interactions with Mercury
1:00 p.m.	USRA Conference Center	Mercury's Interior Structure and Evolution
3:20 p.m.	USRA Conference Center	Mercury: Origin, Geologic History, and Volcanism
5:30 p.m.	USRA Education Gallery	Poster Session and Reception

Wednesday, May 2, 2018

8:30 a.m.	USRA Conference Center	Mercury's Polar Deposits
10:25 a.m.	USRA Conference Center	An Exosphere and Magnetosphere Science Potpourri
1:30 p.m.	USRA Conference Center	Mercury's Crustal Geophysics
3:35 p.m.	USRA Conference Center	Future Mercury Exploration — Beyond BepiColombo

Thursday, May 3, 2018

8:30 a.m.	USRA Conference Center	Sodium: A Major Player in the Exosphere and Magnetosphere
10:15 a.m.	USRA Conference Center	Mercury Geochemistry: Observations and Laboratory Constraints
1:30 p.m.	USRA Conference Center	Exosphere/Magnetosphere: New Results with a Look to the Future
3:10 p.m.	USRA Conference Center	A Veritable Smorgasbord of Mercury Geological Delights

Program

Tuesday, May 1, 2018
WELCOME AND INTRODUCTION
8:45 a.m. USRA Conference Center

Chair: Nancy Chabot

8:45 a.m. Chabot N. L. *
Welcome and Logistics

9:00 a.m. Solomon S. C. *
Mercury, MESSENGER, and Messages Still to Discover

9:15 a.m. Benkhoff J. (Presented by Zender J. *)
BepiColombo — The Next Step of Mercury Exploration with Two Orbiting Spacecraft **[#6007]**
BepiColombo is a joint project between ESA and JAXA. The mission consists of two orbiters — the Mercury Planetary Orbiter and the Mercury Magnetospheric Orbiter. From dedicated orbits, the spacecraft will be studying the planet and its environment.

9:30 a.m. Murakami G. * Hayakawa H. Fujimoto M. BepiColombo Project Team
Overview of Mercury Magnetospheric Orbiter (MMO) for BepiColombo **[#6058]**
The next Mercury exploration mission BepiColombo will be launched in October 2018 and will arrive at Mercury in December 2025. We present the current status, science goals, and observation plans of JAXA's Mercury Magnetospheric Orbiter (MMO).

9:45 a.m. BREAK

Tuesday, May 1, 2018
SOLAR-WIND INTERACTIONS WITH MERCURY
10:00 a.m. USRA Conference Center

Chairs: **Ronald Vervack Jr.**
Suzanne Imber

10:00 a.m. **Invited:** Slavin J. A. *
Mercury's Solar Wind Interaction: The View from MESSENGER **[#6019]**
MESSENGER's three close fly-bys and four years of observations from orbit have revealed that Mercury possesses a highly dynamic and complex magnetic field and plasma environment.

10:15 a.m. Glass A. N. * Tracy P. J. Raines J. M.
First Identification of Foreshock Plasma Populations at Mercury **[#6042]**
Observations of foreshock populations at Mercury are presented for the first time utilizing measurements from the Fast Imaging Plasma Spectrometer (FIPS) aboard MESSENGER, and plausible energization mechanisms are suggested and evaluated.

10:27 a.m. Dong C. F. * Wang L. Hakim A. Bhattacharjee A. Germaschewski K. DiBraccio G. A.
Three-Dimensional, Ten-Moment, Two-Fluid Simulation of the Solar Wind Interaction with Mercury **[#6128]**
We investigate solar wind interaction with Mercury's magnetosphere by using Gkeyll ten-moment multifluid code that solves the continuity, momentum, and pressure tensor equations of both protons and electrons, as well as the full Maxwell equations.

10:39 a.m. Fatemi S. * Poirier N. Holmström M. Wieser M. Barabash S.
Getting Ready for BepiColombo: A Modeling Approach to Infer the Solar Wind Plasma Parameters Upstream of Mercury from Magnetic Field Observations **[#6014]**
We have developed a model to infer the solar wind plasma parameters upstream of Mercury from magnetic field observations in Mercury's magnetosphere. This is important for observations by MESSENGER and the future mission to Mercury, BepiColombo.

10:51 a.m. Philpott L. C. Johnson C. L. * Anderson B. J. Winslow R. M.
The Shape of Mercury's Magnetopause: What Can BepiColombo Tell Us? **[#6046]**
We investigate how limitations in MESSENGER magnetic field data coverage affect our ability to establish asymmetries in Mercury's magnetopause and examine how BepiColombo observations will improve our understanding of the magnetopause shape.

11:03 a.m. Orsini S. * Mangano V. Milillo A. Plainaki C. Mura A. Raines J. M. Laurenza M. De Angelis E. Rispoli R. Lazzarotto F. Aronica A.
Mercury Sodium Exospheric Emission as a Proxy for Solar Perturbations Transit **[#6010]**
We report about recent results published on Scientific Reports @nature.com showing the first evidence of direct relationship between exosphere Na dynamics observed from ground and ICME transit at Mercury, as detected by MESSENGER.

11:15 a.m. Raines J. M. * Wallace K. L. Sarantos M. Jasinksi J. M. Tracy P. J. Dewey R. M. Weberg M. J. Slavin J. A.
First In-Situ Observations of Exospheric Response to CME Impact at Mercury **[#6038]**
We present the first in-situ observations of enhancements to Me90rcury's He exosphere generated by CME impact. These results have implications for understanding exosphere generation and loss processes, as well space weathering of the planet's surface.

11:27 p.m. LUNCH

Tuesday, May 1, 2018
MERCURY'S INTERIOR STRUCTURE AND EVOLUTION
1:00 p.m. USRA Conference Center

Chairs: Catherine Johnson
Erwan Mazarico

1:12 p.m. **Invited:** Genova A. * Goossens S. Mazarico E. Lemoine F. G. Neumann G. A. Kuang W. Sabaka T. J. Smith D. E. Zuber M. T.
A Large Solid Inner Core at Mercury **[#6036]**
New measurements of the polar moments of inertia of the whole planet and of the outer layers (crust+mantle), and simulations of Mercury's magnetic field dynamo suggest the presence of a solid inner core with a Ric ~0.3-0.5 Roc.

1:27 p.m. Huguet L. * Hauck S. A. II Van Orman J. A. Jing Z.
Implications of the Homogeneous Nucleation Barrier for Top-Down Crystallization in Mercury's Core **[#6101]**
Crystallization of solids in planetary cores depends both on ambient temperatures falling below the liquidus and on the ability to nucleate crystal growth. We discuss the implications of the nucleation barrier for thermal evolution of Mercury's core.

Sarid G. * CANCELED
When Mercury Smashed: Dynamics and Composition Through a Grazing Collision with a Larger Planet **[#6127]**
Mercury emerges from a grazing collision with a larger proto-planet. Dynamics and composition evolution are consistent, but — Was it hit once? More? Where and when did it happen?

1:39 p.m. King S. D. * Robertson S.
Geodynamics in a Thin Shell **[#6033]**
At the pressure and temperature regime of Mercury's silicate interior, olivine deforms by dislocation creep (power law rheology). This allows Mercury to maintain a dynamic interior much later in time than earlier estimates using Newtonian rheology.

1:51 p.m. Roberts J. H. * Peplowski P. N. Stickle A. M. Stockstill-Cahill K. R. Denevi B. W. Buczkowski D. L. Barnouin O. S.
Thermochemical Evolution of Mercury's Mantle and the Formation of the Volcanic Plains **[#6122]**
Impacts, convection / Sample different regions / Plains diversity.

2:03 p.m. Oliveira J. S. * Hood L. L.
Unveiling the Early History of Mercury by Studying Its Crustal Magnetic Field **[#6069]**
We study different anomalies that are found on Mercury that were very likely thermoremanently magnetized, to look for true polar wander events and/or understand if they aren't entirely induced in origin.

2:15 p.m. Hood L. L. * Oliveira J. S. Spudis P. D. Galluzzi V.
Further Mapping of Mercury's Crustal Magnetic Field Using MESSENGER Magnetometer Data **[#6079]**
Further mapping of Mercury's crustal magnetic field shows that anomalies are associated with some impact craters but not others. Differences in impactor composition (e.g., iron content) may be indicated by this new observation.

2:27 p.m. Johnson C. L. * Plattner A. M. Phillips R. J. Philpott L. C. Kinczyk M. Prockter L.
The Distribution and Origin of Mercury's Lithospheric Magnetization **[#6052]**
We use low-altitude MESSENGER data to model the spatial distribution of Mercury's lithospheric magnetization and discuss constraints on its origin.

2:39 p.m. Plattner A. M. * Johnson C. L.
Regional Modeling and Power Spectra of Mercury's Crustal Magnetic Field **[#6023]**
Mercury's crustal magnetic field and magnetic power spectra for select regions show distinct patterns for regions without magnetized impact craters, regions with magnetized impact craters, and the region north of Caloris.

2:51 p.m. Wardinski I. Langlais B. * Thébault E.
Correlated Time-Varying Magnetic Fields at Mercury **[#6077]**
Time variation of the Hermean internal and external magnetic field are analyzed and correlated to several orbital parameters, suggesting a variety of external sources for their origin.

3:03 p.m. BREAK

Tuesday, May 1, 2018
MERCURY:
ORIGIN, GEOLOGIC HISTORY, AND VOLCANISM
3:20 p.m. USRA Conference Center

Chairs: **David Rothery**
Christopher Malliband

3:20 p.m. **Invited:** Kamata S. * Kuramoto K.
Mercury as a Probe for the Early Inner Solar System **[#6068]**
Surface chemistry of Mercury infers the early solar system environment not only at its inner edge but also at an outer region including the Earth and asteroids.

3:35 p.m. Boukare C.-E. Parman S. W. * Parmentier E. M. Anzures B. A.
Production and Preservation of Sulfide Layering in Mercury's Magma Ocean **[#6105]**
Mercury's magma ocean (MMO) would have been sulfur-rich. At some point during MMO solidification, it likely became sulfide saturated. Here we present physiochemical models exploring sulfide layer formation and stability.

3:47 p.m. Anzures B. A. * Parman S. W. Milliken R. E.
Effect of Sulfur Speciation on Chemical and Physical Properties of Reduced Mercurian Melts **[#6017]**
Changes in sulfide speciation (FeS, MgS, CaS, Na2S) influence activities, stability of phases, polymerization, and viscosity.

3:59 p.m. Malliband C. C. * Rothery D. A. Balme M. R. Conway S. J.
Small Smooth Units ('Young' Lavas?) Abutting Lobate Scarps on Mercury **[#6092]**
We have identified small units abutting, and so stratigraphy younger than, lobate scarps. This post dates the end of large scale smooth plains formation at the onset of global contraction. This elaborates the history of volcanism on Mercury.

4:11 p.m. Head J. W. * Wilson L.
Magmatic Ascent and Eruption Processes on Mercury **[#6102]**
MESSENGER volcanic landform data and information on crustal composition allow us to model the generation, ascent, and eruption of magma; Mercury explosive and effusive eruption processes differ significantly from other terrestrial planetary bodies.

4:23 p.m. Besse S. * Dorresoundiram A. Griton L.
Analysis of Pyroclastic Deposits Using MESSENGER MASCS Observations **[#6063]**
Pyroclastic Deposits on the surface of Mercury are analysed using MASCS observations and an optimised calibration procedure. Pyroclastic Deposits show similar spectral properties that is explained by isotropic distribution of the ashes.

4:35 p.m. Jozwiak L. M. * Izenberg N. R. Olson C. L. Head J. W.
Investigating the Age of Mercury's Pyroclastic Deposits **[#6089]**
We use a combination of stratigraphic and comparative spectral analysis to investigate the ages of Mercury's pyroclastic deposits. We find that pyroclastic deposits have continued to form into Mercury's recent geologic history.

4:50 p.m. Kinczyk M. J. * Byrne P. K. Prockter L. P. Susorney H. C. M. Barnouin O. S.
Crater Degradation on Mercury: A Global Perspective **[#6116]**
Results from a global catalog of crater degradation are explored and implications for our understanding of Mercury's geological history are discussed.

5:02 p.m. Banks M. E. * Xiao Z. Marchi S. Chapman C. R. Barlow N. G. Fassett C. I.
Revised Age Constraints for Mercury's Kuiperian and Mansurian Stratigraphic Sysytems **[#6124]**
Crater statistics constrain the onset of Mercury's two most recent periods. The Kuiperian likely began ~280 ± 60 Ma and the Mansurian ~1.7 ± 0.2 Ga. Results indicate younger Kuiperian and Mansurian periods than previously assumed..

5:14 p.m. **Invited:** Denevi B. W. * Ernst C. M. Klima R. L. Robinson M. S.
Mercury's Early Geologic History **[#6055]**
A combination of geologic mapping, compositional information, and geochemical models are providing a better understanding of Mercury's early geologic history, and allow us to place it in the context of the Moon and the terrestrial planets.

Tuesday, May 1, 2018
POSTER SESSION: MERCURY
5:30–7:30 p.m. USRA Education Gallery

Malliband C. C. Rothery D. A. Balme M. R. Conway S. J.
1:3M Geological Mapping of the Derain(H-10) Quadrangle of Mercury **[#6091]**
We are making a high resolution geological map of the Derain quadrangle of Mercury. This is part of a coordinated project to create a global set of geological maps for BepiColombo.

Mangano V. Milillo A. Massetti S. Orsini S.
New Results of Statistical Analysis of the Na Exosphere Earth-based Observations of Mercury
The THEMIS database of Na exosphere is re-analyzed in view of the most recent papers in the field of both magnetosphere and plasma interactions.

Morlok A. Charlier B. Klemme S. Namur O. Sohn M. Weber I. Stojic A. Hiesinger H. Helbert J.
Spectroscopy of Synthetic Planetary Analogs for MERTIS on the BepiColombo Mission **[#6078]**
We present an overview of our work on a database of mid-infrared spectra of synthetic analogs for the MERTIS instrument on the BepiColombo mission.

Neumann G. A. Sun X. Cao A. Deutsch A. N. Head J. W.
Reflectance of Mercury's Polar Regions: Calibration and Implications for Mercury's Volatiles **[#6115]**
Calibration of laser altimeter reflectances under widely varying conditions is supported by laboratory data from an engineering simulator to address the distribution of volatile deposits in Mercury's polar cold traps.

Peterson G. A. Johnson C. L. Byrne P. K. Phillips R. J.
Distribution of Areal Strain on Mercury: Insights into the Interaction of Volcanism and Global Contraction **[#6056]**
Wrinkle ridges within volcanic plains on Mercury host just as much shortening strain as lobate scarps and high relief ridges, suggesting that wrinkle ridges have accommodated much more strain from global contraction than previously thought.

Saito Y. Miyake W. Yokota S. Coates A. Fazakery A. Hasegawa H. Ieda A. Machida S. Nagai T. Nagatsuma T. Owen C. Seki K. Shinohara I. Terasawa T.
The MIA (Mercury Ion Analyzer) Instrument Onboard Bepi Colombo MMO (Mercury Magnetospheric Orbiter) **[#6005]**
Current status and future observation plan of MPPE-MIA (Mercury Plasma Particle Experiment — Mercury Ion Analyzer) on BepiColombo/MMO will be presented.

Pegg D. L. Rothery D. A. Balme M. R. Conway S. J.
Geological Mapping of the Debussy Quadrangle (H-14) Preliminary Results **[#6021]**
We present the current status of geological mapping of the Debussy quadrangle. Mapping underway as part of a program to map the entire planet at a scale of 1:3M using MESSENGER data in preparation for the BepiColombo mission.

Schmude R. W. Jr.
Wideband Photometry of Mercury in the U, B, V, R, I, J, and H Filters: A Review **[#6066]**
I review brightness measurements of Mercury made since the 1960s. New J and H band brightness results are also presented.

Shread E. E. Chabot N. L.
Investigating Mercury's South Polar Deposits with High-Resolution Determination of Illumination Conditions **[#6008]**
High-resolution images acquired by MESSENGER's Mercury Dual Imaging System were used to investigate the illumination conditions of Mercury's south polar deposits and to map the areas of permanent shadow in the region to compare with radar imaging.

Stark A. Oberst J. Preusker F. Burmeister S. Steinbrügge G. Hussmann H.
Mercury's Reference Frames After the MESSENGER Mission **[#6114]**
We provide an overview of Mercury's reference frames based on MESSENGER observations. We discuss the dynamical, the principal-axes, the ellipsoid, as well as the cartographic frame, which was adopted for MESSENGER data products.

Vander Kaaden K. E. McCubbin F. M. Rowland R. L. II Morris R. V. Reppart J. J. Klima R. L.
Placing Tighter Constraints on Mercurian Surface Fe Abundances Through the Synthesis and Characterization of Fe-Poor Silicates **[#6011]**
We have crystallized and characterized synthetic Fe-poor minerals to make advancements towards reconciling the discrepancy between the lack of a 1-μm absorption band observed on the surface of Mercury, despite wt% levels of Fe observed by XRS.

Varatharajan I. Maturilli A. Helbert J. Hiesinger H.
Emissivity of Ca-Sulfide in Mid-Infrared Under Simulated Extreme Thermal Environment of Mercury **[#6065]**
Spectral evolution of emissivity of calcium sulfides in mid-infrared is studied for four Mercury daytime temperature cycles under simulated extreme thermal environment of Mercury.

Varatharajan I. Maturilli A. Helbert J. Ulrich G. Born K. Namur O. Kästner B. Hecht L. Charlier B. Hiesinger H.
Nano-FTIR Spectroscopy to Investigate the Silicate Mineralogy of Mercury Analogues: Supporting MERTIS Onboard BepiColombo Mission **[#6067]**
Nano-FTIR Spectroscopy is used to investigate the silicate mineralogy of synthetic Mercury analogues produced under reduced conditions representing different Mercury terrains. The study will support MERTIS payload onboard BepiColombo mission.

Wilbur Z. E. Udry A. McCubbin F. M. Vander Kaaden K. E. Rahib R. R. McCoy T. J.
Aubrite and Enstatite Chondrite Impact Melt Meteorites: Analogs to Mercury? **[#6034]**
We study aubrite and enstatite chondrite impact melt meteorites and compare these data to the mercurian surface data collected by MESSENGER to better understand the mineralogy of Mercury.

Wright J. Rothery D. A. Balme M. R. Conway S. J.
Geological Mapping of the Hokusai (H05) Quadrangle of Mercury: Status Update **[#6062]**
We present the current working version of the first geological map of the Hokusai quadrangle of Mercury.

Wright J. Rothery D. A. Balme M. R. Conway S. J.
Candidate Constructional Volcanic Edifices on Mercury **[#6064]**
We describe two candidate constructional volcanoes on Mercury and suggest how they may have formed on a planet whose effusive volcanism has overwhelmingly generated plains.

Aizawa S. Delcourt D. Terada N.
Sodium Ion Dynamics in the Magnetospheric Flanks of Mercury **[#6090]**
We examine the particle transport via the Kelvin-Helmholtz instability by using simulation. The heavy ions of planetary origin such as Na+ may experience prominent nonadiabatic energization as they ExB drift across large-scale rolled up vortices.

Andre N. Sauvaud J.-A. Aoustin C. Fedorov A. Seran H.-C. Le Comte E. Petiot M. Rouzaud J. Barthe A. Penou E. Saito Y. Yokota S. Moirin D. Moirin D. Garat C. Cadu A. Rouger P. Medale J.-L.
The Mercury Electron Analyzers Onboard the Bepi Colombo Mercury Magnetospheric Orbiter **[#6003]**
Onboard the Bepi Colombo Mercury Magnetospheric Orbiter (MMO), the Mercury Electron Analyzers (MEA) sensors constitute the experiment dedicated to fast electron measurements between 3 and 25,500 eV.

Anzures B. A. Parman S. W. Milliken R. E. Head J. W.
Interior Volatile Reservoirs in Mercury **[#6113]**
More measurements of 1) surface volatiles, and 2) pyroclastic deposits paired with experimental volatile analyses in silicate minerals can constrain conditions of melting and subsequent eruption on Mercury.

Besse S. Benkhoff J. Bentley M. Cornet T. Moissl R. Munoz C. Zender J.
Mercury Science Objectives and Traceability Within the BepiColombo Project: Optimising the Science Output of the Next Mission to Mercury **[#6083]**
The BepiColombo Science Ground Segment is developing, in collaboration with the instrument teams, targeted science traceability matrix of each instrument. They are defined in such a way that they can be tracked during the observation lifecycle.

Bott N. Brunetto R. Carli C. Capaccioni F. Doressoundiram A. Langevin Y. Perna D. Poulet F. Serventi G. Sgavetti M. Borondics F. Sandt C.
Spectroscopy of Minerals Analogs of Mercury Under the Hermean Conditions: The Effect of the Temperature **[#6043]**
We present a preliminary study of the effects of the strong variations of temperature on minerals of the surface of Mercury. We measured a loose powder (75-100 µm) of plagioclase and 5 mm diameter pellets made with the same powder.

Daniels J. W. Neish C. D.
Impact Melt Emplacement on Mercury **[#6018]**
This work proposes that fresh craters on rocky bodies may deposit impact melt externally ultimately according to the strength of its surface gravity, regardless of the body's surface topography and melt abundance.

Delcourt D. Saito Y. Leblanc F. Verdeil C. Yokota S. Fraenz M. Fischer H. Fiethe B. Katra B. Fontaine D. Illiano J.-M. Berthelier J.-J. Belger A. Bubenhagen F. Krupp N. Buhrke U. Michalik H. Krueger H.
The MSA Instrument (Mass Spectrum Analyzer) Onboard Bepi Colombo MMO (Mercury Magnetospheric Orbiter) **[#6002]**
The paper describes the ion spectrometer that will be flown on Bepi Colombo MMO as part of the MPPE consortium and that will provide information on the magnetospheric plasma composition.

Deutsch A. N. Head J. W.
Production Function of Outgassed Volatiles on Mercury: Implications for Polar Volatiles on Mercury and the Moon **[#6121]**
We are interested in the flux of volatiles delivered to the polar regions of Mercury and the Moon through time. We integrate the production functions for volatile delivery from impacts, solar wind, and volcanism, which we focus on initially.

Fastook J. L. Head J. W.
Cold-Based Glaciation on Mercury: Accumulation and Flow of Ice in Permanently-Shadowed Circum-Polar Crater Interiors **[#6059]**
Examining the potential for dynamic flow of ice deposits in permanently-shadowed craters, it is determined that the cold environment of the polar craters yields very small velocities and deformation is minimal on a time scale of millions of years.

Galluzzi V. Guzzetta L. Mancinelli P. Giacomini L. Lewang A. M. Malliband C. Mosca A. Pegg D. Wright J. Ferranti L. Hiesinger H. Massironi M. Pauselli C. Rothery D. A. Palumbo P.
The Making of the 1:3M Geological Map Series of Mercury: Status and Updates **[#6075]**
A complete global series of 1:3M-scale maps of Mercury is being prepared in support to the ESA/JAXA BepiColombo mission. Currently, ~35% of Mercury has been mapped and ~55% of the planet will be covered soon by the maps in progress.

Goossens S. Mazarico E. Genova A. James P. B.
High-Resolution Gravity Field Modeling for Mercury to Estimate Crust and Lithospheric Properties **[#6048]**
We estimate a gravity field model for Mercury using line-of-sight data to improve the gravity field model at short wavelengths. This can be used to infer crustal density and infer the support mechanism of the lithosphere.

Grava C. Livi S. A.
Modeling of Metals in the Hermean Exosphere: Predictions for the Mass Spectrometer Strofio Onboard BepiColombo **[#6039]**
We modeled metals in Mercury's exosphere with a Monte Carlo code. We predict altitude profiles of density for comparison with in situ measurements of Strofio mass spectrometer onboard BepiColombo.

Guzzetta L. Galluzzi V. Ferranti L. Palumbo P.
Geologic Map of the Shakespeare Quadrangle (H03), Mercury **[#6107]**
A 1:3M geological map of the H03 Shakespeare quadrangle of Mercury has been compiled through photointerpretation of the MESSENGER images. The most prominent geomorphological feature is the Caloris basin, the largest impact crater on Mercury.

Ivanovski S. L. Milillo A. Kartalev M. Massetti S.
Coupled Kelvin-Helmholtz and Tearing Mode Instabilities at the Mercury's Magnetopause **[#6074]**
A MHD approach for numerical simulations of coupled Kelvin-Helmholtz and tearing mode instabilities has been applied to Mercury's magnetopause and used to perform a physical parameters study constrained by the MESSENGER data.

Jozwiak L. M. Head J. W. Wilson L.
Characterizing the Morphology, Distribution, and Formation Geometry of Mercury's Pyroclastic Vents **[#6088]**
We present a final catalog of pyroclastic vents on Mercury, identifying 104 candidate pyroclastic vents. We then assess the vent distribution, morphologic variation, and probable formation geometries.

Kinczyk M. J. Prockter L. M. Denevi B. W. Ostrach L. R. Skinner J. A.
A Global Geological Map of Mercury **[#6123]**
An update on mapping progress for the global geological map of Mercury.

Lucchetti A. Pajola M. Galluzzi V. Giacomini L. Carli C. Cremonese G. Marzo G. A. Massironi M. Roush T.
Spectral Clustering and Geomorphological Analysis on Mercury Hollows **[#6028]**
Characterization of hollows located in different craters to understand whether there is a similar trend from a compositional point of view, and whether a possible correlation exists between spectral behavior of hollows and geomorphological units.

Wednesday, May 2, 2018
MERCURY'S POLAR DEPOSITS
8:30 a.m. USRA Conference Center

Chairs: Carolyn Ernst
Lior Rubanenko

8:30 a.m. Neumann G. A. * Sun X. Mazarico E. Barker M. K. Smith D. E. Zuber M. T. Head J. W.
Mercury Laser Altimeter: Highlights from 10 Years in Space **[#6120]**
The Mercury Laser Altimeter made discoveries contributing to our knowledge of the surface environment, geology, tectonics, impact history, volcanism, and interior structure of Mercury.

8:42 a.m. **Invited:** Deutsch A. N. * Head J. W. Neumann G. A.
Differences Between Surface Ice Deposits at the Poles of Mercury and the Moon: Insights into Ages of the Ice **[#6118]**
The poles of Mercury and the Moon both show evidence for water ice, but the deposits on Mercury have a greater areal distribution and a more pure concentration. We explore how these differences may be related to the ages of the ice.

8:57 a.m. Ernst C. M. * Chabot N. L. Barnouin O. S.
Could the Hokusai Impact Have Delivered Mercury's Water Ice? **[#6094]**
Hokusai is the best candidate source crater for Mercury's water-ice inventory if it was primarily delivered by a single impact event. The Hokusai impact could account for the inventory of water ice on Mercury for impact velocities <30 km/s.

9:09 a.m. Susorney H. C. M. * James P. B. Johnson C. L. Chabot N. L. Ernst C. M. Mazarico E. M. Barnouin O. S. Neumann G. A.
Measuring the Thickness of Radar-Bright Deposits on Mercury Using Individual Mercury Laser Altimeter (MLA) Tracks **[#6013]**
We estimated the thickness of Mercury's radar-bright deposits using individual MLA tracks and found an average thickness of radar-bright deposits of 24 m.

9:21 a.m. Rubanenko L. * Mazarico E. Neumann G. A. Paige D. A.
The Depth of Ice Inside the Smallest Cold-Traps on Mercury: Implications for Age and Origin **[#6057]**
We use Mercury Laser Altimeter data and an illumination model to constrain the depth of the smallest ice deposits on Mercury. By comparing this depth to modeled gardening rates, we estimate the age and delivery method of this ice.

9:33 a.m. Chabot N. L. * Neumann G. A. Ernst C. M. Mazarico E. M. Shread E. E.
A Closer Look at Some of Mercury's North Polar Deposits: Three Craters that Could Have Extensive Surface Ice but Don't? **[#6045]**
We investigate three of Mercury's north polar craters that are predicted from their thermal conditions to be conducive to the presence of extensive water ice at the surface, but that may lack such ice.

9:45 a.m. Keane J. T. * Matsuyama I.
True Polar Wander of Mercury **[#6098]**
We use new MESSENGER gravity data to investigate how impact basins and volcanic provinces alter Mercury's moments of inertia. We find that Mercury has reoriented tens of degrees over its history, affecting tectonics, volatiles, and more.

9:57 a.m. Hussmann H. * Steinbrügge G. Stark A. Oberst J. Thomas N. Lara L.-M.
The BepiColombo Laser Altimeter (BELA): Scientific Performance at Mercury **[#6016]**
We discuss the expected scientific performance of BELA in Mercury orbit. Based on a performance model, we present the measurement accuracy of global and local topography, surface slopes and roughness, as well as the tidal Love number h2.

10:09 a.m. BREAK

Wednesday, May 2, 2018
AN EXOSPHERE AND MAGNETOSPHERE SCIENCE POTPOURRI
10:25 a.m. USRA Conference Center

Chairs: Francois Leblanc
Manar Al Asad

10:25 a.m. **Invited:** Killen R. M. * Vervack R. J. Jr.
Mercury's Exosphere: Current Understanding and Conundrums **[#6006]**
Although MESSENGER provided an unprecedented view of Mercury's exosphere, there is much that is not understood, particularly in terms of the physical processes that generate and maintain the exosphere.

10:40 a.m. Hurley D. M. * Prem P. Vervack R. J. Jr. Chabot N. L. Benna M. Farrell W. M. Killen R. M. Li S. Lucey P. G. Hendrix A. R.
Volatiles on Mercury: Lessons from the Moon **[#6084]**
Presenting observations regarding present day sources of water on the Moon for comparison with processes occurring on Mercury.

10:52 a.m. Vervack R. J. Jr. * Hurley D. M. Pryor W. Killen R. M.
MESSENGER Orbital Observations of Mercury's Hydrogen Exosphere **[#6025]**
We present a complete analysis of the MESSENGER H Lyman alpha altitude profiles. These data confirm the two-temperature nature of the Mariner 10 observations of H and address long-outstanding questions on the origin of Mercury's H exosphere.

11:04 a.m. **Invited:** Imber S. M. *
Mercury's Dynamic Magnetosphere **[#6099]**
The global dynamics of Mercury's magnetosphere will be discussed, focussing on observed asymmetries in the magnetotail and on the precipitation of particles of magnetospheric origin onto the nightside planetary surface.

11:19 a.m. Heyner D. *
Concerning the Offset Dipole Magnetic Field of Planet Mercury **[#6072]**
Critical revision of the internal field determination on basis of all available magnetic field data from MESSENGER and derived constraints on the dynamo process of Mercury.

11:31 a.m. Jia X. * Slavin J. Chen Y. Poh G. Toth G. Gombosi T.
An Integrated Modeling Suite for Simulating the Core Induction and Kinetic Effects in Mercury's Magnetosphere **[#6082]**
We present results from state-of-the-art global models of Mercury's space environment capable of self-consistently simulating the induction effect at the core and resolving kinetic physics important for magnetic reconnection.

11:43 a.m. Barabash S. * Wieser M. Futaana Y. Holmström M. Asamura K. Saito Y. Wurz P.
Energetic Neutral Atom (ENA) Imaging of Mercury's Magnetosphere Onboard BepiColombo **[#6117]**
We describe how energetic neutral atoms (ENA) are produced in Mercury's magnetosphere, how they can be used to image the magnetosphere and surface, and how they are measured onboard the BepiColombo mission.

11:55 a.m. LUNCH

Wednesday, May 2, 2018
MERCURY'S CRUSTAL GEOPHYSICS
1:30 p.m. USRA Conference Center

Chairs: Peter James
Hannah Susorney

1:30 p.m. Mazarico E. * Genova A. Goossens S. Neumann G. A. Smith D. E. Zuber M. T.
The Crust of Mercury After the MESSENGER Gravity Investigation **[#6027]**
We present the results of an improved analysis of the entire MESSENGER radio tracking dataset to derive key geophysical parameters of Mercury such as its gravity field. In particular, we derive and interpret a new crustal thickness model.

1:42 p.m. James P. B. *
The Enigma of Mercury's Northern Rise **[#6053]**
Various aspects of the "northern rise" make it hard to explain: Its composition and chronology don't stand out from its surroundings, it seems to have uplifted late, and it has a huge gravity anomaly. We'll discuss the possible formation mechanisms.

1:54 p.m. Baker D. M. H. * Head J. W. Fassett C. I.
Impact-Basin Formation on Mercury: Current Observations and Outstanding Questions **[#6085]**
Mercury provides an important laboratory for understanding impact-basin formation on planetary bodies. MESSENGER observations improved our understanding, but much is still unknown about the formation and evolution of basin features.

2:06 p.m. Barlow N. G. Banks M. E. *
Constraints on the Timing of Tectonic Activity on Mercury's Large-Scale Lobate-Scarp Thrust Faults **[#6126]**
A crater analysis study of Mercury's 30 largest lobate scarps provides new insights into the history of contraction on the planet.

2:18 p.m. Giacomini L. * Massironi M. Galluzzi V. Ferrari S. Palumbo P.
How Old are Mercury's Thrust Systems? New Results and Implications for the Thermal Evolution of the Planet **[#6076]**
We dated the activity of several thrust systems on Mercury. The results allowed us to better constrain the beginning of the contraction and, therefore, the thermal evolution of the planet.

2:30 p.m. Herrick R. R. *
The Nonrandom Distribution of Interior Landforms for ~100-km Diameter Craters on Mercury Suggests Regional Variations in Near-Surface Mechanical Properties **[#6109]**
There is great diversity of appearance in the interiors of ~100-km diameter craters. The spatial distribution of interior landforms is clustered and nonrandom, but does not clearly correlate with Mercury's surface geology patterns.

2:42 p.m. Rodriguez J. A. P. * Domingue D. L. Berman D. C. Kargel J. S. Baker V. R. Teodoro L. F. Banks M. Leonard G.
The Chaotic Terrains of Mercury: A History of Large-Scale Crustal Devolatilization **[#6054]**
Approximately 400 million years after the Caloris basin impact, extensive collapse formed Mercury's chaotic terrains. Collapse likely resulted from regionally elevated heat flow devolatilizing crustal materials along NE and NW extensional faults.

2:54 p.m. Preusker F. * Stark A. Oberst J. Matz K.-D. Roatsch T. Burmeister S. Gwinner K.
High-Resolution Topography from MESSENGER Orbital Stereo Imaging — The Southern Hemisphere **[#6031]**
We will present the current status of the generation of topographic models of the southern hemisphere quadrangles H11 to H15.

3:06 p.m. Kreslavsky M. A. * Zharkova A. Yu. Head J. W.
Decameter-Scale Regolith Textures on Mercury **[#6050]**
Like on the Moon, regolith gardening smooths the surface. Small craters are in equilibrium. "Elephant hide" typical on the lunar slopes is infrequent on Mercury. Finely Textured Slope Patches have no analog on the Moon.

3:18 p.m. BREAK

Wednesday, May 2, 2018
FUTURE MERCURY EXPLORATION — BEYOND BEPICOLOMBO
3:35 p.m. USRA Conference Center

Chairs: **Nancy Chabot**
Steven Hauck II

3:35 p.m. Chabot N. L. *
Introduction to Session

3:40 p.m. **Invited:** Hauck S. A. II * Blewett D. T.
Lessons from the Mercury Lander Study for the 2013-2022 Decadal Survey **[#6024]**
In situ exploration of Mercury is a logical next following the orbital investigations of the planet by MESSENGER and the upcoming BepiColombo mission.

3:55 p.m. Eng D. A. *
Mercury Lander Mission Concept Study Summary **[#6070]**
Provides a summary of the Mercury Lander Mission Concept Study performed as part of the last Planetary Decadal Survey. The presentation will focus on engineering trades and the challenges of developing a Mercury lander mission.

4:10 p.m. Raines J. M. *
Planetary Ions at Mercury: Unanswered Questions After MESSENGER **[#6087]**
We will discuss the key open questions relating to planetary ions, including the behavior of recently created photoions, the near absence of Ca+ / K+ in MESSENGER ion measurements, and the role of ion sputtering in the system.

4:15 p.m. Klimczak C. * Byrne P. K.
Open Questions on the Global Contraction of Mercury **[#6049]**
Substantial progress has been made on determining the amount, timing, and rate of global contraction on Mercury. But many open questions remain to be answered about the process itself, associated landforms, and interactions with other processes.

4:20 p.m. Byrne P. K. * Klimczak C. Whitten J. L. Jozwiak L. M. Denevi B. W. Vander Kaaden K. E. McCubbin F. M. Ostrach L. R. Rothery D. A. Wright J.
Volcanism on Mercury: (Some) Open Questions After MESSENGER **[#6100]**
From MESSENGER data we know, of eruptions, explosions, and flows. But details we lack, so when we go back, here are some questions to pose.

4:25 p.m. Ernst C. M. * Klima R. L. Denevi B. W. Peplowski P. N. Murchie S. L.
Landed Reconnaissance of Mercury in the Low-Reflectance Material (LRM^2) **[#6125]**
Someday, humans will send a landed mission to Mercury. It should explore the low-reflectance material!

4:30 p.m. Chabot N. L. * Lawrence D. J.
The Big Science Questions About Mercury's Ice-Bearing Polar Deposits After MESSENGER **[#6044]**
Mercury's polar deposits provide many well-characterized locations that are known to have large expanses of exposed water ice and/or other volatile materials — presenting unique opportunities to address fundamental science questions.

4:35 p.m. Knibbe J. S. * Luginbhuel S. M. Rivoldini A. Kono Y. Van Hoolst T. van Westrenen W.
Future Seismic Constraints on Mercury's Core Composition **[#6029]**
The composition of Mercury's large core is strongly linked to the planet's origin and magnetic field generation. We present P-wave velocity measurements for liquid Fe-Si and Fe-S metals. A future seismic mission can constrain the core composition.

4:40 p.m. Mazarico E. * Goossens S. Genova A. Sun X. Yang G.
GRAIL at Mercury: Coherent Laser Tracking for Geophysics **[#6026]**
We present an instrument concept for satellite-to-satellite tracking at optical wavelength to measure the gravity field of Mercury with sufficient accuracy and resolution to significantly advance our understanding of its geophysical evolution.

4:45 p.m. *Discussion and Future Plans*

5:15 p.m. Chabot N. L. *
Session Wrap-up

Thursday, May 3, 2018
SODIUM:
A MAJOR PLAYER IN THE EXOSPHERE AND MAGNETOSPHERE
8:30 a.m. USRA Conference Center

Chairs: **Valeria Mangano**
Jim Raines

8:30 a.m. **Invited:** Leblanc F. * Chaufray J. Y.
Mercury's Exosphere: Ground Based Observations as a Support to the Forthcoming Bepi-Colombo **[#6004]**
We will summarize the still open questions regarding Mercury's exosphere, highlighting which new topics Bepi-Colombo set of instruments might be able to address and how ground based observations should contribute to further improve our understanding.

8:45 a.m. **Invited:** Kameda S. * Kagitani M.
Ground-Based Observation of Mercury's Sodium at Haleakala Observatory in 2013–2017 **[#6035]**
In this study, daily variation in Mercury's sodium exosphere was observed at the Haleakala Observatory in Hawaii. We confirmed the seasonal variation of the column density of sodium atoms over the dawn side differs from that over the dusk side.

9:00 a.m. Schmidt C. A. * Leblanc F. Reardon K. Killen R. M. Gary D. E. Ahn K.
Absorption Spectroscopy of Mercury's Exosphere During the 2016 Solar Transit **[#6022]**
Solar transits of Mercury provide a rare opportunity to study the exosphere in absorption and a valuable analog to transiting exoplanet studies. This presentation will characterize the sodium exosphere during the 2016 transit.

9:12 a.m. Gamborino D. * Wurz P.
Statistical Analysis of PDF's for Na Released by Photons from Solid Surfaces **[#6001]**
We analyse the adequacy of three model speed PDF's previously used to describe the desorption of Na from a solid surface either by ESD or PSD. We found that the Maxwell PDF is too wide compared to measurements and non-thermal PDF's are better suited.

9:24 a.m. Savin D. W. * Bostick B. C. Domingue D. L. Ebel D. S. Harlow G. E. Killen R. M.
A Combined Experimental and Modeling Program to Study the Impact of Solar Wind Ions on the Surface and Exosphere of Mercury **[#6012]**
We aim to improve the interpretation of in-situ and remote-sensing data of Mercury. We will use updated exosphere and spectrophotometric models incorporating new data from lab simulations of solar wind ion irradiation of Mercury's regolith surface.

9:36 a.m. Cooper R. * Grande M. Martindale A. Bunce E.
Observational Conditions for the Detection of X-Ray Fluorescence from Sodium by the MIXS Instrument on BepiColombo **[#6080]**
We model the expected fluorescence from the exosphere and surface of Mercury, as observed by the Mercury Imaging X-ray Spectrometer (MIXS) on the upcoming BepiColombo mission, using code modified from that used for the SMART-1 D-CIXS instrument.

9:48 a.m. Jasinski J. M. * Raines J. M. Slavin J. A. Regoli L. R. Murphy N.
Sodium Pick-Up Ion Observations in the Solar Wind Upstream of Mercury **[#6110]**
We present the first observations of sodium pick-up ions upstream of Mercury's magnetosphere. From these observations we infer properties of Mercury's sodium exosphere and implications for the solar wind interaction with Mercury's magnetosphere.

10:00 a.m. BREAK

Thursday, May 3, 2018
MERCURY GEOCHEMISTRY:
OBSERVATIONS AND LABORATORY CONSTRAINTS
10:15 a.m. USRA Conference Center

Chairs: Kathleen Vander Kaaden
Brendan Anzures

10:15 a.m. **Invited:** Charlier B. * Namur O. Cartier C.
Perspectives on Magmatic Differentiation of Mercury **[#6009]**
Silicate/metal liquid immiscibility, crystallization of a magma ocean, partial melting of mantle rocks, and surface crystallization have shaped Mercury as we know it today. We review these processes based on high-T experiments at reducing conditions.

10:30 a.m. Nittler L. R. * Boujibar A. Crapster-Pregont E. Frank E. A. McCoy T. J. McCubbin F. M. Starr R. D. Vander Kaaden K. E. Vorburger A. Weider S. Z.
Heterogeneous Distribution of Chromium on Mercury **[#6095]**
Mercury's surface has an average Cr/Si ratio of ~0.003 (Cr~800 ppm), with at least a factor of 2 systematic uncertainty. Cr is heterogeneously distributed and correlated with Mg, Ca, S, and Fe and anti-correlated with Al.

10:42 a.m. Boujibar A. * Nittler L. R. Chabot N. McCubbin F. M. Righter K. Vander Kaaden K. E. McCoy T. J.
Experimental Investigation of Chromium Behavior During Mercury's Differentiation **[#6112]**
We use experimental data on Cr partitioning and its concentration on Mercury's surface to constrain on Mercury's oxidation state. We found that Mercury's bulk Cr composition can be chondritic and its core segregated at an fO2 of IW- 4.5 to IW-3.

10:54 a.m. Carli C. * Brunetto R. Strazzulla G. Serventi G. Poulet F. Capaccioni F. Langevin Y. Gardes E. Martinez R. Boduch P. Domaracka A. Rothard H.
Investigating Reflectance Properties of Mercury's Surface Material: Effect of Swift Heavy Ion Irradiation **[#6037]**
Mercury's surface is affected by space weathering processes, interesting mineral properties. Here, we present a spectral study of swift heavy ion irradiation of two minerals, olivine and nepheline, as a simulation of heavy ion irradiation at Mercury.

11:06 a.m. Izenberg N. R. * Denevi B. W.
Exploring Space Weathering on Mercury Using Global UV-VIS Reflectance Spectroscopy **[#6081]**
We apply UV analysis methods used on lunar LROC data to Mercury to explore space weathering maturity and possibly evidence of shocked minerals.What says the UV //about shock, maturity //on dear Mercury?

11:18 a.m. Klima R. L. * Blewett D. T. Denevi B. W. Ernst C. M. Murchie S. L. Peplowski P. N. Perera V. Vander Kaaden K.
Carbon on Mercury's Surface — Origin, Distribution, and Concentration **[#6097]**
Low-reflectance material on Mercury, excavated from depth, may contain up to 5wt% carbon in some areas of the planet. We interpret this as endogenic carbon associated with the earliest crust of Mercury.

11:30 a.m. Peplowski P. N. * Stockstill-Cahill K. R.
Mercury's Geochemical Terranes Revisited **[#6032]**
We applied analytical tools to redefine Mercury's major geochemical terranes. The composition and petrology of each terrane will be discussed, along with analyses of gamma-ray data aimed at deriving absolute abundances of Si and Mg in each terrane.

11:42 a.m. Stockstill-Cahill K. R. * Peplowski P. N.
Geochemical Constraints for Mercury's PCA-Derived Geochemical Terranes **[#6119]**
PCA-derived geochemical terranes provide a robust, analytical means of defining these terranes using strictly geochemical inputs. Using the end members derived in this way, we are able to assess the geochemical implications for Mercury.

11:54 a.m. Meslin P.-Y. * Peplowski P. N. Deprez G.
Radon Outgassing from the Surface of Mercury Evidenced by Its Low Th/U Ratio **[#6111]**
The low, subchondritic Th/U ratio measured by MESSENGER can be explained by the release of radon from the Hermean regolith, and the corresponding exhalation rate is significantly larger than on the Moon, possibly indicating a thicker regolith.

12:06 p.m. LUNCH

Thursday, May 3, 2018
EXOSPHERE/MAGNETOSPHERE:
NEW RESULTS WITH A LOOK TO THE FUTURE
1:30 p.m. USRA Conference Center

Chairs: Carl Schmidt
Jamie Jasinski

1:30 p.m. Merkel A. W. * Vervack R. J. Jr. Cassidy T. A. Killen R. M. McClintock W. E. Nittler L. R. Burger M. H.
First Evidence Connecting Mercury's Magnesium Exosphere to the Regional Composition of Mercury's Surface from MESSENGER Observations **[#6104]**
First results revealing a direct connection between the distribution of Mg in the exosphere and the regional distribution of Mg on Mercury's surface.

1:42 p.m. Pokorny P. * Sarantos M. Janches D.
A Comprehensive Model of the Meteoroids Environment Around Mercury **[#6106]**
We present a comprehensive dynamical model for the meteoroid environment around Mercury comprised of meteoroids originating in asteroids, short and long period comets. Our model is fully calibrated and provides predictions for different values of TAA.

1:54 p.m. Sarantos M. * Pokorny P. Janches D. MESSENGER UVVS Team
Correlation of Mercury's Magnesium Exosphere with Micrometeoroids from Jupiter Family Comets **[#6096]**
We show that the peak density of Mg vapor observed by MESSENGER varies with Mercury True Anomaly Angle in the same way as the modeled micrometeoroid vapor from Jupiter Family Comets.

2:06 p.m. Cassidy T. A. *
MESSENGER MASCS/UVVS Observations of Cold Exospheric Calcium **[#6108]**
Exospheric calcium is primarily ejected by a high energy process on the dawn hemisphere. UVVS data also show a sporadic cold component at low altitudes. Its temperature is consistent with laboratory measurements of photodesorption of calcium sulfide.

2:18 p.m. Al Asad M. M. * Johnson C. J. Philpott L. C.
The Topology and Dynamics of Mercury's Tail Plasma and Current Sheets **[#6047]**
In Mercury's environment, the tail plasma and current sheets represent an integral part of the dynamic magnetosphere. Our study aims to understand the time-averaged, as well as the dynamic, properties of these "sheets" in 3D space using MAG data.

2:30 p.m. Dewey R. M. * Slavin J. A. Raines J. M. Baker D. N. Lawrence D. J.
Energetic Electron Acceleration, Injection, and Transport in Mercury's Magnetosphere **[#6073]**
Electrons are accelerated in Mercury's magnetotail by dipolarization events, flux ropes, and magnetic reconnection directly. Following energization, these electrons are injected close to Mercury where they drift eastward in Shabansky-like orbits.

2:42 p.m. Milillo A. * Murakami G. Zender J.
BepiColombo MPO-MMO Coordinated Observations for the Study of the Environment of Mercury **[#6030]**
This presentation intends to show the coordinated activity within the Mercury's environment science community for maximizing the BepiColombo science return.

2:54 p.m. BREAK

Thursday, May 3, 2018
A VERITABLE SMORGASBORD OF MERCURY GEOLOGICAL DELIGHTS
3:10 p.m. USRA Conference Center

Chairs: David Blewett
Indhu Varatharajan

3:10 p.m. Helbert J. * Maturilli A. D'Amore M. Varatharajan I. Hiesinger H. MERTIS team
MERTIS — Unleashing the Power of the Thermal Infrared on Mercury **[#6061]**
MERTIS combines an imaging spectrometer (7-14 µm at 500m spatial resolution) with a radiometer (7 to 40 µm at 2km). The compositional, temperature and thermo-physical properties maps provided will allow unique insights into the evolution of Mercury.

3:22 p.m. Maturilli A. * Helbert J. Varatharajan I. D'Amore M. Hiesinger H.
A Spectral Library of Emissivity Spectra for MERTIS on BepiColombo **[#6060]**
At PSL we measured emissivity spectra in vacuum for a suite of Mercury surface analogues for temperatures from 100°C to >400°C. The spectral library is completed by reflectance on samples fresh and post-heating (0.2 to 200 µm spectral range).

3:34 p.m. Malliband C. C. Conway S. J. * Rothery D. A. Balme M. R.
Potential Identification of Sublimation-Driven Downslope Mass Movement on Mercury **[#6093]**
We have identified a further example of mass movement, in addition to the previously identified example in the pyroclastic vent NE of Rachmaninoff. Both examples show evidence of hollow sublimation being a cause of the mass movements.

3:46 p.m. Blewett D. T. * Chabot N. L. Denevi B. W. Ernst C. M.
The Nature of Mercury's Hollows, and Space Weathering Close to the Sun **[#6051]**
Hollows are a landform that appear to form by loss of a volatile-bearing phase from silicate rock. Hollows are very young and are likely to be forming in the present day. Hollows may be an analog for extreme weathering on near-Sun asteroids.

3:58 p.m. Parman S. W. * Orlando T. M. Milliken R. E. Head J. W. Jones B. M. Anzures B. A.
Experimental Study of Hollow Formation **[#6103]**
Hollows are enigmatic features on the surface of Mercury caused by sublimation and/or space weathering. Here we propose a comprehensive experimental study in which candidate hollows materials are exposed to a range of relevant conditions.

4:10 p.m. Wright J. * Conway S. J. Balme M. R. Rothery D. A.
Post-Deposition (and Ongoing?) Modification of Caloris Ejecta Blocks **[#6071]**
Caloris ejecta blocks have been modified by mass-wasting that has persisted long after their formation. Volatiles may be involved in this process. Block geomorphology therefore has implications for Mercury's interior volatile content.

4:22 p.m. Fassett C. I. * Hirabayashi M. Ostrach L. R. Watters W. A. Whitten J. L.
The Nature and Mobility of Regolith on Mercury's Smooth Plains from Observations of Crater Degradation and Equilibrium Size-Frequency Distributions **[#6129]**
Measurements of the equilibrium size-frequency distribution and crater degradation jointly suggest a thick regolith on Mercury's smooth plains.

4:34 p.m. Whitten J. L. * Ostrach L. R. Fassett C. I.
Analysis of Large-Scale Resurfacing Processes on Mercury: Mapping the Derain (H-10) Quadrangle **[#6086]**
The Derain (H-10) Quadrangle of Mercury contains a large region of "average" crustal materials, with minimal smooth plains and basin ejecta, allowing the relative contribution of volcanic and impact processes to be assessed through geologic mapping.

4:46 p.m. Bott N. * Doressoundiram A. Perna D. Zambon F. Carli C. Capaccioni F.
The Shakespeare (H-03) Quadrangle of Mercury: From Color Mapping to Distinction of Lithological Heterogeneities **[#6040]**
We analysed the spectral properties of the surface in the H-03 quadrangle of Mercury to define its compositional variability and identify spectral units constrained by opportune spectral parameters.

4:58 p.m. **Invited:** Galluzzi V. * Rothery D. A. Massironi M. Ferranti L. Mercury Mapping Team
Towards the Redefinition of the Global Stratigraphy of Mercury: The Case of Intermediate Plains **[#6041]**
Observations based on an average mapping scale of 1:400k provide context for the redefinition of the global stratigraphy of Mercury. Results show that the Intermediate Plains unit should be re-introduced as an official mappable terrain.

5:13 p.m. Adjourn

CONTENTS

Sodium Ion Dynamics in the Megnetospheric Flanks of Mercury. S. Aizawa[1,2] (aizawas@pat.gp.tohoku.ac.jp), D. Delcourt[3], and N. Terada[1] , [1]Department of Geophysics, Graduate School of Science, Tohoku University.(Sendai, Japan), [2]LPP (Paris, France), [2]LPC2E (Orléans, France)

Abstract: We investigate the transport of planetary ions in the magnetospheric flanks of Mercury. In situ measurements from the MESSENGER spacecraft show evidences of Kelvin-Helmholtz instability development in this region of space, due to the velocity shear between the downtail streaming flow of solar wind originating protons in the magnetosheath and the magnetospheric populations. Ions that originate from the planet exosphere and that gain access to this region of space may be transported across the magnetopause along meandering orbits.

We examine this transport using single particle trajectory calculations in model MHD simulations of the Kelvin-Helmholtz instability. We show that heavy ions of planetary origin such as Na^+ may experience prominent nonadiabatic energization as they $\boldsymbol{E}\times\boldsymbol{B}$ drift across large-scale rolled up vortices. This energization is controlled by the characteristics of the electric field burst encountered along the particle path, the net energy change realized corresponding to the maximum $\boldsymbol{E}\times\boldsymbol{B}$ drift energy. This nonadiabatic energization also is responsible for prominent scattering of the particles toward the direction perpendicular to the magnetic field.

The Topology and Dynamics of Mercury's Tail Plasma and Current Sheets M. M. Al Asad[1], C. L. Johnson[1,2], and L. C. Philpott[1] [1]Dept. of Earth, Ocean and Atmospheric Sciences, The University of British Columbia, Vancouver, BC, Canada. [2]Planetary Science Institute, Tucson, AZ. Corresponding author's e-mail address: malasad@eoas.ubc.ca

Introduction: The arrival of MErcury Surface, Space ENvironment, Geochemistry, and Ranging (MESSENGER) at Mercury in 2011 revealed a highly dynamic magnetosphere that interacts strongly with the solar wind and the Interplanetary Magnetic Field (IMF). Mercury's heliocentric distance changes from 0.47 AU at aphelion to 0.31 AU at perihelion, resulting in annual variations in solar wind dynamic pressure [1]. The magnetosphere also responds to shorter time scale variations in IMF and solar wind conditions [2].

Here, we use vector magnetic field data to investigate Mercury's tail plasma and current sheets, and their interaction with the solar wind. First, we establish the time-averaged topology of the tail plasma and current sheets. Second, we investigate how their topology changes in response to dynamic solar forcing.

Time-Averaged Properties: The diamagnetic behavior of the plasma trapped in the night-side equatorial region results in reduced magnetic field strength relative to the field in the tail lobe region. We derive the topology of the plasma "sheet" in 3D by spatially mapping the night-side region in which the field magnitude is reduced. The results (Figure 1) show that: (1) The region of increased plasma density starts at ~0.6 R_M (where R_M is Mercury radius = 2440 km) from the surface of the planet on the night side in the noon-midnight plane, and has a thickness of 0.34 R_M. (2) As distance from the planet increases on the night-side, the plasma sheet thins gradually to 0.28 R_M at the MESSENGER night side observational limit of 2.8 R_M. (3) The plasma sheet thickness increases substantially toward dawn and dusk, to a value of 0.7 R_M at 1.5 R_M distance away from the noon-midnight plane.

Two distinct current distributions have been observed in the plasma sheet. The first, ten times more common than the second, is a bifurcated current sheet structure that has two current density peaks at an average distance of 0.25 R_M north and south of the magnetic equator. The mean maximum current density in this scenario is 100 nAm^{-2}. The second distribution resembles that of a classic Harris sheet [3] in which the current density peaks at the magnetic equator (170 nAm^{-2}) and monotonically decreases away from it.

Dynamic Response: To directly relate the response of the current sheet to the dynamic solar wind, simultaneous measurements of the magnetic field inside and outside Mercury's magnetosphere are desirable. As this was not possible with MESSENGER, several studies [4,5] have attempted to establish proxies for estimating the solar activity while the MESSENGER spacecraft was inside the magnetosphere. We use the disturbance index [4] and the ram pressure [5] to establish the behavior of the current sheet when the solar forcing changes and find two clear responses. The first is an increase in the tail lobe magnetic field (and thus the magnetic pressure) with increasing solar wind pressure. The second is a decrease in thickness of the plasma sheet and an increase in current density of the current sheet embedded in it. The two observations are consistent: increasing the magnetic pressure on the current sheet from the northern and southern tail lobes causes the sheet to thin and compresses the total current into a smaller region, thus increasing its density.

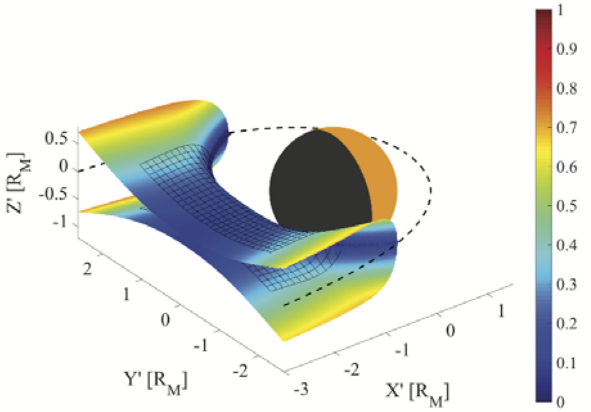

Figure 1: The modelled 3-D shape of Mercury's tail plasma sheet using magnetic field measurements. The colors represent the thickness in R_M. The X', Y', Z' coordinate system is derived from the Mercury-Solar-Orbital, MSO (see e.g., [1]) system, but shifted in the Z_{MSO} direction such that data are aligned relative to the magnetic equator crossing on an orbit-by-orbit basis and then aberrated for solar wind direction.

References: [1] Winslow, R. M. et al. (2013), *JGR Space Physics*, 118, 2213–2227, doi:10.1002/jgra.50237. [2] Slavin, J. A., et al. (2012), *JGR*, 117, A01215, doi:10.1029/2011JA016900. [3] Harris, E. G. (1962), Il Nuovo Cimento Series 10. [4] Anderson, B. J. et al. (2013), *G-cubed*, 14, 3875–3886, doi:10.1002/ggge.20242. [5] Johnson, C. L. et al. (2016), *GRL*, 43, 2436–2444, doi:10.1002/2015GL067370.

The Mercury Electron Analyzers onboard the Bepi Colombo Mercury Magnetospheric Orbiter. N. André[1], J.-A. Sauvaud[1], C. Aoustin[1], A. Fedorov[1], H.-C. Seran[1], E. Le Comte[1], M. Petiot[1], J. Rouzaud[1], A. Barthe[1], E. Penou[1], Y. Saito[2], S. Yokota[2], Q.-M. Lee[1], D. Moirin[1], C. Garat[1], A. Cadu[1], P. Rouger[1], J.-L. Medale[1], [1] IRAP, CNRS/UPS/CNES, Toulouse, France (nicolas.andre@irap.omp.eu), [2]ISAS, Japan

Abstract: Bepi Colombo is a joint mission between ESA and JAXA that is scheduled for launch in 2018 and arrival at Mercury in 2025. A comprehensive set of particle sensors will be flown onboard the two probes that form Bepi Colombo. Onboard the Mercury Magnetospheric Orbiter (MMO) the Mercury Electron Analyzers (MEA) sensors constitute the experiment dedicated to fast electron measurements between 3 and 25,500 eV. They consist of two top-hat electrostatic analyzers for angle-energy analysis followed by microchannel plate multipliers and collecting anodes. A notable and new feature of MEA is that the transmission factor of each analyzer can be varied inflight electronically by a factor reaching up to 100, thus allowing to largely increasing the dynamical range of the experiment. This capability is of importance at Mercury where large changes of electron fluxes are expected from the solar wind to the various regions of the Mercury magnetosphere. Taking advantage of the spacecraft rotation with a 4 s period, MEA will provide for the first time fast three-dimensional distribution functions of magnetospheric electrons, from energies of the solar wind and exospheric populations (a few eVs) up to the plasma sheet energy range (some tens of keV). The use of two sensors viewing perpendicular planes allows reaching a 1=4 spin period time resolution, i.e., 1 s, to obtain a full 3D distribution.

EFFECT OF SULFUR SPECIATION ON CHEMICAL AND PHYSICAL PROPERTIES OF REDUCED MERCURIAN MELTS. B. A. Anzures[1], S. W. Parman[1], R. E. Milliken[1], [1]Department of Earth, Environmental, and Planetary Sciences, Brown University, Providence, RI, 02906. Email: brendan_anzures@brown.edu

Introduction: Mercury is a geochemical and mechanical endmember among the terrestrial planets, largely due to its low oxygen fugacity. The Earth, Moon, and Mars have similar mantle fO_2 between IW-2 and IW+2 [1]. S solubility in magmas is low at these conditions and is present as an important but minor element (<0.1wt%) [2]. In contrast, the Mercurian surface exhibits high S concentrations (1.5-4wt%) [3], suggesting a mantle fO_2 between IW-3 and IW-7 based on silicate-metal-sulfide equilibria [4]. Studies of low fO_2 systems are also applicable to the petrologic evolution of enstatite chondrite parent bodies [5] and perhaps early Earth [6] and exoplanets orbiting C-rich suns [7].

Due to the decreasing O at these low fO_2 conditions, S^{2-} fills in as a 2nd major anion, changing the partitioning behavior of many elements and modifying the physical properties of the silicate melt. In this study, we use S K-edge X-ray Absorption Near Edge Structure (XANES) spectroscopy to quantify the coordination chemistry of S in silicate melts at heavily reduced conditions [8]. The results provide insights into the effect of S on the chemical and physical properties of Mercurian melts.

Results: XANES analysis of the experimental glasses exhibit a positive K-edge shift due to a decrease in the FeS and Na_2S peak as fO_2 decreases. The contribution of MgS is seen in all spectra. CaS is obvious only at the lowest fO_2. The XANES analyses demonstrate that FeS and Na_2S are destabilized at low fO_2, MgS becomes the dominant species, and CaS is a minor species in heavily reduced basaltic melts (Fig 1). These trends are robust over the the compositional range given in wt% (FeO = 0.01-0.12, MgO = 8.91-29.25, CaO = 6.19-11.20, Na_2O = 0.46-4.61), and they show a correlation with Fe, Mg, and Na, but not Ca content. FeS, MgS, and CaS trends are consistent with previous Raman results [2] and prediction of Na^+ for charge balance [9].

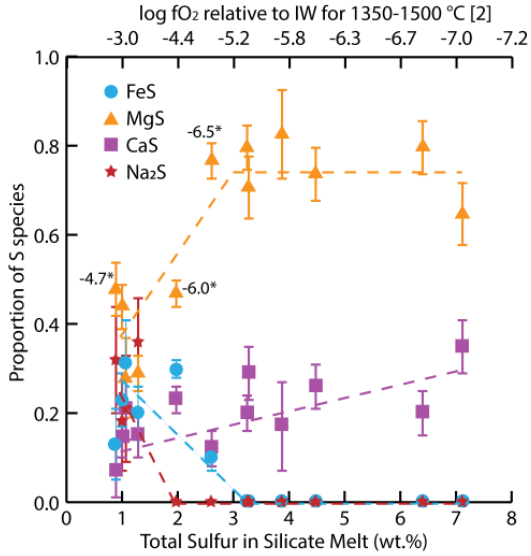

Figure 1. *Sulfide speciation in experimental glasses from LCF analyses of the XANES spectra. The proportion of the S species in the melt represented by FeS and Na_2S decreases, MgS increases, and CaS increases as S content increases and fO_2 decreases. Experiments run at 1GPa and 1250-1475 °C. Error is RSS of the 1σ SD and fitting error. *fO_2 recalculated for lower T*

Discussion: The sulfide speciation trend has important ramifications for Mercurian magmas and other reduced rocky bodies. The bonding of S with Fe, Mg, Ca, and Na will reduce the activites of FeO (when present), MgO, CaO, and Na_2O, affecting the silicate phase equilibria. Applying the S speciation trends to Mercurian melt chemistry, any iron in the silicate melt exists as FeS rather than FeO at these reducing conditions. The effective concentrations of MgO, CaO, and Na_2O are reduced by up to 28%, 53%, and 20% respectively relative to their original values. S complexing also increases the activity of SiO_2. As such, S speciation must be accounted for in thermodynamic models at these reducing conditions, including those calculating fO_2 from activities of FeO [4] or SiO_2 [10].

These changes in activity stabilize pyroxene with respect to olivine [11], and destabilize Ca-bearing silicates like feldspar and clinopyroxene. This implies enstatite should be enriched in the Mercurian mantle. The increased stability of (Mg,Ca)S in the melt suggests it may be the dominant sulfide in Mercury's crust.

Changing S speciation should also affect the physical properties of the melts. Sulfide complexing increases the activity of SiO_2, which should increase polymerization and viscosity [11]. Melt density should be affected by what S species form in the melt: (density Na_2S < CaS, MgS < FeS). Density might also increase with S solublity since S has twice the atomic weight of O. Changing viscosity and density will have substantial influences on both magma eruption dynamics, as well as the evolution of a Mercurian magma ocean.

Methods: See LPSC2018 abstract [12]

References: [1] Wadhwa M. (2008) *RIMG, 68,* 493-510. [2] Namur O. et al. (2016) *EPSL, 448*, 102-114. [3] Nittler L. R. et al. (2011) *Science, 333,* 1847–1850. [4] Zolotov M. Y. et al. (2013) *JGR, 118*, 138-146. [5] Berthet S. et al. (2009) *GCA, 73,* 6402-6420. [6] Dauphas (2017) *Nature, 541*, 521-524. [7] Ebel D. S. et al. (2011) *Planet. & Space Sci., 59,* 1888-1894. [8] Fleet M. E. (2005) *CANMIN, 43*, 1811-1838. [9] Métrich et al. (2009) *GCA, 73,* 2382-2399. [10] Cartier et al. (2014) *Nature, 7*, 573-576. [11] Namur et al. (2016) *EPSL, 439*, 117-128. [12] Anzures et al. (2018) *LPSC XLIX*, Abstract #1694.

INTERIOR VOLATILE RESERVOIRS IN MERCURY. B. A. Anzures[1], S. W. Parman[1], R. E. Milliken[1], J. W. Head[1], [1]Department of Earth, Environmental, and Planetary Sciences, Brown University, Providence, RI, 02906. Email: brendan_anzures@brown.edu

Introduction: Magmatic volatiles such as H, C, S, Cl, N, and F play crucial roles in the production, transport, and eruption of magmas. One significant result from MESSENGER was that Mercury's surface is volatile-rich with high S (1-4 wt.%) [1], C (1-3 wt.%) [2], Cl (0.09-0.48 wt.%) [3], and K/Th [4]. N and F were not measured. There is also extensive geomorphological evidence for explosive volcanism [5] driven by expansion of volatiles exsolved on ascent [6] dated to 1-3.25 Gyr [7]. Volatiles carried by magmas are stored in minerals that make up the crust, mantle and core. The implication is that Mercury's interior is volatile-rich perhaps due to low fO_2 [8,9]. A key path forward is a concerted experimental study of volatiles in minerals at Mercury-relevant conditions. Preliminary data on H, C, S, F and Cl solubility in olivine & orthopyroxene as a function of fO_2 will be presented.

Pyroclastic deposits also provide clues for what volatiles drove their eruption. Explosive volcanism on Mercury has been studied through geomorphology [10-12] with one study of NE Rachmaninoff showing depletion of S and C [13]. However, NE Rachmaninoff may not be representative of all pyroclastic deposits as it is the largest, and one of the few not located within an impact crater [13]. Possible sources of eruption-driving volatiles are 1) degassing in magma derived from mantle source regions, 2) formation of volatile species by chemical reactions in melt or assimilation of crustal wall-rock [8], and 3) volatile build-up in stalled dikes [12]. We concur with Weider et al. [13] that future chemical measurements at higher spatial resolution of pyroclastic deposits should be a priority.

Methods and Preliminary Results: Experimental samples of an estimated Mercurian mantle composition [14] were run in a piston cylinder at 1-2 GPa with fO_2 between IW-3.4 and IW-7.5. Volatile abundances in minerals and glass were analyzed by SIMS at WHOI. Assuming volatile saturation, we expect there to be at most 4-11 ppm S and 0.66-40 ppm C in the silicate mantle seen in fig. 1. However, volatile saturation is unlikely and H has not been measured in Mercurian lavas to date. Mineral-melt partitioning (D) values are $4.3x10^{-4}$ to $2.4x10^{-5}$ for S, and $4.5x10^{-6}$ to $8.0x10^{-4}$ for C for IW-3.4 and IW-5.7, respectively. This implies S and C will be enriched in silicate melts.

Future Measurements: More measurements over a larger range of P, T, fO_2 and mineral compositions are underway. Measurements of volatile speciation in melts, from XANES, FTIR, and Raman, are also required. These are needed to estimate the volatile budget of the mantle at different fO_2, and what volatiles drove formation of pyroclastics. For BepiColombo and beyond, more measurements of 1) surface volatiles and 2) pyroclastic deposits should be emphasized.

Implications: Future volatile measurements at higher spatial resolution paired with experimental results can constrain conditions of melting and subsequent eruption on Mercury. We hope to spark discussion on the following questions: Why are pyroclastic deposits more prevalent (larger number, average size, vent length [12]) on Mercury than on the Moon? What is the speciation of CNOSH volatiles at low fO_2? What are the main mineral repositories of volatiles in the crust and mantle? Does Mercury's volatile-rich nature reflect its end-member low fO_2 geochemistry or require changes in our overall understanding of volatile-depletion in the early Solar System?

References: [1] Nittler L. R. et al. (2011) *Science, 333,* 1847–1850. [2] Peplowski P. N. et al. (2016) *Nature, 9*, 273. [3] Evans L. G. et al. (2015) *Icarus, 257*, 417-427. [4] Peplowski P. N. et al. (2011) *Science, 333*, 1850-1852. [5] Head J. W. et al. (2009) *EPSL, 285*, 227-242. [6] Wilson L. and Head, J. (2017*) Icarus 283*, 146-176. [7] Goudge T. A. et al. (2014) *JGR, 119*, 635-658. [8] Zolotov M. Y. (2011) *Icarus, 212*, 24-41. [9] McCubbin F. M. et al. (2012) *GRL, 39*. [10] Kerber L. et al. (2011) *PSS, 59*, 1895-1909. [11] Thomas R. J. et al. (2014) *JGR, 119*, 2239-2254. [12] Jozwiak, L. et al. (2018) *Icarus 302*, 191-212. [13] Weider S. Z. et al. (2016) *GRL, 43*, 3653-3661. [14] Anzures B. A. et al. (2018) *LPSC XLVIV*, Abstract #1694. [15] Shcheka S. S. et al. (2006) *EPSL, 245*, 730-742. [16] Callegaro S. et al. (2014) *Geology, 42*, 895-898. [17] Dalou C. et al. (2012) *Contributions to Mineralogy and Petrology, 163*, 591-609.

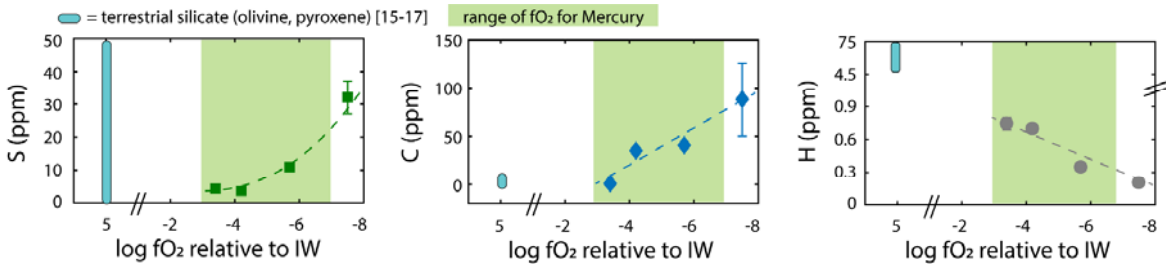

Figure 1. *Volatile content of silicate minerals in experimental Mercurian samples compared with terrestrial silicates. C and S appears to increase, and H appears to decrease with more reducing conditions.*

IMPACT-BASIN FORMATION ON MERCURY: CURRENT OBSERVATIONS AND OUTSTANDING QUESTIONS. David M. H. Baker[1], James W. Head[2], and Caleb I. Fassett[3], [1]NASA Goddard Space Flight Center, Greenbelt, MD USA (david.m.hollibaughbaker@nasa.gov), [2]Dept. of Earth, Environmental and Planetary Sciences, Brown University, Providence, RI USA, [3]NASA Marshall Space Flight Center, Huntsville, AL USA.

Introduction: Mercury provides an important laboratory for understanding the formation of large impact craters and basins due to its large population of such structures and unique gravity environment, impact velocity distribution, crustal structure and thermal profile, and composition. Data from the MESSENGER spacecraft have allowed for detailed analyses of the changes in the geology and morphometry that occur in the size-morphology progression from complex craters to large basin structures. Here, we summarize some of these results and identify outstanding questions for future studies with current datasets and those anticipated from BepiColombo.

Crater to Basin Transition: With increasing size, basin formation is marked by the change in interior uplift structure from a central peak to a ring of peaks ("peak ring") (Fig. 1). Updated catalogs defined the transition diameter for Mercury to be ~110 km [1,2]. Unlike the Moon, multiple interior uplift morphologies for a given size occur over a broad diameter range of 84-168 km, which may be related to the broader range of impact velocities occurring at Mercury. Mercury also has the largest population of peak-ring basins (N=110) and transitional basins, or protobasins (N=70) (Fig. 1), of any planetary body.

Peak-Ring Basin Morphometry: Topography from the Mercury Laser Altimeter (MLA) and MDIS-derived DEMs show that many peak-ring basins have unusually deep central cavities that are lower in elevation than the annular floor between the peak ring and basin wall (Fig. 1). Further, the diameters of central peaks fall along a separate power law trend from the diameter of peak-rings, suggesting an abrupt transition in interior morphology [3].

Peak-Ring and Floor Materials: Many peak rings expose low reflectance material (LRM) that is derived from deeper crustal layers [e.g., 4]. Also common are "hollows," appearing brighter and bluer in MDIS multispectral data [5]. Resurfacing of the floors of peak-ring basins by volcanism, shown by red-colored plains in MDIS data, is also common [4]; however distinguishing between thin volcanic plains and impact melt is often difficult.

Basins >300 km: Peak-ring basins give way to larger, and possibly multi-ring, basins around 300 km. Mercury has 46 "certain and probable" basins (300-1550 km) and 41 additional "suggested but unverified" basins [6]. In contrast to the many well-preserved peak-ring basins on the planet, most large basins (>75%) have only one prominent ring with little evidence for additional rings. These basins appear to be highly resurfaced and often have a deep central depression and surrounding topographic benches (Fig. 1).

Outstanding Questions: Observations from MESSENGER data have left a trove of questions that may be addressed through future data analysis and orbital data from BepiColombo: 1) Why are true multi-ring basins relatively rare on Mercury? What are the relative roles of volcanic resurfacing, lack of ring formation or viscous relaxation? 2) Why are the central floors of peak-ring basins so deep compared with the rest of the floor? 3) What is the composition and sampling depth of peak rings? 4) What are the relative influences of impact velocity and target variations on observed basin structure? 5) What controls the formation of the unique interior structures within protobasins? 6) How can impact melt be confidently identified in and surrounding large impact structures?

References: [1] Baker, D.M.H. et al. (2011) PSS 59, 1932–1948; [2] Baker, D.M.H. and J.W. Head (2013) PSS 86, 91–116; [3] Baker, D.M.H. et al. (2016) Icarus 273, 146–163; [4] Murchie, S.L. et al. (2015) Icarus 254, 287–305; [5] Blewett, D.A. et al. (2011) Science 333, 1856 – 1859. [6] Fassett, C.I. et al. (2012) JGR 117, E00L08.

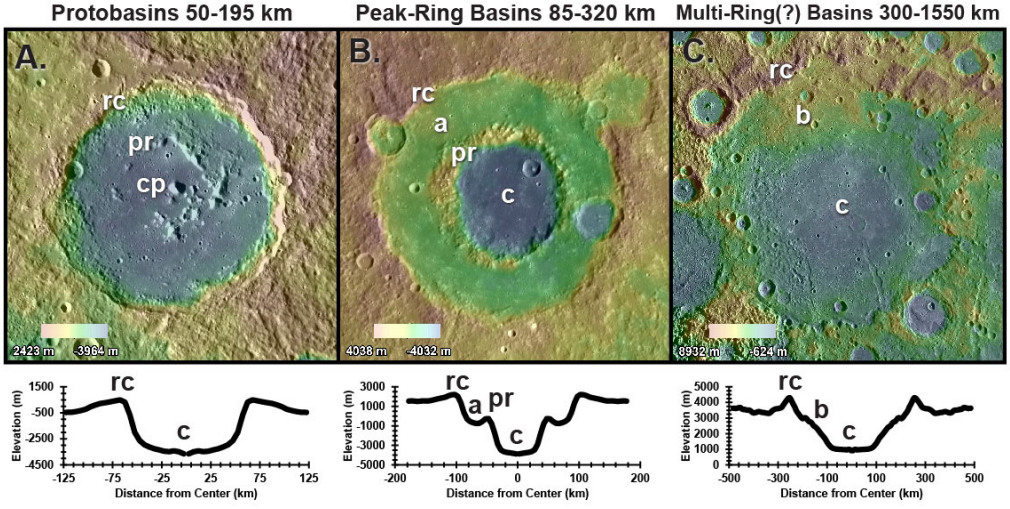

Fig. 1. The transition from protobasins (A, Velasquez), peak-ring basins (B, Dürer), and large (possibly multi-ring) basins (C, Sanai) on Mercury. Top panels are MDIS image mosaics with an MDIS-derived USGS DEM colored topography. Below are azimuthally averaged topographic profiles. rc= rim crest, pr=peak ring, cp=central peak, a=annulus, c=central cavity, b=bench.

REVISED AGE CONSTRAINTS FOR MERCURY'S KUIPERIAN AND MANSURIAN STRATIGRAPHIC SYSTEMS

S. M. E. Banks[1], Z. Xiao[2], S. Marchi[3], C. R. Chapman[4], N. G. Barlow[5], and C. I. Fassett[6], [11]NASA Goddard Space Flight Center, Greenbelt, MD, maria.e.banks@nasa.gov, [2]School of Earth Sciences, China University of Geosciences, Wuhan, Hubei, P. R. China, [3]NASA Lunar Science Institute, Southwest Research Institute, Boulder, CO, [4]Department of Space Studies, Southwest Research Institute, Boulder, CO, [5]Northern Arizona University, Flagstaff, AZ, [6]NASA Marshall Space Flight Center, Huntsville, AL.

Introduction: Following an approach similar to that used for the Moon, Mercury's surface units were subdivided into five time-stratigraphic systems using Mariner 10 images: (oldest to youngest) pre-Tolstojan, Tolstojan, Calorian, Mansurian, and Kuiperian [1]. The absolute time scale originally suggested for the time periods associated with these systems was based on the assumption that a lunar-like impact-flux history applied to Mercury [1] (Table 1). To assess age constraints for the Kuiperian and Mansurian, we use high-resolution and multi-band images obtained by the MErcury Surface, Space ENviroment, GEochemistry, and Ranging (MESSENGER) spacecraft to catalog impact craters interpreted to be Mansurian and Kuiperian in age [2]. Using the recent crater model production function (MPF) and inner solar system chronology of [3], we use the densities of these crater populations to estimate age boundaries.

Data and Method: Morphologically fresh Mansurian- and Kuiperian-aged craters are identified by their crisp and sharp morphologies, well-preserved rims, few or no superposed craters, continuous ejecta with radial lineaments, and well-defined secondary craters [e.g., 1,2, 4, 5, 6]. Kuiperian craters have bright ray systems. Our Kuiperian catalog includes rayed craters identified over 98.4% of Mercury's surface [2,7]. The Mansurian catalog includes craters (Mansurian- and Kuiperian-aged) identified between 40° north and south latitude [2,8]. Craters were included down to diameters of 7 km to assure that the catalogs are complete at larger diameters.

The MPF of [3] incorporates current knowledge and understanding of impact populations. We use the impactor size–frequency distribution of Near Earth Objects, hard rock crater scaling relations, target strength of $Y_0 = 2 \times 10^7$ to 2×10^5 Pa, and target and projectile densities of 3.4 g/cm^3 and 2.6 g/cm^3, respectively. Model age fits were applied to craters ≥20 km in diameter. For comparison, we investigate model ages with the production function of [9] using non-porous scaling relations (Table 1).

Results: We assess relative crater frequency by calculating the cumulative number of craters equal to or larger than a given diameter D, N(D), normalized to an area of 10^6 km^2 (Table 2). Using the MPF of [3], we estimate model ages of ~1.7 ± 0.2 Ga and ~280 ± 60 Ma [2] for the populations of craters formed since the onset of the Mansurian and Kuiperian, respectively (Table 1).

Discussion: Results indicate that both the Mansurian and Kuiperian have shorter time scales and began much more recently than the lunar Eratosthenian and Copernican respectively. Although different PFs [3,9] yield differing estimated ages (Table 1), they consistently indicate ages for the onset of the Mansurian and Kuiperian that are significantly more recent, and indicate time spans that are ≥~40% and ≥~70% shorter in duration, than previously assumed [1]. A more recent onset of the Mansurian also points to a significantly longer time span for the Calorian, which may have extended ~2 billion years after the cessation of volcanism associated with Mercury's youngest widespread smooth plains, ~3.6 Ga [e.g., 10]. Results are consistent with higher impact flux and surface erosion rates on Mercury compared to the Moon. Knowledge of the absolute time scale associated with Mercury's stratigraphic systems provides constraints for our understanding of Mercury's geologic, thermal, and tectonic evolution.

References: [1] Spudis P. D., Guest J. E. (1984) Mercury, Univ. Ariz. Press, 118–164. [2] Banks M. E. et al. (2017), JGR, 122, 1010–1020. [3] Marchi S. S. et al. (2009) ApJ, 137, 4936–4948. [4] Leake M. A. (1982), NASA TM-84894, 3–535. [5] Strom, R. G. et al. (2015) Res. Astron. and Astrophys., 15, 3, 407–434. [6] Banks M. E. et al. (2015), JGR, 120, 1751–1762. [7] Xiao Z. et al. (2012), LPSC 43, #2143. [8] Braden S.E., Robinson M. S. (2013) JGR, 118, 1903–1914. [9] Le Feuvre, M., Wieczorek, M.A. (2011), Icarus, 214, 1–20. [10] Byrne, P.K. et al. (2016), GRL, 43, 7408-7416. [11] Ernst, C.M. et al. (2017) LPSC, 48, #2934..

Time Interval	Approximate Age of Onset		
	Assumed by [1]	PF of [9]	PF [3]
Kuiperian	1.0	0.13[a]	0.28[a]
Mansurian	3.0-3.5	0.85[a]	1.7[a]
Calorian	3.9	3.1[b]	3.7[b]
Tolstojan	3.9-4.0	3.7[b]	3.9[b]

Table 1. Estimated model ages for the base of Mercury's systems (Ga). Ages from [1] and using the PF of [9] are included for reference and comparison. [a][2]. [b][11].

Time Interval		Crater Densities	
		N(20)	N(30)
Kuiperian		1.3 ± 0.1	0.6 ± 0.1
Mansurian		8.9 ± 0.4	4.1 ± 0.3
Calorian	Caloris Basin Rim	~41 ± 9[a]	NA
	Caloris Basin Interior	29 ± 4[a]	NA
Tolstojan (Tolstoj Basin: Goya Formation)		93 ± 15[a]	NA

Table 2. Relative crater frequencies [2]. Error range is ± 1 standard deviation (square root of the number of craters normalized to an area of 10^6 km^2). [a]Spatial density results from [11] included for the Calorian and Tolstojan for comparison.

ENERGETIC NEUTRAL ATOM (ENA) IMAGING OF MERCURY'S MAGNETOSPHERE ONBOARD BEPICOLOMBO. S. Barabash[1], M. Wieser[1], Y. Futaana[1], M. Holmström[1], K. Asamura[2], Y. Saito[2] and P. Wurz[3], [1] Swedish Institute of Space Physics, Box 812, S-98128, Kiruna, Sweden (stas.barabash@irf.se), [2] Institute of Space and Astronautical Science, 3-1-1 Yoshinodai, Sagamihara, Japan, [3]University of Bern, Physikalisches Institut, CH-3012 Bern, Switzerland

ENAs at Mercury: ENAs (Energetic Neutral Atoms) at Mercury are produced by (1) charge-exchange of energetic ions in the near-planet environment with the planetary exosphere, (2) sputtering, and (3) backscattering of precipitating ions from the planetary surface [1], [2], [3]. Mercury has a tenuous exosphere but sufficiently dense to convert solar wind and planetary ions into ENAs via charge - exchange. The ENA fluxes are close to the ones emerging from the Earth's ring current. What is unique for Mercury is the high variability of Mercury's magnetosphere giving rise to pulsating ENA emissions (ENA "flashes") with a period of a minute or less. Due to the small size of the magnetosphere, the particles injected from the tail can fill up the entire dayside magnetosphere [4], making possible ENA imaging the shape of the magnetosphere.

Ions of the solar wind, accelerated in the tail, and planetary ions, precipitate on Mercury's surface, result in sputtering. The energy spectrum of the sputtered products falls off as E^{-2} (Thompson-Siegmund sputtering) and may result in high fluxes at energies larger than 10-100 eV, sufficient for detection.

The third process resulting in ENA production is backscattering of the precipitating solar wind and planetary ions from Mercury's surface. Recently it was shown that the lunar regolith backscatters up to 20% of the impinging protons as neutral hydrogen atoms. Since the solar wind flux impinging on the surface is high (up to 10^9 $cm^{-2}s^{-1}sr^{-1}$) this process results in very high hydrogen ENA fluxes (10^6 – 10^7 $cm^{-2}s^{-1}sr^{-1}$), which will dominate all other sources [5]. The energy of the backscattering hydrogen is up to the energy of the impinging ions and thus well above few 10s eV. ENAs originated from backscattering (and also sputtering) can be used to visualize the precipitation regions in the same way as the terrestrial aurora shows magnetospheric dynamics (ENA "aurora").

ENA instrument: The ENA instrument (ENA, Energetic Neutrals Analyzer) onboard the Mercury Magnetospheric Orbiter (MMO) of BepiColombo (Fig. 1) is based on the surface conversion technique and provides measurements of ENAs in the energy range 10 eV – 3.3 keV. ENAs enter the instrument through an electrostatic charged particle deflector, which rejects ambient charged particles by a static electric field. The incoming neutral atoms are then converted to positive ions on an ionization surface and then pass through an electrostatic analyzer (ESA) of a specific ("wave") shape that effectively blocks photons. The electrostatic analyzer also provides crude energy analysis. After exiting the ESA, ions are post accelerated up to an energy of 1.5 keV and impact on a START surface releasing kinetic secondary electrons and are reflected towards the STOP MCPs where they are detected and produce a STOP pulse. The secondary electrons from the START surfaces are guided to the START MCPs and produce a START pulse. The START and STOP timing gives the particle velocity. Combining the TOF measurements and ESA settings one determines the neutral atoms energy and mass. Measuring the azimuth of the ion hit on the START surface by position sensitive START MCPs allows accurate determination of the arrival azimuth angles of the incoming neutral atoms. The instrument characteristics are given up in Table 1.

Table 1. ENA instrument performance

Parameter	Value
Energy Range	10 eV – 3.3 keV
Energy Resolution,	△E/E = 50%
Mass Resolution	H, O, Heavy
Pure G-Factor/sector	10^{-2} cm^2 sr eV/eV
Total Efficiency	~1 %
Angular resolution	
For < 50 eV (FWHM)	9° x 40°
For > 50 eV (FWHM)	9° x 25°
Field of view	15° x 160°

Fig. 1 ENA instrument on BepiColombo / MMO

References: [1] Barabash S. et al. (2001) PSS, 49, 1685-1692. [2] Lukyanov, A., S. Barabash S. et al. (2004) Adv. Space Res., 33, 1888-1896. [3] Mura, A. et al. (2006) PSS 54, 144-152. [4] Kallio E. and Janhunen P. (2003) Geophys. Res. Lett. 30, 1877. [5] Lue C. et al. (2017) Icarus 296, 39–48.

CONSTRAINTS ON THE TIMING OF TECTONIC ACTIVITY ON MERCURY'S LARGE-SCALE LOBATE-SCARP THRUST FAULTS. N.G. Barlow[1] and M. E. Banks[2], [1]Dept. Physics & Astronomy, Northern Arizona University, Flagstaff, AZ 86011-6010 Nadine.Barlow@nau.edu, [2]NASA/Goddard Space Flight Center, Greenbelt, MD maria.e.banks@nasa.gov.

Introduction: Lobate scarps deform all major geologic units on Mercury, providing valuable insight into the history of horizontal shortening on Mercury [1-2]. These landforms consist of curving or lobate cliffs produced by surface-breaking thrust faults. They can extend more than 500 km in length with up to ~3 km of vertical relief [1-4]. Their formation has been attributed primarily to compressional stresses produced by planetary cooling and global contraction [1–3, 5]. Understanding the history of crustal deformation provides constraints on thermal history models and insight into the interplay between tectonics and volcanism and the cooling and solidification of the interior [5]. We use a combination of cross-cutting relationships, crater morphology, and crater size-frequency distribution (CSFD) analysis to determine relative and absolute ages of Mercury's largest lobate-scarp thrust-faults.

Data and Methods: Orbital images and mosaics from the MErcury Surface, Space ENvironment, GEochemistry, and Ranging (MESSENGER) Mercury Dual Imaging System (MDIS) are used to identify all craters transected by or superposing the scarf face edge of Mercury's 30 large-scale named scarps. Relative ages of the faults were determined from cross-cutting relationships between the craters and scarps based on the crater degradation state; craters of different ages exhibit different amounts of degradation ranging from sharp morphologies and the presence/absence of rays (Kuiperian and Mansurian craters, respectively), to moderately degraded (Calorian craters), and heavily degraded (Tolstojan and pre-Tolstojan craters) morphologies, characterized by subdued rims, infilling of the crater floor, and superposing craters [6-8].

The narrowness of faults led to the Buffered Crater Counting technique (BCCT), which uses only craters and/or their ejecta that directly superpose the fault to determine the fault's age [9]. However, the low number of superposed craters leads to large uncertainties in the age of the fault. We developed a Modified Buffered Crater Counting technique (MBCCT) which uses superposed and transected craters in a larger area surrounding the fault to improve the statistical significance of the resulting absolute age. The MBCCT measures diameters of all craters directly superposing or transected by the fault edge and uses the mean diameter (□) of these craters to calculate a buffer size around the fault, where the distance of the buffer edge from the fault is 1.5□. All craters ≥5-km-diameter within the buffer are included in the analysis and are classified as pre- or post-dating the fault based on their degradation state compared to the craters directly superposing or transecting the fault. A test area indicates the MBCCT gives statistically equivalent results to the BCCT, but with smaller error bars.

Absolute ages were computed using the Marchi crater model production function and inner solar system chronology [10]. Absolute and relative estimated ages of the earliest (transected craters) and most recent detectable activity (end of peak activity; superposing craters) were assessed for each lobate-scarp thrust fault; periods of most-recent activity are shown in Fig. 1 relative to Mercury's stratigraphic periods utilizing the recently revised age boundaries [10-11].

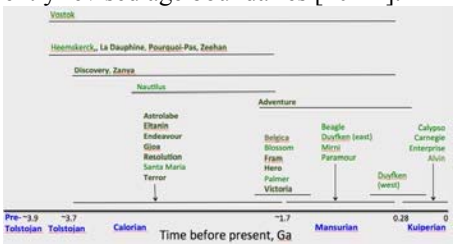

Figure 1: Period of most-recent activity along the large-scale lobate-scarp thrust faults. Length of horizontal lines is the uncertainty. Scarps polewards of 40° latitude shown in green.

Results: All scarps in this study crosscut surfaces Tolstojan or older in age (>~3.7 Ga). The most recent detectable activity along lobate-scarp thrust faults ranges from Calorian to Kuiperian (~3.7 Ga to present). Our MBCCT results complement previous relative-age studies with absolute ages and indicate global contraction continued over the last ~3-4 Gyr. At least some thrust fault activity occurred on Mercury in relatively recent times (<280 Ma).

Scarps poleward of ~40° S latitude generally do not show conclusive evidence of activity on associated thrust faults more recently than the end of the Calorian (~3.7-1.7 Ga). Scarps at latitudes north of ~40° S show evidence of activity ranging from Calorian to the Kuiperian. This might have implications for Mercury's thermal and tectonic evolution near the end of volcanism associated with it's youngest widespread smooth plains, ~3.6 Ga [12].

References: [1] Strom, R. G., Trask, N. J., and Guest, J. E. (1975) *JGR*, *80*, 2478–2507. [2] Watters, T. R. et al. (2009) *Earth Planet. Sci. Lett.*, *285*, 283–296. [3] Watters, T. R., Robinson, M. S., and Cook, A. C. (1998) *Geology*, *26*, 991–994. [4] Watters, T. R. et al. (2004) *GRL*, *31*, L04071, doi:10.1029/2003GL019171. [5] Solomon, S. C. et al. (2008) *Science*, *321*, 59–62. [6] Spudis, P. D. and Guest, J. E. (1984) in *Mercury*, U. Ariz. Press, 118–164. [7] Banks M. E. et al. (2015), *JGR*, *120*, 1751–1762. [8] Banks M. E. et al. (2017), *JGR*, *122*, 1010–1020. [9] Fassett C. I. and Head J. W. (2008) Icarus, 195, 61-89. [10] Marchi, S. S. et al. (2013) *Nature*, *499*, 59–61. [11] Ernst, C.M. et al. (2017) *LPSC*, 48, #2934. [12] [10] Byrne, P.K. et al. (2016), *GRL*, 43, 7408-7416.

BEPICOLOMBO – THE NEXT STEP OF MERCURY EXPLORATION WITH TWO ORBITING SPACECRAFT.

J. Benkhoff[1], [1]ESA/ESTEC, SCI-S, 2200AG Noordwijk, The Netherlands (johannes.benkhoff@esa.int).

Introduction: Mercury is in many ways a very different planet from what we were expecting. In October 2018 BepiColombo [1] will be launched to follow up on answering the fundamental questions about the evolution history of the planet nearest to the sun.

BepiColombo is a joint project between the European Space Agency (ESA) and the Japanese Aerospace Exploration Agency (JAXA). The Mission consists of two orbiters, the Mercury Planetary Orbiter (MPO) and the Mercury Magnetospheric Orbiter (MMO). From their dedicated orbits the two spacecraft will be studying the planet and its environment.

The mission has been named in honor of Giuseppe (Bepi) Colombo (1920–1984), who was a brilliant Italian mathematician, who made many significant contributions to planetary research and celestial mechanics.

Science goals: BepiColombo will study and understand the composition, geophysics, atmosphere, magnetosphere and history of Mercury, the least explored planet in the inner Solar System. In particular, the mission objectives are:

- to understand why Mercury's uncompressed density is markedly higher than that of all other terrestrial planets, Moon included
- to understand and determine the nature of the core of Mercury
- to understand why such a small planet processes an intrinsic magnetic field and investigate Mercury's magnetized environment
- to investigate if the permanently shadowed craters of the Polar Regions contain Sulphur or water ice
- to study the production mechanisms of the exosphere and to understand the inter-action between planetary magnetic field and the solar wind in the absence of an ionosphere
- to obtain new clues about the composition of the primordial solar nebula and about the formation of the solar system
- to test general relativity with improved accuracy, taking advantage of the proximity of the Sun. Since and considering that the advance Mercury's perihelion was explained in terms of relativistic space-time curvature.

Science Payload: The MPO scientific payload comprises eleven instruments/instrument packages and the MMO comprises 5 instruments/instrument packages to study the planet itself and its environment, respectively. The MPO will focus on a global characterization of Mercury through the investigation of its interior, surface, exosphere and magnetosphere. In addition, it will be testing Einstein's theory of general relativity. The MMO will focus on the plasma and particle environment and the magnetosphere. .

Expected results: Together, the scientific payload of both spacecraft will provide the detailed information necessary to understand Mercury and its Magnetospheric environment and to find clues to the origin and evolution of a planet close to its parent star. The BepiColombo mission will complement and follow up the work of NASA's MESSENGER [2] mission by providing a highly accurate and comprehensive set of observations of Mercury. In addition, the BepiColombo mission will provide a rare opportunity to collect multi-point measurements in a planetary environment. This will be particularly important at Mercury because of short temporal and spatial scales in the Mercury's environment. The foreseen orbits of the MPO and MMO will allow close encounters of the two spacecraft throughout the mission.

References: [1] Benkhoff, J., et al. (2010) Planet. Space Sci. 58, 2-20. [2] McNutt R.L., S.C. Solomon, R.E. Gold, J.C. Leary and the MESSENGER Team (2006) Adv. in Space Res. 38, 564-571.

MERCURY SCIENCE OBJECTIVES AND TRACEABILITY WITHIN THE BEPICOLOMBO PROJECT : OPTIMIZING THE SCIENCE OUTPUT OF THE NEXT MISSION TO MERCURY. S. Besse[1], J. Benkhoff[2], M. Bentley[1], T. Cornet[1], R. Moissl[1], C. Munoz[1], J. Zender[2], [1]ESA/ESAC, Bepi Colombo Science Ground Segment, Madrid, Spain (sbesse@sciops.esa.int), [2]ESA/ESTEC, Bepi Colombo Science Ground Segment, Noordwijk, Netherlands.

Introduction: BepiColombo is Europe's first mission to Mercury. It will set off in 2018 on a journey to the smallest and least explored terrestrial planet in our Solar System. When it arrives at Mercury in late 2025, it will gather data during its 1 year nominal mission, with a possible 1-year extension. The mission comprises two spacecraft: the Mercury Planetary Orbiter (MPO) and the Mercury Magnetospheric Orbiter (MMO). BepiColombo is a joint mission between ESA and the Japan Aerospace Exploration Agency (JAXA), executed under ESA leadership.

Science at Mercury: The scientific interest in going to Mercury lies in the valuable information that such a mission can provide to enhance our understanding of the planet itself as well as the formation of our Solar System; information which cannot be obtained with observations made from Earth. The science mission will consist of two separate spacecraft that will orbit the planet. ESA is building one of the main spacecraft, the Mercury Planetary Orbiter (MPO), and the Institute of Space and Astronautical Science (ISAS) at the Japan Aerospace Exploration Agency (JAXA) will contribute the other, the Mercury Magnetospheric Orbiter (MMO).
The BepiColombo mission relies on the valuable observations and science discoveries obtained by the MESSENGER and Mariner 10 missions in the past years and decades. Those discoveries shape the description of science objectives to be performed by the 11 instruments onboard the MPO spacecraft, and the 5 instruments onboard the MMO. In order to optimize the science planning and outcome of the mission, the BepiColombo Science Ground Segment (SGS) is developing strategies, tools, and workflows that will enable the science teams of the MPO spacecraft to maximize the science to be performed at Mercury.

Science Objectives and Traceability: As for every mission, the overall scientific goals are discussed in numerous documents. For Bepicolombo, those objectives are well summarized in [1]. They cover three main areas of scientific investigation of Mecury: Surface, Interior, and Exosphere. The BepiColombo Science Working Team (SWT) is supported by three scientific Working Groups (WG) that represents these science themes, 1) Surface and Composition, 2) Geodesy and Geophysics, and 3) Hermean Environment. Following the mission science objectives, those working groups provide a more detailed Science Traceability Matrix (WG-TMX) that helps to define the observation strategies and priorities.

To close the gap between the WG-TMX and the implementation of observations performed by individual instrument teams, the SGS is developing, in collaboration with the instrument teams, targeted science traceability matrix of each instruments (Inst-TMX). These Inst-TMX (linked to the WG-TMX) represent the essence of the science objectives of Bepicolombo. The SGS is using the TMX concept in a similar way to other projects (e.g., Cassini, JUICE), with an emphasisis on tracking them.

The Inst-TMX are defined in such a way that they can be tracked (using specific IDs) during the observation lifecycle (request, planning, commanding to the spacecraft, and downlink) until product generation. For instance, requirements on the spacecraft and instruments operations are listed (e.g., pointing, duration, etc..). This information is critical to ensure:

- the evaluation of observations success needed to perform science investigations, and
- a progress report on the evolution of the observations, in order to reschedule if needed and optimize the planning

In addition, measurements performed and received data will be analysed, quality checked, and traced back to the TMX.

During the conference, we will present the developement status of the science-observation tracking system for BepiColombo. The SGS welcomes any suggestions, improvements, and new or refined science goals that will help improving the science done at Mercury.

References:

[1] Benkhoff et al. (2010) PSS.

ANALYSIS OF PYROCLASTIC DEPOSITS USING MESSENGER MASCS OBSERVATIONS. S. Besse[1], A. Dorresoundiram[2], L. Griton[2], [1]ESA/ESAC, Madrid (sbesse@sciops.esa.int), [2]Observatoire de Paris Meudon, France.

Introduction: Volcanism exposed on the surface of planets is a unique opportunity to have a view within the interior, and Mercury is no exception with the confirmation of widespread volcanism on the surface [1,2,3]. In addition, the surprising high concentration in volatile elements [4], and the poor concentration in iron of its surface with respect to its core are highlighting the complex history of Mercury.
While [3] have shown that Pyroclastics Deposits (PDs) are spectrally flat and similar in albedo to those on the Moon, [5] highlighted the ultraviolet (UV) and visible (VIS) characteristics of 35 PDs. [6] detailed analysis of Caloris' PDs have confirmed the UV and VIS properties of the PDs, and also added that PDs are distinguishable in the near-infrared (NIR) domain with respect to Mercury's background. [6] also demonstrated that similarly to the Moon [7], spectral properties of PDs of the Caloris basin change as a function of distance to the source.

In this follow up analysis of [6], the number of individual PDs studied is increased, covering different latitudes and longitudes of Mercury's surface in addition to different geological context. This help to disregard space weathering as the primary factor for the spectral properties changes of Mercury's PDs in the UV, VIS or NIR. We use the latest delivery of spectra to the Planetary Data System (PDS) by the MESSENGER science team to increased both the number of spectra that can be analysed, and the spatial resolution of the footprints with dedicated observations of some PDs. This aspect is very important to confirm the spectral variability of PDs as a function of distance first noticed by [6], and analysed if this is a common characteristics observed for all PDs on Mercury.

Analysis: Using the prodedures of [6], the spectral analysis of PDs located close to the Hesiod crater is performed, so as the well recognised NE-Rachmaninoff PDs, together with other localised PDs such as Lermontov, Mistral and Murasaki. All the PDs presented in this study, and previously [6], show a decrease of the VIS-slope and UV-downturn as a function of distance to the source of the PDs. In the case of NE-Rachmaninoff, both the absolute value of the slope of the UV and VIS parameters are similar whatever the spatial location they are taken from. The selected orbits of NE-Rachmaninoff are covering different location of the deposits, Figure 1. This spatial consistency of the parameters is indicating an isotropic distribution of the parameters. The fact that the deposits are isotropic is a fundamental information to understand the formation mechanism of the PDs. The variability of the Hesiod deposits is however indicating the differences between the PDs at the scale of the planet. Hesiod D and E show lower absolute value of the parameters, and lower decrease as a function of distance (i.e., shallower slope).

Variations of the UV-downturn produced by mean of space weathering was described as less likely by [5,6]. Using the careful selection of spectra, and with the better statistical analyses, no correlation can be found between the variability of the UV-downturn and/or VIS-slope with the longitude of the PDS. Additionally, comparisons of PDs spectral behavior with fresh looking impact craters does not support space weathering as responsible for the spectral properties of PDs.

During the conference, we will present our best understanding of the spectral and spatial variability of the PDs. The implications of these results in the understanding of the formation mechanism will be discussed at length.

References:
[1] Head J. et al. (2011) Science. [2] Prockter L. et al. (2010) Science. [3] Kerber L. et al. (2011) PSS. [4] Nittler L. et al. (2011) Science. [5] Goudge T. et al. (2014) JGR. [6] Besse S. et al. (2015) JGR. [7] Jawin E. et al. (2015) JGR.

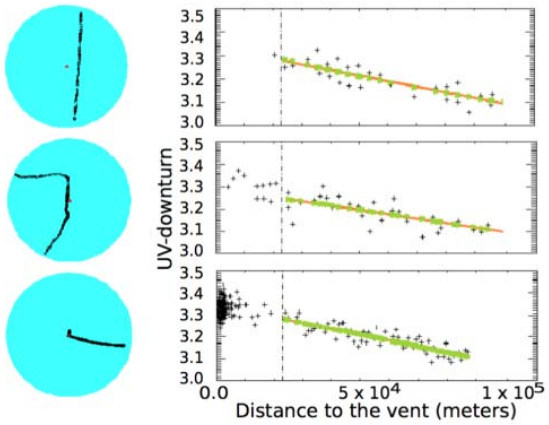

Figure 1: On the left, footprints of three orbits from the MASCS instrument above the NE-Rachmaninoff PDs. On the right, spatial decrease of the UV-downturn as a function of distance from the centre of the PDs.

THE NATURE OF MERCURY'S HOLLOWS, AND SPACE WEATHERING CLOSE TO THE SUN. David T. Blewett[1,*], Nancy L. Chabot[1], Brett W. Denevi[1], and Carolyn M. Ernst[1]. [1]Johns Hopkins University Applied Physics Laboratory, Laurel, USA. (*david.blewett@jhuapl.edu).

Introduction: Mercury's hollows are shallow, irregularly shaped, rimless depressions, often with high-reflectance interiors and haloes [1–4]. Their morphology suggests that they are relatively young and formed via sublimation-like loss of a volatile-bearing phase through solar heating, UV photolysis/destruction, contact with molten rock, or bombardment by micrometeoroids and/or ions.

Hollows are almost always found in association with impact craters and basins, occurring on the floors, walls, ejecta, and central peaks. The presence of hollows on Mercury is likely an expression of the planet's surprisingly high content of volatile elements [e.g., 5, 6]. Candidate phases involved in hollows formation include sulfides [1, 2, 7], chlorides [2, 8] and graphite [9, 4].

Depths: Hollows have flat floors and walls that are straight (brink to floor). It appears that as the volatile is lost, the remaining material weakens and crumbles, leading to ground collapse and scarp retreat of the kind thought to form similar landforms on icy surfaces (Mars, icy satellites) [10]. During an examination of all MESSENGER images with pixel scales <20 m and incidence angles <85°, shadow-length measurements made on 552 images yielded the depths of 2608 hollows [4]. The mean depth is 24 ± 16 m. The narrow range of depths, despite formation within units that are of much greater and more variable thickness, could result from development of a lag that thickens as the volatile-bearing phase is lost, eventually protecting the substrate from further assault.

Formation Rates: Estimates of the rate at which hollows form can be made if the age of an impact crater that hosts hollows can be determined. The size–frequency distribution of Mercury's rayed (Kuiperian) craters >7 km in diameter gives absolute model ages of 130 to 280 Myr [11], depending on the crater production model. Hollows on the western floor of the Kuiperian crater Balanchine appear to have formed by scarps retreating by a distance of ~300 m [4]. The average rate of hollows formation by horizontal scarp retreat for a 130 Myr model age would be 1 cm per ~4300 Earth years. If Balanchine formed 280 Myr ago, then the average growth rate would be 1 cm per ~9300 yr. These are lower limits because it is not known if the hollows began to grow immediately after the Balanchine-forming impact. For context, the erosion of kilogram-sized rocks on the lunar surface by micrometeoroid bombardment is ~1 cm per 10^7 yr [12]. Aeolian abrasion rates of different rock types in Antarctica [13] are between 1 cm per 667 yr and 1 cm per 100 yr.

Haloes: Photometric evidence [14] indicates that the high-reflectance haloes are characterized by finer particle size or lower sub-resolution roughness than ordinary regolith. How are the high-reflectance haloes formed? Previous suggestions [2] included comet-style lofting of dust by gases generated as volatiles sublime. Consideration of the physics of dust lofting [4] indicates that, given Mercury's high surface gravitational acceleration, unreasonably high fluxes of sublimating gas would be needed to lift micrometer-size silicate grains. Therefore, the bright haloes may instead form by dispersal via energetic thermal decomposition, electrostatic dust levitation, re-condensation of sublimated material, or by physical modification or chemical alteration of the surface by re-deposited sublimation products.

Near-Sun Asteroids: Phaethon is a C-complex, Near-Sun asteroid (NSA) with a perihelion distance of 0.14 AU. Phaethon develops a dust tail near perihelion [15], likely because of thermal dehydration of phyllosilicates and degradation of organic components [16].

The environment of Mercury (perihelion distance = 0.31 AU), with a high flux of high-speed micrometeoroids, high solar-wind flux, and high temperatures, is more similar to that of NSAs than other explored Solar System bodies. Phaethon may have space weathering outcomes that differ from those of Main Belt or near-Earth C-complex asteroids. Observations of Phaethon by the JAXA DESTINY spacecraft may reveal the presence of unusual landforms produced by extreme space weathering [17], analogous to Mercury's hollows.

References: [1] D.T. Blewett et al. (2011), Science 333, 1856. [2] D.T. Blewett et al. (2013), JGR 118, 1013. [3] R.J. Thomas et al. (2014), Icarus 229, 221. [4] D.T. Blewett et al. (2016), JGRP 121. [5] S.Z. Weider et al. (2012), JGRP 117, E00L05. [6] L. Kerber et al. (2011), PSS 59, 1895. [7]. J. Helbert et al. (2013), EPSL 369–370, 233. [8] L. Evans et al. (2015), Icarus 257, 417. [9] S.L. Murchie et al. (2015), Icarus 254, 287. [10] J.M. Moore et al. (1996), Icarus 122, 63. [11]. M.E. Banks et al. (2017), JGRP 122, 1010. [12] D.G. Ashworth (1977), in Cosmic Dust, Wiley. [13]. M.C. Malin (1987), Antarctic J. U.S. 22, 38. [14] D.T. Blewett et al. (2014), Icarus 242, 142. [15] D. Jewitt et al. (2013), Ap. J. Lett. 771, L36. [16] M. Delbo and P. Michel (2011), Ap. J. Lett. 728, L42. [17] D.T. Blewett (2018), LPSC 49, #1038.

SPECTROSCOPY OF MINERALS ANALOGS OF MERCURY UNDER THE HERMEAN CONDITIONS: THE EFFECT OF THE TEMPERATURE. N. Bott[1], R. Brunetto[2], C. Carli[3], F. Capaccioni[3], A. Doressoundiram[1], Y. Langevin[2], D. Perna[1,4], F. Poulet[2], G. Serventi[3], M. Sgavetti[3], F. Borondics[5], and C. Sandt[5], [1]LESIA - Observatoire de Paris - CNRS-Sorbonne Université - Université Paris-Diderot (5 place Jules Janssen, 92195 Meudon, France; nicolas.Bott@obspm.fr), [2]Institut d'Astrophysique Spatiale - CNRS - Université Paris-Sud, Orsay, France, [3]Istituto di Astrofisica e Planetologia Spaziali - INAF, Roma, Italy, [4]Osservatorio Astronomico di Roma - INAF, Monte Porzio Catone, Italy, [5]Synchrotron SOLEIL, Saint-Aubin, France.

Introduction: A major result of the MESSENGER mission was to reveal the volcanic hermean surface poor in iron [1], but unexpectedly rich in volatile elements [2]. The high abundance of sulfur on Mercury is particularly interesting, because its sublimation is suggested to trigger the formation of hollows [3]. Laboratory experiments whose aim is to study the evolution of sulfides in the conditions of Mercury's surface are in progress [4]. However, to understand the spectral properties of the surface we need to consider how minerals can be affected by the hermean environment. We present a preliminary study to focus on the effects of these extreme conditions, in particular the strong variations of temperature. The effects of temperature and space weathering on minerals have been already studied [5,6] but rarely at Mercury's conditions [7].

Samples and Setups: We began our activities measuring a loose powder (75-100 µm) of plagioclase Pl3 [8] and 5 mm diameter pellets made with the same Pl3 powder. To simulate the hermean high T conditions, we used a LINKAM (nitrogen purged) cell to heat and cool our samples which allows to measure VIS-IR (0.4-15 µm) spectra as a function of temperature (298-623K). Finally, we used two setups for our spectroscopic analyses: 1) a visible-near infrared spectrometer Maya2000 Pro coupled with a microscope through optical fibers; 2) a near to mid infrared spectrometer coupled with an Agilent microscope, installed at the SMIS beamline [9] of the synchrotron SOLEIL.

Analytical Method: In a typical heating experiment, the powder or the pellet was placed inside the purged heating cell and reflectance spectra were recorded every 50K of increasing temperature. The heating ramp was 5K/min, with a 10-20 min plateau to record the spectrum at a given temperature. A similar cooling cycle was then performed and spectra were measured as a function of deceasing temperature from 623K to 302K.

Preliminary Results: Figure 1 shows the thermal infrared where the Christiansen feature (CF) and the Reststrahlen absorption bands (RB) of silicates are studied. A preliminary qualitative analysis showed a shift towards greater wavelengths for several RB peaks (e.g. at ~9.0 and ~10.5 µm) as a function of increasing T, whereas the CF does not shift. A more quantitative analysis will be presented and discussed.

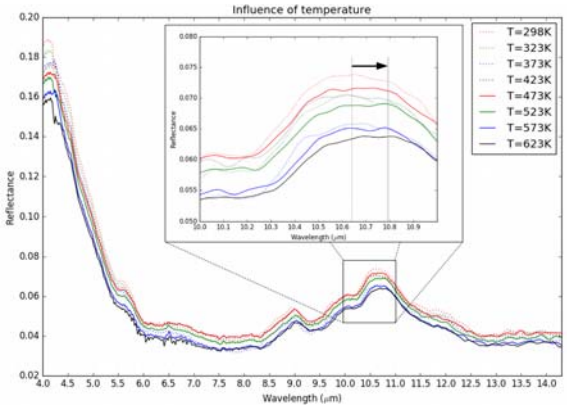

Fig. 1. Mid infrared spectra of a pellet of plagioclase taken at different temperatures (from 298K to 623K).

Future activities: In the next future, we plan to perform more heating experiments to study the evolution of natural minerals, as well as synthetic Mercury-like glasses [10] at temperature during day time. In addition, we consider to take measurements in cold conditions as it is the case on the floor of polar craters of Mercury. Finally, we plan to irradiate our samples with 40 keV ion beams with different fluences as a simulation of slow solar wind irradiation of Mercury.

Acknowledgements: This work is partly supported by the Centre National d'Études Spatiales. The microspectroscopy activities are suppored by grants from Région Ile-de-France (DIM-ACAV) and SOLEIL. D. Perna received funding from the European Union's Horizon 2020 research & innovation programm under the Marie Sklodowska-Curie grant agreement n.664931

References: [1] Peplowski et al. (2011) PSS, 59, 1654-1658. [2] Nittler et al. (2011) Science, 333, 1847-1850. [3] Blewett et al. (2013) JGR, 118, 1013-1032. [4] Varatharajan et al. (2017) EPSC2017-60, 11. [5] Suto et al. (2006) MNRAS, 370, 1599-1606. [6] Brunetto et al. (2014) Icarus, 237, 278-292. [7] Helbert et al. (2013) EPSL, 371, 252-257. [8] Serventi et al. (2013) Icarus, 226, 282-298. [9] Dumas et al. (2006) IP&T, 49, 152-160. [10] Vetere et al. (2017) JGR, 122, 1522-1538.

THE SHAKESPEARE (H-03) QUADRANGLE OF MERCURY: FROM COLOR MAPPING TO DISTINCTION OF LITHOLOGICAL HETEROGENEITIES.

N. Bott[1], A. Doressoundiram[1], D. Perna[1,2], F. Zambon[3], C. Carli[3], F. Capaccioni[3], [1]LESIA - Observatoire de Paris - CNRS - Sorbonne Université - Université Paris-Diderot (5 place Jules Janssen, 92195 Meudon, France; nicolas.Bott@obspm.fr), [2]Osservatorio Astronomico di Roma - INAF, Monte Porzio Catone, Italy, [3]Istituto di Astrofisica e Planetologia Spaziali - INAF, Roma, Italy.

Introduction: Mercury mapping campaign started to support the observational strategy of the SIMBIO-SYS instrument onboard the future BepiColombo spacecraft. A goal is to integrate the color variations due to differences in composition to the photo-interpreted geology of the innermost planet. The used data are image mosaics from the Mercury Dual Imaging System (MDIS) Wide Angle Camera (WAC) onboard MESSENGER spacecraft. Authors identified three major color units (high-reflectance plains, intermediate terrains and low-reflectance material) and two minor color units (red spots and hollows) [1]. We analysed the spectral properties of the surface in the H-03 quadrangle to define its compositional variability and identify units constrained by opportune spectral parameters.

Data Set: The surface of Mercury is subdivided into 15 quadrangles. Some have already been mapped [2,3], others are in progress [4]. Here we focus on the H-03 quadrangle, Shakespeare, with 22.5° < latitude < 65° and 180° < longitude < 270°. We used the data of the 8 following filters: 433.2, 479.9, 558.9, 628.8, 748.7, 828.4, 898.8 and 996.2 nm. The other filters (698.8, 947.0 and 1012.6 nm) can not ensure the coverage of the quadrangle.

Method: To produce the color map, we used the software ISIS (USGS) and we proceeded as follows: 1) Importation of raw data into ISIS format; 2) Georeferencing using SPICE kernels and a DEM produced at DLR [5]; 3) Radiometric calibration; 4) Equirectangular projection; 5) Kaasalainen-Shkuratov photometric correction [6, Table 9] to report the data at standard illumination conditions (inc. i=30°, em. e=0°); 6) Coregistration of images to obtain the mosaic of Shakespeare

Results: Color mapping. We applied techniques of image analysis, such as RGB color combinations and Principal Component Analysis [7], to emphasize differences in spectral properties which can be correlated to variations in composition. Examples of RGB maps of Shakespeare have been shown recently [8]. We will expose and discuss the last updates.

Spectral mapping. From the mosaic 8-color mapping, it is possible to infer interesting spectral parameters to identify units associated to specific terrains. Considering a thresholding of the values of a spectral parameters (reflectance at 750 nm, PC2...), we obtained indications of units, showing different terrains with probable differences in composition (Figure 1).

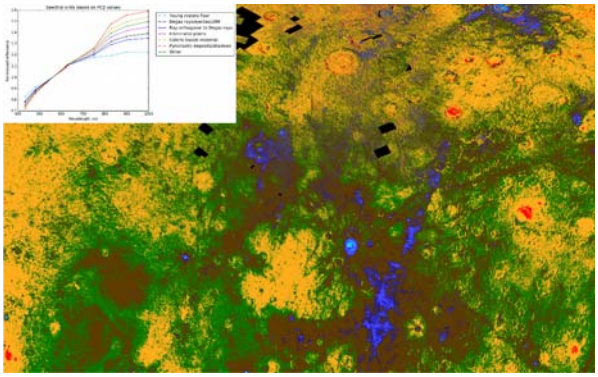

Fig. 1. Example of spectral parameter map of the Shakespeare quadrangle using a thresholding of PC2 values.

For example, it appears on the above map that the floor of Degas crater (cyan) is clearly distinct from other terrains (Sobkou planitia, in yellow on the left) in term of values of PC2. As PC2 highlights the spectral slope variations, it means that the floor of this young crater has a spectral slope distinct from the rest of the quadrangle. This is confirmed on the plot of the normalized averaged spectra of each unit defined by the threshold of this parameter (embedded graph, Fig. 1). More analyses of spectral parameters will be presented.

Future Works: This work on spectral properties of the surface material present in the Shakespeare quadrangle will be integrated to the geological map of the Shakespeare quadrangle produced by [9], and aims to define higher level units to produce a more accurate map of this quadrangle.

Acknowledgements: This work is partly supported by the Centre National d'Etudes Spatiales. D. Perna received funding from the European Union's Horizon 2020 research and innovation programm under the Marie Sklodowska-Curie grant agreement n.664931.

References: [1] Blewett et al. (2009) E&PSL., 285, 272-282. [2] Galluzzi et al. (2016) Journ. of Maps, 12, 227-238. [3] Zambon et al. (2016) Geophys. Research Abstracts, 18, EGU2016-16909. [4] Giacomini et al. (2017) Geophys. Research Abs., 19, EGU2017-14574. [5] Preusker et al. (2017) LPS XLVIII, abstract #1441 [6] Domingue et al. (2016) Icarus, 268, 172-203. [7] Denevi et al. (2009) Science, 324, 613-618. [8] Bott et al. (2017) EPSC abstracts, 11, EPSC2017-283. [9] Guzzetta et al. (2017) Journ. of Maps, 13, 227-238.

EXPERIMENTAL INVESTIGATION OF CHROMIUM BEHAVIOR DURING MERCURY'S DIFFERENTIATION. A. Boujibar[1,2], L. R. Nittler[3], N. Chabot[4], F. M. McCubbin[2], K. Righter[2], K. E. Vander Kaaden[5], T. J. McCoy[6], [1]Geophysical Laboratory, Carnegie Institution for Science, 5251 Broad Branch Rd NW, Washington, DC 20015 (aboujibar@carnegiescience.edu), [2]NASA Johnson Space Center, Houston, TX 77058, [3]Department of Terrestrial Magnetism, Carnegie Institution for Science, Washington, DC 20015, [4]John Hopkins Applied Physics Laboratory, Laurel, MD 20723, [5]Jacobs, NASA JSC, Houston, TX 77058, USA, [6]National Museum of Natural History, Smithsonian Institution, Washington, DC 20013.

Introduction: Mercury is the most reduced terrestrial planet with the largest core/mantle size ratio and highest sulfur concentration on the surface [1, 2]. The MErcury Surface, Space ENvironment, GEochemistry, and Ranging (MESSENGER) spacecraft data allowed mapping of Mercury's surface elemental composition. Recent chromium mapping suggests Mercury's surface has on average 800 ppm Cr with the highest values in the High Magnesium Region [3, 4]. These new data can give clues about Mercury's internal structure and the redox conditions under which it differentiated. In the present study, we present experimental data on the distribution of Cr among metal, silicate and sulfide liquids. We then combine them with data from previous studies and a model of planetary differentiation to discuss Mercury's bulk composition and its oxidation state.

Methods: Experiments were conducted from 0.5 to 5 GPa and 1250 to 1700 °C using piston cylinder and multi anvil press apparatuses at NASA Johnson Space Center. We used a synthetic powder similar to enstatite chondrites in composition. Measurement of Cr concentration in coexisting phases with electron microprobe (EPMA) allowed determining Cr solubility in liquid sulfide and its partition coefficient between liquid metal and silicate.

Results and discussion:

Experimental results. We found that Cr is highly compatible with sulfide liquids (2 to 7 wt%), and its abundance increases with pressure. On the other hand, Cr becomes increasingly siderophile as fO_2 decreases, with the metal-silicate partition coefficient ($D_{Cr}^{met/sil} = X_{Cr}^{metal}/X_{Cr}^{silicate}$) ranging from 5 to 80 at log fO_2 of IW-3 to IW-5 respectively. We compiled literature data on Cr partitioning with our experimental data and retrieved a linear relationship giving log $D_{Cr}^{met/sil}$ as a function of log fO_2.

Model of Mercury's differentiation. Using these results and a model of Mercury's differentiation, we can investigate whether a chondritic bulk composition for Mercury could yield the observed Cr concentration on its surface (800 ppm) [3, 4]. For that, we calculated the distribution of Cr between Mercury's mantle, crust, Fe-rich core and possible sulfide layer at the base of the mantle [2], assuming a chondritic Cr concentration for bulk Mercury of 0.33 [5]. We also considered core and crust mass fractions of 0.68 and 0.032 based on Mercury's gravity field [2, 6] and a distribution of Cr between mantle and crust of 0.05 to 1 based on literature data [7]. Results show that Cr concentration on Mercury's surface is compatible with a chondritic bulk Cr composition. For a model of Mercury's differentiation without any sulfide layer between core and mantle, Mercury's core segregation should have occurred at an fO_2 of 4.5 to 3 log units below iron-wüstite buffer (Fig. 1A), which is in agreement with previous estimations [8-10]. With the presence of a sulfide layer containing 2 to 7 wt% Cr (based on our experimental data), Mercury's fO_2 would be more oxidized (Fig. 1B).

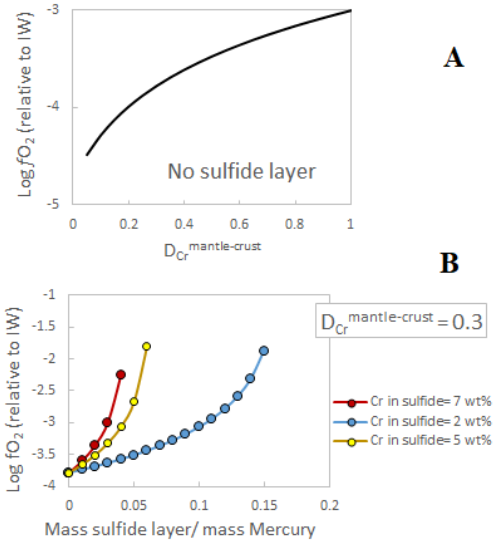

Figure 1: **A:** Resulting oxygen fugacity during Mercury's differentiation, based on surface Cr concentration, as a function of the assumed Cr distribution between mantle and crust, for a model without any sulfide layer at the base of the mantle. **B:** Calculated oxygen fugacity during Mercury's differentiation as a function of the relative mass of the possible sulfide layer.

References: [1] Nittler L. R., et al. (2011) *Science, 333,* 1847–1850. [2] Smith et al. (2012) *Science,* 336, 214-217. [3] Nittler L. R., et al. (2018) *LPS 49*, Abstract #2070. [4] Nittler L. R., et al. (2018), *this meeting.* [5] Wasson J. T. & Kallemeyn, W. (1988) *Phil. Trans. R. Soc. Lond. A,* 325, 535-544. [6] Hauck II et al. (2013) *JGR Planets*, 118, 1204-1220. [7] Cartier C. et al. (2014) *GCA,* 130, 167-187. [8] McCubbin et al. (2012) *GRL, 39*, L09202. [9] Namur O., et al. (2016) *EPSL*, 448, 102–114. [10] McCubbin et al. (2017) *JGR Planets,* 112, 2053-2076.

Production and preservation of sulfide layering in Mercury's magma ocean C.-E. Boukaré [1], S.W. Parman[1], E.M. Parmentier[1], B. Anzures[1], [1]DEEPS, Brown University, 324 Brook St, Providence, RI 02912, stephen_parman@brown.edu

Introduction: Here, we investigate the potential formation of sulfide layering produced by the solidification of a global magma ocean in Mercury. We use experimentally determined sulfur solubility in silicate melts [1] to predict the depth at which sulfides precipitate. The model produces primordial sulfide layers whose thickness and locations depend upon the oxygen fugacity and initial sulfur content of the Mercurian magma ocean. A geodynamic model is then used to test under which conditions the initial mineralogical layering can be preserved during the very early evolution of the Mercury's mantle.

Initial sulfur stratification – We consider the evolution of an essentially iron-free MMO occurring after core mantle segregation (or formation of an FeS layer). We assume that a vigorously convecting molten magma ocean overlies a solid cumulate pile. The oxygen fugacity is equal and uniform in both layers. For simplicity, sulfur content at sulfur saturation (SCSS) in the melt depends only on oxygen fugacity and temperature.

The temperature in the molten region follows an adiabat, whereas it follows the freezing temperature in the cumulate pile. As temperature increases with depth, SCSS also increases with depth. The density of sulfides remains poorly constrained, therefore two end-member models are considered: (1) sulfides perfectly float in the magma ocean (2) sulfides perfectly settle and accumulate when they form. In the first case, we assume that sulfides exsolve at shallow depth (in the top thermal boundary layer of the MO) and are buoyant enough to not be entrained by convection. In the second case, we assume that the saturation condition (SC) in the molten layer is dictated by the temperature at the solidification front. It is important to note that sulfides can also precipitate as liquid at high temperature. If they are negatively buoyant, they would be trapped in the cumulate pile and freeze later upon cooling.

Our approach is based on mass-balance in which the total amount of sulfur is conserved. Figure 1 shows the effects of varying initial sulfur content, oxygen fugacity and sulfides buoyancy on the initial sulfur stratification of the Mercury's mantle. The model demonstrates that the low fO_2 of Mercury can lead to a variety of sulfide layering in the mantle (Figure 1). We are currently investigating the preservation of such primordial sulfur stratification in the Mercury's mantle using a geodynamical model developed for the lunar magma ocean [2,3]. In particular, the last sulfides to precipitate in the MMO would be enriched in radioactive elements such as U, Th and K that could significantly affect the early thermal evolution of Mercury and the composition of magmas erupted on the surface. We are also investigating the evolution of sulfide composition, which should have significant effects on sulfide saturation and buoyancy.

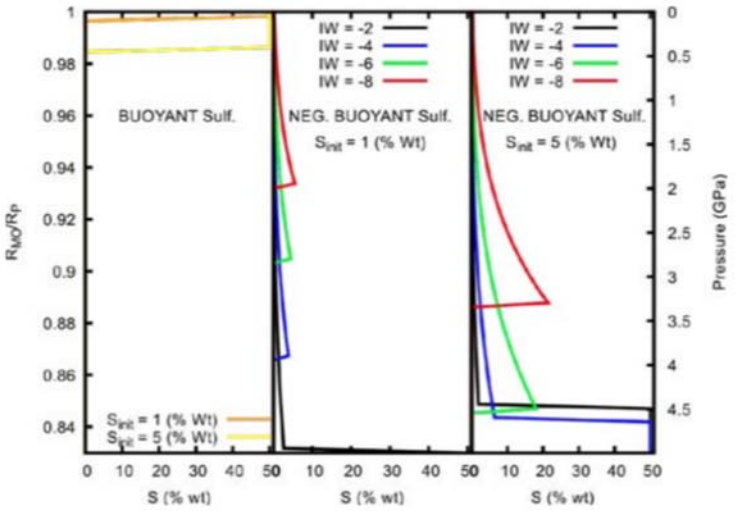

Figure 1. Primitive sulfur stratification imposed by Mercury's magma ocean solidification. (left) Buoyant sulfides- Sulfides exsolve close to surface due to the low surface temperature that induces very low saturation conditions. If surface temperature is low enough (< 1000K) and oxygen fugacity high enough (IW > -8), the size of this "sulfides" crust depends only on the initial sulfur content. (middle) Negatively buoyant sulfides – initial S = 1wt%. As low fO_2 increases SCSS, more reducing conditions delays sulfide saturation in the MO and decreases the depth at which sulfides start to precipitate. (right) Negatively buoyant sulfides – initial S = 5 wt%. Mercury's magma ocean can be saturated in sulfur prior to silicate precipitation if IW < -4. A sulfide layer forms at the bottom of the mantle.

References: [1] Namur et al. (2016) EPSL 448, 102 – 114. [2] Boukaré et al., (2018), EPSL, in revision. [3] Boukaré et al., (2017), LPS XLVIII, Abstract #2494.

VOLCANISM ON MERCURY: (SOME) OPEN QUESTIONS AFTER MESSENGER. Paul K. Byrne[1], Christian Klimczak[2], Jennifer L. Whitten[3], Lauren M. Jozwiak[4], Brett W. Denevi[4], Kathleen E. Vander Kaaden[5], Francis M. McCubbin[6], Lillian R. Ostrach[7], David A. Rothery[8], and Jack Wright[8], [1]Planetary Research Group, Department of Marine, Earth, and Atmospheric Sciences, North Carolina State University, Raleigh, NC 27695, USA (paul.byrne@ncsu.edu), [2]Department of Geology, University of Georgia, Athens, GA 30602, USA, [3]National Air and Space Museum, Smithsonian Institution, Washington, DC 20560, USA, [4]The Johns Hopkins University Applied Physics Laboratory, Laurel, MD 20723, USA, [5]Jacobs, NASA Johnson Space Center, Houston, TX 77058, USA, [6]ARES NASA Johnson Space Center, Houston, TX 77058, USA, [7]U.S. Geological Survey, Flagstaff, AZ 86001, USA, [8]School of Physical Sciences, The Open University, Milton Keynes, MK7 6AA, UK.

Introduction: The MESSENGER mission enabled a remarkable advancement in our understanding of Mercury's volcanic character and history, but the legacy of that mission has also been to challenge us with yet more questions of the innermost planet.

The View After MESSENGER: Recognition that Mercury's two primary surface units, the smooth plains and the intercrater plains, share a similar mode of emplacement [1,2] is strong evidence for voluminous flood-mode volcanism early in the planet's history. Hints of serial effusive eruptions preserved in some smooth plains deposits [3] suggest similar processes for the formerly smooth intercrater plains [2], although geological boundaries along which these older plains can be divided are only starting to be recognized [4]. The identification of such discrete portions would better constrain estimates of effusive volcanic fluxes early in Mercury's history. Similarly, establishing how to distinguish between fluidized ejecta deposits and flood basalts would assist in determining the relative contribution of each of these materials to the early, widespread resurfacing of the planet [2,5,6]. The surprising discovery of explosive volcanism on Mercury [7] also required a reassessment of the planet's volatile inventory [8]. The volatile species that drove these eruptions remain uncertain, as does the timing and duration of pyroclastic activity.

A major outstanding issue relates to the composition of Mercury's rocks, most of which are volcanic. Geochemical measurements from the MESSENGER XRS and GRS indicate that the dominant rock types on the planet are alkali-rich komatiites and boninites [9]. Yet the spatial resolution of these measurements varies considerably across Mercury, and so there may be local differences in surface composition that cannot be resolved with available data, especially in the southern hemisphere. And, at present, there is no independent means by which we can verify these compositions at the outcrop scale or their petrological or mineralogical interpretations: there are no robust candidates for samples from Mercury in any of the world's meteorite collections. As a result, the precise compositions (and compositional variability) of the rocks on the surface of the planet remain to be fully characterized.

Equally unclear is the character of Mercury's very earliest volcanic activity: What were conditions like at the onset of major plains volcanism? Was there a substantial if transient atmosphere from early volcanic outgassing? And is there a record in the planet's crustal stratigraphy of a change in composition from deep to shallow levels that reflects progressively lower degrees of partial melting as interior cooling took hold? Tackling these questions would further enhance our understanding of the thermal evolution of Mercury, and of terrestrial planets in general.

The interplay between the planet's volcanic and tectonic evolution requires more study. For example, the initial state of global contraction is characterized by extension at the surface [10] and so, as Mercury's early lithosphere cooled initially at a rate faster than the interior, it must have experienced tensile stresses in a manner similar to the thermal contraction of ponded lavas [e.g., 11]. Incipient extension has not been substantially investigated for Mercury, and any such deformation probably preceded the emplacement of even the oldest surface now preserved on the planet [6]. Yet an early phase of rifting, in which those rifts facilitated the rapid and widespread eruption of material onto the surface, is consistent with the growing body of evidence that Mercury's early history featured widespread effusive volcanism.

Outlook: Our understanding of Mercury's volcanic character has never been more comprehensive, but there is much left to learn. The MESSENGER mission has given us compelling reasons to continue to investigate Mercury, and it is worth going back [12].

References: [1] Head J. W. et al. (2011) *Science*, *333*, 1853–1856. [2] Whitten J. L. et al. (2014) *Icarus*, *241*, 97–113. [3] Ostrach L. R. et al. (2015) *Icarus*, *250*, 602–622. [4] Denevi B. W. et al. (2016) *LPSC 47*, #1624. [5] Denevi B. W. et al. (2013) *JGR*, *118*, 891–907. [6] Marchi S. et al. (2013) *Nature*, *499*, 59–61. [7] Head J. W. et al. (2009) *EPSL*, *285*, 227–242. [8] Boynton W. V. et al. (2007) *SSR*, *131*, 85–104. [9] Vander Kaaden K. E. et al. (2017) *Icarus*, *285*, 155–168. [10] Dana J. D. (1873) *Am. J. Sci.*, *5*, 423–443. [11] Blair D. M. et al. (2013) JGR, *118*, 47–58. [12] Benkhoff J. et al. (2010) *PSS*, *58*, 2–20.

INVESTIGATING REFLECTANCE PROPERTIES OF MERCURY'S SURFACE MATERIAL: EFFECT OF SWIFT HEAVY ION IRRADIATION.

C. Carli[1], R. Brunetto[2], G. Strazzulla[3], G. Serventi[4], F. Poulet[2], F. Capaccioni[1], Y. Langevin[2], E. Gardes[5], R. Martinez[5], P. Boduch[5], A. Domaracka[5], and H. Rothard[5], [1]IAPS-INAF (Via Fosso del Cavaliere 100, 00133 Roma, Italy; cristian.carli@iaps.inaf.it), [2]IAS-CNRS (Université Paris-Sud, 91405 Orsay, France), [3]OACT-INAF (Via S. Sofia 78, 95123 Catania, Italy) , [4]University of Parma (Parco Area delle Scienze, 11/a, 43124 Parma, Italy), [5]CIMAP, Normandie Univ, ENSICAEN, UNICAEN, CEA, CNRS (CIMAP-Ganil BP 5133, 14070 Caen Cedex 05, France).

Introduction: Mercury's surface is mainly volcanic in origin, spectrally variegate, with evidences indicating low FeO in silicates (e.g. <1% [1]). MESSENGER mission measured the surface composition by XRS and GRS [2]. Geochemical terrains vary from high Mg/Si, in older plains with high Ca/Si, locally high S/Si, and low Al/Si ratios. Northern young plains have higher Al/Si, Na, K, and lower Mg/Si, Ca/Si [e.g. 3]. C was suggested as rest of a primary crust due to floating of graphite [4,5]. Thus, olivine (ol), pyroxene, plagioclase, quartz, and in minor abundance, corundum, nepheline (neph), and Mg-Ca sulfides are proposed as principal minerals in the crust [e.g. 6,7]. Nevertheless, Mercury's surface can be affected by weathering processes, due to the proximity of the Sun and the absence of atmosphere. Thus, spectral properties, from the VNIR to the Thermal Infrared (TIR), can be affected by the environment (e.g. [8]). Here, we present a spectral study of swift heavy ion irradiation of two minerals, ol and neph, as a simulation of heavy ion irradiation of Mercury.

Samples: Ol (Fo_{90}) and neph were prepared in four cm-sized chips. We covered half of the surface of each with a thin film of C. Three chips of each mineral were irradiated at GANIL-IRRSUD (France) with 88 MeV Xe^{23+} ions with fluences of 10^{11}, 10^{12} and 10^{13} ions/cm^2. The sputtering of nepheline was investigated in [9].

Analytical Methods: Spectra were acquired from the VNIR to the TIR (0.4-1.1, 1.1-15 μm) on the unirradiated and irradiated targets. Two setups were used: a) The VNIR spectra were acquired at IAS-Orsay in a diffuse bidirectional configuration, i 30° and e 0°, using a grating spectrometer Maya2000 Pro (Ocean Optics), coupled to an optical microscope (see [10]); b) The NIR-TIR confocal reflectance was investigated with FTIR micro-spectrometers (Agilent Cary 670/620, Thermo Scientific Continum XL and iN10) available at SMIS beamline of synchrotron SOLEIL.

Results: Preliminary analyses show: 1) the film of C reduces the reflectance in the VNIR, whereas it has no effect on the TIR; 2) reflectance in the NIR increases with the ion fluence for samples without C, while it decreases in the VIS, with a consequent reddening. In the TIR, the Christiansen Feature does not shift, whereas the Reststrahlen band peaks are shifted to longer wavelengths with increasing fluence. This continues until the highest fluence, where the samples show signs of amorphisation (Fig.1). Similar trends were observed in ion irradiated meteorites [11,12].

Future works: In preparation of BepiColombo mission, where VNIR and TIR will be investigated by SIMBIO-SYS and MERTIS [13], we plan to investigate several samples, natural and Mercury-like synthetic samples, as suggested by [6,7], and more irradiation conditions than those presented here (e.g. lighter ions and lower energies).

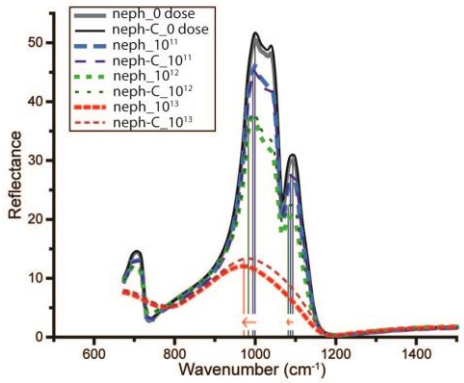

Figure 1 – TIR nepheline spectra with different fluences; we highlighted the major shifts (red arrows).

Acknowledgments: This research was supported by ASI, SIMBIO-SYS project. The microspectroscopy activities are supported by grants from Région Ile-de-France (DIM-ACAV) and SOLEIL. Authors thanks to F.Borondics, C.Sandt, and N.Bott for help and support at SOLEIL and A.Doressoundiram for discussion.

References: : [1] Klima R.. et al., 2014, Whispers; [2] Solomon S.C. et al., 2007, Sp.Sci.Rev., 131, 3-39; [3] Weider S.Z. et al., 2015, EPSL, 416, 109–120; [4] Peplowski P.N. et al., 2016, Nature Geoscience, 9, 273-276; [5] Vander Kaaden K.E. and McCubbin F. 2015, JGR 120, 195-209; [6] Namur O. et al. 2016, EPSL 439, 117-128; [7] Vander Kaaden K.E. et al. 2017, Icarus 285, 155–168; [8] Domingue D.L. et al., 2014, Sp.Sci.Rev. 181, 121–214; [9] Martinez et al. 2017, NIMPB, 406, 523-528; [10] Bonal L. et al. 2015, MAPS, 50, 1562–1576; [11] Brunetto R. et al. 2014, Icarus, 237, 278-292; [12] Lantz C. et al. 2017, Icarus, 285, 43-57, [13] Benkhoff J. et al. 2010, PSS 58, 2-20.

MESSENGER MASCS/UVVS Observations of Cold Exospheric Calcium.

T. A. Cassidy[1]
[1]Laboratory for Atmospheric and Space Physics, University of Colorado (timothy.cassidy@lasp.colorado.edu)

Introduction: MESSENGER's Mercury Atmospheric and Surface Composition Spectrometer-Ultraviolet and Visible Spectrometer (UVVS) regularly observed exospheric calcium. Analyses by the UVVS team found that it is primarily ejected by a high energy process (temperature equivalent on the order of 10^4-10^5 K) on Mercury's dawn hemisphere [1,2]. UVVS data also show a possible cold component at low altitudes. Its temperature (on the order of 10^3 K) is consistent with laboratory measurements of the photodesorption of calcium from calcium sulfide [3].

Observations: The data used are limb scans taken above Mercury's dayside (local times from 6:00 to 18:00). These scans provide profiles of exospheric emission as a function of line-of-sight tangent altitude above Mercury's limb. The calcium emission is due almost entirely to resonant scattering of sunlight near a wavelength of 423 nm. These observations were typically made while MESSENGER was far south of Mercury and were most sensitive to emission at low latitudes. Examples of calcium limb scans are shown in Fig. 1.

Interpretation: Identification of the cold component required subtraction of the dominant energetic component. This component is seen most clearly in limb scans taken near 6:00 local time (Fig. 1 top panel). In order to subtract this component we first modeled it with a modified Chamberlain model. Though a rough approximation, it had the advantage of computational simplicity and only requires two free parameters: temperature and surface density. The Chamberlain model was altered to include the rapid photoionization of calcium. The energetic component was assigned a temperature of 70,000 K [1], which matched observations well at all local times. Density was allowed to vary.

The cold component appears as an excess of emission above the energetic component at low line-of-sight tangent altitudes (Fig. 1, bottom and middle panels). It was observed at all dayside local times (8:00 to 16:00) but not at dawn and dusk (6:00 and 18:00). Most observations occurred pre-noon. The cold component was often a prominent feature but was seen only sporadically. The vast majority of limb scans little to no evidence of it.

The temperature of the cold component was estimated with the modified Chamberlain model as 500-1500 K. The temperature is difficult to constrain given the scatter in the data. The temperature is consistent with laboratory measurements of photodesorbed calcium from calcium sulfide, a candidate for the volatile material that degrades to leave behind hollows features [3]. That experiment showed that CaS is efficiently disintegrated by near-UV light. The calcium is ejected from the surface, leaving behind pure sulfur that quickly evaporates. They found that the calcium energy distribution was well approximated by a sum of two Maxwellians (~600 K and 1400 K).

Conclusion: UVVS observations show the possible presence of a cold component in Mercury's calcium exosphere. Estimates of its temperature are consistent with laboratory measurements of the photodesorption of calcium from calcium sulfide, a candidate hollows material. It is a possible exospheric signature of the disintegration of hollows material.

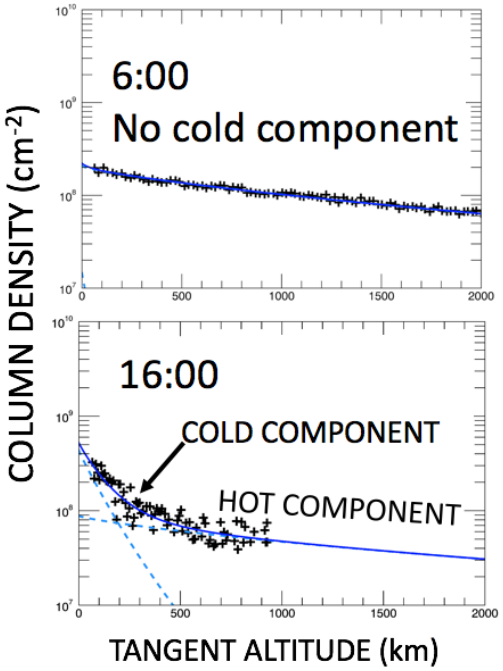

Figure 1: Examples of limb scans at indicated local times. The data are crosses, the model fits are blue lines. The top panel (6:00) shows the energetic component without a cold component. The example at 16:00 shows the possible presence of a cold component at low altitudes.

References: [1] Burger, M. H. et al. (2014) Icarus, 238, 51-58. [2] Killen, R. M. (2016) Icarus, 268, 32-36. [3] Bennett, C. J., McClain, J. L., et al. (2016) JGR, 121, 137-146.

THE BIG SCIENCE QUESTIONS ABOUT MERCURY'S ICE-BEARING POLAR DEPOSITS AFTER MESSENGER.

Nancy L. Chabot[1] and David J. Lawrence[1], [1]Johns Hopkins Applied Physics Laboratory, 11100 Johns Hopkins Rd, Laurel, MD, 20723, USA. (Nancy.Chabot@jhuapl.edu).

Introduction: Earth-based radar observations [e.g, 1] and MESSENGER measurements [e.g., 2–7] have provided multiple lines of evidence that Mercury's polar deposits are dominantly composed of water ice, answering a fundamental question about the distribution of water ice in the Solar System. BepiColombo [8] is positioned to provide the first in-depth exploration of water ice near Mercury's south pole when it orbits Mercury in 2025. With our new understanding from extensive orbital datasets, now is the time to ask new questions – What are the big open science questions about Mercury's ice-bearing polar deposits?

Open Science Questions: MESSENGER datasets have fully revealed Mercury's polar regions for the first time and led to substantial new knowledge about Mercury's polar deposits, enabling a new set of fundamental science questions:

- What is the origin of Mercury's water ice? Do the ice deposits represent ancient reservoirs, as they are located in regions where ice is stable for billions of years? Or did the ice deposits result from a recent or ongoing process, as supported by their fresh-looking appearances?
- What other volatiles are trapped at Mercury's poles? MESSENGER provided strong evidence that Mercury's polar deposits contain large amounts of water ice but that there are other volatile materials too. Do Mercury's polar deposits preserve organic-rich volatile compounds that were perhaps delivered to all of the inner planets?
- How do Mercury's polar deposits relate to the inventory of inner Solar System volatiles? Why does Mercury have extensive polar water ice deposits but the Moon does not [9]? What processes act in permanently shadowed regions to produce or to destroy water ice? What are the implications of Mercury's water ice deposits for water ice in the inner Solar System and on Earth and the other terrestrial planets?

Future Exploration Potential: Mercury's polar deposits provide many well-characterized locations for in situ landed investigations – locations that are known to have large expanses of exposed water ice and/or other volatile materials (Fig. 1). A landed science mission could determine the composition, age, heterogeneity, and physical properties of these deposits, answering big open science questions about the delivery, evolution, and retention of water and organics to the terrestrial planets, with comparisons to lunar polar cold traps and potential implications for early Earth.

References: [1] Harmon J. K. et al. (2011) Icarus, 211, 37-50. [2] Chabot, N. L. et al. (2012) GRL, 39, L09204. [3] Lawrence D. J. et al. (2013) Sci., 339, 292-296. [4] Neumann G. A. et al. (2013) Sci., 339, 296-300. [5] Paige D. A. et al. (2013) Sci., 229. 300-303. [6] Chabot N. L. et al. (2014) Geology, 42, 1051-1054. [7] Deutsch A. N. et al. (2016) Icarus, 280, 158-171. [8] Benkhoff et al. (2010) Plant. Space Sci., 58, 2-20. [9] Lawrence D. J. (2017) JGR Planets, 122, 21-52.

Acknowledgements: NASA DDAP grant NNX15AK89G to N.L.C.

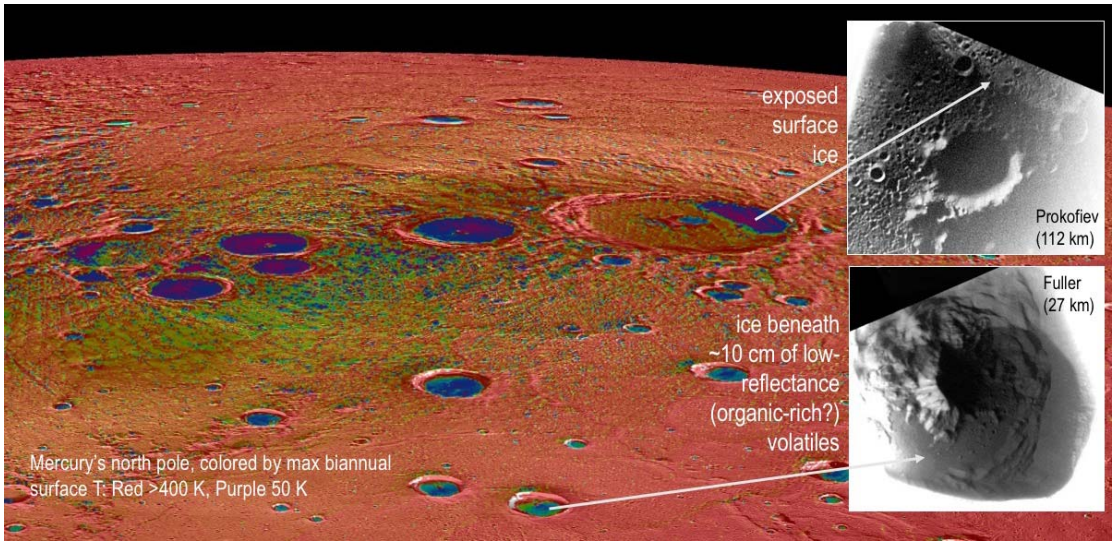

Figure 1. Mercury's north polar region, colored by the maximum biannual surface temperature [5].

A CLOSER LOOK AT SOME OF MERCURY'S NORTH POLAR DEPOSITS: THREE CRATERS THAT COULD HAVE EXTENSIVE SURFACE ICE BUT DON'T? Nancy L. Chabot[1], Gregory A. Neumann[2], Carolyn M. Ernst[1], Erwan M. Mazarico[2], and Evangela E. Shread[1] [1]Johns Hopkins Applied Physics Laboratory, 11100 Johns Hopkins Rd., Laurel, MD 20723, USA (Nancy.Chabot@jhuapl.edu), [2]NASA Goddard Space Flight Center, Greenbelt, MD 20771, USA.

Introduction: Earth-based radar observations [e.g, 1] and MESSENGER measurements [e.g., 2–7] have provided multiple lines of evidence that Mercury's polar deposits are dominantly composed of water ice. As MESSENGER was the first spacecraft to fully map the planet, the majority of the first studies using the mission results were appropriately focused on large-scale analyses of the full polar regions rather than specific polar craters. The next logical step for investigations of Mercury's polar deposits using currently available data is to examine specific craters of interest in more detail, to follow up on questions raised by the global studies. In this work, we focus on three craters predicted from their thermal conditions to be conducive to the presence of extensive water ice at the surface but may lack such ice.

Craters Studied: An overview of the three craters that are the focus of this work is shown in Fig. 1. The craters are located between 81°–85°N, 210°–230°E and are of particular interest because the thermal modeling results [5, 8] show sizable regions within their permanently shadowed interiors that are conducive to hosting water ice exposed at the surface for a billion years. However, unlike other craters closer to the north pole that are believed to host surface water ice [4, 6, 9], large high-reflectance areas for these three craters have not been observed [4, 9]. The radar-bright regions [1] associated with these three craters are also considerably smaller than the permanently shadowed areas [7]. Does this mean that these craters lack water ice deposits, providing more evidence for the uneven distribution of water ice between Mercury's polar cold traps [7,10]? Or is there evidence in MESSENGER measurements for surface water ice in these craters or viewing limitations that impeded the radar observations of these craters?

We are investigating the Mercury Laser Altimeter (MLA) and Mercury Dual Imaging System (MDIS) datasets for these craters. We have identified MDIS images that reveal the surfaces within these craters and are registering those images to MLA surface reflectance measurements, as well as to the radar observations, permanently shadowed regions, radar visibility, and thermal models, and we will present our latest results.

References: [1] Harmon J. K. et al. (2011) Icarus, 211, 37-50. [2] Chabot, N. L. et al. (2012) GRL, 39, L09204. [3] Lawrence D. J. et al. (2013) Sci., 339, 292-296. [4] Neumann G. A. et al. (2013) Sci., 339, 296-300. [5] Paige D. A. et al. (2013) Sci., 229. 300-303. [6] Chabot N. L. et al. (2014) Geology, 42, 1051-1054. [7] Deutsch A. N. et al. (2016) Icarus, 280, 158-171. [8] Chabot N. L. et al. (2018) In Mercury: The View after MESSENGER, in press. [9] Deutsch A. N. (2017) GRL 10.1002/2017GL074723. [10] Chabot N. L. et al. (2018) JGR, 10.1002/2017JE005500.

Acknowledgements: NASA DDAP grant NNX15AK89G to N.L.C; APL ASPIRE and NASA/APL intern programs for E.E.S.

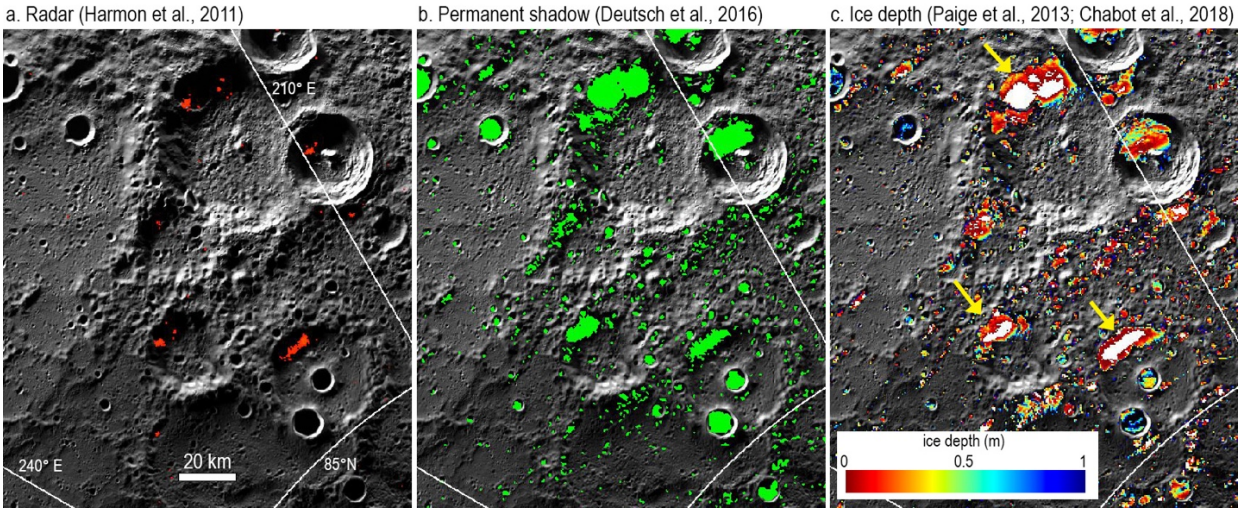

Figure 1. MESSENGER mosaic of a region near Mercury's north pole showing: a. locations of radar-bright features in red, b. permanently shadowed regions in green, and c. modeled depth at which long-term water ice is stable within 1 m of the surface. Yellow arrows identify three craters where sizable surface water ice could be stable (white regions).

PERSPECTIVES ON MAGMATIC DIFFERENTIATION OF MERCURY. B. Charlier[1], O. Namur[2] and C. Cartier[1,3], [1]Department of Geology, University of Liege, Belgium (b.charlier@uliege.be), [2]Department of Earth and Environmental Sciences, KU Leuven, Belgium, [3]CRPG, Université de Lorraine, Nancy, France.

Introduction: Magmatic activity on Mercury has been intense over the first billion years. Silicate/metal liquid immiscibility, crystallization of a magma ocean, partial melting of mantle rocks, and surface crystallization of magmas that form the secondary crust are the main magmatic events responsible for the differentiation into core, mantle and crust. The highly reducing conditions that prevailed during differentiation have resulted into an unexpected behavior for some elements with, for example, silicon partitioning into the core [1], sulfur going into the silicate portion of the planet [2], and graphite being stable at the surface [3].

Surface imaging of Mercury by MESSENGER has revealed that cratering and volcanism were widespread. The surface chemistry has been measured by X-Ray [4, 5] and Gamma-Ray spectrometry [6], and these compositional data can be used to infer magmatic processes, from deep mantle melting to surface crystallization. In this contribution, we review some results we gained by combining compositional data with melting/crystallization experiments in the laboratory performed under high-temperature, low to high-pressure conditions, and reducing oxygen fugacity.

Melting conditions and secular cooling: The compositions of surface melts provide the principal evidence for interpreting the P-T conditions of magma generation in the mantle, the mantle sources and the melting processes [7]. Experiments and modelling with the MELTS/pMELTS algorithms have shown that the mantle potential temperature required to form Mercurian lavas and the initial depth of melting decreased from the older High-Mg IcP-HCT terrane (1650°C and 360km) to the younger lavas covering the NVP regions (1410°C and 160km). The average melting degree is lower for the young NVP (0.27 ±0.04) than for the older IcP-HCT (0.46 ±0.02), indicating that melt productivity decreased with time. This evolution supports strong secular cooling of Mercury's mantle between 4.2 and 3.7Ga and explains why very little magmatic activity occurred after 3.7Ga. More data on age determination and compositions for specific geological provinces are however needed to refine our constraints on the thermal evolution of Mercury.

Interior structure and the FeS layer: We have conducted experiments in conditions relevant for mantle/core equilibration at the bottom of Mercury's magma ocean (IW-5.4, 5 GPa and near liquidus temperatures) to determine the metal/silicate and sulfide/silicate partition coefficients of Ti. Our experimental results show that Ti is chalcophile under reducing conditions (and not siderophile) which makes Ti a useful tracer of extraction of a sulfide melt. We use our partitioning data in a model to calculate the relative depletion of Ti (normalized to Al) in the bulk silicate Mercury as a function of the thickness of the FeS layer. By comparing the model results and surface data we show that the most likely scenario is that Mercury does not have an FeS layer. Data on Cr and Ni at the surface of the planet would be very useful to refine the details of our model of deep structures.

Surface mineralogy: Low-pressure crystallization experiments on selected surface compositions show that several mineralogical provinces can be identified [8]: the Northern Volcanic Plains and Smooth Plains, dominated by plagioclase, the High-Mg province, strongly dominated by forsterite, and the Intermediate Plains, comprised of forsterite, plagioclase and enstatite. This implies a temporal evolution of the mineralogy from the oldest lavas, dominated by mafic minerals, to the youngest lavas, dominated by plagioclase, consistent with progressive shallowing and decreasing degree of mantle melting over time. New spectral data to be acquired by MERTIS on BepiColombo will provide high-resolution mapping of the surface mineralogy that will be used to gain more information on small scale magmatic processes such as impact basin crystallization, crystallinity and magma effusivity.

References: [1] Chabot N. L. et al. (2014) *EPSL*, 390, 199-208. [2] Namur O. et al. (2016), *EPSL*, 448, 102-114. [3] Peplowski P. N. *et al.* (2016) *Nature Geosci,* 9, 273-276. [4] Nittler L. R. *et al.* (2011) *Science,* 333, 1847-1850. [5] Weider S. Z. *et al.* (2015) *EPSL*, 416, 109-120. [6] Peplowski P. N. *et al.* (2011) *Science*, 333, 1850-1852. [7] Namur O. *et al.* (2016) *EPSL*, 439, 117-128. [8] Namur O. and Charlier B. (2017) *Nature Geosci*, 10, 9-13.

Observational conditions for the detection of X-ray fluorescence from sodium by the MIXS instrument on Bepi-Columbo. R. Cooper[1], M. Grande[1], A. Martindale[2], E. Bunce[2], [1]Aberystwyth University, Aberystwyth, Ceredigion, SY23 3BZ (roc17@aber.ac.uk), [2] University of Leicester, Leicester, UK, LE1 7RH

Abstract: We model the expected fluorescence from the exosphere and surface of Mercury, as observed by the Mercury Imaging X-ray Spectrometer (MIXS) on the upcoming BepiColumbo mission, using code modified from that used for the SMART-1 D-CIXS instrument. Modifications include detector parameters, solar proximity, surface elemental composition, and emission from the optically thin exosphere. From this, preferential observation parameters have been determined for MIXS during its orbit. Modelling of these observations is conducted, with particular emphasis on the sodium component. Observations of fluorescence from several surface regions are compared for both MIXS-C and MIXS-T, as well as considering the capabilities of previous detectors such as those on the MESSENGER mission.

Introduction: X-ray fluorescence is typically considered to be a laboratory technique, yet has been found to have numerous uses in planetary science. Due to the high solar flux at Mercury, this planet is considered a prime target for using this method for elemental abundance detection. The main focus of this work is the MIXS detectors on the BepiColumbo Mission, which is due to launch in October 2018. MIXS is comprised of two detectors, a collimated channel MIXS-C and a telescope MIXS-T [1]. Their primary aim is to measure surface elemental abundances; however it is feasible that MIXS will be able to answer more of the major questions about Mercury.

In this work, we consider the potential for MIXS to observe fluorescence from Mercury's exosphere. From this, an improved understanding of surface-exosphere interactions and how abundances of material in these regions varies over a Mercurian day can be determined. The main target of this fluorescence detection is the sodium component. This is due to the fact that sodium is one of the more abundant, and volatile elements present in Mercury's exosphere. To evaluate the optimal configuration of these detectors for viewing the fluorescence, a model of the fluorescence from both the surface and exosphere of Mercury has been produced.

Fluorescence model. The model used for this work was originally designed for D-C1XS on the SMART-1 mission to the Moon [2], and has been adapted for this new purpose. As the fluorescence calculations originally used will still be correct [3], they require no changes. The alterations required focus mainly on the elemental abundances, proximity to the Sun, and increased solar flux and differences in detector design.

Observational capabilities of MIXS: We consider the observational specifications of both MIXS, with the aim of modelling the expected observations of the detectors and therefore optimising their usability at Mercury.

Surface regions. We investigate the possibility of distinguishing fluorescence signatures of different geological terranes on Mercury. This will aid in understanding the geological evolution of Mercury, regarding which there are still numerous uncertainties.

Exosphere. Due to the collisionless nature of the exosphere, this makes it a very low density region to observe with X-ray fluorescence. We discuss observational conditions that would be beneficial for allowing MIXS to capitalise on observing this region, including the exospheric sodium tail and the cold pole enhancement.

Particle induced X-ray events. There have been observations of particle induced X-ray events at Mercury from the MESSENGER mission [4]. We consider the opportunity for MIXS to also observe these events on the nightside of Mercury during its mission.

Summary and Conclusions: The potential to observe X-ray fluorescence events at Mercury with MIXS should be capitalised on. At certain points in the proposed orbital paths around Mercury, MIXS will be in a position to observe this fluorescence, allowing for additional data for currently planned exospheric investigation. From these observations, predictions on MIXS' ability to explore the sodium tail of Mercury's exosphere will be possible, along with interactions between the exosphere and magnetosphere of the planet.

Acknowledgments: The authors would like to thank Adrian Martindale and the members of the Leicester University space research centre for access to the MIXS grasp data, and the author of the original program Bruce Swinyard.

References: [1] Fraser, G. W. et al (2010), *Planetary and Space Science, 58*, 79-95. [2] Grande, M. et al (2003*), Planetary and Space Science, 51*, 427-433. [3] Clark, P. E. & Trombka, J. I. (1997), *Journal of Geophysical Research*, *102*, 16,361-16,384. [4] Lindsay, S. T. (2016), *Planetary and Space Science, 125,* 72-79

IMPACT MELT EMPLACEMENT ON MERCURY. J. W. Daniels[1] and C. D. Neish[1], [1]The University of Western Ontario, London, ON, Canada (jdanie4@uwo.ca).

Introduction: This work looks to build on prior work completed for Venus and the Moon [1, 2], applying the methods used there towards understanding melt emplacement around complex impact craters on the planet Mercury. Its surface resembles more the Moon than Venus, yet it possesses a higher gravity field than the Moon does. Results so far suggest that melt emplacement on Mercury exhibits a pattern closer to what is observed on Venus than on the Moon, implying gravity plays a dominant role in how impact melt is emplaced on any given rocky body.

Background: *The Moon.* From [1], it was found that a large number of lunar complex craters exhibit ejected melt ponds and flows near to their respective rim crest low ("RCL"). The low gravity and fairly high topographic variation present on the Moon may be responsible for impact-generated melts being preferentially ejected from the RCL. On the Moon, the craters are deeper, and contain less melt, than craters on Venus [3, 4]. This means the forces involved in ejecting melt from lunar craters must expel that melt over comparatively higher rim elevations [see 4], favouring ejection over the RCL.

Venus. From [2], comparing complex craters on Venus and on the Moon, it was suggested that the shallower crater depths and larger melt volumes on Venus compared to the Moon might explain why the distribution of ejected melt material on Venus was more evenly distributed about the crater rim. Due to its higher gravity, craters on Venus tend to be shallower than those on the Moon and contain proportionally more melt [3]. This means the momentum left over from the initial impact event may be sufficient to eject the melt in the direction of impact. The observation that Venusian impact melts tend to be emplaced downrange was first made by [4].

Mercury: *Methods.* We analyzed a total of 26 potentially melt-bearing, fresh, complex craters on Mercury for further study, using the Mercury Quickmap and crater data from [3, 4], to determine how those deposits were emplaced. We wish to determine whether melt deposits on Mercury are emplaced more like the Moon, subject primarily to higher overall topographic variation, or like Venus, subject primarily to higher surface gravity. The third possibility is that Mercury's melt-bearing craters might plot as a hybrid between these two "extremes."

Due to the nature of MESSENGER's elliptical orbit around Mercury, the resolution of the Mercury Laser Altimeter (MLA) data for Mercury's southern hemisphere was too low to be useful in locating crater RCL. Therefore, only craters in the northern hemisphere were selected for further study. Craters that lay north of 45ºN latitude were optimal; for those craters south of 45ºN where MLA data was poor, we used the Mercury MESSENGER Global DEM 665m map created by [7, 8]. Mercury Dual Imaging System (MDIS)-WAC and -NAC data for each crater was superimposed under the elevation data in QGIS. Melt ponds were identified and outlined in the MDIS data. The greatest concentration of melt ponds was assigned a dominant direction using a 16-part pie-shaped grid and compared to the dominant RCL direction via that same grid. If both directions were within the same grid slice, we categorized the crater as "coinciding"; if both were within 45º of each other, then it was categorized as "within 45º"; if both reside between 45º and 90º of each other, then it was categorized as "within 90º"; the remainder of the possibilities are collectively categorized as "90º or greater."

Results. Four of the craters in the initial catalog had to be removed from the analysis. The resolution of MLA imagery was too low for three of these craters to allow for RCL determination, while the resolution of MDIS imagery was too low to resolve the melt deposits, if any existed, about the fourth crater. The remaining 22 craters had sufficient data to allow for further analyses. Of these, 23% fell under "coincide," 18% under "within 45º," 32% under "within 90º," and the remaining 27% fell under "90º or greater." The mercurian distribution is similar to that noted by [2] for Venus, implying gravity plays a greater role on Mercury than topographic variation does. There appears to be a threshold wherein a celestial body with a gravity field below this threshold will show an exterior melt deposit emplacement distribution similar to the Moon, whereas bodies lying above this threshold will show a distribution similar to Venus and Mercury.

References:

[1] Neish C. D. et al. (2014) *Icarus, 239,* 105-117. [2] Neish C. D. et al. (2017) *Icarus, 297,* 240-251. [3] Cintala M. J. and Grieve R. A. F (1998) *Meteor. & Planet. Sci., 33*, 24. [4] Chadwick D. J. and Schaber G. G. (1993) *Journal of Geophys. Res., 98, E11,* 20,891-20,902. [5] Banks M. E. et al. (2017) *Journal of Geophys. Res., 122*, 1010-1020. [6] Kalynn J. et al. (2012) *Geophys. Res. Letters, 40*, 38-42. [7] USGS Astrogeology Science Center (2016) *USGS*, astrogeology.usgs.gov. [8] Solomon S. C. et al. (2001) *Planet. Space Sci., 49*, 1445-1465.

THE MSA INSTRUMENT (MASS SPECTRUM ANALYZER) ONBOARD BEPI COLOMBO MMO (MERCURY MAGNETOSPHERIC ORBITER). D. Delcourt[1] (dominique.delcourt@lpp.polytechnique.fr), Y. Saito[2], F. Leblanc[1], C. Verdeil[1], S. Yokota[2], M. Fraenz[3], H. Fischer[3], B. Fiethe[4], B. Katra[1], D. Fontaine[1], J.-M. Illiano[1], J.-J. Berthelier[5], A. Belger[4], F. Bubenhagen[4], N. Krupp[3], U. Buhrke[3], H. Michalik[4], and H. Krueger[3], [1]LPP (Paris, France), [2]ISAS (Sagamihara, Japan), [3]MPS (Göttingen, Germany), [4]IDA (Braunschweig, Germany), [5]LATMOS (Paris, France).

Abstract: The launch of the Bepi Colombo spacecraft, MPO (Mercury Planetary Orbiter) and MMO (Mercury Magnetospheric Orbiter), will take place in the fall 2018 for an arrival and orbit insertion at Mercury at the end of 2025. The objective of the MMO spacecraft that is under responsibility of JAXA, is to thoroughly investigate the magnetized environment of Mercury. On this purpose, MMO payload includes in particular the MPPE (Mercury Plasma Particle Experiments) consortium that is an instrumental suite dedicated to particle measurements. MSA is one of these instruments that focuses on measurements of the magnetospheric plasma composition. Taking advantage of MMO spin (4s period), MSA will measure three-dimensional ion distributions over a large range of masses (1-60 amu) and energies (from 1 eV/q up to 38 keV/q). MSA consists of a spherical top-hat analyzer for energy selection, followed by a Time-Of-Flight chamber for mass identification. With its "reflectron" design, MSA offers a high mass resolution (typically, $m/\Delta m > 50$) that will allow for instance to distinguish between ^{39}K and ^{40}Ca ions. This capability will be of particular importance to identify the various species that populate Mercury's magnetosphere and to characterize the interaction between the planet surface and the solar wind.

MERCURY'S EARLY GEOLOGIC HISTORY. B. W. Denevi[1], C. M. Ernst[1], R. L. Klima[1], M. S. Robinson[2], [1]Johns Hopkins University Applied Physics Laboratory, Laurel, MD, [2]Arizona State University, Tempe, AZ.

A narrative for the formation of Mercury's early crust is taking shape from a combination of geologic mapping, compositional information, and geochemical models. Though resurfacing was extensive, a global view of crater densities on Mercury points to some areas where early crustal materials may be exposed at the surface, albeit in a heavily gardened form [1]. The geology and stratigraphy of the most extensive such region is consistent with an early crust rich in low-reflectance material (LRM) exposed from beneath a more mixed regolith. As LRM is thought to be enriched in graphite relative to average surface material [2,3], these observations are compatible with geochemical models that suggest a cooling magma ocean on Mercury may have developed an early graphite flotation crust [4]. However, graphite may have been the only buoyant mineral in such a magma ocean [4], and LRM is thought to contain only <5 wt% graphite [2].

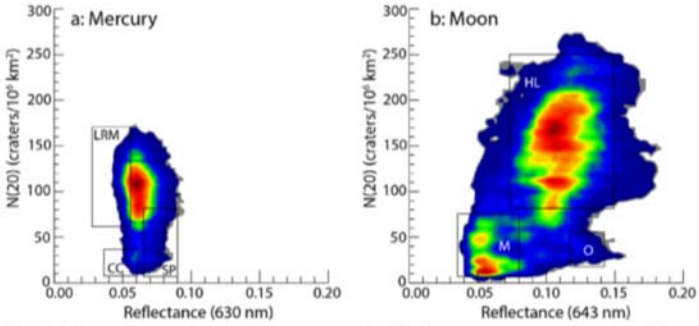

Fig. 1. Two-dimensional histogram of reflectance versus crater density; colors indicate frequency (blue is low, red is high). (a) Mercury. Boxes indicate the approximate extent of LRM, circum-Caloris plains (CC), and smooth plains (SP). (b) The Moon. Boxes indicate the highlands (HL), maria (M), and Orientale ejecta (O) [9].

Adiabatic melting during cumulate overturn was a possible source of large-scale volcanism [e.g., 5] that formed the first stable silicate crust. The ratio of early mantle-derived melt to graphite flotation crust must have been high, to account for the low weight fraction of carbon in Mercury's modern crust. The relation of LRM to this early silicate crust on Mercury is not clear. With existing observations, it may not be possible to determine whether LRM formed via flotation, as a product of early volcanism, or both, because these early crustal materials were substantially modified by later magmatism and impact disruption and mixing. Though its composition and mode of formation are not well understood, an early stable crust formed and was able to support the large-scale emplacement of younger magmas and the formation of impact basins. If graphite were concentrated in the early crust, subsequent volcanic material derived from partial melting of the mantle would be generally higher in reflectance, as is observed for inter-crater and smooth plains [2,7,8].

The early history of Mercury appears to have been much different from that of the Moon, where the bulk of the plagioclase flotation crust is thought to constitute a large fraction of the highland crust and effusive volcanic activity was more limited. Mercury's narrow range of compositions and low abundance of iron likely meant that magmas on Mercury were not inhibited from reaching the surface by a low-density crust, as on the Moon. In fact, partial melts from Mercury's mantle would be buoyant at all depths and a greater fraction of mantle partial melt may have erupted on Mercury's surface [4].

These differences between the Moon and Mercury are highlighted by the relative reflectance and crater density distributions of each body (Fig. 1). In contrast to the relatively narrow range of reflectance and crater density seen for Mercury because of its extensive volcanism, the Moon shows a clear bimodal distribution between the heavily cratered highlands and less cratered volcanic maria. There are, however, areas of high-reflectance, low crater density that result from impact resurfacing of the ancient highlands. Areas with low reflectance and low crater densities on Mercury include the circum-Caloris plains; determining whether any young regions of low reflectance are of volcanic origin or include impact deposits is important to evaluating the origin of these and older crustal units. Further work to understand Mercury's color–stratigraphic relationships will aid in deciphering the global picture apart from regional effects of impacts and volcanism. But the overall picture is clear: unlike the Moon, Mercury does not a have a well-preserved flotation crust with a composition that contrasts strongly with mantle-derived magmas.

Instead, Mercury may have followed an early evolutionary track similar to other terrestrial planets. Basaltic volcanism likely formed the earliest martian crust [10]. We have no record of the earliest crust of Venus, though volcanism has clearly been of crucial importance in its evolution, and Earth's original crust appears to have been lost, but it may also have been basaltic [e.g., 11].

References: [1] Denevi B.W. et al. (2016) LPSC 47, Abs. 1624. [2] Murchie S.L. et al. (2015) Icarus, 254, 287–305. [3] Peplowski P.N. et al. (2016) Nature Geo., 9, 273–276. [4]Vander Kaaden K.E. and McCubbin F.M. (2015) JGRP, 120, 195–209. [5] Brown S.M. and Elkins-Tanton L.T. (2009) EPSL, 286, 446–455. [7] Robinson M.S. et al. (2008) Science, 321, 66–69. [8] Denevi B.W. et al. (2009) Science, 324, 613–618. [9] Denevi B. W. et al (2018) in Mercury: The View After MESSENGER, eds. Solomon S.C. et al., Cambridge Univ. Press, in press. [10] Elkins-Tanton L.T. et al. (2005) JGR, 100, E12S01. [11] Kamber B.S. et al. (2007) in The Earth's Oldest Rocks, eds. van Kranendonk M. et al., Elsevier, 75–89.

PRODUCTION FUNCTION OF OUTGASSED VOLATILES ON MERCURY: IMPLICATIONS FOR POLAR VOLATILES ON MERCURY AND THE MOON. Ariel N. Deutsch[1], James W. Head[1], [1]Department of Earth, Environmental and Planetary Sciences, Brown University, Providence, RI, 02912 (ariel_deutsch@brown.edu).

Introduction: Critical to the understanding of current polar volatiles on the Moon and Mercury are: (1) volatile sources [internal, delivered (impacts of comets, asteroids, and micrometeorite debris), and environmental (e.g., solar wind)], (2) variations in the delivered volatiles for each source as a function of time (the production functions), (3) the delivery pathway from sources to sinks (primarily polar cold traps), (4) sequestration, storage, and retention processes, and (5) variations in cold-trap stability through time.

Water ice has been observed at the poles of both Mercury and the Moon; however, ice deposits on Mercury appear to be more extensive and pure than those on the Moon. We are interested in the overall flux of volatiles delivered to the polar regions of these two airless bodies (the *production functions*). It is possible that a difference in relative sources of the volatiles may contribute to the differences between the polar deposits observed today. In this contribution, we focus on the possible sources for volatile delivery to Mercury and the Moon including (1) comets/asteroids, (2) micrometeorites, (3) solar wind implantation, and (4) volcanic outgassing, which we focus on initially.

On the Moon, the contribution of volatiles from pyroclastic [1] and mare eruptions are currently being assessed. The contribution of volatiles from volcanism on Mercury has not been carefully estimated; thus, questions remain about how the production function of volatiles has evolved through the planet's history.

Methodology: Following the approaches of [2–4], first the production of volcanic basalt released through the major volcanic smooth plains from Mercury is determined as a function of time. Next, the release of volatiles derived from the volcanic plains as a function of time is estimated. The total mass of erupted lava is calculated by multiplying the estimated volume of volcanic deposits [e.g., 5] by the bulk density of typical smooth plains on Mercury (~3014 kg/m3) [6]. This mass is multiplied by estimates of volatile species [e.g., 7–8], to estimate mass ranges of potential volatiles for mercurian plains.

We then compare the estimated production functions of volatiles released over the histories of Mercury (from this analysis) and the Moon (from [2]). Finally, geologic maps are constructed of the polar regions of Mercury and the Moon through time to estimate the mean and peak fluxes of volatiles to cold traps. Specifically, maps of polar topography are used to reconstruct each era of mercurian and lunar history on the basis of crater ages [e.g., 9–10]. For each era, estimates of volatiles are added to existing cold traps, as delivered from (1) impactors [e.g., 11], (2) solar wind implantation [e.g., 12], and (3) volcanic eruptions (as estimated for Mercury in this analysis and for the Moon in [2]). These estimates do not account for losses; therefore, these maps provide maximum estimates.

Results: While volcanic activity may have occurred as recently as ~1 Ga on Mercury [13–14], the majority of effusive volcanic activity occurred early in the planet's history [3]. Overall, the volume of flood basalts produced peaked ~3.5 Ga and diminished through time. The duration of effusive volcanic activity on Mercury and the Moon is similar [3, 15].

Implications: The delivery of volatiles to both Mercury and the Moon peaked >3 Ga. While ice on the Moon appears to be relatively ancient on the basis of its degraded nature, the ice on Mercury appears to be relatively fresh, given (1) distinct albedo surfaces, [16], (2) sharp albedo boundaries [16], and spatial coherence within PSRs. Given that Mercury is subjected to the same space weathering and impact processes as the Moon, and possibly even higher regolith overturn rates [17], we expect any relatively old ice on Mercury to exhibit similar heterogenic traits as observed for the lunar ice. Thus, given the chronology of volatile fluxes derived here, we ask what the ultimate fate of these early-delivered volatiles is. It is possible that older volatiles are trapped in Mercury's subsurface, below the sensing depths of radar observations and neutron detections. In summary, the Moon provides a framework from which to investigate Mercury for traces of ancient volatiles.

References: [1] Milliken and Li (2017) *Nat. Geosci. 10,* 561–565. [2] Needham and Kring (2017) *EPSL 478,* 175–178. [3] Head and Wilson (2017) *Icarus 283,* 176–223. [4] Wilson and Head (2017) *Icarus 283,* 146–175. [5] Byrne et al. (2016) *GRL 43,* 2016GL069412. [6] Padovan et al. (2015) *GRL 42,* 2014GL062487. [7] Kerber et al. (2009) *EPSL 285,* 285–271. [8] Zolotov (2011) *Icarus 212,* 24–41. [9] Prockter et al. (2016) *LPS XLVII,* Abstract #1245. [10] Wilhelms et al. (2013) *USGS,* I-1062. [11] Bruck Syal and Schultz (2015) *LPS XLVI,* Abstract #1680. [12] Crider and Vondrak (2000) *JGR 105,* 26773–26782. [13] Prockter et al. (2010) *Science 329,* 668–671. [14] Jozwiak et al. (2018) *LPS XLIV,* Abstract #2324. [15] Hiesinger et al. (2003) *JGR 108,* 5065. [16] Chabot et al. (2016) *GRL 43,* 2016GL070403. [17] Domingue et al. (2014) *SSR 181,* 121–214.

DIFFERENCES BETWEEN SURFACE ICE DEPOSITS AT THE POLES OF MERCURY AND THE MOON: INSIGHTS INTO AGES OF THE ICE. Ariel N. Deutsch[1], James W. Head[1], and Gregory A. Neumann[2], [1]Department of Earth, Environmental and Planetary Sciences, Brown University, Providence, RI 02912 (ariel_deutsch@brown.edu), [2]NASA Goddard Space Flight Center, Greenbelt, MD 20771, USA.

Introduction: The poles of Mercury and the Moon both show evidence for water ice, but the deposits on Mercury have a greater areal distribution [1] and a more pure concentration [2]. Earth-based radar observations revealed an estimated ~25,000 m^2 of ice at Mercury's poles [1] that was modeled to be ~95 wt. % pure water ice [2]. Images [3] and reflectance measurements [4] acquired by the MErcury Surface, Space ENvironment, GEochemistry, and Ranging (MESSENGER) spacecraft showed that these deposits are spatially homogeneous within permanently shadowed regions (PSRs).

In contrast to the relatively pure water-ice deposits on Mercury [2], polar deposits on the Moon are rather heterogeneous. For instance, multiple volatiles were detected in the ejecta plume of the LCROSS experiment that impacted into Cabeus at the Moon's south pole, suggesting that the deposits are not pure water ice [5–6]. Additionally, mapping of UV albedo spectra and surface temperature revealed a highly spatially heterogeneous distribution of water frost within PSRs [7].

Here, we explore how these differences in purity and spatial homogeneity of ice at Mercury and the Moon may be related to the ages of the ice.

Methodology: *Mercurian crater statistics.* Using images acquired by the Wide-Angle Camera during MESSENGER's low-altitude campaign [8], we identify small craters in the PSRs that are correlated with high reflectance, suggestive of excavated material. While the majority of craters observed in the PSRs may be pre-existing topography emplaced before the deposition of the ice [e.g., 10], the anomalous small craters associated with high-reflectance material may have formed after the emplacement of the ice. If so, then these small craters superposing the ice deposit can be used to date the ice surface. We estimate the absolute ages of Laxness, Bechet, and Ensor craters using CraterstatsII [11] and chronology and production systems from [12].

Lunar ice heterogeneity measurements. We explore the relationship between the spatial heterogeneity of ice and the age of host craters at the lunar poles. The spatial heterogeneity of a polar deposit is quantified as the percent of the cold trap occupied by ice. We define cold traps as regions with maximum surface temperatures ≤ 110 K, as measured by the Diviner Lunar Radiometer Experiment [13]. To determine what percent of cold traps are occupied, we use maps of anomalously high reflectance measured at 1064 nm, consistent with surface ice detections [14]. Craters are classified into lunar geologic periods through the combined analyses of crater age dating [15], geologic maps [16], and morphological crater classification schemes [e.g., 17].

Results: *Mercurian crater statistics.* The estimated derived ages for the ice surfaces within Laxness, Bechet, and Ensor craters are 48 ± 20 Ma, 91 ± 40 Ma, and 220 ± 60 Ma, respectively. These ages are slightly higher than the 50 Ma predicted by regolith gardening models [18], but consistent with the ice being deposited relatively recently. These ages are also consistent with the ice being delivered by the Hokusai impactor [19].

Lunar ice heterogeneity measurements. We find that for the south pole on the Moon, the youngest ice-bearing craters [14] are the most spatially homogenous, suggesting that age has some control over the spatial distribution of surface ice at the Moon. It is possible that older ice deposits have undergone more space weathering and impact bombardment [20–21], contributing to a more spatially heterogeneous deposit.

Implications: The same impact bombardment and space weathering processes operate on Mercury and the Moon, and Mercury's regolith may be overturned even more frequently than the lunar regolith [22]. Thus, the lack of apparent degradation of Mercury's ice deposits also suggests that these deposits are relatively young. We suggest that the spatial homogeneity and purity of Mercury's polar deposits within a given PSR may be explained by relatively younger ice in comparison to relatively older ice within the Moon's polar cold traps.

References: [1] Harmon J.K. et al. (2011) *Icarus, 211,* 37–50. [2] Butler B.J. et al. (1993) *JGR, 98,* 15003–15023. [3] Chabot N.L. et al. (2014) *Geology, 42,* 1051–1054. [4] Neumann G.A. et al. (2013) *Science, 339,* 296–300. [5] Colaprete A. et al. (2010) *Science, 330,* 463–468. [6] Schultz P.H. et al. (2010) *Science, 330,* 468–472. [7] Hayne P.O. et al. (2015) *Icarus, 225,* 58–69. [8] Chabot N.L. et al. (2016) *GRL, 43,* 2016GL070403. [9] Chabot N.L. et al. (2016) *GRL, 43,* 9461–9468. [10] Deutsch A.N. et al. (2018) *Icarus, 305,* 139–148. [11] Michael G.G. and Neukum G. (2010) *EPSL, 294,* 223–229. [12] Neukum G. et al. (2001), *PSS, 49,* 1507–1521. [13] Paige D.A. et al. (2010) *SSR, 150,* 125–160. [14] Fisher E.A. et al. (2001) *Icarus, 292,* 74–85. [15] Tye A.R. et al. (2015) *Icarus, 255,* 70–77. [16] Wilhelms D.E. et al. (2013) *USGS,* I-1162. [17] Kinczyk M.J. et al. (2016) *LPS, XLVII,* Abstract #1573. [18] Crider D. and Killen R.M. (2005), *GRL, 32,* L12201. [19] Ernst C.M. et al. (2016) *LPS, XLVII,* Abstract #1374. [20] Pieters C.M. and Noble S.K. (2016) *JGRP, 121,* 2016JE005128. [21] Hurley D.M. et al. (2012) *GRL, 39,* L09203. [22] Domingue D.L. et al. (2014) *SSR, 181,* 121–214.

Energetic electron acceleration, injection, and transport in Mercury's magnetosphere

Ryan M. Dewey[1,*], James A. Slavin[1], Jim. M. Raines[1], Daniel N. Baker[2], David J. Lawrence[3]

[1]Department of Climate and Space Sciences and Engineering, University of Michigan, Ann Arbor, MI, USA.
[2]Laboratory for Atmospheric and Space Physics, University of Colorado, Boulder, CO, USA.
[3]The Johns Hopkins University Applied Physics Laboratory, Laurel, MD, USA.
[*] corresponding author: rmdewey@umich.edu

MESSENGER frequently observed energetic electrons (>10 keV) in Mercury's magnetosphere via both direct (EPS) and indirect (NS, GRS, XRS) measurements. While instrumental limitations complicate unifying these measurements, these instruments typically observe bursts of energetic electrons (timescales ~1-10 s) near the dawn terminator. To understand these observations, a terrestrial-like model of magnetotail acceleration followed by planetward injection is commonly evoked as the basis for Mercury's energetic electron environment. In this Near-Mercury Neutral Line model, reconnection in the near-magnetotail accelerates electrons to relativistic speeds and transports them close to Mercury where they begin to gradient drift eastward about the planet. As a result of the small magnetospheric scales, electrons are rapidly lost from the system, preventing the formation of permanent radiation belts but allowing for quasi-trapped populations. We discuss this model of Mercury's energetic electron environment in light of recent magnetospheric observations, including the asymmetry of reconnection across the magnetotail, the pattern of energetic electron precipitation on the planet's nightside surface, and the highly compressed dayside magnetosphere. Using high temporal resolution GRS measurements (10 ms), we find that electrons (1) are dominantly accelerated by dipolarization events in the magnetotail, (2) exhibit hemispherical asymmetry in transport and precipitation, and (3) drift about the planet in Shabansky-like orbits. We place these observations in context to future prospects from BepiColombo.

Three-dimensional, Ten-moment Two-fluid Simulation of the Solar Wind Interaction with Mercury. C. F. Dong[1], L. Wang[2], A. Hakim[1], A. Bhattacharjee[1], K. Germaschewski[2], and G. A. DiBraccio[3], [1]Princeton University (C. F. Dong: dcfy@princeton.edu), [2]University of New Hampshire, [3]NASA Goddard Space Flight Center

Introduction: Mercury's magnetosphere is highly dynamic as a consequence of its close proximity to the Sun and Mercury's weak internal magnetic field [1,2]. Compared with Earth, Mercury possesses a magnetosphere whose size is only 5% of that of the Earth and the planet itself occupies a large fraction of the magnetosphere. In addition, the unique aspects of Mercury's interaction with solar wind also result from Mercury's large conducting core with a radius of ~ 0.8 R_M (R_M = 2440 km) [3] and the offset of its dipole center northward by 0.2 R_M from the equator [4].

Method: In order to capture the kinetic behavior of Mercury's magnetosphere during the process of soalr wind interacton, we investigate Mercury's magnetosphere by using Gkeyll ten-moment multifluid code that solves the continuity, momentum and pressure tensor equations of both protons and electrons, as well as the full Maxwell equations [5]. Non-ideal effects like the Hall effect, inertia, and tensorial pressures are self-consistently embedded without the need to explicitly solve a generalized Ohm's law. Previously, we have benchmarked this approach in classical test problems like the Orszag-Tang vortex and GEM reconnection challenge problem [6].

Results: We first validate the model by using MESSENGER magnetic field data through data-model comparisons (Figure 1). Both day- and night-side magnetic reconnection are studied in detail (Figure 2). In addition, we include a mantle layer (with a resistivity profile) and a perfect conducting core inside the planet body to accurately represent Mercury's interior. The intrinsic dipole magnetic fields may be modified inside the planetary body due to the weak magnetic moment of Mercury. By including the planetary interior, we can capture the correct plasma boundary locations (e.g., bow shock and magnetopause), especially during a space weather event. This study has the potential to enhance the science returns of both the MESSENGER mission and the upcoming BepiColombo mission (to be launched to Mercury in 2018).

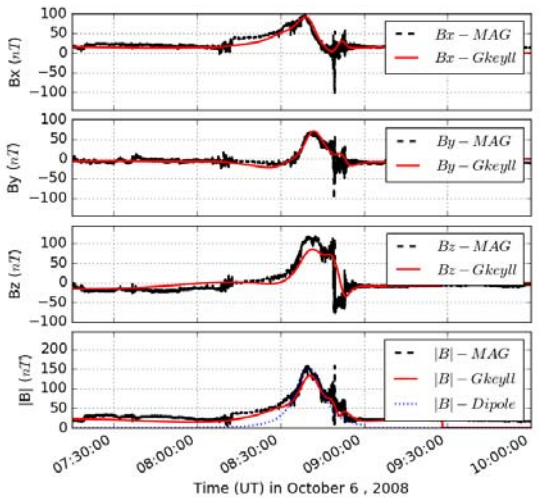

Figure 1 The data-model comparion of magnetic fields along MESSENGER's second flyby trajectroy.

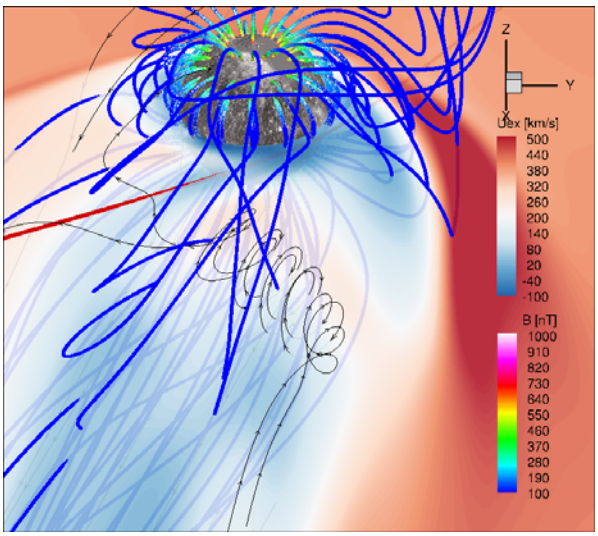

Figure 2: Tail flux rpoes in Mercury's magnetosphere.

References: [1] Ness N. F. et al. (1974) Science, 185, 151-160. [2] Slavin J. A. et al. (2007) Space Sci Rev, 131, 133-160. [3] Smith, D. E. et al. (2012) Science, 336, 214-217. [4] Anderson B. J. et al. (2011) Science, 333, 1859-1862. [5] Dong C. F. et al. (2017) AGU. [6] Wang L. et al. (2016) Phys Plasmas, 22, 012108.

Mercury Lander Mission Concept Study Summary.

D.A. Eng, The Johns Hopkins University Applied Physics Laboratory, doug.eng@jhuapl.edu

Introduction: In 2010 a Mercury lander mission concept was explored as part of the National Academies of Sciences, Engineering, and Medicine Space Studies Board (SSB) Planetary Science Decadal Survey. It was conducted by the JHU/APL Space Department in partnership with Marshall Space Flight Center, Glen Research Center, and Steven Hauck from Case Western Reserve University. The focus of the study was to determine the feasibility of the mission to be executed within a PI-led mission cost cap such as New Frontiers. The science questions addressed included determining Mercury's bulk composition, the nature of the magnetic field, surface history, internal structure, and surface-solar wind interactions. Instruments included a panoramic stereo imager, magnetometer, thermal emission spectrometer, descent imager, alpha proton X-ray spectrometer, a Raman spectrometer, a microscopic imager, and a communications system that supports radio science.

The challenge of a landed Mercury mission was found to be large amount of launch energy and ΔV required. Reaching Mercury within a reasonable launch energy requires planetary flybys with either a low-thrust approach using solar electric propulsion (SEP) or a ballistic approach similar to the one used on MESSENGER. In addition to this launch energy challenge, landing on Mercury requires on the order of 4.4 – 4.7 km/s of onboard ΔV to land. No existing or planned deep-space missions have a ΔV requirement even close to this magnitude.

In this study, both a ballistic chemical and SEP trajectory approach were explored with the constraint of the ability to launch on an Atlas V 551 or equivalent launch vehicle. The ballistic/chemical approach was found to be potentially feasible but its performance was on the edge of being able to fit within the launch vehicle constraints. A low thrust option was also explored using a separating SEP cruise stage. This option had the potential of a higher payload mass and was able to accommodate the full robust payload on an Atlas V 541 sized launch vehicle.

The design concept included NEXT Ion propulsion, solid rocket motors for large required DV maneuvers such as a braking burn for landing, and on NASA Advanced Sterling Radioisotope Generator (ASRG) technology that never matured to completion. The primary risks of this concept was a dependency on high-temperature solar cell technology, the complexity of a multi-stage vehicle, and the dependency on solid rocket motors that would need to be stored and ignited several years after launch.

The cost estimate for all options exceeded that of a PI cost cap mission of $900M (FY15$) established for the study. The ballistic/chemical option was estimated at $1.2B with a reduced payload and included launch on an Atlas V 551. The SEP option with a robust payload was over $1.5B.

.

References:

[1] S.A. Hauck II, D.A. Eng, G. J. Tahu. (2010) Mercury Lander Mission Concept Study.

Could the Hokusai Impact Have Delivered Mercury's Water Ice?

Carolyn M. Ernst[1], Nancy L. Chabot[1], and Olivier S. Barnouin[1], [1]Johns Hopkins Applied Physics Laboratory, 11100 Johns Hopkins Rd, Laurel, MD 20723, USA (carolyn.ernst@jhuapl.edu).

Introduction: Hokusai is the most prominent large young impact crater on Mercury – if the bulk of Mercury's water-ice inventory was indeed delivered by a single recent impact event, Hokusai is the best candidate source crater. We have previously constrained the impact conditions that created Hokusai from morphological and color observations of the crater and its ejecta [1]. Here, we use these parameters to update estimates of the possible contribution of the Hokusai impact to water ice on Mercury.

Projectile Mass: Assuming a 35º impact angle (measured from the horizontal) [1] and using crater scaling rules [e.g., 2], we estimate the projectile size necessary to form a crater of Hokusai's size for both asteroidal (2250 kg/m^3) and cometary (500 kg/m^3) impactors over the impact velocity range of 10–80 km/s expected at Mercury [3, 4]. These calculations indicate a projectile diameter in the range of 6–31 km. This diameter range equates to a total impacting mass ranging from 2.6 × 10^{17} to 8.0 × 10^{18} g. Depending on the assumed water content of the projectile, 1.3 × 10^{16} to 8.0 × 10^{17} g of the impacting mass is water for an asteroidal impactor (5–10% water by mass), and 1.6 × 10^{16} to 2.6 × 10^{18} g is water for a cometary impactor (6–33% water by mass).

Delivered Water Mass: To estimate the mass of water potentially delivered to Mercury's polar cold traps from Hokusai, we apply the velocity-dependent water retention efficiencies of both analytical [5] and scaled numerical [6] studies, and use a water migration survival rate of 10% [7]. The results of these calculations are shown in Figure 1. The water mass retained drops off steeply with increasing velocity, due to the fact that both the water retention factor and projectile size decrease with increasing velocity. At the low end of the velocity range, both asteroidal and cometary impactors could account for the 10^{16}–10^{18} g estimates of water ice in Mercury's polar deposits.

Implications: On the basis of these calculations, the Hokusai impact is within the scope of having contributed sufficient water ice to account for Mercury's estimated polar deposit inventory, if the inventory is on the lower end of current estimates. The contributed mass increases with lower velocity and higher water content. Higher retention and migration rates would act to enhance the total mass delivered. An impact velocity <~30 km/s is estimated as necessary in order for the Hokusai impact to have delivered >10^{16} g of water to Mercury's polar cold traps, a velocity which is achieved by 24–32% of impacts into Mercury, depending on the size distribution model employed [3, 4]. Intriguingly, this velocity limit is consistent with the velocity constraints suggested by Hokusai's high impact melt volume; an impact velocity of ~23–26 km/s would produce the largest volume of melt for a crater of Hokusai's size.

References: [1] Ernst, C.M. and Chabot, N.L. (2016) LPS, 47, 1374. [2] Holsapple, K.A. (1993) Ann. Rev. Earth Planet. Sci., 21, 333–373. [3] Marchi, S. et al. (2009) ApJ, 137, 4936–4948. [4] Le Feuvre, M. and Wieczorek, M.A. (2011) Icarus, 214, 1–20. [5] Moses, J.I. et al. (1999) Icarus, 137, 197–221. [6] Ong, L. et al. (2010) Icarus, 207, 578–589. [7] Butler, B.J. (1997) JGR, 102, 19283–19292.

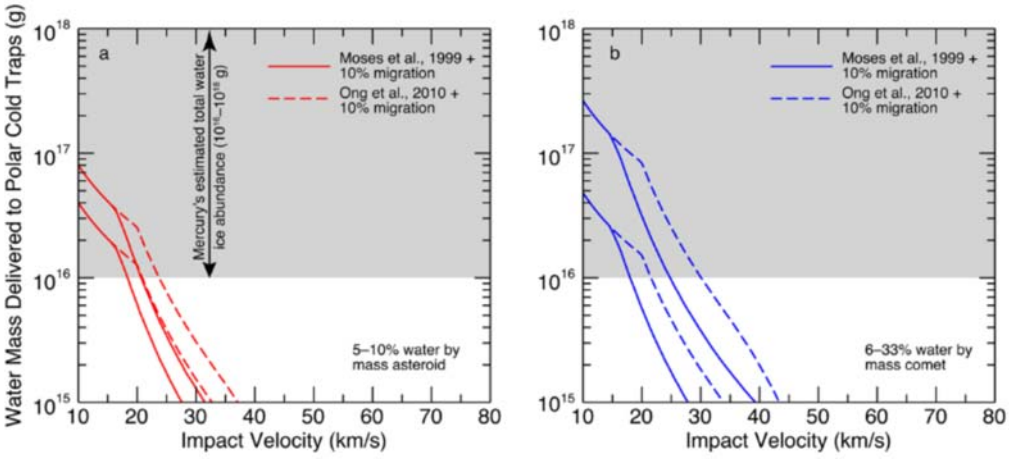

Figure 1. The mass of water delivered to the polar cold traps by a Hokusai impactor versus velocity for (a) a 5–10% water by mass asteroidal impactor and (b) a 6–33% water by mass cometary impactor. To account for 10^{16} g of water, a 10%-water-by-mass asteroidal projectile would need to have had an impact velocity <~20 km/s, and a 33%-water-by-mass cometary projectile would need to have had an impact velocity <~30 km/s.

Landed Reconnaissance of Mercury in the Low-Reflectance Material (LRM^2).

Carolyn M. Ernst[1], Rachel L. Klima[1], Brett W. Denevi[1], Patrick N. Peplowski[1], and Scott L. Murchie[1], [1]Johns Hopkins Applied Physics Laboratory, Laurel, MD 20723, USA (carolyn.ernst@jhuapl.edu).

Introduction: Global observations by the MErcury Surface, Space ENvironment, GEochemistry, and Ranging (MESSENGER) spacecraft have enabled the characterization of Mercury's low-reflectance material (LRM). The most prominent occurrences of LRM are associated with impact craters and basins, implying an origin at depth [e.g., 1-3]. Craters ranging in age from Kuiperian to pre-Tolstojian have excavated LRM [2], suggesting that the original deposits could be quite old. The most widespread areas of LRM appear in the southern hemisphere, as diffuse regions that correlate with Mercury's oldest surfaces [4]. Observations of LRM excavated by Mercury's largest basins suggest that the LRM darkening agent is derived mainly from the lower crust [5].

What is the composition of this lower crustal material? Visible-near infrared spectral [3] and low-altitude neutron spectroscopic [6] measurements are consistent with carbon enhancements of 1–5 wt% over the global abundance, supporting carbon as the darkening agent in LRM. This may be evidence for a proposed graphite flotation crust [7], buried in most places under many layers of lava over the course of Mercury's history.

A majority of the hollows found on Mercury are located within LRM, indicating that they may have a common origin [8-10]. The steep-sloped scarps within hollows suggest collapse due to volatilization of some material, perhaps sulfides [11]. This may provide further evidence that the LRM represents an ancient, exotic, volatile-rich layer.

Open Science Questions: Though MESSENGER has provided tantalizing evidence that LRM is associated with the earliest crust, many questions remain. These range from fundamental questions about understanding the nature of the bulk LRM and the evolution of Mercury's surface, to characterizing the volatile inventory of the planet and the distribution of elements in the protoplanetary disk [12]. Furthermore, Mercury may be an appropriate analog for exoplanets around carbon-rich stars [13]. Specific open questions include:

- Does Mercury's low-reflectance material preserve an ancient carbon-rich crust? What is the age of the diffuse LRM deposits corresponding to the oldest terrain? What are the implications for early crust formation on terrestrial planets and the distribution of volatiles in the early solar system?
- What is the bulk composition of the low-reflectance material? Although carbon has been identified at percent levels, what other major and minor components are present? What are the connections to planetary differentiation and Mercury's bulk composition? Are there other minerals or elements found in association with LRM that might sublimate and result in hollows formation?
- How does the low-reflectance material relate to geologic processes, particularly hollows formation? Are there unique processes, like hollows formation, or more common processes, like space weathering?

Landed Science is the Key! The BepiColombo spacecraft, set to arrive at Mercury in 2025, will build upon MESSENGER discoveries advance our understanding or Mercury. But in situ composition and chronology measurements are required to address many of the outstanding questions. Direct, high-resolution elemental and mineralogical measurements of minor elements and mineral phases would provide tests of the graphite flotation and hollows formation hypotheses. These would further help to characterize the bulk composition of Mercury and to understand its early thermal evolution. Direct measurement of oxygen fugacity could confirm low oxygen content measurements made by the MESSENGER gamma-ray spectrometer [14], which could address the hypothesis that the silicon was smelted by magmas passing through an ancient graphite crust [15]. Absolute age measurements would directly test whether the LRM-bearing material was formed during Mercury's earliest history, and provide critical constraints to the chronology Mercury and the inner solar system.

References: [1] Denevi, B.W. et al. (2009) Science, 324, 613–618. [2] Ernst, C.M. et al. (2010) Icarus, 209, 210–223. [3] Klima, R.L. et al. (2018) LPS, 49, 2257. [4] Denevi, B.W. et al. (2016) LPS, 47, 1624. [5] Ernst, C.M. et al. (2015) Icarus, 250, 413–429. [6] Peplowski, P.N. et al. (2016) Nature Geosci., 9, 273–276. [7] Vander Kaaden, K.E. and McCubbin, F.M. (2015) JGR: Planets, 120, 195–209. [8] Thomas, R.J. et al. (2014) Icarus, 229, 221–235. [9] Thomas, R.J. et al. (2016) Icarus, 1–35. [10] Blewett, D.T. et al. (2013) JGR: Planets, 118, 1013–1032. [11] Blewett, D.T. et al. (2016) JGR: Planets, 121, 1798–1813. [12] Ebel, D.S. and Alexander, C.M.O. (2011) PSS, 59, 1888–1894. [13] Moriarty, J. et al. (2014) ApJ, 787, 1–10. [14] Evans, L.G. et al. (2012) JGR, 117, E00L07. [15] McCubbin, F.M. et al. (2017) JGR: Planets, 122, 2053–2076.

THE NATURE AND MOBILITY OF REGOLITH ON MERCURY'S SMOOTH PLAINS FROM OBSERVATIONS OF CRATER DEGRADATION AND EQUILIBRIUM SIZE-FREQUENCY DISTRIBUTIONS. C.I. Fassett[1], M. Hirabayashi[2], L.R. Ostrach[3], W.A. Watters[4], J.L. Whitten[5]. [1]NASA Marshall Space Flight Center, Huntsville, AL, [2]Dept. of Aerospace Engineering, Auburn University, Auburn, AL, [3]USGS Astrogeology Science Center, Flagstaff, AZ, [4]Dept. of Astronomy, Wellesley College, Wellesley, MA, [5]Center for Earth and Planetary Studies, Smithsonian Institution, Washington, DC (caleb.i.fassett@nasa.gov).

Introduction: There are both observational and theoretical reasons to suspect that the smooth plains of Mercury are mantled by a ubiquitous regolith, akin to the regolith on the lunar maria [1-3]. This abstract describes observations which suggest the regolith on Mercury's smooth plans is thicker and transported with greater efficiency than regolith on the Moon.

Crater Degradation on Mercury: In a recent study, 204 measurements of depth/Diameter (d/D) ratios were made for craters of 2.5 to 5 km in diameter on the smooth plains [4]. Measurements for this purpose were drawn from both MLA and DTMs derived from targeted stereo pairs from MDIS [5]. The median d/D observed was 0.13. Lunar craters in the same size range have a median d/D ratio nearly indistinguishable from the fresh value of ~0.21. The hypothesis we favor for this difference is that craters on Mercury's plains degrade much more quickly than those on the Moon.

Even assuming that Mercury's plains are on average older (~3.7 Ga) than areas measured on the lunar maria (~3.44 Ga) as a baseline, crater degradation has to be faster by a factor of ~2× on the smooth plains than on the lunar maria to explain the degree of crater infilling, suggesting much more rapid regolith development and transport on Mercury.

The Equilibrium Size-Frequency Distribution: Most measurements of crater size-frequency distribution (SFD) on the smooth plains have focused on trying to estimate relative or (more uncertain) absolute ages. For this reason, measurements have typically been of large craters (D>5-10 km) to avoid secondaries and other complicating factors. Here we are interested in much smaller sizes (D>50-100 m), because these smaller craters are likely to have reached equilibrium, where new craters form at the same rate old craters are degraded beyond recognition [e.g., 6]. When the crater production function has a steep size-distribution, the portion of the observed SFD in equilibrium is recognizable because there is a transition to a shallower power law slope from the production slope.

For three smooth plains regions with very high resolution MDIS NAC strips (~12.5 m/px), we measured crater populations with the goal of determining the equilibrium behavior on Mercury. An example is shown in Fig. 1. The transition in the three areas we measured occurs around D_{eq}~500-800 m, which is much larger than on typical maria. This larger equilibrium diameter implies that regolith must be thicker on Mercury's plains. In addition, these measurements preliminarily suggest that (1) the equilibrium density on Mercury's plains typically falls below the lunar value (consistent with faster degradation), and (2) the power-law slope of the equilibrium function might be slightly shallower on Mercury than the Moon.

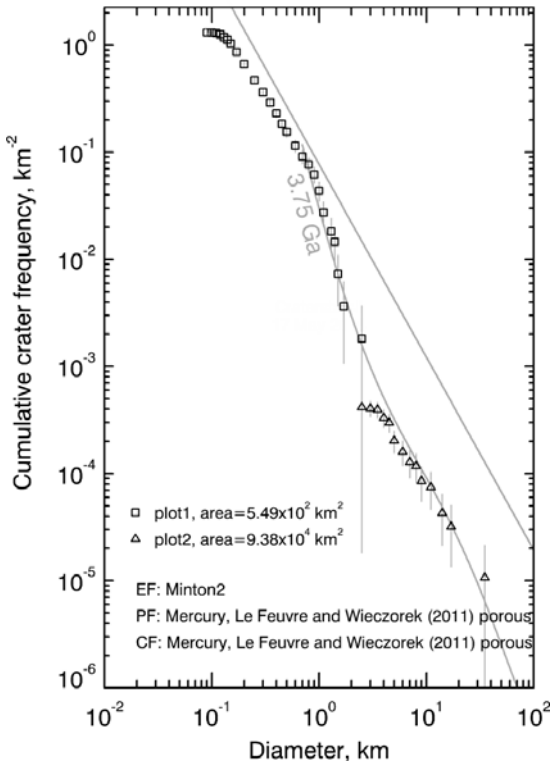

Figure 1. Measurements of crater size-frequency distribution in a region of the northern smooth plains (65°N, -83°E). This is a nested count; craters >~2 km (triangles) are drawn from a region within ~200 km of the narrow high resolution image strip where craters <2 km (squares) were measured. The equilibrium diameter here is ~800m. Note that the equilibrium function here is from the Moon (power-law slope -1.8).

Acknowledgments: This abstract draws from work with Lindy Crowley, Darby Dyar, Clarissa Leight, David Minton, and Brad Thomson. Support is acknowledged from NASA grants NNX14AR88G and 80NSSC17K0216.

References: [1] Langevin, Y. (1997) PSS, 45, 31-37. [2] Kreslavsky, M.A. et al. (2014), GRL, 41, 8245-8251. [3] Kreslavsky, M.A., Head, J.W. (2015), LPSC, 46, 1246. [4] Fassett, C.I et al. (2017), GRL, 44, 5326-5335. [5] Fassett, C.I. (2016), PSS, 134, 19–28. [6] Gault, D.E. (1970), Radio Sci., 5, 273–291.

COLD-BASED GLACIATION ON MERCURY: ACCUMULATION AND FLOW OF ICE IN PERMANENTLY-SHADOWED CIRCUM-POLAR CRATER INTERIORS.

J. L. Fastook[1] and J. W. Head[2], [1]University of Maine, Orono, ME, 04469, fastook@maine.edu, [2]Brown University, Providence, RI, 02912.

Introduction: Radar evidence exists for the presence of ice in permanently shaded polar craters on Mercury. Ice is thermally stable under these conditions, and a detailed energy-balance model suggests an annual mean temperature of 110 K in pemanent shade and close to 400 K in sunlit regions. We describe the dynamic properties of possible ice deposits to delineate the effects of ice deformation and the potential for flow that would modify these deposits in the time interval for which they are believed to have existed.

Modeling: We use a simple geometry, a function of crater diameter and latitude, that defines the shape of the crater walls and floor, as well as the permanently shaded volume that defines the ice surface. Depth of the crater is determined from the d/D ratio, and a power-law fit. Fig. 1 shows an example based on the 50 km Crater C at a latitude of 87.5°.

The ice dynamics model is a thermomechanical shallow-ice approximation model that has been used extensively both on Earth and Mars, here adapted for Mercury gravity. An ablation rate of 1.0 m/yr is assumed in the sunlit areas, while minor accumulation (10^{-10} m/yr) is assumed for the ice surface. Boundary conditions for the thermodynamic component, used to calculate the ice hardness, include mean-annual surface temperature and basal heat flux. Because the ice is thin (basically the crater depth) and the slope is shallow (basically the sun angle), as well as the fact that the ice is cold, modeled velocities are very low, on the order of 10^{-10} m/yr for a uniform heat flux of 50 mW/m^2. Velocity, shown in Fig. 1, is highest at the base of the crater wall where thickness is greatest.

Lateral Transport of Heat: We also consider the lateral transport of heat from the warm sunlit surroundings of the cold shaded crater interior. A 2D solution of the steady-state heat flow equation for a rectangular domain with a "cold spot" on the surface results in a depression and warping of the isotherms below the cold spot that directs additional heat from the surroundings beneath the hot surface terrain into the center of the cooler region beneath the cold spot. Fig. 2 shows the base-10 logarithm of the maximum velocity observed in each model run for the uniform flux case (left) and the non-uniform lateral transport case (center). Labelled stars indicates the position of craters with known deposits. Since depth depends on diameter, in the uniform flux case larger craters display faster velocities, due to the thicker ice that can exist in the deeper craters.

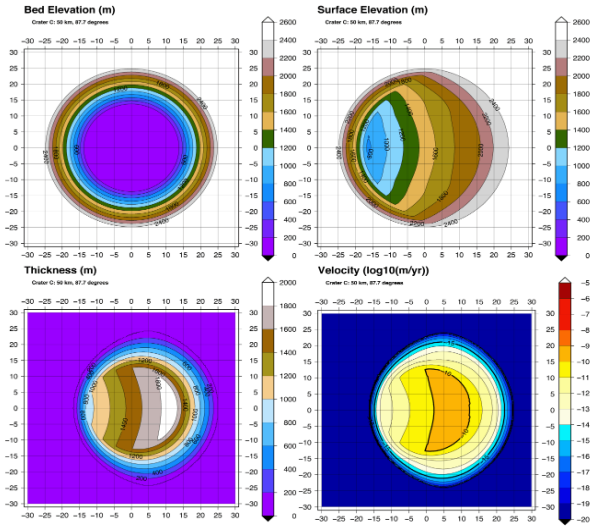

Figure 1: Geometry based on Talpe et al. (2012) and Crater C, with 50 km diameter at latitude 87.5°.

With lateral heat transport, we obtain a very different pattern of velocities, (Fig. 2 center). The greater heat fluxes result in warmer ice, which being softer yields higher velocities. The relative speedup (Fig. 2 right) is greatest for the smallest craters at the highest latitudes, reaching in some cases six orders of magnitude, attaining velocities of 10^{-5} m/yr.

The highest velocities are observed in a 10 km crater at a latitude of 89°, and Fig. 3 shows the evolution of the ice surface in such a crater over a billion years. Thinning upstream and thickening downstream results in a flattening of the surface where the velocity is a maximum.

Conclusions: The thickest deposits with the greatest surface slope have the largest driving stresses as well as the warmest, softest ice at the bed, and hence the fastest velocities. However, accounting for the enhanced flux of heat from the surrounding hot sun-lit terrain is extremely important, offering orders of magnitude speedup over the uniform flux case, with the effect most pronounced for small craters where the greatest lateral heat flux is delivered to the centers of the craters. Even with the enhanced heat fluxes, the cold environment of the Mercury polar craters yields very small velocities and deformation is minimal on a time scale of millions of years. Even at it most rapid flow velocity, the ice surface would move only a kilometer in a hundred million years. These predictions can be used to compare to the observed deposit distributions and characteristics.

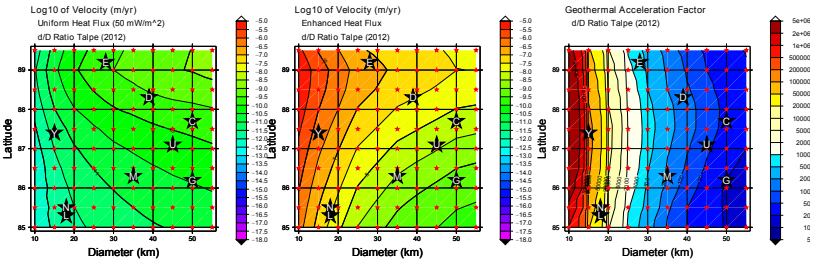

Figure 2: Base-10 log of velocity for the uniform flux case (left), the lateral heat transport case (center), and the ratios of these (right).

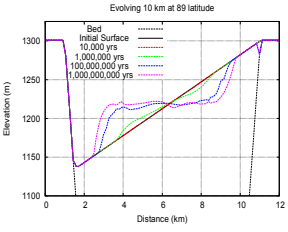

Figure 3: Evolution of a 10 km crater at 89°, showing initial surface and deforming surface at 10^4, 10^6, 10^8, and 10^9 years.

References: see Fastook & Head (2016) LPS47 #1162 for complete references.

GETTING READY FOR BEPICOLOMBO: A MODELING APPROACH TO INFER THE SOLAR WIND PLASMA PARAMETERS UPSTREAM OF MERCURY FROM MAGNETIC FIELD OBSERVATIONS.

S. Fatemi[1], N. Poirier[2], M. Holmström[1], J. Lindkvist[3], M. Wieser[1], S. Barabash[1], [1]Swedish Institute of Space Physics (shahab@irf.se), [2]École Nationale Supérieure de Mécanique et d'Aérotechnique, Chasseneuil-du-Poitou, France, [3]Department of Physics, Umeå University, Umeå, Sweden.

Introduction: The lack of an upstream solar wind plasma monitor when a spacecraft is inside the highly dynamic magnetosphere of Mercury limits interpretations of observed magnetospheric phenomena and their correlations with upstream solar wind variations. A detailed and accurate knowledge about the solar wind plasma and its variations as it interacts with Mercury is crucial to better understand the morphology of the interaction, structure of the magnetosphere of Mercury, and its associated phenomena and their correlations with solar wind variations.

Model: We use AMITIS, a three-dimensional GPU-based hybrid model of plasma (particle ions and fluid electrons) [1] to infer the solar wind plasma parameters upstream of Mercury by comparing our simulation results with Messenger magnetic field observations inside the magnetosphere of Mercury. We select a few orbits of Messenger, which have been analysed and compared with simulations before. Then, we run nearly 40 simulation runs for each orbit with different solar wind plasma parameters to find the best agreement between our simulations and Messenger magnetic field observations inside Mercury's magnetosphere.

Results: Figure 1 shows a preliminary magnetic field comparison between our hybrid simulations (red lines), Messenger magnetometer observations (black lines), and the undisturbed intrinsic magnetic dipole of Mercury (blue dashed lines) along the trajectory of Messenger on 23 April 2011 (DOY 113) between 16:00 and 21:00 UTC. Our model estimated solar wind dynamic pressure for this orbit is ~3 nPa, which is lower than the typical solar wind dynamic pressure at the orbit of Mercury (~7 nPa). However, Figure 1 shows that there is a good agreement between our hybrid simulation results and Messenger magnetic field observations for the estimated solar wind plasma parameters upstream of Mercury [2]. We also use our model to determine the location of the magnetospheric boundaries, i.e. bow shock, magnetopause, and magnetotail, and their correlations and variations with the solar wind plasma and compare them with those previously estimated from observations [2].

Conclusion: We show that our model can be used as an upstream solar wind plasma monitor for Mercury to provide estimates of the solar wind variations from magnetic field observations inside Mercury's magnetosphere. These results have important implications for observations by Messenger, and for the future ESA/JAXA mission to Mercury, BepiColombo [2].

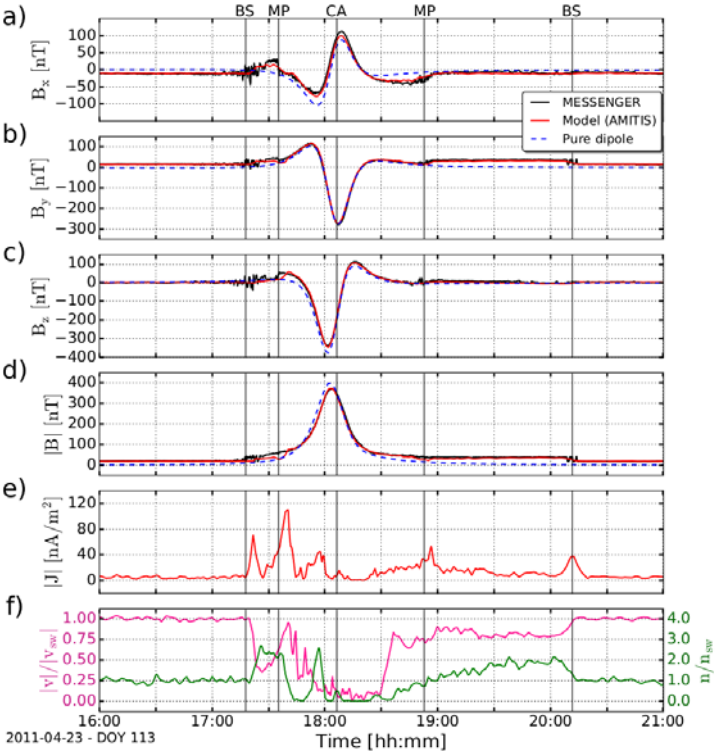

Figure 1. (a,d) Magnetic field comparison between our hybrid model simulations (red lines), Messenger magnetometer observations (black lines), and undisturbed intrinsic magnetic dipole of Mercury (blue dashed lines) along the trajectory of Messenger on 23 April 2011. (e) Magnitude of the electric current density, and (f) solar wind bulk flow speed normalized to the upstream solar wind speed 314 km/s (purple line) and solar wind plasma density normalized to the upstream plasma density 22 cm^{-3} obtained from our hybrid model simulations along the trajectory of Messenger. The location of the bow shock (BS) and magnetopause (MP) boundaries estimated by Winslow et al., 2013 [3] are shown by the vertical lines.

References

[1] Fatemi et al., (2017) J. of Phys. Conf. Ser., 837(1)
[2] Fatemi et al., (2018) A&A, (submitted)
[3] Winslow et al., (2013) J. Geophy. Res., 118 (5)

THE MAKING OF THE 1:3M GEOLOGICAL MAP SERIES OF MERCURY: STATUS AND UPDATES.

V. Galluzzi[1], L. Guzzetta[1], P. Mancinelli[2], L. Giacomini[1], A. M. Lewang[3], C. Malliband[4], A. Mosca[5], D. Pegg[4], J. Wright[4], L. Ferranti[5], H. Hiesinger[3], M. Massironi[6], C. Pauselli[2], D. A. Rothery[3], and P. Palumbo[7,1], [1]INAF, Istituto di Astrofisica e Planetologia spaziali (IAPS), Via del Fosso del Cavaliere 100, 00133, Rome, Italy (valentina.galluzzi@iaps.inaf.it), [2]Dipartimento di Fisica e Geologia, Università degli Studi di Perugia, Perugia, Italy, [3]Institut für Planetologie, Westfälische Wilhelms-Universität, Münster, Germany, [4]School of Physical Sciences, The Open University, Milton Keynes, UK, [5]DiSTAR, Dipartimento di Scienze della Terra, dell'Ambiente e delle Risorse, Università "Federico II", Naples, Italy, [6]Dipartimento di Geoscienze, Università degli Studi di Padova, Padua, Italy, [7]Dipartimento di Scienze & Tecnologie, Università degli Studi di Napoli 'Parthenope', Naples, Italy.

Introduction: By the end of the NASA Mariner 10 mission, 45% of Mercury's surface had been imaged by the M10 Television Experiment and over 2000 useful pictures were available at a resolution better than 2 km, up to 100 m. These results led to the production of 1:5M geologic maps of seven of the fifteen quadrangles of Mercury [1]. The NASA MESSENGER mission filled the gap by imaging 100% of the planet with a frame resolution up to 8 m/pixel at the north pole, and a global average resolution of 200 m/pixel, enabling preparation of a new global 1:15M geologic map [2]. Today, a complete global series of 1:3M-scale maps of Mercury is being prepared in support to the ESA/JAXA BepiColombo mission [3]. Born from individual geologic quadrangle maps [4, 5, 6], it has evolved into a coordinated global mapping plan, and carried on with the aim of exploiting MESSENGER images at the best resolution available (i.e., global average resolution) in order to set up the context for BepiColombo operations and help re-define mission goals as appropriate.

Current status: Currently, H02 Victoria [4], H03 Shakespeare [6] and H04 Raditladi [5] have been completed; H05 Hokusai [7], H06 Kuiper [8], H07 Beethoven [e.g., 9], H10 Derain [10] and H14 Debussy are being mapped (Fig. 1). The produced geologic maps were merged adjusting mismatches along the quadrangle boundaries. At the current stage, ~35% of Mercury has now a complete 1:3M-scale map and ~55% of the planet will be covered soon by the maps that are being prepared. This series of 1:3M-scale quadrangle maps cannot be merged into a single physical 1:3M-scale global map. However, the global merged output will be used as a digital full-scale product, which will permit detailed global or regional analyses of Mercury's surface. This project will lead to a fuller grasp of the planet's stratigraphy and surface history and is an important goal in preparation for the forthcoming ESA/JAXA BepiColombo mission to aid selection of scientific targets and to provide context for interpretation of new data.

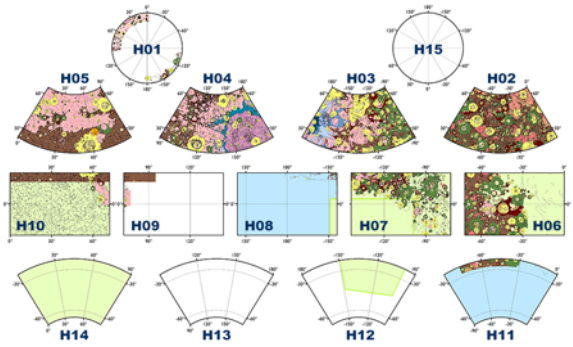

Figure 1. Current status of the 1:3M-scale geological map series of Mercury. The used projections are centered on each quadrangle: H01 and H15 Polar Stereographic; H02 to H05 Lambert Conformal Conic with standard parallels at 30°N and 58°N; H06 to H10 Equidistant Cylindrical; H11 to H14 Lambert Conformal conic with standard parallels at 30°S and 58°S. Background colors indicate quadrangles with mapping in progess (green) or scheduled work (blue).

Acknowledgements: This research was supported by the Agenzia Spaziale Italiana (ASI) within the SIMBIOSYS project (ASI-INAF agreement n. I/022/10/0).

References: [1] Spudis P. D. & Guest J. E. (1988), In: Vilas, F., et al. (eds), *Mercury*, 118–164. [2] Prockter L. M. et al. (2016), *LPS XLVII*, Abstract #1245. [3] Benkhoff J. et al. (2010), *PSS*, *58*, 2–20. [4] Galluzzi V. et al. (2016), *JoM, 12*, 227–238. [5] Mancinelli P. et al. (2016), *JoM*, *12*, 190–202. [6] Guzzetta L. et al. (2017), *JoM*, *13*, 227–238. [7] Wright J. et al. (2018), *LPS XLIX*, Abstract #2164. [8] Giacomini L. et al. (2017), *EGU*, *19*, Abstract #14574. [9] Lewang A. M. et al. (2018), *LPS XLIX*, Abstract #1846. [10] Malliband C. et al. (2017), *LPS XLVIII*, Abstract #1476.

TOWARDS THE REDEFINITION OF THE GLOBAL STRATIGRAPHY OF MERCURY: THE CASE OF INTERMEDIATE PLAINS. V. Galluzzi[1], D. A. Rothery[2], M. Massironi[3], L. Ferranti[4], and the Mercury Mapping Team, [1]INAF, Istituto di Astrofisica e Planetologia spaziali (IAPS), Via del Fosso del Cavaliere 100, 00133, Rome, Italy (valentina.galluzzi@iaps.inaf.it), [2]School of Physical Sciences, The Open University, Milton Keynes, UK, [3]Dipartimento di Geoscienze, Università degli Studi di Padova, Padua, Italy, [4]DiSTAR, Università "Federico II", Naples, Italy.

Introduction: On Mercury 'surface morphology reflects the age, composition, lithology, and mode of formation of the underlying rock unit' [1] and Mercury's geological provinces must be 'characterized by a similar inferred origin or a distinctive history' [2, 3]. Based on these statements, three main morphological units were defined for Mercury on the basis of Mariner-10 images: Smooth Plains (SP), Intercrater Plains (ICP) and Intermediate Plains (IMP). All are now accepted on the basis of MESSENGER images to be essentially volcanic, but the validity of IMP as a mappable unit has been questioned [4].

Morphology vs. color. Mercury's plains units defined by morphological criteria rarely show unique correspondence with the color-compositional units. ICP may encompass several color variations, including low reflectance material [e.g., 5]. It is commonly accepted that at least two SP regions (i.e. the northern plains and the Caloris plains) pertain to distinct volcanic events, although in some cases they share the same colors [e.g., 6, and references therein]. Nonetheless, the definition of IMP is still controversial, because of a lack of a distinctive crater population [4]. Thus, it can be said that both the morphological and color classification of rock units work well independently from one another, however, they are still not working well in concert. In view of a global geological survey, we aim at redefining the global stratigraphy of Mercury by better characterizing the IMP regions, mapped with sole morphological criteria, by means of crater population, color and chemical analysis.

The Intermediate Plains case: The IMP unit forms 'planar to undulating surfaces that have higher crater density than smooth plains material, but are less heavily cratered than intercrater plains material' [7]. However, recent works conclude that there is no clear contrast between IMP and the adjacent terrains, such that they can be encompassed into either SP or ICP units [6], and that the age of IMP and ICP seem to overlap [4]. For these reasons, the IMP unit has been lately discarded from some geological maps [6, 7]. The recent production of the first in a series of 1:3M-scale geological maps, however, led to the re-introduction of this unit due to evident morphological peculiarities that are visible at the mapping scale (~1:400k) [9, 10]. By using the data collected by MESSENGER's MDIS, a thorough analysis of the morphology of the IMP areas mapped by [9] was made. We estimated the relative and absolute age of IMP and its overlapping features by means of crater counting techniques. Then, we correlated these results to the geochemical terranes detected by [11], and the available MDIS color basemaps. Current results show that the analysed IMP areas seem to remain a distinct unit both for their morphology and for their age [9]. However, they pertain to two different geochemical terrains detected by [11], and this might lead to the distinction of IMP into two sub-units in the future.

Concluding remarks: With plains effusion continuing and waning through the late heavy bombardment, we hardly expect a bimodal distribution of SP versus ICP. On the contrary, we should expect plains with all kinds of crater density, as is indeed found [e.g., 7]. However, how many divisions should be made for mapping purposes, when arbitrarily dividing such a continuum? Our observations are based on an average mapping scale of 1:400k, which, for cartographic rules, should be the lowest scale to use when considering the average resolution provided by the major MESSENGER datasets [see 9]. The results lead to the retention of IMP as an official unit of Mercury that could, at the same time, encompass two or more subunits when considering terrain composition. In this view, the distinction of Mercury's plains into fewer than three units seems hard to support. However, how a 3-fold (or more) distinction could be applied consistently at various mapping scales is still to be debated.

Acknowledgments: This research was supported by the Agenzia Spaziale Italiana (ASI) within the SIMBIOSYS project (ASI-INAF agreement n. I/022/10/0).

References: [1] Trask N. J. & Guest J. E. (1975), *JGR*, *80*, 2461–2477. [2] Spudis P. D. & Guest J. E. (1988), in: Vilas F., et al. (eds), *Mercury*, 118–164. [3] McCauley J. F. & Wilhelms D. E. (1971), *Icarus*, *15*, 363–367. [4] Whitten J. L. et al. (2014), *Icarus*, *241*, 97–113. [5] Murchie S. et al. (2015), *Icarus*, *254*, 287–305. [6] Denevi B. W. et al. (2013), *JGR: Planets*, *118*, 891–907. [7] Spudis P. D. & Prosser J. G. (1984), *USGS*, Map I-1659. [8] Prockter L. M. et al. (2016), *LPS XLVII*, Abstract #1245. [9] Galluzzi V. et al. (2016), *JoM*, *12*, 227–238. [10] Guzzetta L. et al. (2017), *JoM*, *13*, 227–238. [11] Weider S. Z. et al. (2015), *EPSL*, *416*, 109–120.

STATISTICAL ANALYSIS OF PDF'S FOR Na RELEASED BY PHOTONS FROM SOLID SURFACES

D. Gamborino[1] and P. Wurz[1], [1] (Physics Institute, University of Bern. Sidlerstrasse 5, 3012, Bern, Switzerland. (diana-gamborino@space.unibe.ch; peter.wurz@space.unibe)

Introduction: We investigate the adequacy of three model speed distributions functions that have been previously used in several studies to describe the desorption of atoms from a solid surface either by electron or by photon bombardment, namely: the Maxwell-Boltzmann (M-B) distribution, the empirical distribution proposed by Wurz et al. [2010] for PSD (E-PSD), and the Weibull distribution.

We use the few available measurements reported by Yakshinskiy and Madey [2000, 2004] (Figure 1) to test these model distributions and determine which one fits best (statistically) and we discuss their physical validity. We do so by means of the Graphical Residual Analysis (GRA), which is commonly used to determine how well a given model distribution function fits a given data sample.

Our results show that the measured speed distributions of released Na atoms are too narrow compared to the ``high" temperature M-B fits used by Yakshinskiy and Madey [1999, 2000, 2004]. We found that a good fit with M-B is only achieved with an offset of the whole distribution to higher speeds and a low temperature, yet showing no correlation with the surface temperature.

On the other hand, the Weibull distributions are ostensibly better fits for which an increase in the temperature to that of the surface is not needed, though an offset towards higher speeds is required. We interpret this offset as the excess of energy the electron or photon provides after the electronic excitation event leading to the dissociation from the surface.

The GRA shows that the M-B fits are statistically less adequate compared to the other non-Maxwellian distributions, not to mention that the M-B are not physically applicable to this kind of experiments.

The GRA also shows that the E-PSD distribution is particularly better suited to the measurements and the parametrization has a better physical interpretation.

Our results confirm that Electron-Stimulated Desorption (ESD) and Photon-Stimulated Desorption (PSD) should produce non-thermal speed (energy) distributions of the atoms released via these processes, which is expected from surface physics.

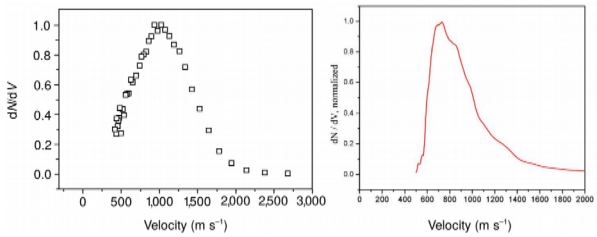

Fig. 1.- Measurements reported by Yakshinskiy and Madey [2000 (left), 2004 (right)].

Results:

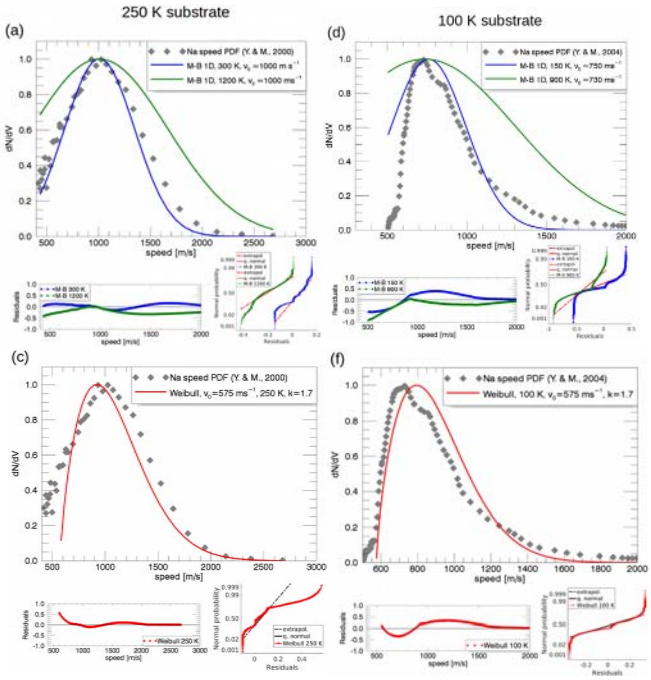

References:

P. Wurz, J.A. Whitby, U. Rohner, J.A. Martín-Fernández, H. Lammer, and C. Kolb. (2010). Self-consistent modelling of Mercury's exosphere by sputtering, micro-meteorite impact and photon-stimulated desorption, Planet.\ Space Science 58 1599--1616.

Yakshinskiy, B.V,Madey, T.E., 2000. Desorption induced by electronic transitions of Na from SiO: relevance to tenuous planetary atmospheres, Surface Science, Volume 451, Issue 1, Pages 160-165, ISSN 0039-6028.

Yakshinskiy, B.V., Madey, T.E., 2004. Photon-stimulated desorption of Na from a lunar sample: temperature-dependent effects, Icarus, Volume 168, Issue 1, Pages 53-59, ISSN 0019-1035.

A Large Solid Inner Core at Mercury. A. Genova[1,2], S. Goossens[2,3], E. Mazarico[3], F. G. Lemoine[3], G. A. Neumann[3], W. Kuang[3], T. J. Sabaka[3], D. E. Smith[1] and M. T. Zuber[1], [1]Department of Earth, Atmospheric and Planetary Sciences, Massachusetts Institute of Technology, Cambridge, MA 02139-4307, USA (antonio.genova@nasa.gov); [2]Center for Research and Exploration in Space Science and Technology, University of Maryland, Baltimore County, Baltimore, MD 21250, USA; [3]NASA Goddard Space Flight Center, Greenbelt, MD 20771, USA.

Introduction: The MErcury Surface, Space ENvironment, GEochemistry, and Ranging (MESSENGER) mission addressed key scientific objectives focused on the interior of the planet with dedicated magnetic and gravity investigations. The measurement of the magnetic field offset and amplitude, for example, allowed the characterization of some properties of the outer core [1]. In addition, the combination of the planet's orientation (obliquity -- angle between spin and orbital axis -- and physical longitudinal librations) with gravity measurements (degree 2 in spherical harmonics) have constrained the size of the molten outer core [2, 3].

However, there are still open questions concerning the mass distribution within the different layers of the planet interior and, in particular, nature and size of the solid inner core. The analysis of the entire MESSENGER radio science dataset, which includes the low-altitude campaign, enabled us to substantially improve the knowledge of Mercury's gravity field and obliquity of the spin axis. These geophysical quantities are necessary to refine the polar moment of inertia of the whole planet which bears on the level of differentiation [4].

Data and Method: Our new gravity solution provides refined estimates of the spin axis coordinates (right ascension and declination) that permits the retrieval, for the first time, of the average obliquity of the whole planet, which we find in perfect agreement with the Cassini state.

The normalized polar moment of inertia, C/MR^2, resulting from the new obliquity is significantly lower than the previous estimate of 0.346 ± 0.011 [5] and with an uncertainty improved by a factor of 3 [6]. Our refined estimate of the polar moment of inertia suggests that Mercury is much more differentiated than initially thought.

We implemented a Markov-chain Monte Carlo (MCMC) algorithm to obtain solutions that match bulk density and radius and our latest estimates of the normalized polar moment of inertia, C/MR^2, and the fractional polar moment of inertia, C_{cr+m}/C.

Results: We integrate the governing differential equations for pressure and density under hydrostatic equilibrium (using 1 km thick layers) to retrieve models that are self-consistent and physically realistic in terms of their pressure, temperature and density profiles [7]. However, this approach requires an initial assumption on the light element that is present in the core. A possible scenario is an inner and outer core of Fe-Si alloy. Figure 1 shows the ratio between inner core (r_{ic}) and outer core radii (r_{oc}) as a histogram for the Multi-layer ensemble. These results suggest the presence of a solid inner core with a $r_{ic} \approx 0.3\text{-}0.7\ r_{oc}$.

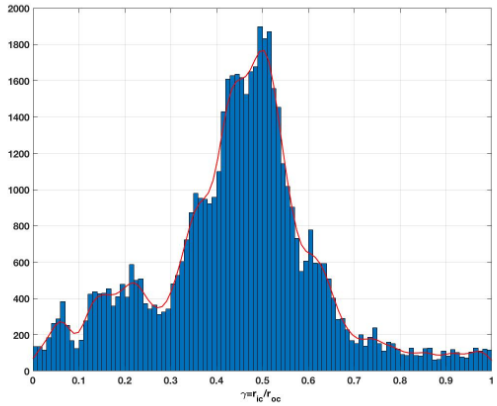

Figure 1. Ratio between the inner and outer core radii as a histogram for the samples of the Multi-layer MCMC solutions.

Summary: Our new measurements of the polar moments of inertia of the whole planet and of the outer layers (crust+mantle) suggest a more differentiated internal structure for Mercury. These geophysical quantities improve the constraint on the size of the solid inner core. Furthermore, simulations of Mercury's magnetic field dynamo confirm that the presence of a solid inner core with a $r_{ic} \leq 0.5\ r_{oc}$ is consistent with a magnetic field, thus providing an additional constraint on the size of the solid inner core.

References: [1] Anderson B. J. et al. (2012) J. Geophys. Res. 117, E00L12. [2] Margot J. L. et al. (2007) Science 316, 710-714. [3] Margot J. L. et al. (2012) J. Geophys. Res. 117, E00L09. [4] Peale S. J. et al. (2002) Meteorit. Planet. Sci. 37, 1269-1283. [5] Stark A. et al. (2015) Geophys. Res. Lett. 42, 7881-7889. [6] Genova A. et al. (2018) In prep. [7] Hauck S. A. II et al. (2013) J. Geophys. Res. 118, 1204-1220.

HOW OLD ARE MERCURY'S THRUST SYSTEMS? NEW RESULTS AND IMPLICATIONS FOR THE THERMAL EVOLUTION OF THE PLANET. L.Giacomini[1] , M. Massironi[2] , V. Galluzzi[1], S. Ferrari[3] and P. Palumbo[4]. [1]INAF, Istituto di Astrofisica e Planetologia Spaziali, via Fosso del Cavaliere 100, 00133, Roma, Italy (lorenza.giacomini@iaps.inaf.it). [2]Dipartimento di Geoscienze, Università degli Studi di Padova, via Gradenigo 6, 35131, Padova, Italy, [3]CISAS, via Venezia 15, 35131, Padova, Italy. [4]Dipartimento di Scienze e Tecnologie, Università degli Studi di Napoli "Parthenope", Centro Direzionale, Isola C4 80143 Napoli, Italy.

Introduction: The global tectonic scenario of Mercury is dominated by contractional features mainly represented by thrust faults. These structures are features widely distributed on Mercury and are linear or arcuate, tens to hundred kilometers in length. Since they display a broad distribution of orientations, they are thought to be related to a global contractional strain due to the planet's interior cooling [1]. The age determination of these features will permit to better constrain the timing of the contractional process, and, in turn, will give us new clues to understanding the thermal evolution of Mercury.

Mercury's thrust systems: We identified several thrust systems widely distributed on the planet's surface. We classified as "thrust system" a series of clustered thrust segments characterized by a coherent trend. In this work we dated five thrust systems that we named after the main features (i.e. lobate scarps or craters) encompassed in the system. In particular, we took into account the Thakur, Victoria, Villa Lobos, Al-Hamadhani and Enterprise systems (Fig.1).

Dating the thrust systems activity: We dated the systems through the buffered crater counting technique [2,3,4], which can be used to derive absolute model ages of linear landforms such as faults, ridges and channels. We included in the counting all the craters whose rim directly cut the thrusts. A fault buffer width of 2r has been considered (where r is the radius of the crater). Subsequently, the results of the crater counting have been arranged as a crater size–frequency distribution (CSFD), which describes the frequency of craters of specified size per unit area. Finally, the CSFD have been compared with the Neukum Production Function (NPF) [5], and the more recent Le Feuvre and Wieczorek Production Function (LWPF) [6], to gain the absolute age for the end of activity of the systems.

Results: The age obtained suggested that the activity of the thrust systems considered in this work ended between a time span ranging from 3.6 to 3.8 Ga, according to NPF, and between 2.9 and 3.7 Ga following LWPF (Fig.1). For this latter we considered the porous scaling law which has been thought to be the more appropriate due to the characteristics of the surrounding terrains, since the systems cut intercrater plains for the most part of their length. The results are comparable to that estimated for the Blossom Rupes system, dated at about 3.5-3.7 Ga [4]. All these data suggest that the activity along major rupes all around planet Mercury have most probably begun before 3.5 Ga. However, the most recent Mercury thermal evolution models estimate the start of the global contraction at about 3.0 Ga [e.g. 7,8] and, therefore, do not account for such an early beginning of contractional tectonic landforms' formation. Moreover, the detection of strike-slip kinematic indicators [9] and of a non-uniform spatial distribution and density of large-scale contractional structures [e.g. 10] cannot be explained solely by contraction. These results seem to support a revision of the current thermal models, where other processes, like tidal despinning and/or mantle convection, could have contributed to Mercury's evolution.

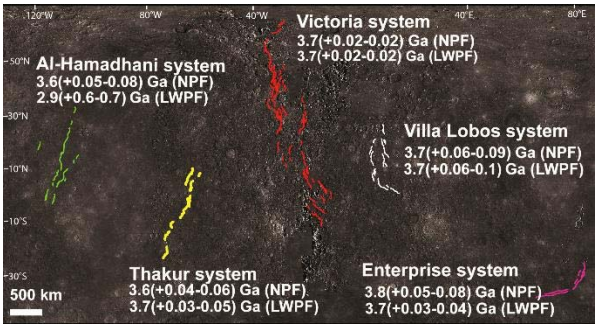

Figure 1. Thrust systems considered in this work with the respective ages, estimated both with Neukum Production Function (NPF) and Le Feuvre and Wieczorek Production Function (LWPF). The basemap is a MESSENGER MDIS global mosaic in equirectangular projection. Scale is true at the equator.

Acknowledgements: This research was supported by the Agenzia Spaziale Italiana (ASI) within the SIMBIOSYS project (ASI-INAF agreement n. I/022/10/0).

References: [1] Watters T. R. et al. (1998), *Geology*, *26*, 991–994. [2] Tanaka K. L. (1982), *NASA TM-85127*. [3] Fassett C. I. and Head III J. W (2008), *Icarus*, *198*, 37–56. [4] Giacomini L. et al. (2015), *GSL*, *Special Publications*, *401*, 291–311. [5] Neukum G. et al. (2001), *PSS*, *49*, 1507–1521. [6] Le Feuvre M. and Wieczorek M. A. (2011), *Icarus*, *214*, 1–20. [7] Grott M. et al. (2011), *EPSL*, *307*, 135–146. [8] Tosi N. et al. (2013), *JGR Planets*, *118*, 2474–2487. [9] Massironi M. et al. (2015), *GSL*, *Special Publications*, *401*, 269–290. [10] Watters T. R. et al. (2015), *GRL*, *42*, 3755–3763.

FIRST IDENTIFICATION OF FORESHOCK PLASMA POPULATIONS AT MERCURY. A. N. Glass[1], P. J. Tracy[2], and J. M. Raines[2], [1]Climate and Space Sciences and Engineering, University of Michigan (anglass@umich.edu), [2] Climate and Space Sciences and Engineering, University of Michigan.

Observations of foreshock populations at Mercury are presented for the first time utilizing measurements from the Fast Imaging Plasma Spectrometer (FIPS) aboard MESSENGER. The magnetosphere and foreshock system at Mercury exist in a unique parameter space, due to the planet's relatively weak magnetic dipole and its close proximity to the Sun. Previous investigations have questioned whether foreshock populations can exist at Mercury, due to the small spatial scale of its bow shock, but the observations of this work show foreshock populations, similar to those seen in the terrestrial foreshock, upstream of the Hermean bow shock. Furthermore, these populations are organized by the bow shock geometry in a manner similar to those at Earth.

Observations by FIPS also suggest energization mechanisms for the Field Aligned Beams (FABs) and Diffuse particle populations observed in Mercury's foreshock. In the case of FABs, results suggest the energization process to be Shock Drift Acceleration, which is not limited by the small spatial size of Mercury's bow shock. For diffuse populations it is shown through estimates of the diffusion coefficient, IMF-bow shock connection times, and the Fermi acceleration time scale that a connection-time-limited diffusive shock acceleration is likely responsible.

HIGH-RESOLUTION GRAVITY FIELD MODELING FOR MERCURY TO ESTIMATE CRUST AND LITHOSPHERIC PROPERTIES. Sander Goossens[1,2], Erwan Mazarico[2], Antonio Genova[2,3], Peter James[4,5]. [1]Center for Research and Exploration in Space Science and Technology, University of Maryland Baltimore County, Baltimore MD, USA (email: sander.j.goossens@nasa.gov), [2]NASA Goddard Space Flight Center, Code 698, Greenbelt, MD 20771, USA, [3]Department of Earth, Atmospheric and Planetary Sciences, Massachusetts Institute of Technology, Cambridge, MA 02139-4307, USA, [4]Baylor University, Department of Geosciences, One Bear Place #97354, Waco, TX 76798, USA, [5]Lunar and Planetary Institute, USRA, Houston, TX 77058, USA

Introduction: The MErcury Surface, Space ENvironment, GEochemistry, and Ranging (MESSENGER) [1] mission has, among others, resulted in the first detailed maps of topography [2] and gravity [3,4] of Mercury. Due to the highly eccentric orbit of MESSENGER, both data sets have the best resolution in the northern hemisphere. During its second extended mission (March 2013 until April 2015, the end of mission), MESSENGER orbited Mercury as low as 15 to 25 km above the surface, resulting in a wealth of information about the gravity field at small scales. However, standard methods of gravity field determination have difficulties in extracting all the information from the data: geographically-varying data coverage requires the smoothing of the solutions to prevent unrealistic variations in the gravity, thus suppressing short-wavelength signals. In turn, this means that current publicly available gravity field models, despite using the complete tracking data set of MESSENGER, can only be used for geophysical interpretation of the longer-wavelength structure of Mercury. However, parameters such as the crustal density, important in geophysical studies of the thickness and support of the crust, can only be unambiguously determined from gravity and topography at smaller scales. If estimates of crustal density can be obtained, a more robust analysis of the thickness and flexure of the lithosphere is also within reach. An analysis of lithospheric thickness combined with estimations of the crustal density will improve our knowledge of Mercury's structure and thermal evolution.

Methods and Results: Because of the varying geographical coverage of the data, we transform Doppler data residuals from standard gravity field determination techniques [4] into Line-of-Sight (LOS) accelerations. These LOS accelerations have a better sensitivity to local features which will enable us to improve the gravity field at short-wavelengths. Using a subset of the available data, we have derived a model for Mercury's gravity field up to degree and order 120 in spherical harmonics. We compare our new model to a standard gravity field model in Figure 1. The standard Doppler solution shows streaks along the satellite orbits. On the other hand, the new model shows less striping and resolves many circular features, which results in improved correlations between gravity and topography. We can use such models with improved topography correlations to determine the local crustal density and lithospheric support mechanism.

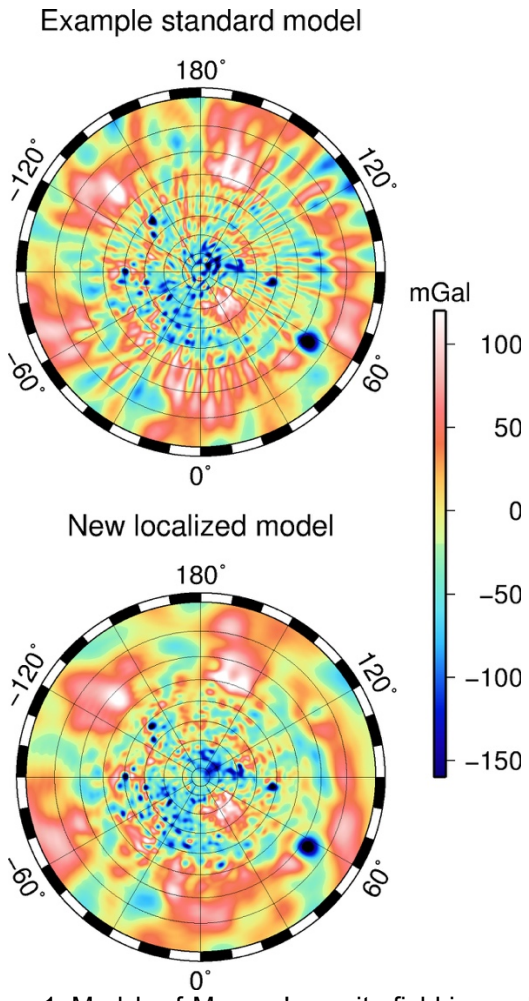

Figure 1: Models of Mercury's gravity field in a polar stereographic projection centered on the north pole. Top: a standard global model; bottom: a new model based on a localized approach.

References: [1] Solomon S.C. et al. (2007), Sp. Sci. Rev., 113, 3-39. [2] Zuber M.T. et al. (2012), Science, 336, 217-220. [3] Smith D.E. et al., Science, 336, 214-217. [4] Mazarico E. et al. (2014), J. Geophys. Res. Planets, 119, 2417-2436.

MODELING OF METALS IN THE HERMEAN EXOSPHERE: PREDICTIONS FOR THE MASS SPECTROMETER STROFIO ONBOARD BEPICOLOMBO. C. Grava and S. A. Livi, Southwest Research Institute, 6220 Culebra road, San Antonio, TX, 78238, USA (cgrava@swri.edu).

Introduction: Mercury's exosphere is created by the interaction between external drivers (solar wind or magnetospheric plasma, micrometeoroids, and solar photons) and Mercury's surface. The characteristics and dynamics of Mercury's exosphere therefore depend on the process with which the species were ejected (thermal desorption, electron- and photon-stimulated desorption, micrometeoroid impact vaporization, and ion sputtering), and each species creates its own, independent, exosphere. Source and loss processes have different relative importance depending on the species considered, on the local time, and on the position of Mercury along its orbit [1,2]. The Mercury Surface, Space Environment, Geochemistry, and Ranging (MESSENGER) spacecraft, which orbited Mercury between 2004 and 2015, improved our understanding of the Mercurian exosphere, shedding light on the connection between the external environment and the exosphere (e.g., the dust stream of comet Encke is responsible for the unusual spike of Ca [3,4]), discovering Mg [5], Al, and Mn [6], but also leaving us with open questions (e.g. why O density is so low compared to stoichiometric predictions?)

BepiColombo: BepiColombo is the next step in the Mercury exploration. A twin spacecraft developed by ESA and JAXA, BepiColombo [7] will be launched in October 2018 and will start a 1-year mission to Mercury in 2025, where it will study the surface-exosphere-magnetosphere environment in unprecedented detail [8]. Both spacecraft will share the same periherm (~400 km altitude). The Mercury Magnetosphere Orbiter (MMO), on an elongated orbit with apoherm of ~12,000 km, will study Mercury's magnetosphere, while the Mercury Planetary Orbiter (MPO), with apoherm of ~1500 km altitude, will focus on Mercury's exosphere.

Strofio: SERENA [9] is a suite of 4 instruments onboard MPO that will map the ion and neutrals of both Mercury's exosphere and the solar wind. Of these 4 instruments, Strofio is a mass spectrometer that will measure ions and neutrals with high mass resolution ($m/\Delta m \sim 100$ at mass 18). It will be the first mass spectrometer to ever measure *in situ* the composition of Mercury's exosphere. Because of the relatively high altitude of the periherm, Strofio will be especially sensitive to neutrals that were lifted off the surface with enough energy to reach the instrument. Many of these neutrals are metals, including the refractories Ca and Mg and the volatiles Na and K, ejected from the surface by energetic processes such as ion sputtering and micrometeoroid impact vaporization. The density measured by Strofio will be convolved with the MPO velocity, since Strofio aperture is in the ram direction of the spacecraft.

Our code: To help planning the observations and maximize the scientific return of Strofio, we developed a Monte Carlo code that tracks several test particles along their ballistic trajectories until they are lost (e.g. via photo-ionization). The code was originally developed for Ar on the Moon [10], which is ejected primarily with thermal desorption, and has been modified to include other species and other ejection processes. The model output includes the density and the energy distribution of neutrals as a function of latitude, altitude, and local time. By convolving the resulting densities with Strofio's response function (depending on MPO's velocity), it is possible to predict the density actually measured by it as a function of latitude, altitude, and local time.

We will present "a day at Strofio" for several species (Si, Na, K, O, etc.), to show that the density and velocity distribution inferred by Strofio will constrain the relative importance of source and loss processes for several species.

References: [1] Leblanc F. and Johnson R. E. (2003) *Icarus*, *164*(2), 261-281. [2] Leblanc F. and Johnson R. E. (2010) *Icarus*, *209*(2), 280-300. [3] Killen R. M. and Hahn J. M. (2015) *Icarus 250*, 230-237. [4] Christou A. A. et al. (2015) *GRL, 42*(18), 7311-7318. [5] McClintock W. E. et al. (2009) *Science*, *324*(5927), 610-613. [6] Vervack R. J. et al. (2016) *GRL*, *43*(22), 11545-11551. [7] Benkhoff J. et al. (2010), *Planetary and Space Science*, *58*(1-2), 2-20. [8] Milillo A. et al. (2010) *Planetary and Space Science*, *58*(1-2), 40-60. [9] Orsini S. et al. (2010) *Planetary and Space Science*, *58*(1-2), 166-181. [10] Grava C. et al. (2015) *Icarus*, *255*, 135-147.

GEOLOGIC MAP OF THE SHAKESPEARE QUADRANGLE (H03), MERCURY. L. Guzzetta[1], V. Galluzzi[1], L. Ferranti[2], and P. Palumbo[3,1], [1]INAF, Istituto di Astrofisica e Planetologia spaziali (IAPS), Rome, Italy (laura.guzzetta@iaps.inaf.it), [2]DiSTAR, Dipartimento di Scienze della Terra, dell'Ambiente e delle Risorse, Università "Federico II", Naples, Italy, [3]Dipartimento di Scienze & Tecnologie, Università degli Studi di Napoli 'Parthenope', Naples, Italy.

Introduction: A 1:3M geological map of the H03 Shakespeare quadrangle of Mercury (Fig. 1) has been compiled through photointerpretation of the remotely sensed images of the NASA MESSENGER mission. This quadrangle, located at middle latitude of the northern hemisphere of the planet, is characterized by the occurrence of three main types of plains materials and four basin materials, pertaining to the Caloris basin, the largest impact crater on Mercury's surface. The geologic boundaries have been redefined compared to the previous 1:5M map of the quadrangle [1] and the craters have been classified privileging their stratigraphic order rather than morphological appearance. Based on the dominant contractional nature of Mercury's tectonics [2, 3], the structures have been interpreted and mapped as thrusts or as wrinkle ridges.

Data and Methods: Mapping was performed on a reference monochromatic basemap of reflectance at 166 m/pixel resolution. A suite of a lower resolution basemaps, useful for their different lighting conditions, and two available DTM's, useful in sectors with non-optimal lighting geometry, were also consulted. The datum adopted is that used in the data sets released by the MESSENGER team, in which Mercury's IAU radius (2439.7 km) is approximated to 2440.0 km. The most suitable projection at middle-latitudes is the Lambert conformal conic, as it reduces area distortions. The geological features were digitized within a geographic information system with a variable mapping scale between 1:300k and 1:600k. Craters were distinguished according to their diameter size in 'small' ($10 \leq D < 20$ km), for which only rim crests were mapped, and 'major' ($D \geq 20$ km), for which also crater materials were mapped and grouped into three morpho-stratigraphic classes (c1-c3) according to their overlapping relationships [4]. The geologic contacts were mapped as 'certain' where they are clear and sharp, or 'approximate' where they are uncertain or gradational. The geologic units were distinguished according to their morphological aspects and following definitions of previous authors [1]. Other geomorphological elements such as 'hollows', crater chains and clusters, light coloured ejecta and bright deposits have also been mapped when their width is ≥ 3 km.

Map description: The intercrater plain (ICP) and smooth plain (SP) materials are the main plain materials of the quadrangle occurring in the eastern and west-central sector, respectively. The intermediate plain (IMP) materials occur only as small patches, mostly in the eastern area of the map. The western sector of the quadrangle is occupied by a portion of the Caloris basin and associated materials, that have been distinguished according to four formations (Caloris Group) termed with official names [5]. Tectonic structures, mapped as thrusts, if they show a relevant break in slope and a sinuous trace, or as wrinkle ridges, if show a less prominent ridge and occur within smooth plain materials and basins, mainly occur in the western sector of the quadrangle. The detected morpho-structures will contribute to better evaluation of past stress states of the planet.

This geologic map can be considered an important support to future advanced local studies and target selection for the scheduled ESA-JAXA BepiColombo mission to Mercury.

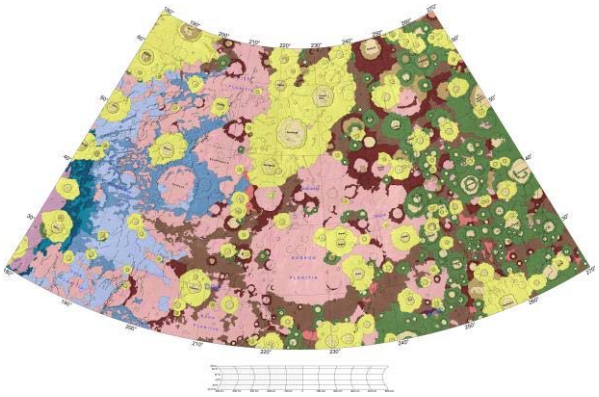

Figure 1. 1:3M geologic map of the Shakespeare quadrangle (H03) of Mercury.

Acknowledgements: This research was supported by the Agenzia Spaziale Italiana (ASI) within the SIMBIOSYS project (ASI-INAF agreement n. I/022/10/0).

References: [1] Guest, J. E. & Greeley, R. (1983), *USGS, Misc. Inv. Ser. Map I-1408*. [2] Byrne, P. K., et al. (2014) *Nat. Geosci.*, *7*, 301–307. [3] Watters, T. R. & Nimmo, F. (2010), In: Watters T. R. et al. (eds.), *Planetary tectonics*, 15–80. [4] Galluzzi V. et al. (2016), *JoM*, *12*, 227–238. [5] McCauley, J. F., et al. (1981), *Icarus*, *47*, 184–202.

LESSONS FROM THE MERCURY LANDER STUDY FOR THE 2013-2022 DECADAL SURVEY. Steven A. Hauck, II[1], David T. Blewett[2], [1]Department of Earth, Environmental, and Planetary Sciences, Case Western Reserve University, Cleveland, OH, hauck@case.edu, [2]Planetary Exploration Group, Johns Hopkins University Applied Physics Laboratory, Laurel, MD david.blewett@jhuapl.edu

Introduction: The planet Mercury has been explored by two spacecraft: Mariner 10 and MESSENGER. In 1974 and 1975, Mariner 10 made a series of three flybys of the innermost planet that provided the first ever views of less than half the surface, discovered the presence of a global magnetic field, and paved the way for starting to place Mercury in context with the other planets in the Solar System [1, 2]. However, it was not until the MESSENGER spacecraft, with its three additional flybys in 2008–2009 and 4 years of orbital operations from 2011 to 2015 that a global reconnaissance of Mercury was first possible [3]. The next step in the exploration of Mercury is the dual-spacecraft, ESA/JAXA BepiColombo mission that will also explore Mercury from a different vantage point in orbit [4]. BepiCololmbo's dual spacecraft design, less elliptical orbit for the Mercury Planetary Orbiter element, and its range of instrumentation will lead to addressing questions raised by MESSENGER observations and undoubtedly lead to new questions as well. These new data sets will be crucial for addressing global questions about Mercury's origin and evolution.

A logical next step in the study – and understanding – of Mercury is in situ exploration of the surface. A landed surface element will permit investigation of the planet at scales currently unachievable from orbit and in a manner able to provide ground-truth for orbital based investigations. Landed spacecraft also provide a perspective for making observations that cannot be made in other ways (e.g., access to the surface is necessary, low-altitudes, static perspective with respect to the rotation of the planet).

Decadal Lander Study: During the development of the 2013-2022 Decadal Survey in 2009, mission concepts for a range of Solar System destinations were studied, focusing on concepts anticipated to be at the scale of NASA's New Frontiers program or Flagship-class missions. Anticipating that a logical follow-on to MESSENGER's orbital reconnaissance of Mercury would be to place a lander on the surface, a conceptual study was initiated [5].

The timing of the Decadal Survey process coincided with the time period during and after MESSENGER's flybys of Mercury, but prior to its orbital investigation. Thus, while MESSENGER had observed more of Mercury than had been previously observed [6] and gained additional traverses of the magnetosphere and gravity field, the primary questions around which the MESSENGER mission was designed had yet to be addressed [e.g., 3]. Further, several key discoveries from the mission's orbital phase (e.g., hollows [7], crustal magnetism [8]) had yet to be made.

Concept: The Decadal Mercury lander study was guided by objectives to: (a) Characterize the chemical composition of Mercury's surface (major and minor elements). (b) Characterize the mineralogy and structural state of the materials at Mercury's surface. (c) Investigate the magnitude and time dependence of Mercury's magnetic field, for at least one location on the surface. (d) Characterize geologic activity (e.g., volcanism, tectonism, impact cratering) at scales ranging from regional to local. (e) Determine the rotational state of Mercury.

The study found the science goals could be achieved with a dusk landing providing 2 days of sunlight, followed by 3 weeks of science operations through Mercury's night with power from an advanced Stirling radioisotope generator (ASRG). While not explored in detail, an extended mission through the entire night and until the extreme heat of Mercury's day ended spacecraft operations was possible. The advantage of this approach is that a wide range of latitudes are regularly accessible for landing and operations. High-latitude sites with similar operational timeframes are available throughout Mercury's year.

Decadal Disposition: The Mercury Lander Study was aimed at exploring the feasibility of accessing the planet's surface to address a broad range of questions within a cost-capped mission analogous to NASA's New Frontiers mission. However, study estimates placed the concept beyond the NF cap. At the time, with MESSENGER's impending orbital mission likely to define new, high-priority questions for in situ investigation of Mercury, further study of a lander was deferred to the future.

References: [1] Murray, B. C., et al. (1974) Science, 185, 169. [2] Ness, N. F., et al. (1974) Science, 185, 151. [3] Solomon, S. C., et al. (in press), Mercury: The view after MESSENGER. [4] Benkhoff, J., et al. (2010) PSS, 58, 2-20. [5] Vision and Voyages, NRC (2011). [6] Solomon, S. C., et al. (2008) Science, 321, 59. [7] Blewett, D. T., et al. (2011) Science, 333, 1856. [8] Johnson, C. L., et al. (2015) Science, 348, 892.

MAGMATIC ASCENT AND ERUPTION PROCESSES ON MERCURY. J. W. Head[1] and L. Wilson[2] [1]Earth, Environmental & Planetary Sciences, Brown University, Providence, RI 02912 USA (james_head@brown.edu). [2]Lancaster Environment Centre, Lancaster University, Lancaster LA1 4YQ, UK (L.Wilson@Lancaster.ac.uk).

Introduction: Data from MESSENGER on the presence, absence, and distribution of various specific volcanic landforms and units, together with information on Mercury's crustal composition, allow us to model the generation, ascent and eruption of magma on Mercury.

Melt generation: (a) Convection present. The variation of mantle temperature with pressure in a zone of pressure-release partial melting is essentially independent of planet size, and so if bodies have similar enough bulk compositions that the temperature range over which melting occurs is the same, then the pressure range will also be the same. But pressure increases with depth in a planet in proportion to the acceleration due to gravity, and to a first approximation acceleration due to gravity is proportional to body size. Thus in a smaller body the same pressure range requires a greater range of depths, and a larger vertical extent of the mantle will be involved, in inverse proportion to the radius, in generating the melts that form the crust. Partial melting over an ~ 85 km vertical depth range in the Earth's mantle scales to ~220 km for Mercury's mantle and implies a volcanically-generated crust ~2.2 times thicker on Mercury than Earth. (b) Convection absent. The poor thermal conductivity of silicates causes a radioactively-heated planet's interior to have a slowly-increasing temperature beneath a conductively controlled thermal boundary layer of depth B. For example, after 300 Ma B is ~130 km and after 1 Ga B is ~240 km. Thus even if a magma ocean is formed by rapid terminal accretion, its presence is less important than the deeper, post-formation internal temperature. We approximate the temperature as a function of depth and time for a given initial mantle temperature. Melting starts when the temperature at any depth crosses the mantle solidus. For an initial mantle temperature near 900 K, melting starts after ~800 Ma at a depth of ~220 km and the top of the melt zone progressively rises to ~90 km. Thus, whether mantle convection is present or absent on Mercury, vertically extensive planet-wide zones of partial melting should be present in the first half of its history, with variations in timing of onset, peak melt production and cessation as a function of the planetary formation conditions. In both cases, large volumes of mantle melt are available for eruption. The presence of extensive lava plains and absence of major shield volcanoes suggests that flood volcanism dominated on Mercury, with mantle partial melts collecting at a density or rheological boundary near the mantle-crust interface and erupting directly to the surface.

Magma Transport Through the Crust: If the crust of Mercury consists largely of solidified mantle melt, the crust density should be ~10% greater than typical melt density and the melt density should be ~20% less dense than the mantle density. However, magma gas vesicles cause crusts consisting of accumulated volcanics to be much less dense than coherent rock when a significant atmosphere is absent, as on Mercury, even if only small amounts of volatiles are present. Crustal density increases with depth due to compaction. In the case of Mercury the mean crustal density may be close to the mean magma density averaged over the vertical extent of the crust. We therefore explored the geometries of elastic dikes penetrating through the crust and the magma flow rates through them for a range of plausible values of crust thickness, vertical extent of melt pond at the base of the crust, stress threshold for fracturing the crust, crustal elastic properties, magma viscosity, and wall friction factor. We find that magma typically rises in a turbulent fashion at ~8 m s^{-1} through a dike with mean width ~18 m feeding a surface fissure of length ~90 km from which ~13 x 10^6 m^3 s^{-1} of lava is discharged. Magma motion in dikes this wide will be turbulent for all magma viscosities up to ~1000 Pa s, covering the entire range from komatiite-basalt-basaltic andesite, and so these eruption conditions are independent of magma composition.

Surface Lava Flows: Several tens of meters flow thicknesses and 10-100s km-long boundaries imply flows that commonly inflate after emplacement. We model emplacement of flows with initial thicknesses 10-100 m. Such flows are consistent with magma eruption rates of order ~10^7 m^3 s^{-1}, similar to lunar eruptions. Flows 10, 30 and 100 m thick would have had speeds of ~3.5, 6 and 11 m s^{-1}, attaining lengths of 300 km in ~24, 14 and 8 hours. Flows 10, 30 and 100 m thick would have been turbulent for all magma viscosities less than ~100, ~540 and 3300 Pa s, respectively, confirming that all basaltic and komatiitic flows would have been turbulent. Grätz numbers show that flow lengths were supply limited, not cooling limited.

Explosive volcanism: Consideration of the energetics of eruptions in a vacuum shows that to reach the observed deposit radii, mainly in the range 20-50 km, required the erupting magma to contain ~4000 to 12000 ppm CO or the equivalent of other volatiles. Candidate volatiles depend on the oxidation state of Mercury's interior and include CO, N_2, S_2, CS_2, S_2Cl, Cl, Cl_2 or COS (reducing interior, most likely) or CO, CO_2, H_2O, SO_2, or H_2S (oxidizing interior, less likely). Equilibrium release from ascending magmas of up to 12000 ppm volatiles is not expected given the current understanding of Mercury's composition and oxidation state. This suggests that some process may be required to concentrate volatiles into the tops of ascending dikes that fail to breach the surface to form lava flows.

Summary: Theoretical treatment of the ascent and eruption of magma shows that eruption process are likely to differ from those on other terrestrial planetary bodies, consistent with the geological observations from the MESSENGER mission.

MERTIS – Unleashing the power of the thermal infrared on Mercury. J. Helbert[1], A. Maturilli, M. D'Amore[1], I. Varatharjan[1] , H. Hiesinger[2] and the MERTIS team, [1]Institute for Planetary Research, DLR, Rutherfordstrasse 2, 12489 Berlin, Germany (joern.helbert@dlr.de), [4]Institute for Planetology, Wilhelms University, Münster, Germany

Introduction: The MErcury Radiometer and Thermal infrared Imaging Spectrometer (MERTIS) [1] is part of the payload of the Mercury Planetary Orbiter spacecraft of the ESA-JAXA BepiColombo mission that will be launched in October 2018. MERTIS combines an imaging spectrometer covering the wavelength range from 7-14 µm with a radiometer covering the wavelength range from 7 to 40 µm. The instrument will map the whole surface of Mercury with a spatial resolution of 500m for the spectrometer channel and 2km for the radiometer channel. The compositional map of Mercury provided by MERTIS will allow unique insights into the evolution of the least explored terrestrial planet. MERTIS will also address directly questions raised by the NASA MESSENGER mission. For example we will be able to provide spatially resolved compositional information on the hollows and pyroclastic deposits and answer the question whether hollows are actually predominately sulfide deposits.

The MERTIS instrument: The availability of uncooled microbolometer arrays allowed a new generation of thermal infrared instruments [2, 3]. Based on this technology we MERTIS in 2003 for the ESA-JAXA BepiColombo mission.

MERTIS combines IR grating spectrometer (TIS) with a radiometer (TIR), both operating in a push-broom mode. It represents a modular concept of the sensor head, electronic units and power/calibration systems within a mass budget of only 3.0 kg and power consumption of less than 12 W nominal.

TIS operates between 7 and 14 µm with a 200nm spectral resolution and will record the day-side emissivity spectra from Mercury at a spatial resolution up to 280m. The instrument uses an uncooled microbolometer, developed under ESA contract at LETI and ULIS in France. This is the first space-qualified microbolometer developed and built in European. It is based on the commercial detector with 160 x 120 pixels with a pixel size of 35 µm. A part of the development the detector was not only space qualified but also the sensitivity was significantly increased and the cut-on wavelength was reduced from 8 to 7 µm. The detectivity (NEP) of the detector is in the range of 10-15 pW.

Sharing the same optical path a pushbroom radiometer (TIR) is implemented by an in-plane separation arrangement, effectively acting as the slit of the spectrometer. The TIR uses a thermopile line detector arrays of 7 10^8 cm $Hz^{1/2}$ W^{-1} detectivity. TIR is going to measure the surface temperature at day- and night side at a spatial resolution of 2km with two broadband channels. The 7-14 µm channels facilitates cross calibration with the spectrometer, while the 7-40µm channel allows to accurately measure the nightside temperatures of Mercury with a noise equivalent temperatures difference (NETD) of 1K at 80K.

The optical design of MERTIS combines a three mirror anastigmat (TMA) with a modified Offner grating spectrometer. A pointing device allows viewing the planet (planet-baffle), deep space (space-baffle), and two black bodies at 300 K and 700 K temperature, respectively. The combination of spectrometer and a radiometer channel using the same optics and calibration sources allows retrieving emissivity, surface temperature and thermal inertia independently.

Getting ready for Mercury: The scientific goals of MERTIS drive the instrumental performance. Small spectral contrasts of diagnostic features of the regolith soil, and high temperature contrasts (70K at night and 700K at day) require a high dynamic range with respect to the spectral, radiometric, and spatial resolution. To verify the performance of the integrated instrument measurements have obtained at the Planetary Spectroscopy Laboratory PSL at DLR in Berlin [4, 5]. In this worldwide unique facility samples can be heated to Mercury daytime peak temperatures under vacuum conditions in a planetary simulation chamber. Both the MERTIS qualification and flight model have been calibrated at validated at PSL.

Over the last decade we have collected at PSL at DLR an extensive database of emissivity spectra in the mid and near-infrared over the range of dayside temperatures expected for Mercury [6-9]. These measurements include major silicates such as bytownite, anorthoclase, synthetic glass, olivine, enstatite, nepheline basanite, rocks like komatiite, tektite, Johnson Space Center lunar simulant (1A), and synthetic powdered sulfides which includes MgS, FeS, CaS, CrS, TiS, NaS, and MnS [10].

References: [1] H. Hiesinger, and J. Helbert, Planetary and Space Science, 58(1-2), 144-165 (2010). [2] I. Walter, G. Paez, T. Zeh et al., SPIE, 8154, 81540Y (2011). [3] G. Peter, J. Helbert, H. Hiesinger et al., SPIE, 8867, 886707 (2013). [4] C. Paproth, T. Säuberlich, H. Jahn et al., "Mertis-system theory and simulation." 7808, 78080M-78080M-8. [5] J. Helbert, H. Hiesinger, I. Walter et al., SPIE, 7808, 78080J (2010). [6] J. Helbert, F. Nestola, S. Ferrari et al., Earth and Planetary Science Letters, 371-372, 252-257 (2013). [7] A. Maturilli, J. Helbert, J. M. St. John et al., Earth and Planetary Science Letters, 398, 58-65 (2014). [8] S. Ferrari, F. Nestola, M. Massironi et al., American Mineralogist, 99(4), 786-792 (2014). [9] Maturilli et al this meeting [10] Varatharajan et al this meeting

THE NONRANDOM DISTRIBUTION OF INTERIOR LANDFORMS FOR ~100-KM DIAMETER CRATERS ON MERCURY SUGGESTS REGIONAL VARIATIONS IN NEAR-SURFACE MECHANICAL PROPERTIES. R. R. Herrick, Geophysical Institute, University of Alaska Fairbanks, Fairbanks, AK 99775-7320 (rrherrick@alaska.edu).

Introduction: A group of undergraduate students and I recently completed and have submitted for publication a global database of Mercurian impact craters with diameters $D > 5$ km [1, manuscript in review w/ *JGRP*]. As part of this effort, for craters with $D > 10$ km we classified the craters as "filled" or "unfilled", and then for the unfilled craters we made a number of morphological classifications, including characterizing the crater's interior structure. A general progression with size for a crater's interior structure exists, with classifications as follows: central peak (cp), multiple isolated peaks (mp), a small pseudocircular arc of peaks (ringed peak cluster, rpc), central peak plus ring of peaks (protobasin, pb), and fully developed peak ring (pr). There is considerable overlap in the diameter ranges for which these landforms occur, with the most diversity occurring at $D \approx 100$ km. Assuming an approximate impact energy scaling of D^3, $74.9 < D < 128$ km spans a factor of five in impactor energy and provides a well-distributed global sampling of craters.

Results: When we plot the interior morphologies of craters in this diameter range (Figure 1), we see a nonrandom clustering of the ringed interior landforms (rpc, pb, pr). Because we are looking at craters of roughly the same size (and thus impact energy), the clustering strongly implies regional variations in the mechanical properties of the upper several km of Mercury's crust. We do not have a good understanding on what the main differences in mechanical properties are likely to be, although cohesiveness, porosity, and layering seem like possibilities. If the clustering correlates to some surface geologic setting on Mercury, then it is beyond my ability to discern that correlation. I plotted the data in Figure 1 versus global topography, crater density, proximity to large basins, and color maps of the surface, and saw no apparent correlations with these data sets. Unfortunately, the data sets indicating mineral abundance, and the gravity data, are not well enough resolved globally to truly test near-surface composition or crustal porosity/thickness variations as potential causes of the observed pattern. Both our data and previous works also show nonrandom distributions of craters with hollows [2,3] and large pits in the crater floor [4], but we could not discern any clear relationships between the pattern in Figure 1 and the distribution of hollows or pits.

References: [1] Herrick R. R. et al. (2016) *47th LPSC*,abs #2766. [2] Blewett D. T. et al. (2011) *Science, 333*, 1856-1859. [3] Thomas R. J. et al. (2014) *Icarus, 229*, 221-235. [4] Thomas R. J. et al. (2014) *JGRP, 119*, 2239-2254. [5] Denevi B. W. et al. (2013) *JGRP, 118*, 891-907.

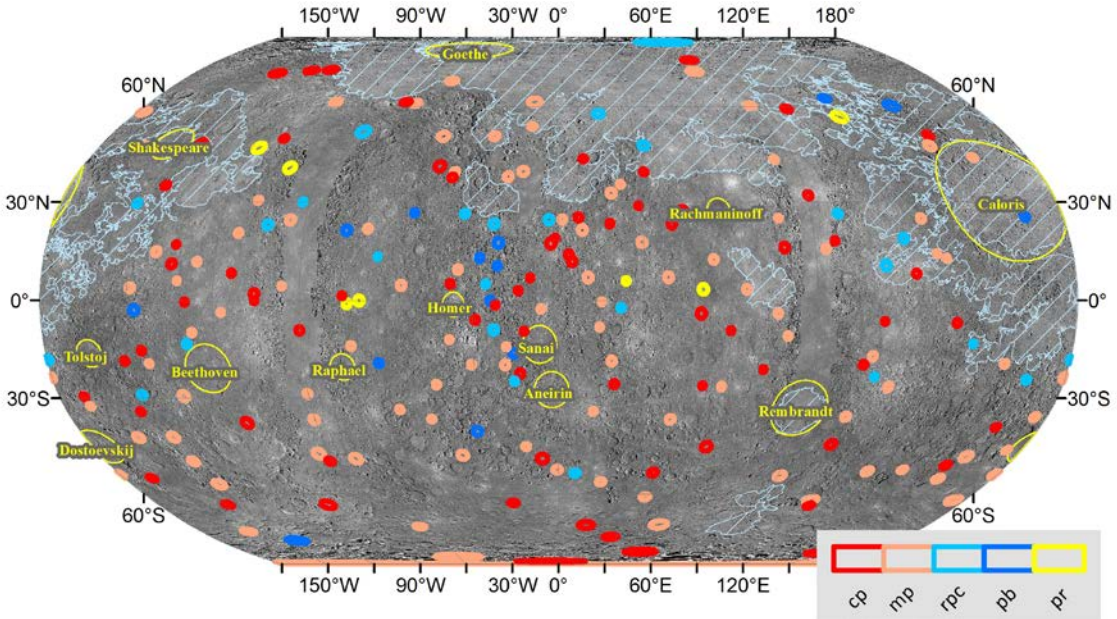

Figure 1. Geopgraphical distribution of different interior central structures for craters with $74.9 < D < 128$ km. The distributions of the different crater types are nonrandom, with clustering of craters with interior ring structures (rpc, pb, pr). Named craters with $D > 300$ km are outlined in yellow, and the five largest smooth plains units from [5] are hachured in light blue.

CONCERNING THE OFFSET DIPOLE MAGNETIC FIELD OF PLANET MERCURY.

D. Heyner[1], [1]TU Braunschweig, Braunschweig, Germany, d.heyner@tu-bs.de.

The MESSENGER mission revealed an asymmetry in the magnetic field of planet Mercury. In the far field, the magnetic equator is offset northwards by 0.19 planetary radii. The magnetic field inside the magnetosphere was only measured in the northern hemisphere, thus internal and external Gauss coefficients may not be determined independently without the aid of a magnetospheric model. This magnetospheric model in turn requires an internal dipole field. The effect of taking this offset-dipole model determined from the far-field measurements as initial assumption for the magnetospheric model utilized in the spherical harmonic analysis for the internal field is examined for a possible bias. In the analysis, all magnetic field data from entire mission is used. It is found that the bias effect is mainly visible in the quadrupolar and octupolar Gauss coefficients. These new values are extrapolated to the core-mantle boundary to demonstrate the required field asymmetry produced by dynamo models designed to explain the still peculiar magnetic field of Mercury.

FURTHER MAPPING OF MERCURY'S CRUSTAL MAGNETIC FIELD USING MESSENGER MAGNETOMETER DATA. L. L. Hood[1], J. S. Oliveira[2,3], P. D. Spudis[4], V. Galluzzi[5], [1]Lunar & Planetary Lab, 1629 E. University Blvd., Univ. of Arizona, Tucson, AZ 85721, USA; lon@lpl.arizona.edu, [2]ESA/ESTEC, SCI-S, Keplerlaan 1, 2200 AG Noordwijk, Netherlands; [3]CITEUC, Geophysical & Astronomical Observatory, University of Coimbra, Coimbra, Portugal (joliveira@cosmos.esa.int); [4]Lunar & Planetary Institute, USRA, Houston, TX; [5]INAF, Istituto di Astrofisica e Planetologia Spaziali, Rome, Italy.

Introduction: A valuable data set for investigating crustal magnetism on Mercury was obtained by the NASA MESSENGER mission during the final year of its existence [1]. Altitude normalized maps of the crustal field covering part of one side of the planet (90°E to 270°E; 35°N to75°N) have previously been constructed from low-altitude magnetometer data using an equivalent source dipole (ESD) technique [2,3]. Results showed that the strongest crustal field anomalies in this region are concentrated around and within the 1550 km diameter Caloris impact basin. A second smaller concentration was mapped over and around Sobkou Planitia, which contains an associated older 770-km diameter impact basin. In general, anomalies over high-reflectance volcanic plains were relatively weak while anomalies over low-reflectance material that has been reworked by impact processes were relatively strong.

In this work, results of mapping low-altitude MESSENGER data over part of the other side of the planet (270°E to 90°E; 35°N to 75°N) are reported. Initial objectives include: (a) investigating in more detail the occurrence of anomalies associated with impact basins/craters; and (b) identifying anomalies that are suitable for paleomagnetic pole estimation.

Results: Figure 1 plots the calculated crustal field magnitude at 40 km altitude estimated using the ESD technique. As seen in the figure, some anomalies appear to correlate with impact crater/basin locations. These include two relatively strong anomalies (numbered 1 and 2) over Rustaveli (200 km in diameter, centered at 83°E, 52°N) and Vyasa (300 km in diameter, centered at 275°E, 50°N). These anomalies have filtered amplitudes of about 6 nT at 40 km altitude. For comparison, the strongest anomalies at the same altitude near and within Caloris had filtered amplitudes of about 8 nT [3]. On the other hand, some other named craters (e.g., Abedin and Hokusai, 116 and 114 km in diameter, respectively) have no associated anomalies. Similarly, several larger impact basins appear to have associated magnetic anomalies while others do not. Relatively weak anomalies are present over the northern lowlands, most of which has been volcanically resurfaced. Anomalies are, however, present over the northern rise. This includes a relatively strong (> 6 nT) anomaly centered at about 28°E, 67°N.

Overall, the association of anomalies with some impact craters/basins but not others represents a new constraint on crustal magnetic source models. An important remaining issue is whether some anomalies may be dominantly induced rather than remanent.

Acknowledgment : Supported by the NASA DDAP.

References: [1] Johnson C. et al. (2015) Science, 348, 892-895. [2] Hood L. (2015) GRL, 42, 10565-10572. [3] Hood L. (2016) JGR Planets, 121, 1016-1025.

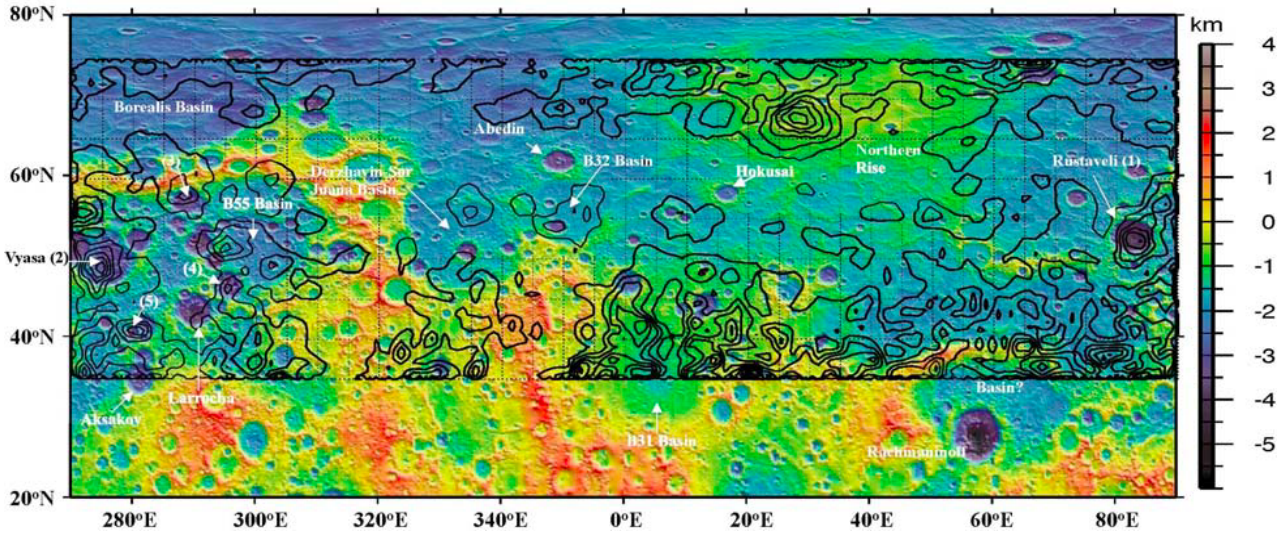

Figure 1: Calculated crustal field magnitude at 40 km altitude according to the ESD solution after two-dimensional filtering. The contour interval is 1 nT and the field map is superposed onto a MESSENGER Laser Altimeter elevation map (G. Neumann, priv. comm., 2016).

Implications of the homogeneous nucleation barrier for top-down crystallization in Mercury's core

Ludovic Huguet[1], Steven A. Hauck II[1,] and James A. Van Orman[1], Zhicheng Jing[1], Department of Earth, Environmental, and Planetary Sciences, Case Western Reserve University, Cleveland, OH 44106, USA (ludovic.huguet@case.edu)

Introduction: Where and when solids in planetary cores begin crystallizing depends on the secular cooling rate, on the difference between the thermal gradient and the liquidus gradient, and crucially on the ability to nucleate crystal growth. It has been suggested that Mercury's core can crystallize from the top of the outer core, i.e. at the core-mantle boundary [e.g., 1]. Canonically, this "iron snow" regime of crystallization has been modeled with iron crystals nucleating from the bulk liquid and sinking and re-melting (or sedimenting) on to a solid inner core [2]. However, this model neglects the energy barrier to the formation of the first stable crystal nucleus, which is commonly represented in terms of the critical supercooling required to overcome the barrier.

Homogeneous nucleation barrier: The crystallization of the first solid in a fully homogeneous liquid requires that the temperature drops below the melting temperature. The necessary supercooling for liquid metals is ~20-30% below the melting temperature [3]. At the pressure conditions of the core-mantle boundary of Mercury, the required supercooling for homogeneous nucleation is at least 400K. Such a supercooling is prohibitive due to the small secular cooling rate and due to the small pressure dependence of the liquidus in Mercury's core. The presence of another solid could considerably reduce this barrier or even almost cancel it. However, silicates and oxides, which are the main constituents of the mantle, reduce the nucleation barrier only slightly [3]. Thus, either mantle processes must deliver appropriate nucleation sites (able to reduce significantly the energetic barrier) to the core-mantle boundary, or Mercury's core may experience a phase of top-down, kinetically-controlled rapid growth in a supercooled liquid.

Implications for the inward crystallization of Mercury's core: Bulk crystallization as suggested in the different regimes of iron snow [1,4] are precluded due to the large energetic barrier for homogeneous nucleation. The presence of the core-mantle boundary should provide nucleation sites able to trigger the inward crystallization of the outer core. The nucleation barrier at the CMB could be reduced by the presence of metallic phases. Here, we assumed that iron solid can crystallize from the CMB with a small or negligible nucleation barrier. The crystallization of iron alloys in planetary cores is thought to lead to the formation of a mushy layer, a two-phase region in which solid iron-rich dendrites coexist with a light elements-rich iron melt [5]. Dendritic inward solidification has been suggested for small asteroid cores [6]. Fig. 1 shows a schematic view of one possible thermal evolution scenario for an iron-rich system. A dendritic layer grows from the CMB (Fig. 1(a)). This partially solid zone is thought to be at thermochemical equilibrium. Because solid iron is denser than molten iron alloy, this layer should be unstable and sink by gravitational instability or by necking [7]. Fe sediments that are not dissolved during their sinking would form the inner core (Fig. 1(b)). The inner core grows by sedimentation of solid iron produced at the CMB and transported to the center of the core (Fig. 1(c)). We discuss potential consequences, paths, and open questions for the thermal evolution and the dynamo action in Mercury's core.

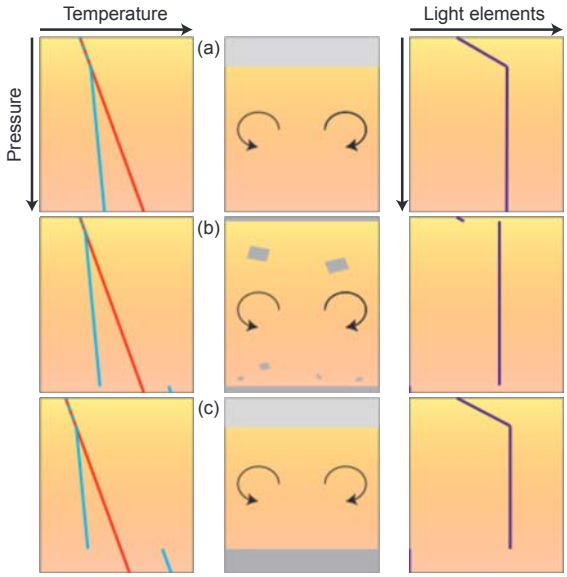

Figure 1: Crystallization evolution of Mercury's core (Left, temperature as a function of the pressure, Right, light elements composition as a function of the pressure).

References:

[1] Chen et al., (2008), GRL., 35, L07201. [2] Hauck et al., (2006), JGR., 111, (E09008). [3] L. Huguet et al. (2018) EPSL, 487, pp 9-20. [4] Dumberry and Rivoldini, (2015), Icarus, 248, pp 254-268. [5] Deguen et al., (2007) PEPI, 164, pp 36-49. [6] Haack and Scott, (1992), JGR, 97, pp 14727-14734. [7] Scheinberg et al., (2015), JGR, 21, pp 2-20.

VOLATILES ON MERCURY: LESSONS FROM THE MOON. D. M. Hurley[1], P. Prem[1], R. J. Vervack, Jr.[1], N. L. Chabot[1], A. R. Hendrix[2], M. Benna[3], W. M. Farrell[3], R. M. Killen[3], S. Li[4], P. G. Lucey[4], and K. D. Retherford[5], [1]Johns Hopkins Applied Physics Laboratory, 11100 Johns Hopkins Rd., Laurel MD 20723, USA (dana.hurley@jhuapl.edu), [2]Planetary Science Institute, Boulder, CO, USA, [3]NASA Goddard Space Flight Center, Greenbelt, MD, USA, [4]University of Hawaii, Manoa, HI, USA [5]University Southwest Research Institute, San Antonio, TX, USA.

Introduction: Mercury's permanently shadowed regions (PSRs) contain vast quantities of water and other volatiles [1-2]. The large quantities, relative purity, and sharp boundaries imply that the volatiles are either the result of a recent delivery, are presently in a period of accumulation from ongoing processes, or are very efficient in maintaining the deposits. The Moon also has water and other volatiles in its PSRs [3-5]. However, the Moon's PSRs contain lower abundances and demonstrate heterogeneity, suggesting the Moon's volatile deposits are either old, being supplied very slowly compared to regolith and surface modification processes, or are very inefficient in concentrating ices. Why are volatiles on the Moon and Mercury so different? While we do not know the answer to this question, we can examine the data for the Moon and Mercury to understand each system separately and compare the important processes on the two bodies. We present the current state of knowledge of the sources, migration, and sinks of water to PSRs on the Moon.

Observations: In addition to the volatiles in lunar PSRs, multiple observations confirm that water/OH exists on the surface as adsorbed molecules in illuminated regions on the Moon [6-7]. Furthermore, the adsorbed water varies as a function of latitude and local time [7-9], suggesting that it is evolving on a diurnal basis. Many potential mechanisms can be invoked to explain this distribution and work is ongoing to determine which mechanisms are important on the Moon. One mechanism is the steady state production and loss of H_2O by the balance of incident solar wind flux and thermal diffusion and desorption timescales. This is supported by the apparent association between magnetic shielding by magnetic anomalies and surface OH abundances [10] and some IR observations of a magnetotail effect [11]. However, the apparent lack of change in surface OH abundance during the Moon's passage through the magnetotail is a counterindicator [7;12].

Multiple observations have constrained the role of solar wind as the supply of volatiles on the Moon. Protons in the solar wind bombard the surface of the Moon, neutralize, and implant within the regolith [13]. While Apollo samples contain small amounts of trapped H [14], most of the incident solar wind must leave the regolith after some residence time through branching ratios for the various exit pathways, including backscattered H^+ [15], backscattered H [16], thermal H, H_2 [17], CH_4 [18], and OH/H_2O. The branching ratios for solar wind to thermal H and OH/H_2O are not quantified for the Moon. At Mercury, thermal atomic H in the exosphere has been quantified [19]; however, the other quantities have not. BepiColombo may be able to provide some of these necessary measurement in Mercury's exosphere.

Another potential mechanism for the diurnal variation is the distribution being modulated by residence times of migrating water, where transport is relatively efficient. This mechanism requires great efficiency in migration, a resistance to loss, and a significant quantity of water in the Moon's exosphere. This exospheric water has not been observed on the Moon [20]. Instead, water in the lunar exosphere appears to occur in discrete events, likely triggered by meteoroid impacts releasing adsorbed water from a subsurface reservoir [20].

Implications: The differences between the Moon and Mercury include: significant global magnetic field on Mercury; higher surface gravity on Mercury; longer rotation period on Mercury; higher speed and flux of meteoroid impacts on Mercury; higher solar wind flux at Mercury orbit; higher daytime temperature on Mercury; surface composition and volcanic history differences; regolith adsorption sites; potential more recent comet impact on Mercury; history of spin-orbit evolution on the Moon; and passage through Earth's magnetotail for Moon. It is not clear which combination of these factors leads to the difference in volatile inventories between the Moon and Mercury. However, we provide a standard against which to compare the roles of these items as more data from the Moon and Mercury become available.

References: [1] Slade M. et al. (1992) Science 258, 635. [2] Lawrence D. et al. (2013) Science 339, 292; [3] Colaprete A, et al. Science 330, 2010. [4] Gladstone G. et al. JGR 117, 2012. [5] Feldman W. et al. (1998) Science 281, 1496. [6] Pieters C. et al. (2009) Science 326, 568. [7] Sunshine J. et al. (2009) Science 326, 565. [8] Hendrix, A. et al. (2012) JGR 117, E12001. [9] McCord T. et al. (2011) JGR 116, E00G05. [10] Kramer G. et al. (2011) JGR 116, E00G18; [11] Li S. et al. (2018) LPSC. [12] Hendrix A. et al. (2017) LPSC #2149. [13] Zeller E. et al. (1966) JGR 71, 4855. [14] Heiken G. et al. (1991) Lunar Sourcebook; [15] Saito Y, et al. (2008) GRL 35, L24205. [16] Wieser M. et al. (2010) GRL 37, L04103. [17] Stern S. and Cook J. (2013) Icarus 226, 1210. [18] Hodges R. (2016) GRL 43, 6742. [19] Broadfoot A. et al. (1976) Geophys. Res. Lett. 3, 577-580. [20] Benna M. et al. (2015) LPSC #1863.

THE BEPICOLOMBO LASER ALTIMETER (BELA): SCIENTIFIC PERFORMANCE AT MERCURY.

H. Hussmann [1], G. Steinbrügge [1], A. Stark [1], J. Oberst [1], N. Thomas [2] and L.-M. Lara [3]
[1] DLR, Institute of Planetary Research, Rutherfordstr. 2, 12489 Berlin, Germany, hauke.hussmann@dlr.de,
[2] Physikalisches Institut, University of Bern (UBE), Sidlerstrasse 5, 3012 Bern, Switzerland
[3] CSIC, Instituto de Astrofísica de Andalucía (IAA), Glorieta de la Astronomia s/n, 18008 Granada, Spain

The BepiColombo joint mission by the European Space Agency (ESA) and the Japan Aerospace Exploration Agency (JAXA) consists of two spacecraft, the Mercury Planetary Orbiter (MPO) and the Mercury Magnetospheric Orbiter (MMO), which will complement and extend the information collected by NASA's MErcury Surface, Space ENvironment, GEochemistry, and Ranging (MESSENGER) mission. The BepiColombo spacecraft stack will be launched in October 2018 and conduct a one year nominal mission in Mercury orbit, with the possibility of an extension by one additional year [1].

One of the instruments aboard the MPO is the BepiColombo Laser Altimeter (BELA) [2]. While previous laser altimeters used matched filters followed by leading edge detection in analogue, BELA uses matched filters in digital implemented in an FPGA [2]. We explore the scientific perspectives and present an updated semi-analytical instrument performance model estimating the signal to noise ratio, single shot probability of false detection, range error and pulse-width reconstruction accuracy.

The model is generally applicable for other laser altimeters using matched filter algorithms for pulse detection and has been validated against the recently tested BELA flight model after integration on the BepiColombo spacecraft. Further, we perform numerical simulations of the instrument performance expected in orbit about Mercury. In particular, we study the measurement accuracy of topography, slopes and surface roughness, which will allow us to estimate local and global topographic coverage based on the current trajectory design. We also assess the potential for measuring the tidal Love number h_2 using cross-over points, which we estimate to be constrained with an absolute accuracy of 0.14 corresponding to a relative accuracy of about 18% after two years in Mercury orbit. Implications for the interior structure model, in particular for the inner core size of Mercury will be discussed.

References:

[1] Benkhoff et al (2010) Planet. Space Sci. 58, 1-20.
[2] Thomas et al. (2007) Planet. Space Sci., 55:1398-1413

MERCURY'S DYNAMIC MAGNETOSPHERE

Suzanne M. Imber

Department of Physics and Astronomy, University of Leicester, UK

Mercury's magnetosphere is the most extreme planetary environment in our solar system, driven by the intense solar wind in the inner heliosphere. Magnetic reconnection is the primary mechanism by which energy and momentum are transferred from the solar wind to the planetary magnetosphere, and observations by MESSENGER's suite of instruments have shown that the dayside reconnection rate at Mercury is many times greater than that observed at the Earth. Magnetic energy builds up in Mercury's magnetotail and is eventually released by reconnection between oppositely directed tail lobe field lines. This storage and release of energy in the magnetotail drives global magnetospheric dynamics and is akin to a terrestrial substorm.

Several observations of reconnection-related signatures in Mercury's magnetotail (such as statistical studies of flux ropes and dipolarisation fronts) have suggested that the reconnection site is shifted towards the dawn side of the magnetotail, in stark contrast to the situation at the Earth, where such signatures have been preferentially observed at dusk. Another key difference between Mercury and the Earth is that Mercury has no atmosphere, such that particles accelerated along field lines by reconnection are likely to impact the surface. Observations of the resulting X-ray emission with MESSENGER's X-ray spectrometer have revealed that this emission is both hemispherically asymmetric (due to the offset of the planetary dipole to the north), and is preferentially observed on the dawn side of the planetary surface. These asymmetries will be discussed, along with a look forward to the measurements that will be made by ESA's BepiColombo mission.

COUPLED KELVIN HELMHOLTZ AND TEARING MODE INSTABILITIES AT THE MERCURY'S MAGNETOPAUSE. S. L. Ivanovski[1,2], A. Milillo[1], M. Kartalev[3,4], S. Massetti[1], [1]INAF - Institute for Space Astrophysics and Planetology, Via Fosso Del Cavaliere 100, 00133, Rome, Italy, stavro.ivanovski@iaps.inaf.it, [2]Università Parthenope, Centro Direzionale, Isola C4, 80143 Naples, Italy, [3]Geospace Consult Ltd, Sofia, Bulgaria, [4]Institute of Mechanics, Bulgarian Academy of Sciences, Acad. G. Bontchev St., bl. 4, 1113 Sofia, Bulgaria.

Abstract: How the transport of momentum and plasma occurs across a boundary remains a question of outstanding scientific interest. Kelvin-Helmholtz (KH) waves and magnetic reconnection are believed to be the key drivers of plasma transport and planetary magnetospheres are excellent laboratories to investigate them. Based on a flexible numerical incompressible magnetohydrodynamic (MHD) approach [1] implemented for studying a coupled Kelvin-Helmholtz (KH) and tearing mode (TM) instabilities, as a first step, we are investigating the applicability of this approach to Mercury's magnetopause and by means of numerical simulations perform physical parameters study based on MESSENGER data.

References: [1] Ivanovski S. et al. (2011) Journal of Theoretical and Applied Mechanics, Vol. 41, No. 3, 31-42.

EXPLORING SPACE WEATHERING ON MERCURY USING GLOBAL UV-VIS REFLECTANCE SPECTROSCOPY. N. R. Izenberg[1] and B. W. Denevi[1], [1]Johns Hopkins University Applied Physics Laboratory, MD (noam.izenberg@jhuapl.edu).

Introduction: Ultraviolet (UV) reflectance has proven for the Moon to be a useful tool for exploring variations in exposure of surface materials to space weathering, and the effects of shock in some impact craters [1]. In particular, the use of UV reflectance and spectral slopes utilizing wavelengths from 321 to 415 nm in the Lunar Reconnaissance Orbiter Camera (LROC) Wide Angle Camera (WAC) has provided a tool with which to examine the Moon for these effects, particularly in areas with low iron content (i.e., the lunar highlands).

The Mercury Surface Space Environment, Geochemistry, and Ranging (MESSENGER) mission's Mercury Atmosphere and Surface Composition Spectrometer (MASCS) [2] was a point spectrometer that mapped over 96% of the surface of Mercury with over 5 million individual observations. Individual spectral footprints of MASCS' Visible and Infrared Spectrograph (VIRS) component varied from ~80 m by 3-4 km in the northern hemisphere to nearly circular footprints of ~6 km diameter in the southern hemisphere, and each spectral observation covered the wavelength range 300–1450 nm. This UV component of the VIRS data-set allows us to pursue similar analyses for Mercury on a global scale as was done for the Moon using LROC.

UV Maps of Mercury: Using the VIRS Global Spectral Cube [3] we create regional and global mosaics of UV reflectance and reflectance ratios that parallel those produced for the Moon (Fig 1). When compared with multispectral imaging from the Mercury Dual Imaging System (MDIS) [4] and VIRS global UV-through Near Infrared color (Fig. 3) [5]. Fig. 1 parallels the maturity / "shock" maps of [1]. Younger, fresher craters (A, E, in both figures) are bright and bluish in MDIS color (shallower spectral slope), and yellow-red in VIRS color (high visible reflectance, and near UV spectral slope, low Vis-IR spectral slope), and stand out as red or pink in the VIRS UV map, possibly indicating lower maturity and/or shocked materials. Older craters (C, D) are more subdued in MDIS and VIRS color, with Chekov's (C) low reflectance materials standing out as dark in MDIS and cyan in VIRS color (The red in Fig 3. Associated with D is a pyroclastic deposit within the older, subdued crater). Copley Crater (B) is an intermediate or compositionally different case, appearing morphologically fresh and rayed, but spectrally not as bright as A or E. The VIRS UV color mosaic shows subtle differences in the older craters which may indicate a more complex relationship between UV reflectance properties and both maturity and other physical effects. It is more difficult to distinguish the low reflectance material of Chekov from the background plains. This is possibly a function of both the relative maturity of the crater and surroundings and the resolution of VIRS footprints covering the crater.

Space Weathering on Mercury: The surface if Mercury is likely much more heavily space weathered than that of the Moon [6]. Utilizing UV wavelengths to assess space weathering on Mercury is in its beginning stages and presents different challenges and potentially different revelations than on the Moon.

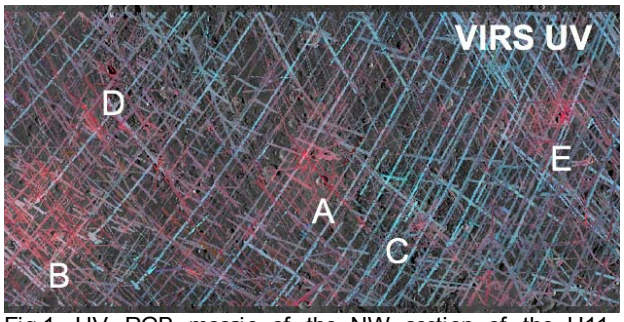

Fig.1. UV RGB mosaic of the NW section of the H11 (Discovery) quadrant of Mercury. Red = 414 nm reflectance, Green = 321 nm / 414 nm reflectance ratio, Blue = 321 nm / 358 nm reflectance ratio. Letters indicate craters: A) Popova, B) Copley, C) Chekov, D) Matisse, E) Unnamed, rayed.

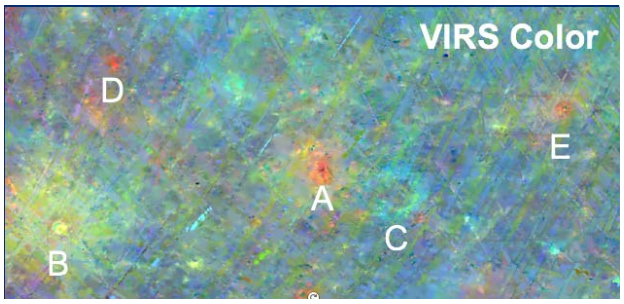

Fig.2 VIRS Color mosaic [5] of the same region as Fig. 1. Red = 575 nm reflectance, Green = reflectance ratio of 415 nm / 750 nm, Blue = reflectance ratio of 310 nm / 390 nm.

References [1] Denevi et al., (2014) JGR Planets 119 (5) 976-997. [2] McClintock W. E. and Lankton M. R. (2007) Space Sci. Rev. 131, 481–522. [3] Izenberg et al., (2017) MESSENGER Advanced Product Specification, Planetary Data System, Geoscience Node. [4] Hawkins III et al., (2007) SSR 131, 247-338. [5] Izenberg et al. (2014) Icarus 228, 364-374. [6] Domingue et al., (2014) SSR 181.1-4: 121-214.

THE ENIGMA OF MERCURY'S NORTHERN RISE. Peter James[1,2], [1]Lunar and Planetary Institute, USRA, 3600 Bay Area Blvd., Houston, TX 77058, USA, [2]Baylor University, Department of Geosciences, One Bear Place #97354, Waco, TX 76798, USA.

Setting the stage: The northern rise on Mercury is a broad, dome-shaped topographic swell situated in the northern smooth plains. It was first detected by the MErcury Surface, Space ENvironment, GEochemistry, and Ranging (MESSENGER) [1] mission, but the formation history and present-day compensation remain a mystery. Three key observations about the northern rise remain difficult to explain: (1) the rise does not appear to be compositionally or chronologically distinct from the surrounding plains; (2) ghost craters on the flanks of the northern rise appear to be tilted along with the long-wavelength trend of topography, which suggests that uplift post-dated the formation of the smooth plains by some amount of time; (3) gravity/topography admittance and coherence are both notably high at long-wavelengths (Fig. 1).

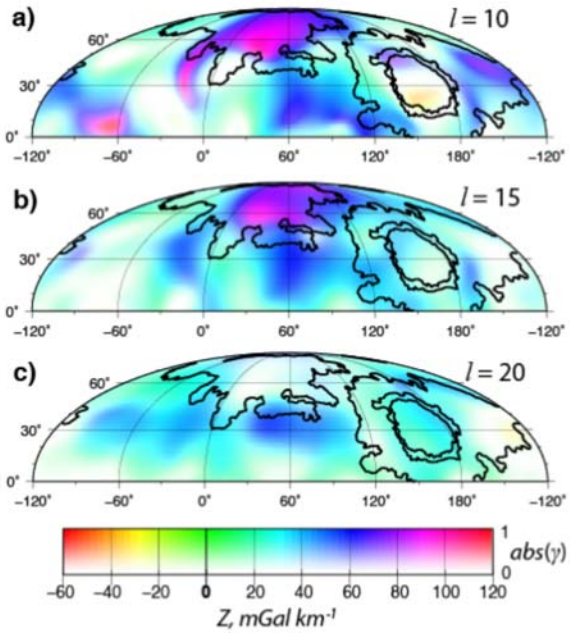

Figure 1: Admittance and correlation in Mercury's northern hemisphere, from [2]. The northern rise is centered approximately on 68°N, 32°E.

The prime suspects: Observation #3 is consistent with either lithospheric top-loading or compensation deep in the mantle. Possible mechanisms are described below along with their strengths and weaknesses.

"Blister" top loading. A traditional understanding of top-loading would violate observations #1 and #2, since there is no evidence for the ~10^6 km^3 of extrusive volcanism that would be required to create the observed load. Massive intrusive magmatism could resolve this discrepancy, but such intrusions would need to form within the uppermost several kilometers of the crust—akin to a blister—in order to reproduce the observed gravity/topography admittance.

CMB compensation. A downward deflection of the core-mantle boundary would explain observations #1 and #3, but there has not yet been a good explanation for how such a deflection may form relatively late in Mercury's history. Viscous relaxation of a FeS layer was explored in [2] as a means of uplifting initially-flat surface topography, but the theorized FeS layer is now considered to be "dead and buried" (as declared by Dr. Nancy Chabot, 3/24/2017). Even if a CMB deflection were to occur, lower mantle viscosity would need to exceed 10^{23} Pa-s in order to support the requisite CMB deflection over billion-year timescales [2].

Locally buoyant mantle. Low mantle density under the northern rise would support the uplifted topography, and would be consistent with gravity only if the crust is thinner than in the remainder of the northern smooth plains [2]. This mechanism needs to be reconciled with observation #1, since a chemically distinct mantle would be expected to produce chemically distinct volcanism. Such variations do exist within the northern smooth plains, but they are not obviously centered on the northern rise. It also does not offer a mechanism by which uplift of the rise would occur late in Mercury's evolution (observation #2).

Are there accomplices on the run? At first glance, the northern rise appears to be a one-off phenomenon. However, the northern rise is situated in a region with particularly uniform crustal thickness [3], and the mechanisms responsible for the formation of the northern rise could be at work elsewhere on the planet if they are obscured by crustal thickness variations. Two possibilities include the Budh-Sobkou rise and the northern Caloris rise. Both features include a long-wavelength topographic signal and tilted crater floors. The elusive history of the northern rise could therefore be the key to understanding a fundamental aspect of Mercury's inner workings.

Future leads: Analysis of extended mission gravity data [see Goossens et al., this mtg.] will illuminate the properties of the lithosphere, which are crucial to this problem. Magnetic anomalies concentrated on the northern rise could also test whether the lower crust is distinct from that of the surrounding plains.

References: [1] Solomon S.C. et al. (2007), Sp. Sci. Rev., 113, 3-39. [2] James P. et al. (2015), J. Geophys. Res. Planets.120 287-310. [3] Smith D.E. et al., Science, 336, 214-217.

Sodium pick-up ion observations in the solar wind upstream of Mercury

Jamie M. Jasinski[1,2,*], Jim M. Raines[1], James A. Slavin[1], Leonardo H. Regoli[1] and Neil Murphy[2]

[1]Climate and Space Sciences and Engineering Dept., University of Michigan, Ann Arbor, MI, USA.
[2]NASA Jet Propulsion Laboratory, Pasadena, CA, USA.
* Primary author contact details: jmjasins@umich.edu

Introduction: The pickup ion process is an important process that occurs when neutral particles are ionized and then "picked-up" by the local magnetic and electric fields of the solar wind. Pick-up ions are observed at many bodies, e.g. comets, moons of the Giant Planets, Mars and Venus [1,2,4]. Observations of pick-up ions are important as they allow to infer exospheric properties as well as loss processes from these bodies.

The MESSENGER spacecraft orbited Mercury in 2011-2015. Sodium ions were observed at Mercury's magnetosphere and dominate the planetary species [3]. Sodium is mostly observed in the magnetospheric cusp and plasma sheet, however they have also been observed in the magnetosheath.

Observations at Mercury with the MESSENGER spacecraft: We present the first observations of sodium pick-up ions upstream of Mercury's magnetosphere. The MESSENGER spacecraft's Fast Imaging Plasma Spectrometer observed multiple events of high sodium counts in the solar wind upstream of Mercury. The events display a shell velocity distribution, which is the characteristic signature of freshly picked up ions in the solar wind. From these observations we infer properties of Mercury's sodium exosphere and implications for the solar wind interaction with Mercury's magnetosphere.

References:

[1] Coates, A. J., Ion pickup at comets, Advances in Space Research, Vol. 33, Issue 11, Pages 1977-1988, 2003.

[2] Cravens, T. E. et al., Pickup ions near Mars associated with escaping oxygen atoms, J. Geophys. Res., 107(A8), 2002.

[3] Raines, J. M., et al., Structure and dynamics of Mercury's magnetospheric cusp: MESSENGER measurements of protons and planetary ions, J. Geophys. Res. Space Physics, 119, 6587–6602, 2014.

[4] Tokar, R. L., et al., Cassini detection of water-group pick-up ions in the Enceladus torus, Geophys. Res. Lett., 35, L14202, 2008.

An Integrated Modeling Suite for Simulating the Core Induction and Kinetic Effects in Mercury's Magnetosphere

Xianzhe Jia[1], James A. Slavin[1], Yuxi Chen[1], Gangkai Poh[1], Gabor Toth[1], and Tamas I. Gombosi[1]
[1]Department of Climate and Space Sciences and Engineering, University of Michigan, Ann Arbor, MI (Email: xzjia@umich.edu).

Introduction: Mercury, the innermost planet in the solar system, possesses a mini-magnetosphere arising from the interaction of its relatively weak internal field with the solar wind. Previous missions to Mercury, especially MESSENGER, have revealed many unique aspects of Mercury's space environment. In particular, the planetary field is believed to be generated by dynamo action in a highly conducting core whose radius is about 80% of the planetary radius [1]. The close proximity of the core to Mercury's surface and the magnetospheric boundaries suggests that the planetary interior has significant influences on the way Mercury responds to the forcing by the external solar wind [2]. Moreover, the ambient solar wind in the inner heliosphere that interacts with Mercury typically has a low Alfvénic Mach number (~ 2 - 4), implying that magnetopause reconnection at Mercury might occur with high efficiency. MESSENGER observations have indeed shown that reconnection in Mercury's magnetosphere appears to be very intense, and the global dynamics is dominated by effects of reconnection [3].

A Global MHD Model with Coupled Interior: Understanding the coupled solar wind-magnetosphere-interior interaction at Mercury requires not only analysis of observations but also a modeling framework that is both comprehensive and inclusive. We have developed a global magnetohydrodynamics (MHD) model for Mercury in which the planetary interior is modeled as layers of different electrical conductivities that electromagnetically couple to the surrounding plasma environment [4]. This modeling capability allows us to characterize the dynamical response of Mercury to time-varying external conditions in a self-consistent manner. We have applied this new model to both idealized solar wind conditions and a set of extreme solar events (CMEs and High-speed Streams) observed by MESSENGER to quantify the induction effect at the core and the erosion effect from reconnection. Based on comparisons of our model results with MESSENGER observations, we find that induction and magnetopause reconnection appear to play an equally important role in determining the structure of Mercury's dayside magnetosphere.

Resolving Kinetic Effects through a Coupled Fluid-kinetic Model (MHD-EPIC): Given that reconnection is the dominant driver of Mercury's magnetospheric dynamics, we have developed a two-way coupled fluid-kinetic model for Mercury, MHD with Embedded Particle-in-Cell (MHD-EPIC) [5-7], which enables simulating reconnection at kinetic scales while simultaneously capturing large-scale effects of reconnection on a global magnetosphere. The MHD-EPIC model has been applied to Mercury to investigate reconnection-driven phenomena in the magnetotail, including the formation and characteristics of tail X-line, generation and propagation of plasmoids, and potential dawn-dusk asymmetries [8].

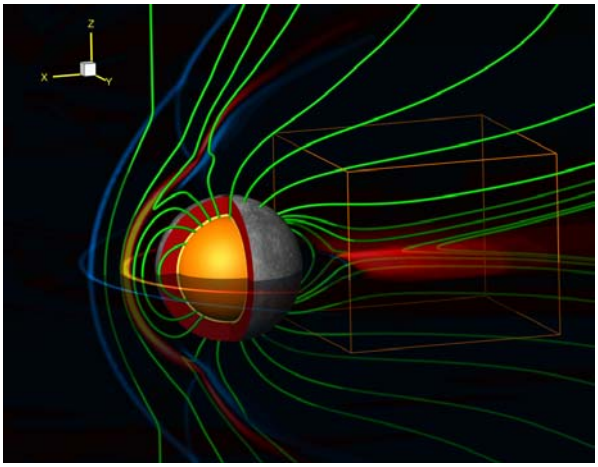

Figure-1: A 3D perspective of the coupled magnetosphere-interior system at Mercury. The colors represent the current density (J_y), the green traces show sample magnetic field lines, and Mercury's interior is color-coded with the resistivity. The orange box shows the PIC-modeled region within the MHD model [8]. The figure is made based on results from the global model published in [4].

References:

[1] Smith, D., et al. (2012) Science, 336, 214. [2] Slavin, J. A., et al. (2014) JGR, 119, doi: 10.1002/2014JA020319. [3] Slavin, J. A., et al. (2010) Science, 329, 665. [4] Jia, X., et al. (2015) JGR, 120, doi: 10.1002/2015JA021143. [5] Daldorff, L., et al. (2014) JCP, 268, 236-254. [6] Toth, G., et al. (2016) JGR, 121. [7] Chen, Y. et al. (2017) JGR, 122, 10318. [8] Chen, Y. (2017) Ph.D Thesis, Univ. of Michigan.

THE DISTRIBUTION AND ORIGIN OF MERCURY'S LITHOSPHERIC MAGNETIZATION. Catherine L. Johnson[1,2], Alain M. Plattner[3], Roger J. Phillips[4], Lydia C. Philpott[1], Mallory Kinczyk[5] and Louise Prockter[6], [1]Dept.of Earth, Ocean and Atmospheric Sciences, University of British Columbia, Vancouver, BC, V6T 1Z4, Canada, cjohnson@eoas.ubc.ca. [2]Planetary Science Institute, Tucson, AZ 85719, USA. [3]Dept. of Earth and Environmental Sciences, California State University, Fresno, CA 93740, USA. [4]Dept. of Earth and Planetary Sciences, Washington University, St Louis, MO 63130, USA. [5]Dept. of Marine, Earth, and Atmospheric Sciences, North Carolina State University, Raleigh, NC, 27695, USA. [6]Lunar and Planetary Institute, Houston, TX 77058, USA.

Overview: Magnetic field data obtained by the MErcury Surface, Space ENvironment, GEochemistry, and Ranging (MESSENGER) spacecraft contain signatures of lithospheric magnetization on Mercury [1-4]. We present models for the spatial distribution of magnetization and discuss their implications.

Magnetization Models: Magnetic field measurements at spacecraft altitudes are dominated by non-lithospheric sources that we estimate and subtract [1, 5], to isolate lithospheric fields with wavelengths less than ~700 km. Magnetization models were generated using an equivalent source dipole (ESD) technique [6] and a bootstrap approach [5]. We inverted 100 random data sets, each subsampled from the full data set to have a more equal-area-distribution. As in a traditional bootstrap approach, the resulting average model is equivalent to a model obtained from inverting the full data set and the standard deviation among the models provides an estimate of the uncertainty in magnetization that results from the data distribution.

Results and Discussion: The largest amplitude magnetizations are found in the Caloris region (Fig. 1). Individual instances of correlations of magnetization with crater interiors and ejecta materials are seen (e.g., Rustaveli crater at ~83°E, 52°N). However, no global systematic trends with crater location or the age proxy of degradation state [8] have been observed, suggesting that crater-related magnetizations reflect primarily variations in magnetic carrier distributions (source depth and/or iron content). Weak magnetizations are typically associated with the northern smooth plains. The exceptions are a localized signal over the northern rise, with no obvious surface geological expression, and crater-related signals, included some associated with buried craters [8].

Lithospheric field signals constrain the magnetization-thickness product (M-h). We calculated M-h for magnetizations induced in the present field for two scenarios (Fig. 2), using average susceptibilities appropriate for likely magnetic mineralogies and the average iron concentration of the crust [1]. If confined to a layer that is at most 10 km thick (Fig 2a), induced magnetizations typically cannot explain the observed signals. However, for a thicker layer, or higher susceptibilities, induced magnetizations could account for the observed signals except in the strongly magnetized regions (Fig. 2b). In such regions, locally enhanced iron concentrations and/or remanent magnetizations acquired in a strong ancient field [1] are required.

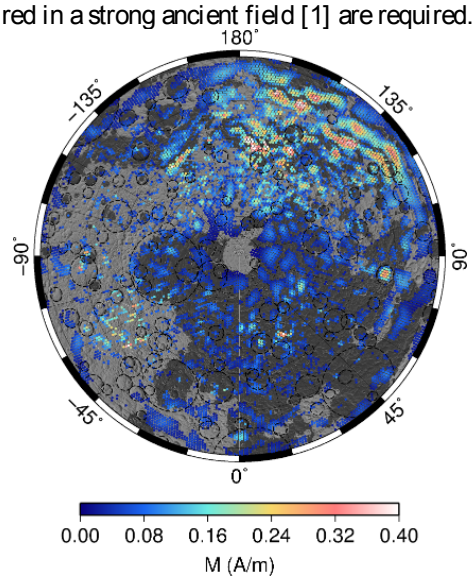

Figure 1. Magnetization strength, M, for ESD model with an assumed 10-km thick source layer, h, at 20 km depth and a dipole spacing of ~27 km. M shown where M > 0 at the 1-sigma level. Craters (dashed black) with 100 km < D < 1000 km and one proposed basin [7] are shown. Lambert azimuthal equal area projection from 38° to 90° N.

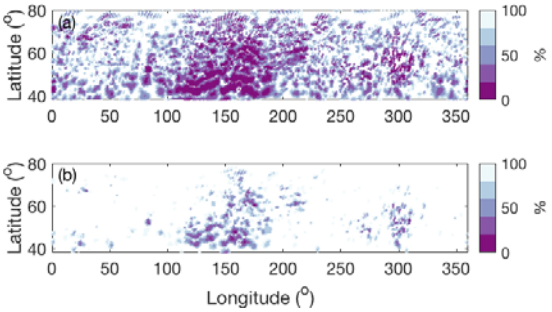

Figure 2. Percentage of the M-h product for the model in Fig. 1 predicted by magnetizations induced in the present field in (a) a layer 10 km thick, (b) the entire crustal column. White regions indicate locations where magnetizations can be fully accounted for by induced signals.

References: [1] Johnson, C. L. et al. (2015) Science, 348, 892. [2] Hood, L. L. (2015) GRL, 42, 10,565. [3] Hood, L. L. (2016) JGR, 121, 1016. [4] Johnson et al. (2016) LPS XXXXVII, #1391. [5] Johnson et al. (2018) LPS XXXXIX, #1505. [6] B. Langlais et al. (2004) JGR, 109, E02008. [7] Fassett, C. I. et al. (2012), JGR, 117, 2156-2202. [8] Kinczyk, M. et al. (2016) LPS XXXVII, #1573.

CHARACTERIZING THE MORPHOLOGY, DISTRIBUTION, AND FORMATION GEOMETRY OF MERCURY'S PYROCLASTIC VENTS. L. M. Jozwiak[1] , J. W. Head[2], and L. Wilson[3], [1]Johns Hopkins University Applied Physics Laboratory, Laurel, MD, USA., [2]Department of Earth, Environmental, and Planetary Science, Brown University, Providence, RI, USA. [3]Lancaster Environment Centre, Lancaster University, Lancaster LA1 4YQ, UK. (corresponding author: lauren.jozwiak@jhuapl.edu)

Introduction: Prior to the MESSENGER (MErcury Surface, Space ENvironment, GEochemistry, and Ranging) mission [1], there was active debate about the presence and nature of volcanic features on the planet [e.g. 2,3,4]. The mission quickly revealed substantial evidence for effusive smooth volcanic plains [5], and unexpected evidence of explosive volcanism in the form of pyroclastic vents and deposits [5]. The locations and characteristics of these vents and deposits were mapped throughout the duration of the mission [6,7,8,9]. Here we present a final MESSENGER catalog of Mercury's pyroclastic vents, an analysis of their distribution and morphologic character, and hypotheses for the dominant formation geometry [9].

For identification, we required all candidate vents to possess a rimless depression, morphologically distinct from an impact crater [5,6]. Most vent candidates also possess a red/orange color anomaly surrounding the vent, observed using the MDIS enhanced color maps [e.g. 10], and interpreted to represent a fine-grained pyroclastic deposit [6, 11]. Using these criteria, we identify 104 candidate pyroclastic vents.

Distribution: Unlike the Moon, where pyroclastic deposits are primarily located along the edges of impact basins and mare deposits [12], pyroclastic deposits on Mercury are anti-correlated with the locations of smooth volcanic deposits, and (with the exception of Caloris and Tostoj basins) are not strongly correlated with the edges of large basins [9]. The locations of pyroclastic vents are, however, strongly correlated with the interiors of impact craters, with 82% of vents being located inside craters. Additionally 10% of vents are located on a lobate scarp [2, 13], although in most cases cross-cutting relationships are ambiguous.

Vent Morphologies: From the 104 candidate pyroclastic vents in our catalog, we identified three morphologic classes: simple vent, pit vent, and vent-with-mound. The simple vent morphology (57% of vents) is characterized by an elongated shape with a semimajor axis resolvably longer than the semiminor axis, and walls sloping to a relatively narrow floor. The pit vent morphology (36% of vents) is characterized by more equant axis lengths and a wider floor profile. The pit vent morphology encompasses depressions that are circular or elliptical, and also more complex shapes, such as the kidney-shaped vent to the northeast of the Rachmaninoff basin. The vent-with-mound morphology (7% of vents) is characterized by a central mound of material circumscribed by a prominent vent. This morphology includes both circular features (located outside the Caloris basin), and more irregular morphologies (located inside the Caloris basin).

Formation Geometry: We investigated five possible formation geometries including: 1) a shallowly stalled dike forming a sill/laccolith, 2) a shallowly stalled dike forming a sill beneath the dike tip level, 3) a dike propagating to the surface and erupting, 4) a shallowly stalling dike without sill formation, and 5) dike propagation and eruption along a critically stressed thrust fault.

Our morphologic and morphometric analyses of these scenarios concluded that the dominant formation geometry was probably variations on a dike propagation scenario, with the dike erupting at the surface, or shallowly stalling and subsequently erupting. These geometries would be capable of producing both the elongated simple vent, and equant pit vent morphologies. We observed no evidence of shallow sill formation and crater floor deformation of the kind observed in lunar floor-fractured craters [14-16].

Conclusions: The discovery and confirmation of explosive volcanism on Mercury is one of the most important and unexpected results of the MESSENGER mission. Utilizing all of the data returned by the mission, we have compiled a catalog of all candidate pyroclastic vents. Our analyses show that pyroclastic vents on Mercury are located across the surface of the planet and not correlated with smooth plains deposits. Vents display a range of morphologies and sizes, and are likely to have been formed by variations in local dike propagation and eruption conditions.

References: [1] Solomon, S. C., et al. (2007) *Space Sci. Rev. 131*, 3-39. [2] Strom, R. G., et al. (1975) *JGR 80*, 2478-2507. [3] Wilhelms, D. E. (1976) *Icarus 28*, 551-558. [4] Head, J. W., et al. (2007) *Space Sci. Rev. 131*, 41-84. . [5] Head, J. W., et al. (2008) *Science 321*, 69-72. [6] Kerber, L., et al. (2009) *EPSL 285*, 263-271. [7] Goudge, T. A., et al. (2014) *JGR Planets 119*, 3, 635-658. [8] Thomas, R. J., et al. (2014) *JGR Planets 119*, 10, 2239-2254. [9] Jozwiak, L. M., et al. (2018) *Icarus 302*, 191-212. [10] Murchie, S. L., et al., (2008) *Science 321*, 73-76. [11] Blewett, D. T., et al. (2009) *EPSL 285*, 272-282. [12] Gaddis, L. R., et al. (2003) *Icarus 161*, 262-280. [13] Byrne, P. K., et al., (2014) *Nature Geosci. 7*, 301-307. [14] Schultz, P. H. (1976) *The Moon 15*, 241-273. [15] Jozwiak, L. M., et al., (2012) *JGR Planets 117*, E11. [16] Wilson, L. and Head, J. (2018) *Icarus 305*, 105-122.

INVESTIGATING THE AGE OF MERCURY'S PYROCLASTIC DEPOSITS. L. M. Jozwiak[1], N. R. Izenberg[1], C. L. Olson[1,2], and J. W. Head[3], [1]Johns Hopkins University Applied Physics Laboratory, Laurel, MD, USA. [2] University of Maryland, College Park, MD, USA. [3]Department of Earth, Environmental, and Planetary Science, Brown University, Providence, RI, USA (corresponding author: lauren.jozwiak@jhuapl.edu)

Introduction: The geologic history of Mercury has been interpreted to fall into two distinct periods: early mercurian history was dominated by the successive emplacement of generations of effusive volcanic plains [1], followed by a protracted period of cooling and contraction dominated by the formation of lobate scarps and other compressional tectonic features [2, 3]. Effusive volcanic plains appear to have ceased formation ~3.5 Ga [4] during the early Calorian period. In contrast, lobate scarp formation and activation appears to have begun in the mid-Calorian period and extended through the remainder of Mercury's history [3, 5]. The MErcury Surface, Space ENvironment, GEochemistry, and Ranging (MESSENGER) mission [6] revealed for the first time, evidence for explosive volcanism on Mercury [e.g. 7]. How these features fit into the established framework of mercurian geologic history is still unknown, but holds important information about the thermal and geologic evolution of the planet.

We use two different methods to constrain the ages of the pyroclastic vent formation: 1) the stratigraphic age of features hosting pyroclastic vents, and 2) relative values of deposit reflectance as a measure of degree of space weathering.

Stratigraphic Method: Unlike many planetary surfaces, crater size frequency distribution analysis cannot be used to determine the model age of pyroclastic deposits because of the difficulty in superposition relationships between craters on the deposit and under the deposit, and uncertainties in how the fine-grained pyroclastic material retains craters [8]. Instead, we utilize stratigraphic relationships between the pyroclastic vents and other local features of known stratigraphic age (i.e. impact craters) to place bounds on vent formation [9, 10]. The majority (82%) of pyroclastic vents are located inside of impact craters [10], such that the chronostratigraphic age of the host crater can be used to constrain the oldest possible age for a vent [9].

Using the MESSENGER-revised crater degradation classification scheme developed by Prockter et al. [11] and Kinczyk et al. [12], we investigated the host crater ages of all applicable vents in the Jozwiak et al. [10] catalog. This population represents 70% of the recognized vents on Mercury, excluding those not located in impact craters, and those located in craters with diameter less than 40 km.

Spectral Characteristics Method: In order to assess all vents regardless of location, and assess the ages of vents relative to each other, we employ a second dating method. The spectral characteristics method utilizes the results of Goudge et al. [9], which states that the two principle spectral characteristics of pyroclastic deposits are depth of UV absorption and reflectance at 700 nm. It has been hypothesized [9] that the variations in reflectance at 700 nm are due to variations in space weathering, and therefore, deposit age.

We use the VIRS dataset to extract the UV absorption depth and 700 nm reflectance for all pyroclastic deposits, and ratio these data to local background material. We then plotted the data according to stratigraphic age to assess whether host crater stratigraphic age is a good predictor of overall deposit reflectance. We are also currently investigating correlations between vent geomorphologic degradation and deposit reflectance.

Results and Ongoing Work: Our stratigraphic analysis indicated that the majority of vents were located in Tolstojian and Calorian period craters, similar to the result seen in Goudge et al. [9]; however, given that the majority of impact craters on Mercury are associated with these periods, this result is unsurprising. Our analysis also revealed 10 vents associated with the Mansurian period and one vent associated with the boundary of the Mansurian and Kuiperian periods. These vents located in geologically young craters are striking because revised constraints on the ages associated with the mercurian stratigraphic periods suggest that the Mansurian began ~1.7 Ga, and the Kuiperian as recently as ~280 Ma [5]. Thus, our results suggest that explosive volcanism on Mercury was not confined to the early effusive volcanic period, and may have operated into geologically recent periods of Mercury's history. Our continuing analysis of deposit reflectance will allow us to further explore the relative ages of pyroclastic vents, and more fully characterize the overall duration of explosive volcanism on Mercury.

References: [1] Denevi, B. W., et al. [2013] *JGR Planets 118*, 891-907. [2] Byrne, P. K., et al. [2014] *Nature Geosci. 7*, 301-307. [3] Crane, K. T., and Klimczak, C. [2017] *GRL 44*, 3082-3089. [4] Byrne, P. K., et al., [2016] *GRL 43*, 7408-7416. [5] Banks, M. E., et al. [2017] *JGR Planets 122*, 1010-1020. [6] Solomon, S. C., et al. [2007] *Space Sci. Rev. 131*, 3-39. [7] Head, J. W., et al. [2008] *Science 321*, 69-72. [8] Luchitta, B. K., and Schmitt, H. H. [1974] *LPS V*, 223-234. [9] Goudge, T. A., et al. [2014] *JGR Planets 119*, 635-658. [10] Jozwiak, L. M., et al. [2018] *Icarus 302*, 191-212. [11] Prockter, L. M., et al. [2016] *LPSC 47*, Abstr. #1245. [12] Kinczyk, M. J., et al. [2016] *LPSC 47*, Abstr. #1573.

MERCURY AS A PROBE FOR THE EARLY INNER SOLAR SYSTEM. S. Kamata[1] and K. Kuramoto[2], [1]Creative Research Institution, Hokkaido University, N21 W10, Kita-ku, Sapporo, Japan, [2]Dept. Cosmosciences, Hokkaido University, N10 W8, Kita-ku, Sapporo, Japan.

Introduction: Mercury is an end-member of terrestrial planet: the innermost, hottest, airless, waterless, and smallest planet. Among the characteristics of Mercury, the large size of the core leads to its formation scenario distinctively different from that for other terrestrial planets; the building blocks are those formed in a very hot environment, leading incomplete solidification of silicates [e.g., 1], or a large portion of the silicate mantle is stripped off by a giant impact [e.g., 2]. The detailed exploration of Mercury by the MESSENGER spacecraft seems to emphasize the uniqueness of this planet. For example, a sulfur- and carbon-rich surface [e.g., 3, 4] is in contrast to other terrestrial planet. However, findings by MESSENGER imply that such a unique planet may play a key role in understanding the early stage of terrestrial planets, including the Earth.

Chemical Composition: MESSENGER found that the major-element composition of the surface of Mercury is similar to that of enstatite chondrites [3]. Enstatite chondrites are a rare type of undifferentiated meteorites characterized by the redox state of iron; iron mostly occurs as metallic Fe or sulfides (FeS), not as oxides (FeO). Spectral images of Mercury also indicate that the surface is depleted in FeO [5]. These facts indicate that both the building blocks of Mercury and enstatite chondrites are formed under a highly reduced (O-poor) condition. Because the degree of iron oxidation should decrease with increasing temperature, enstatite chondrites are believed to be formed near the Sun, and thus are proposed as major building blocks of Mercury [6].

Nevertheless, Mercury's surface chemistry also indicates that its building blocks are not simple condensates at the hottest region of the Solar nebula; the significant amount of sulfur is detected [3]. A chemical equilibrium calculation assuming the Solar composition indicates that sulfur starts to condense as FeS at a low temperature [7], and most FeS should be partitioned to the metallic core, resulting in a S-poor surface. In addition, the S/Si ratio of Mercury is correlated not to the Fe/Si ratio but to Ca/Si and Mg/Si ratios, suggesting that major sulfur compounds are CaS and/or MgS [8].

Carbon-rich Inner Solar Nebula: It is possible for CaS and MgS to be high-temperature condensates if the Solar nebula is rich in carbon [7]. In addition, C-rich environment is highly reduced since carbon consumes oxygen forming CO, leading Fe to be metallic. Moreover, if the nebula is rich in C, C-bearing condensates are expected [7], and a part of C as well as S is partitioned to silicate under a reducing condition [9]. Thus, a C- and S-rich surface of Mercury supports a C-rich inner Solar nebula. Such a nebula may be achieved if dusts and/or pebbles containing organic material are transported from the outer region and are vaporized due to a high-temperature inner Solar nebula at an early stage of the Sun.

Insight for the Early Earth: In terms of chemical composition, the Earth is different from enstatite chondrites. However, it has been known that isotopic compositions of terrestrial mantle are similar to those of enstatite chondrites for most elements and are quite different from those of other types of chondrites. In particular, material accreted by the Earth after its core formation (Late Veneer; ~0.5% Earth mass) that can be inferred from the isotopic composition of highly siderophile (iron-loving) elements needs to be nearly completely enstatite chondritic [10]. In fact, such a view is also supported from an orbital evolution model of asteroids; the migration of giant planets (i.e., the Nice model) scatters asteroids located inner than the main asteroid belt where E-type asteroids, which are thought to have enstatite-chondrite like surface chemical composition, are located today [11]. The currently oxidized mantle of the Earth could be the result of a strong oxidation after the accretion. The loss of a large amount of hydrogen-rich proto-atmosphere via hydrodynamic escape [e.g., 12] may account for the oxidation of the atmosphere and the bulk silicate Earth. Thus, the difference in redox state between the Earth and Mercury may reflect the difference in the planetary processes, and therefore Mercury may be considered as a planet that tells us the early stage of terrestrial planets.

References: [1] Lewis J. S. (1972) *EPSL, 15,* 286–290. [2] Benz W. et al. (1988) *Icarus, 74,* 516–528. [3] Nittler L. R. et al. (2011) *Science, 333,* 1847–1850. [4] Peplowski P. N. et al. (2015) *Planet. Space Sci., 108,* 98–107. [5] Blewett D. T. et al. (2009) *EPSL, 285,* 272–282. [6] Wasson J. T. (1988) In: *Mercury,* 622–650. [7] Wood J. A. and Hashimoto A. (1992) *Geochim. Cosmochim. Acta, 57,* 2277–2388. [8] Weider S. Z. et al. (2014) *Icarus, 235,* 170–186. [9] Li Y. et al. (2016) *Nature Geosci, 9,* 781–785. [10] Dauphas N. (2017) *Nature, 541,* 521–524. [11] Bottke W. F. et al. (2012) *Nature, 485,* 78–81. [12] Kuramoto K. et al. (2014) *EPSL, 375,* 312–318.

GROUND BASED OBSERVATION OF MERCURY'S SODIUM AT HALEAKALA OBSERVATORY IN 2013-2017. S. Kameda[1] and M. Kagitani[2], [1]Rikkyo University (3-34-1 Nishi-Ikebukuro, Toshima, Tokyo 171-8501, Japan), [2]Tohoku University.

Introduction: Mercury's exospheric sodium has been most investigated in exospheric species to understand the dynamics and source process of surface-bounded exosphere because its emission is the brightest in exospheric emission. Since its discovery [1], a lot of ground-based observations for more than three decades and MESSENGER observations have been done and sodium atoms are thought to be released from the surface by photon-stimulated desorption [2, 3], thermal de- sorption [4], chemical sputtering [5], solar wind ion sputtering [6, 7], and micrometeoroid vaporization [8, 9].however, the source process of sodium is yet to be clarified.

Observation: In this study, daily variation in Mercury's sodium exosphere was observed at the Haleakala Observatory in Hawaii by using a 40 cm Schmidt Cassegrain telescope, a high-dispersion spectrograph, and a charge coupled device (CCD) camera. During observation seasons, elongation between Mercury and the Sun is more than 15 °, and the observation time varies from 30 min to 1 h before sunrise or after sunset. The exospheric emission observed from the ground is part rather than entire of dayside. The ratio of the observed emission varies by phase angle. Thus, we estimated the averaged column density of sodium atoms by using the exospheric model and assuming constant exospheric temperature.

We confirmed that the column density of sodium atoms over the dawn side differs from that over the dusk side. We originally focused on column density over the dawn side, which had been observed until January 2015 and confirmed the seasonal variation greater than that of dusk side. However, our observational data of March 2015 confirmed significant variation over the dusk side. In addition, we examined the ratio between the dawn and dusk sides. Although roughly 1 in the true anomaly angle (TAA) of >180° , the ratio is greater than 2 at maximum in the TAA of <180°.

Model: In the observational data of the dawn side, the local maximums of the column density of sodium atoms were present near the TAAs of 140° and 320°, which indicates contribution by interplanetary dust impact. Interplanetary dust is known to be distributed densely in the dust symmetry plane; however, its detailed distribution in the vicinity of Mercury is unknown. By applying the dust distribution model by Kelsall et al. [1998], these TAAs show the points at which Mercury passes through the dust symmetry plane. To verify the contribution of interplanetary dust to exospheric yield over the dawn side, model parameters that maximize the correlation coefficient were derived, revealing a value of 0.822. Therefore, the column density of sodium atoms may correlate highly with the interplanetary dust density.

However, the variation in column density over the dusk side showed a local maximum near the TAA of 180°. Therefore, such variation cannot be explained by the consideration applied to the dawn side. Thus, it is necessary to examine factors indicating the differences in variation between the dawn and dusk sides.

We also took into account the transportation effect by solar radiation pressure. The result shows this process is effective and may explain the temporal variation of sodium density at the dusk side. Additionally, we consider the adsorption to the night-side surface, which explains the temporal variation at the dawn side.

Future work: We started continuous observation using the same telescope and spectrograph in 2013, and the system is still working. Recently, we succeeded in fully automatic observation of Mercury, i.e., unmanned guiding and spectroscopic observation with calibration data. Due to the high clear-sky occurrence rate at Haleakala, we can obtain the data constantly. We also plan to keep this facility and Mercury observation to 2025 when BepiColombo will arrive there to perform simultaneous observation and to clarify the relationship between solar cycle and temporal variation of Mercury's sodium.

References: [1] Potter, A. E. and Morgan, T. H. (1985) Science 229, 651–653. [2] McGrath, M. A. et al. (1986) Nature 323, 694–696. [3] Yakshinskiy, B. V. and Madey, T. E. (1999) Nature 400, 642–644. [4] Leblanc, F. and Johnson, R. E. (2003) Icarus 164, 261–281. [5] Potter, A. E. (1995) GRL 22, 3289-3292. [6] Potter, A. E. and Morgan, T. H. (1997) Adv. Space Res. 19, 1571–1576. [7] Killen, R. M. et al. (2004) Icarus 171, 1–19. [8] Morgan, T. H. et al. (1988) Icarus 75, 156–170. [9] Cremonese, G. et al. (1997) Ap. J. Lett. 490, 199–202. [10] Kelsall, T. et al. (1998) Ap. J. 508, 44–77.

TRUE POLAR WANDER OF MERCURY. J. T. Keane[1] and I. Matsuyama[2]; [1]California Institute of Technology, Pasadena, CA 91125, USA (jkeane@caltech.edu); [2]Lunar and Planetary Laboratory, University of Arizona, Tucson, AZ 85721, USA.

Introduction: The spin of a planet is not constant with time. Planetary spins evolve on a variety of timescales due to a variety of internal and external forces. One process for changing the spin of a planet is true polar wander (TPW). TPW is the reorientation of the bulk planet with respect to inertial space due to the redistribution of mass on or within the planet. The redistribution of mass alters the planet's moments of inertia (which are related to the planet's spherical harmonic degree/order-2 gravity field). This process has been measured on the Earth, and inferred for a variety of solar system bodies [1]. TPW can have significant consequences for the climate, tectonics, and geophysics of a planet.

In this work, we investigate the possibility of TPW of Mercury using the high quality geophysical dataset returned by the MESSENGER mission [e.g. 2-4]. The last investigation of true polar wander of Mercury used pre-MESSNEGER data [5]. We find that Mercury's large impact basins and volcanic provinces likely reoriented the planet by tens of degrees.

Methodology: We have developed a technique for isolating the contribution of geologic features to the moments of inertia of planetary bodies [6]. Since most planetary-scale features (e.g. impact basins) are axisymmetric, we model the gravity fields of Mercury's large gravity anomalies using a set of concentric spherical caps. Spherical caps are advantageous both for their simplicity and because their degree-2 gravity field can be directly determined by fitting their higher-order gravity field. We fit for the mass anomalies of around a dozen mass anomalies on Mercury, including Caloris, Sobkou, the northern rise, and several unidentified gravity anomalies in the southern hemisphere. Despite the low resolution of the global gravity field of Mercury, the field is of sufficient quality to do this analysis as we are primarily interested in long-wavelength structures.

Mercury's Anomalous Figure: Mercury, like the Moon, possesses a significantly larger degree-2 gravity field than expected by hydrostatic equilibrium and Mercury's present orbit and rotation state. Mercury's dynamical oblateness is $J_2=50\times10^{-6}$ (unnormalized spherical harmonics), while the predicted, hydrostatic dynamical oblateness is only $J_2^{hydrostatic}=1\times10^{-6}$. Removing the contribution of impact basins and volcanic provinces only decreases the dynamical oblateness slightly: $J_2^{corrected}=41\times10^{-6}$. There are a few possible explanations for this excess deformation (sometimes referred to as a "fossil" or "remnant" figure). One explanation is to assume that this figure formed when Mercury was closer to the Sun and subject to stronger tidal and rotational forces. However, even with this corrected dynamical oblateness, the required orbital configuration appears unreasonable–requiring semimajor axes <0.1 AU [5]. An alternative explanation may be that a large fraction of Mercury's figure is a "thermal" figure, set Mercury's close proximity to the Sun and its unique spin-orbit resonance [7-8]

True Polar Wander of Mercury: While Mercury's impact basins and volcanic provinces cannot explain Mercury's anomalous figure, they still have an important effect on planet's moments of inertia and orientation. Removing all of Mercury's mass anomalies reveals a figure misaligned with the present-day figure of Mercury by ~20°. The Caloris basin, Sobkou basin, and northern volcanic rise each resulted in 5-10° of reorientation (true polar wander). Figure 1 shows a preliminary TPW path of Mercury, in response to the formation of these large impact basins and volcanic provinces

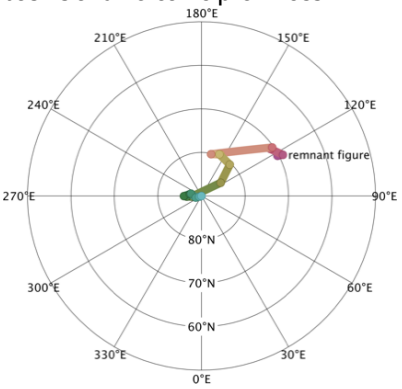

Figure 1: Preliminary true polar wander chronology of Mercury. Each point is an inferred paleopole based on the gravity anomaly associated with Mercury's impact basins and volcanic provinces.

This large magnitude of inferred TPW has a variety of important consequences for the geology of Mercury. TPW may help explain the nature/orientation of Mercury's fault population. TPW of Mercury likely affected the long-term stability of polar volatiles [9]. The reorientation of Mercury may also be recorded in Mercury's paleomagnetic history [10].

References: [1] Matsuyama, I., Nimmo, F., Mitrovica, J. X. (2014) Annu. Rev. Earth & Planet. Sci., 42, 605. [2] Smith, D. E. et al. (2012) Science, 336, 214. [3] Mazarico, E. et al. (2014) JGR: Planets, 119, 2417. [4] Perry, M. E. et al. (2015) GRL, 42, 6951. [5] Matsuyama, I. & Nimmo, F (2009) JGR, 114, E01010. [6] Keane, J. T. & Matsuyama, I. (2014) GRL, 41, 6610. [7] Phillips, R. J. et al. (2014) LPSC, 45, 2634. [8] Tosi, N et al. (2015) GRL, 42, 7237. [9] Siegler, M. A. et al. (2016) Nature, 531, 480. [10] Oliveria, J. S. & Hood, L. L. (2018) Mercury 2018.

MERCURY'S EXOSPHERE: CURRENT UNDERSTANDING AND CONUNDRUMS. R. M. Killen[1] and R. J. Vervack, Jr.[2], [1]NASA Goddard Space Flight Center, 8800 Greenbelt Road, Greenbelt MD 20771 USA (rosemary.killen@nasa.gov), [2]Johns Hopkins Univ. Applied Physics Lab., 11100 Johns Hopkins Rd., Laurel MD 20723 (ron.vervack@jhuapl.edu).

Introduction: Mercury's exosphere has been studied for the past 45 years following the ground-breaking Mariner 10 mission that discovered H and He [1]. Decades of ground-based spectroscopic studies and the more recent MESSENGER mission have revealed the additional presence of Na, K, Mg, Ca, Al, Fe, and Mn in Mercury's exosphere. Extensive temporal and spatial studies of the species Na, K, and Ca have been performed using ground-based telescopes [2]. During its four years in orbit, the MESSENGER Ultraviolet and Visible Spectrometer (UVVS) regularly observed Na, Mg, Ca, and H, primarily but not exclusively with line-of-sight radial sweeps tangent to the near-equatorial surface and back-and-forth sweeps perpendicular to the Sun-Mercury line in the nightside tail region [3]. During the last few Mercury orbits of MESSENGER, Al, Mn, and Ca^+ were observed by UVVS [4]. Finally, Al and Fe have been observed using the Keck telescope on Mauna Kea [5].

Although MESSENGER provided an unprecedented view Mercury's exosphere, there is much that is not understood, particularly in terms of the physical processes that generate and maintain the exosphere. Furthermore, there are apparent discrepancies between the ground-based observations and those by UVVS that need to be explained. We present several examples of the conundrums that exist with respect to Mercury's exosphere.

Example 1. The Ca exosphere was initially reported to be of high temperature, roughly 20,000 K, from ground-based data [6]. UVVS observations confirmed this high temperature, with values up to 70,000 K reported [7]. These temperatures are not only very large compared with the temperatures found for the other species but their origin, while speculated [8], is not fully understood.

Example 2. A puzzling discrepancy may exist in the spatial distribution between ground-based observations of Ca and UVVS observations. Burger et al. [7] determined a dawn-centered source for Ca. Although this may be consistent with ground-based observations, it is not certain whether they are in fact consistent. The ground-based data imply extensive Ca in high northern and southern latitudes and anti-sunward of the planet [9]. The UVVS tail region observations were sampled primarily north-south whereas the ground-based data were obtained east-west. It remains to show that the antisunward data from both sets of observations are consistent.

Example 3. Another difference between the ground-based and space-based observations is seen in the Na data. Ground-based data often show high-latitude peaks, either in the north or in the south or both [10]. These high-latitude peaks were not seen in the UVVS data. Although UVVS obtained some observations tangent to the south pole, it rarely made observations near the north pole due to the high northern latitude of periherm and geometry restrictions. These differences could be due to observational geometry or to the limitations inherent in both the ground and space-based techniques.

Example 4. A final conundrum concerns the apparently sporadic nature of the Al, Fe, Mn, and Ca^+, which were searched for on many occasions both from the ground and with UVVS. With the exception of one unusual Ca^+ detection by UVVS during the third flyby of Mercury, these species were only observed during the last few Mercury years of the MESSENGER mission [4] and only on a few observing runs at the Keck [5]. The reasons for the sporadic nature of these observations is unknown.

Future Work: The spatial and temporal variations in Mercury's exosphere and their sources require more investigation. In particular, high-latitude variability and its possible correlation with the magnetic cusps needs to be investigated. The reasons for sporadic variability in weakly emitting and/or less abundant species like Al should be studied. Finally the interaction of the plasma environment with the surface and exosphere, and the roles of dust, meteor streams and cometary streams in the production of exospheric species should be elucidated to provide a more complete understanding of the source processes for the exosphere.

References: [1] Broadfoot A. L. et al. (1974), Science. 185, 166-169. [2] Killen, R. M. et al. (2007) Space Sci. Rev. 132, 433-509. [3] Killen, R. M. et al. (2018), In: Mercury: The View after MESSENGER. [4] Vervack R. J. et al. (2016), Geophys. Res. Lett., 10.1002/2016GL071284. [5] Bida, T. A. and R. M. Killen (2017) Icarus 289, 227-238. [6] Killen R. M. et al. (2015) Icarus 250, 230-237. [7] Burger M. H. et al. (2012) Geophys. Res. Lett. 117. [8] Killen R. M. (2016) Icarus 268, 32-36. [9] Killen R. M. (2005) Icarus 173, 300-311. [10] Mangano, V. et al. (2015) Planet. Space Sci. 115, 102-109.

CRATER DEGRADATION ON MERCURY: A GLOBAL PERSPECTIVE. Mallory J. Kinczyk[1], Paul K. Byrne[1], Louise M. Prockter[2], Hannah C. M. Susorney[3], Olivier S. Barnouin[4]. [1]Planetary Research Group, Department of Marine, Earth, and Atmospheric Sciences, North Carolina State University, Raleigh, NC 27695, [2]The Lunar and Planetary Institute, Houston, TX 77058, [3]Department of Earth and Planetary Sciences, The Johns Hopkins University, Baltimore, MD 21218, [4]The Johns Hopkins University Applied Physics Laboratory, Laurel, MD 20723.

Introduction: Impact craters are the most ubiquitous geological feature in the Solar System. Manifest in numerous shapes and sizes, all impact craters are affected by the erosive forces acting upon their host body. From water and wind to viscous relaxation and micrometeorite bombardment, these processes work to subdue the crater form on geologic timescales. This results in an assortment of crater morphologies that can shed light on a planet's geological history and evolution. With the global image dataset collected by the MErcury Surface, Space ENvironment, GEochemistry, and Ranging (MESSENGER) spacecraft, it is now possible to characterize impact crater morphology across the entire surface of Mercury.

Global Classification: In this study, we developed a globally consistent degradation classification scheme for Mercury's craters [1] by reviewing previous descriptions of crater classification [e.g., 2,3] (**Fig. 1**). This approach labeled the most degraded craters as "Class 1" and the best preserved craters as "Class 5." We utilized multiple global monochrome image mosaics with a variety of viewing and illumination conditions, complemented with topography derived from stereophotoclinometry, to classify all craters ≥40 km in diameter. We also subdivided observations based on initial crater diameter and morphology [4]. This subdivision is a key aspect of the analysis because, although this particular crater property was not incorporated in previous classification systems, it has been recognized that size contributes to the overall appearance of crater features at varying degrees of degradation [3,5].

Roughness of Crater Ejecta: In addition to the visual classification system described above, we sought to identify whether surface roughness—the scale-dependent measure of topographic change [6]—could be used as a proxy for crater degradation. Using Fourier transform analysis, altimeter tracks acquired by the Mercury Laser Altimeter (MLA) were analyzed to determine whether a measureable, quantitative difference exists in surface roughness at the kilometer scale of continuous ejecta deposits [7]. By comparing roughness measurements across Class 3 and Class 4 craters (**Fig. 1**), we searched for differences that may represent further evidence of a morphological change over time, and to test the basis by which these craters were classified in the first place [1].

Results: Our results provide the first comprehensive assessment of how craters of various states of degradation are distributed across Mercury and, therefore, a characterization of the planet's impact cratering history. We find fewer mid-sized (i.e., ~40–100 km-diameter) craters of the most degraded (and thus presumably oldest) class than expected, implying that the earliest record of impact bombardment of Mercury's intercrater plains is only partially preserved [8].

In addition, we find that there is no statistically resolvable difference in roughness between Class 3 and Class 4 craters even with the highest-resolution MLA tracks. The upcoming ESA/JAXA BepiColombo mission will provide an excellent opportunity for further investigation into crater roughness at a range of scales.

References: [1] Kinczyk, M. J. et al. (2016) *LPS, 47,* #1573. [2] Trask, N. J. (1967) *Icarus, 6,* 270–276. [3] McCauley, J. F. et al. (1981) *Icarus, 47,* 184–202. [4] Baker, D. M. H. et al. (2011) *Planet. Space Sci., 59,* 1932–1948. [5] Pohn, H. A. & Offield, T. W. (1970) *Geo. Surv. Resear., 700-C,* C153–C169. [6] Shepard, M. K. et al. (2001) *JGR, 106,* 777–795. [7] Kinczyk, M. J. et al. (2017) *LPS, 48,* #2717. [8] Marchi, S. et al. (2013) *Nature, 499,* 59–61.

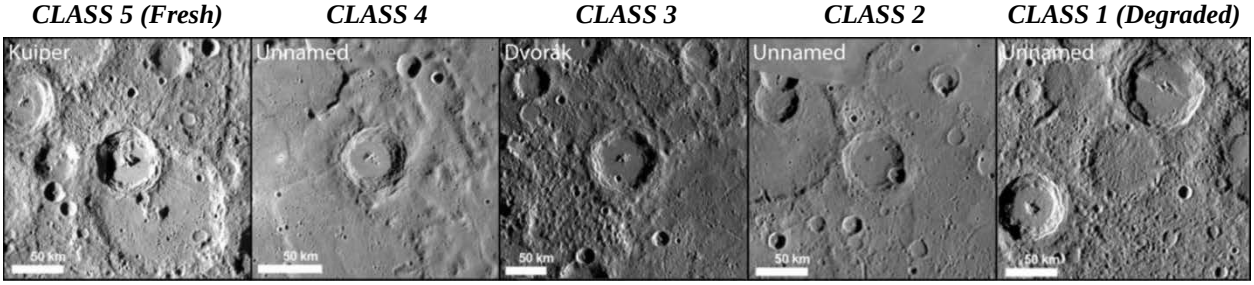

Fig. 1. Crater degradation in a subset of Mercurian craters [1]. Fresh craters have crisp rims, continuous ejecta, and a continuous field of secondary craters. Heavily degraded craters have little to no topographic relief and are heavily overprinted by subsequent primary and secondary craters.

A GLOBAL GEOLOGICAL MAP OF MERCURY. Mallory J. Kinczyk[1], Louise M. Prockter[2], Paul K. Byrne[1], Brett W. Denevi[3], Lillian R. Ostrach[4], James A. Skinner[4]. [1]Planetary Research Group, North Carolina State University, Raleigh, NC 27695. [2]The Lunar and Planetary Institute, Houston, TX 77058. [3]The Johns Hopkins University Applied Physics Laboratory, Laurel, MD 20723. [4]U.S. Geological Survey, Astrogeology Science Center, Flagstaff, AZ 86001.

Introduction: One of the principal outcomes of the MErcury Surface, Space ENvironment, GEochemistry, and Ranging (MESSENGER) mission was the collection of a global dataset of images. This dataset has allowed for the comprehensive analysis of the geological evolution of Mercury on a global scale. Numerous studies have investigated Mercury's tectonic [1], volcanic [2,3], and cratering [4,5] histories through mapping with these data. The next logical step is to create a global geological map to aid in the scientific analysis of a variety of geological formations across Mercury's surface, as well as the development of the first global stratigraphic column, and to place observations made with MESSENGER data into the context of earlier studies with Mariner 10 images.

Map Status: A global map was developed at the 1:15M scale [6] (**Fig. 1**) by the MESSENGER science team. We now have additional support to rework the map as part of the US Geological Survey (USGS) Scientific Investigations Map (SIM) series. Maps published following the USGS SIM guidelines incorporate detailed community feedback that result in products consistent with the methods used for other planets and moons. This effort will result in a product that will provide a robust basis for future scientific investigations and exploration efforts, such as the upcoming ESA/JAXA BepiColombo mission.

In our global USGS SIM product, geomorphologic units are defined based on texture, color, and topographic relief. Major units include impact crater facies of large craters and basins [e.g., 7–9], smooth plains [10], and intercrater plains [11]. Other datasets that have previously been compiled will be incorporated into the map including tectonic landforms [1], hollows [2], and pyroclastic vents [4,5].

Ongoing work: Current efforts are focused on improving mapped unit boundaries based on the final MESSENGER PDS data release [12], and determining whether additional map units are warranted [13]. Upon completion, the map will go through a rigorous peer-review process and a review by the USGS, before publication in the 2021 time frame.

References: [1] Byrne, P.K. et al. (2014) *Nature Geosci., 7,* 301–307. [2] Thomas, R.J. et al. (2014) *J. Geophys. Res. Planets, 119,* 2239–2254. [3] Jozwiak, L. M. et al. (2018) *Icarus, 302,* 191–212. [4] Susorney, H. C. M. et al. (2016) *Icarus, 271,* 180–193. [5] Kinczyk, M. J. et al. (2016) *LPS, 47,* #1573. [6] Prockter, L.M. et al. (2016) *LPS, 27,* #1245. [7] Prockter, L.M. et al. (2009) *LPS, 40,* #1758. [8] Buczkowski, D.L. et al. (2015) *LPS, 46,* #2287. [9] Hynek, B.M. et al. (2016) *LPS, 47,* #2312. [10] Denevi, B.W. et al. (2013) *J. Geophys. Res. Planet, 118,* 891–907. [11] Whitten, J.L. et al. (2014) *Icarus, 241,* 97–113. [12] Chabot, N.L. et al. (2016) *LPS, 47,* #1256. [13] Denevi, B.W. et al. (2016) *LPS, 47,* #1624.

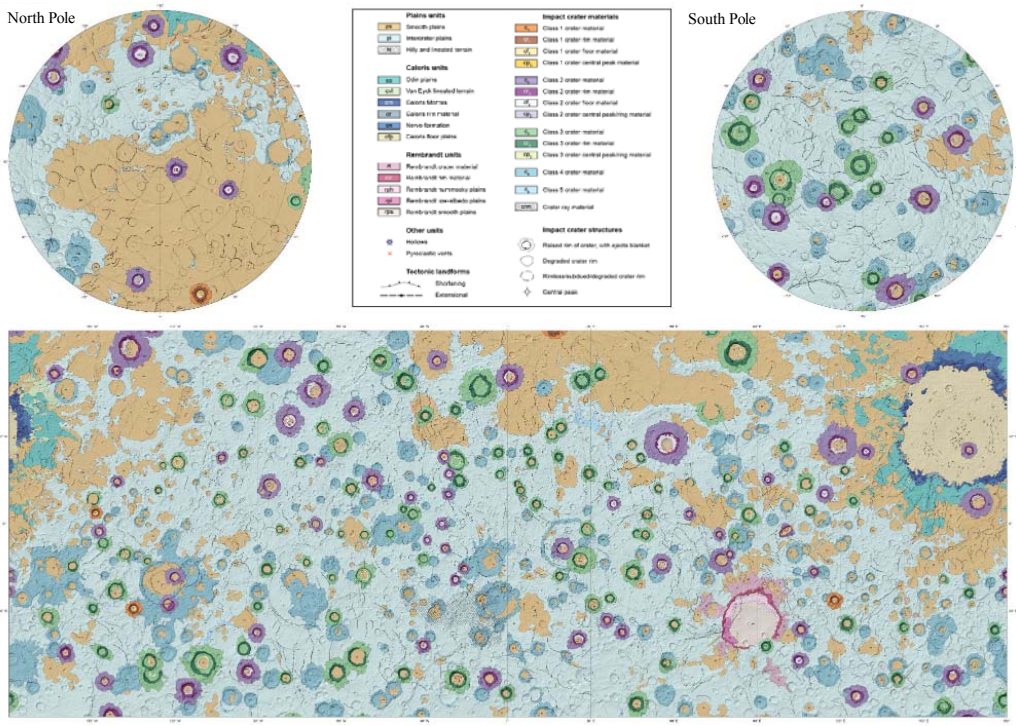

Fig. 1. Draft version of the global geological map of Mercury at 1:15M scale, showing major plains units and classified craters ≥90 km in diameter.

GEODYNAMICS IN A THIN SPHERICAL SHELL. S. D. King[1] and S. Robertson[2], Department of Geoscience, 4044 Derring Hall, Virginia Tech, Blacksburg, VA (sdk@vt.edu), [2]Physical Science Department, Embry-Riddle University, Daytona Beach, FL 32114 (robers24@my.erau.edu).

Over the pressure and temperature range of Mercury, dislocation creep (power-law rheology) is the weakest deformation mechanism for olivine. To illustrate we plot the ratio of dislocation creep to diffusion creep as a function of pressure and temperature using the parameters from [1] (Figure 1). In the red region diffusion creep is the weakest mechanism, while in the blue region dislocation creep is the weakest mechanism. Deformation will occur by the weakest mechanism. Here we assume a mineral grain size of 1 cm for the diffusion creep mechanism, a common assumption for Earth's mantle, and a strain-rate of 10^{-17}, two orders of magnitude smaller than Earth's upper mantle. We chose a value 100 times smaller than typical for Earth because, if convection occurs within Mercury it is far more sluggish. If we had chosen a larger value, then the plot would be entirely in the dislocation (power-law) creep regime. Previous geodynamic models [2-4] have assumed a diffusion creep rheology. Based on this data, the assumed rheology is too strong, overestimating the retarding forces of viscous resistance on convection and underestimates the potential for convection.

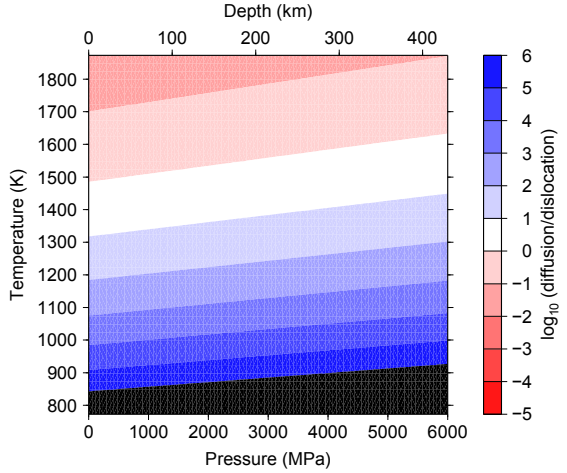

Figure 1: Ratio of diffusion to dislocation creep from [1] using a mineral size of 10 mm and strain-rate of 10^{-17} s^{-1}. Dislocation creep is the weakest mechanism where the ratio is great than 1.

Based on this information, we used the regime diagrams from [5] which delineate the regimes in Rayleigh number/viscosity contrast space where convection should occur. Those plots are shown in Figure 2 below. The region labeled (I) is mobile-lid convection (much like constant viscosity convection), region (III) is stagnant-lid convection, where a thick, stiff lid overlies a convective zone, and region (II) is a transitory region. The region in blue is our estimate of the Rayleigh number and viscosity contrast for Mercury assuming a 600 km thick mantle (as was assumed in [2]) while the region in yellow is our estimate of the Rayleigh number and viscosity contrast for Mercury assuming a 400 km thick mantle. For diffusion creep (Figure 2. right) the thinner mantle shell, estimated using MESSENGER gravity [6] (yellow box) is marginally convecting at best. In the case of power-law (dislocation creep) rheology (Figure 2 right), the regime is in the stagnant-lid convection regime.

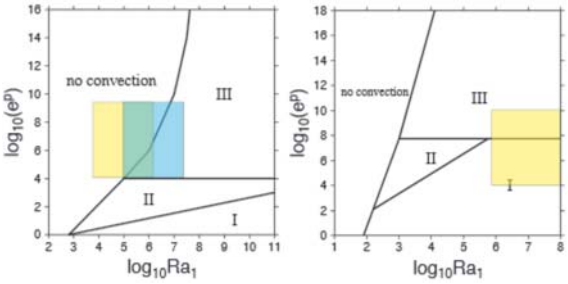

Figure 2: The Rayleigh number/viscosity contrast conditions illustrating where convection occurs for Newtonian (left) and power-law (right) rheology. Area (I) is mobile-lid convection, area (III) is stagnant-lid convection and area (II) is an intermediate state. Figure based on [5]. The blue box is our estimate of Mercury mantle thickness pre-MESSENGER and the yellow box reflects the [6] mantle estimate.

We verify Figure 2 using power-law rheology calculations in 3D spherical shell geometry [7]. For cases with a 450 or even 350 km thick shell, we find convecting solutions using reasonable estimates for Mercury mantle properties with a power-law rheology (Figure 3). This calculation has a 366 km thick silicate shell shown at 4500 Myrs model evolution. Hot upwelling sheets, represented by the orange isosurface, while downwelling sheets (not pictured) form between the upwellings in a linear roll-like pattern. The calculation shown does not include hotlines, decreasing radiogenic heating with time, or a cooling core boundary condition.

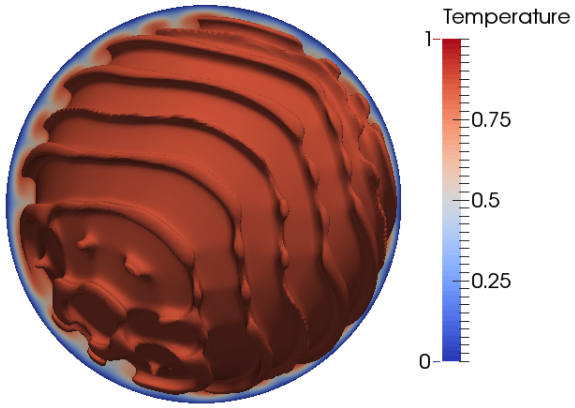

Figure 3: Hot isotherms from convection in 366-km thick spherical shell a power-law fluid from [7].

References: [1] Karato, S. and Wu P. (1993), Science, 260, 771-778. [2] King, S. D. (2008) Nat. Geosci., 1, 229-232. [3] Grott et al. (2011) EPSL, 307, 135-146. [4] Michel et al. (2013) JGR, 118, 1033-1044. [5] Moresi, L. N. and Solomatov, V. S. (1995) Phys. Fluids, 7, 2154-2162. [6] Smith et al. (2012) Science, 336, 214-217. [7] Robertson, S. and King, S. D. (2016), Fall AGU Meeting, DI41A-2615.

CARBON ON MERCURY'S SURFACE – ORIGIN, DISTRIBUTION AND CONCENTRATION. Rachel L. Klima (Rachel.Klima@jhuapl.edu)[1], David T. Blewett[1], Brett W. Denevi[1], Carolyn M. Ernst[1], Scott L. Murchie[1], Patrick N. Peplowski[1], Virange Perera[1] and Kathleen Vander Kaaden[2]. [1]Johns Hopkins University Applied Physics Laboratory, Laurel, MD 20723, USA [2]Jacobs, NASA JSC, Houston, TX 77058, USA.

Introduction: Distinctive low-reflectance material (LRM) was first observed on Mercury in Mariner 10 flyby images [1]. Visible to near-infrared reflectance spectra of LRM are flatter than the average reflectance spectrum of Mercury, which is strongly red sloped (increasing in reflectance with wavelength). From Mariner 10 and early MErcury, Surface, Space, ENvironment, GEochemistry, and Ranging (MESSENGER) flyby observations, it was suggested that a higher content of ilmenite, ulvöspinel, carbon, or iron metal could cause both the characteristic dark, flat spectrum of LRM and the globally low reflectance of Mercury [1,2]. Once MESSENGER entered orbit, low Fe and Ti abundances measured by the X-Ray and Gamma-Ray Spectrometers ruled out ilmenite, and ulvöspinel as important surface constituents [3,4] and implied that LRM was darkened by a different phase, such as carbon or small amounts of micro- or nanophase iron or iron sulfide dispersed in a silicate matrix. Low-altitude thermal neutron measurements of three LRM-rich regions confirmed an enhancement of 1–3 wt% carbon over the global abundance, supporting the hypothesis that LRM is darkened by carbon [5].

Carbon on Mercury: Two explanations for carbon on Mercury's surface had been proposed. The first suggests that carbon could be exogenic, delivered gradually by comets over Mercury's history [6]. The second is an endogenic origin: any carbon that did not partition into the core of the planet would crystallize as graphite, and would have risen to the surface creating a primordial graphite flotation crust [7]. Across the surface of Mercury, LRM shows clear evidence of having been excavated from depth [8–10]. In cases where it is not clearly associated with specific craters, it occurs in patchy spots within broad regions of heavily cratered, ancient terrain where the ejecta from numerous small craters overlap [11–12]. This evidence, from global-scale mapping efforts, supports the hypothesis that this carbon is sourced from the remnants of a magma ocean flotation crust.

Extrapolating the Carbon Content of LRM: In [5], the 600-nm band depth ratio described above was found to correlate with abundance of carbon as measured during low-altitude neutron detector measurements. Although there were only three locations that could be measured, within uncertainty, there is a clear linear relationship between the average ~600 nm band depth for each LRM deposit. Based on the derived band-depth to carbon relationship, we estimated carbon contents for several LRM deposits (Fig. 1). Our results suggest that some regions may contain as much as 5 wt% carbon above the global mean, a value consistent with the carbon content required to produce their low reflectances [9].

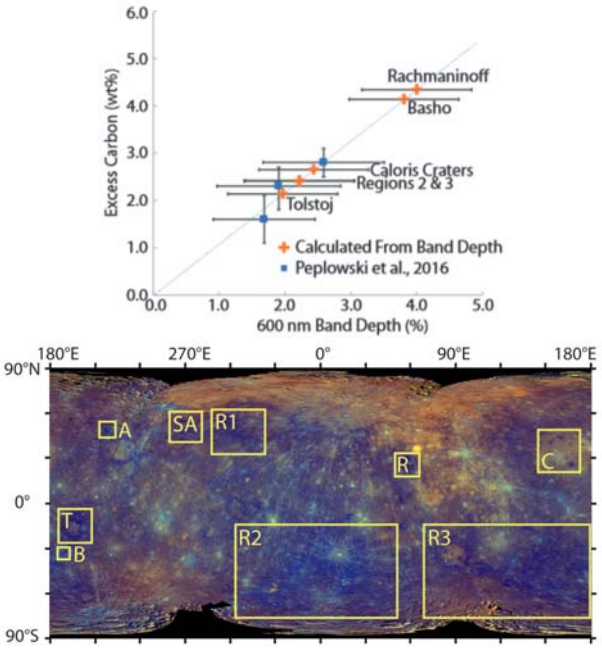

Fig. 1. (top) Extrapolated carbon content for different regions of the surface. Blue squares were measured directly in [5], orange plusses were calculated from the derived band depth relationship. (bottom) Enhanced color composite of Mercury with R=PC1, G=PC2, B=430/1000 nm slope. Locations of LRM-enriched craters measured in [5] A-Akutagawa, SA-Sholem-Aleichem, and R1-region LRM-A are shown, along with derived values for B-Basho, T-Tolstoj, R-Rachmaninoff and C-Craters within Caloris and two additional regional enhancements (R2, R3).

Implications: The geophysical and geochemical implications of the carbon abundances measured from orbit and extrapolated to the planet as a whole are yet to be investigated. For example, if LRM is derived from a graphite flotation crust, what could be forming the hollows that are found in association with LRM? Can we estimate the depth and thickness of the LRM layer? How would a graphite floatation crust have affected the thermal and chemical evolution of Mercury's magma ocean?

References: [1] Hapke, B. et al. (1975) JGR 80, 2431. [2] Robinson, M.S. et al. (2008) Science 321, 66. [3] Nittler, L.R. et al., (2011) Science 333, 1847. [4] Evans, R.G. et al. (2012) JGR 117, E00L07. [5] Peplowski, P.N. et al. (2016) Nat. Geosci. 9, 273-278. [6] Bruck Syal, M. et al. (2015), Nat. Geosci. 8, 352. [7] Vander Kaaden, K.E. and McCubbin, F.M. (2015) JGR Planets 120, 195. [8] Klima, R.L., et al. (2016), LPSC 47, Abstract#1195. [9] Murchie, S.L. et al. (2015) Icarus 254, 287. [10] Ernst, C.M. et al. (2015) Icarus 250, 413. [11] Denevi, B. et al., (2016), LPSC 47, Abstract#1624. [12] Leeburn et al. (2017), LPSC 48, Abstract#1964.

OPEN QUESTIONS ON THE GLOBAL CONTRACTION OF MERCURY.

Christian Klimczak[1] and Paul K. Byrne[2], [1]Structural Geology and Geomechanics Group, Department of Geology, University of Georgia, Athens, GA 30602, USA (klimczak@uga.edu), [2]Planetary Research Group, Department of Marine, Earth, and Atmospheric Sciences, North Carolina State University, Raleigh, NC 27612, USA.

Introduction: Mercury's tectonic history is dominated by global contraction driven by secular planetary cooling, which is expressed on its surface by thousands of thrust fault-related landforms. Although substantial progress has been made on determining the amount, timing, and rate of global contraction [1–3], many unanswered questions remain regarding the temporal aspects of this process, the associated structural styles of faulting, and the interaction of global contraction with other planetary-scale processes.

Timing and rate of global contraction: Given that the planet's extant magnetic field requires a molten core, and so there remains a flow of heat from the interior to the surface, Mercury must be contracting at present. Geologic observations do not confirm that global contraction-induced large-scale thrust faults are presently active [2], but relatively small, well-preserved thrust fault-related landforms probably formed within the past several hundred million years [4]. As the rate of global contraction has likely substantially decreased over time [2], it remains to be determined if shortening from global contraction at a very slow rate is entirely partitioned into weaker regolith materials, as suggested for the Moon [3], or if strain is also accommodated along larger structures that experience periods on the order of tens to hundreds of millions of years of quiescence.

The timing of the onset of global contraction is not yet well understood, in part because Mercury's record of tectonic deformation may date to no earlier than the end of the late heavy bombardment (LHB), and because there is an initial phase of global contraction that is not expressed in the geologic record [2]. Additionally, it has yet to be explored how fast Mercury's early lithosphere cooled relative to the interior. If it initially cooled at a faster rate than the interior, the lithosphere should have undergone extension in a manner similar to thermal contraction of lavas. Such incipient extension has not been substantially investigated for Mercury, however, and any such deformation probably preceded the emplacement of even the oldest surface units now preserved on the planet. Yet the growing body of evidence that Mercury's early history featured voluminous effusive volcanism is consistent with an early phase of rifting, perhaps contraction-induced, with those rifts facilitating the rapid and widespread eruption of flood basalts onto the surface of the planet [5].

Shortening structures: Our earlier distinction of types of shortening structures with respect to terrain, e.g., "smooth plains structure" [1], was motivated by the observation that such landforms often share morphological characteristics that defy traditional classifications such as "wrinkle ridge" or "lobate scarp". The broad morphological variety of these structures has not been sufficiently quantified for Mercury. Therefore, there is as yet no robust characterization of key structural information on thrust system architecture at the surface and in the susbsurface that would further shed light on the strain rates and diversity of structural styles of thrusting on Mercury, or permit their classification in a consistent structural manner.

Tidal despinning: The influence on global contraction of the slowing of Mercury's rotation to its present spin–orbit resonance remains to be fully explored. For scenarios under which despinning occurred early in the planet's history and spanned hundreds of millions of years, or started during or even after the LHB but for a much shorter duration, it is not difficult to imagine it overlapping temporally with global contraction [e.g., 6]. On the other hand, despinning may have been rapid and/or operated only before the LHB. For this process to influence the tectonic pattern Mercury retains today, then, any despinning structures that formed must have been sufficiently deep-seated to survive resurfacing from impact bombardment and effusive volcanism responsible for erasing any of the planet's surface older than ~4.1 Ga [7]. Determining whether or not the perceived ~north–south fabric of Mercury's shortening structures [1,6] is an artifact of solar illumination is also an important objective, as the answer will either update existing models for the planet's tectonic and thermal evolution or call for the formulation of new ones.

Influence of other processes: Assessments of areal strain recorded by shortening structures in the intercrater versus smooth plains may indicate whether stresses from vertical loading have contributed to the formation of landforms found in smooth plains [8]. Similarly, the effects of solar tidal stresses, long-wavelength topographic changes, and thermal stresses from Mercury's spin–orbit resonance on its lithosphere and on its global fault pattern remain largely unexplored.

References: [1] Byrne, P. K. et al. (2014) Nature Geosci., 7, 301–307. [2] Klimczak, C. (2015) JGR, 120, 2135–2151. [3] Crane K. T. & Klimczak, C. (2017) GRL, 44, 3082–3089. [4] Watters T. R. et al. (2016) Nature Geosci., 9, 743–747. [5] Byrne P. K. et al. (2018) this mtg. [6] Klimczak, C. et al. (2015) EPSL, 416, 82–90. [7] Marchi S. et al. (2013) Nature, 499, 59–61. [8] Peterson, G. et al. (2018) this mtg.

FUTURE SEISMIC CONSTRAINTS ON MERCURY'S CORE COMPOSITION. J. S. Knibbe[1,*], S. M. Luginbhuel[1], A. Rivoldini[2], Y. Kono[3], T. Van Hoolst[2], and W. van Westrenen[1], [1]VU University Amsterdam, The Netherlands, [2]Royal Observatory of Belgium, [3]HPCAT, Geophysical Laboratory of the Carnegie Institution for Science, APS, Argonne, Chicago, USA, ([*]j.s.knibbe@vu.nl).

Introduction: Mercury's large core and its associated high metallic iron (Fe) bulk content of 60-80 wt% is difficult to reconcile within the conventional accretion theory of terrestrial planet formation [1]. Although condensates from the early solar nebula close to the Sun may have been hot, reduced and metal-rich [2], protoplanetary collisions are thought to have chemically mixed the inner solar system [3]. Explanations for Mercury's high metal/silicate ratio are that (1) the trend of metal-rich material nearby the Sun was enhanced by additional metal-silicate fractionation mechanisms in early planetary accretion phases [4], (2) after its core-mantle differentiation, large impacts have stripped Mercury from its mantle silicates [5], or (3) Mercury's mantle silicates were vaporized by an early super-luminous (hot) Sun and removed from the planet by solar wind interaction [6]. Each of these theories are associated with some hot and/or reducing event or origin and are therefore problematic in light of the measured high volatile content of Mercury's surface measured by the MESSENGER mission [7]. Planetary formation mechanisms (1) and (2) have been modified to not require extremely high temperatures and still obtain a high metal/silicate ratio for Mercury [8, 9]. However, the high MgO and low FeO surface concentrations of Mercury are consistent with a highly reduced bulk planet [10], such that Mercury's surface chemistry yields mixed-signals as to whether the original formation scenarios are truly refutable.

In contrast to the composition of Mercury's surface, the composition of its core has a simple relation to the conditions during core-mantle differentiation and is more directly linked to the planet's formation history. The most prominent core alloying light element is likely either silicon (Si) if core mantle differentiation occurred under highly reducing conditions, or S if core mantle differentiation occurred under more oxidized conditions [11].

Another important feature of Mercury is its active magnetic field, which low-intensity and broad-scale geometry is likely related to a stable layer in the liquid outer core [12]. The stability of this layer is either caused by a compositionally stratifying Fe-snow process just below the CMB in an Fe-S core [13], or by the absence of compositional convection in an Fe-Si core, such that stability is a direct consequence of sub-adiabatic CMB heat fluxes [14].

The upcoming ESA-JAXA Bepi-Colombo space mission will greatly improve the understanding of Mercury's surface and magnetic field, but a detailed plan for improving constraints on Mercury's formation and the origin of the stably stratified outer-core layer is currently unavailable.

Future seismic measurements can provide compositional constraints on Mercury's core: Ultrasonic P-wave velocities (V_P) of liquid Fe-S alloys have been measured at Mercury's CMB pressures (4.5±0.5 GPa) and show a decrease of V_P with S content [15]. Measurements of V_P trough Fe-Si liquids are only reported at ambient pressure conditions and show an increase of V_P with Si content [16]. At the HPCAT beamline 16-BM-B of the Advanced Photon Source synchrotron facility, Chicago, USA, we have performed V_P measurements through Fe-Si and Fe-S liquids at pressures up to Mercury's CMB pressure, obtaining a dataset to which future seismic V_P measurements of Mercury's liquid core can be compared to constrain its composition. Seismic V_P at similar depths in our Moon have been measured with a accuracy <10% [17]. The difference in V_P for Si-rich and S-rich Mercurian cores exceeds 10%, suggesting that it is likely feasible to place strong bounds on Mercury's core composition by a seismic endeavor. A determination of Mercury's core composition will strongly improve our understanding of terrestrial planet formation and core magneto-hydro-dynamics.

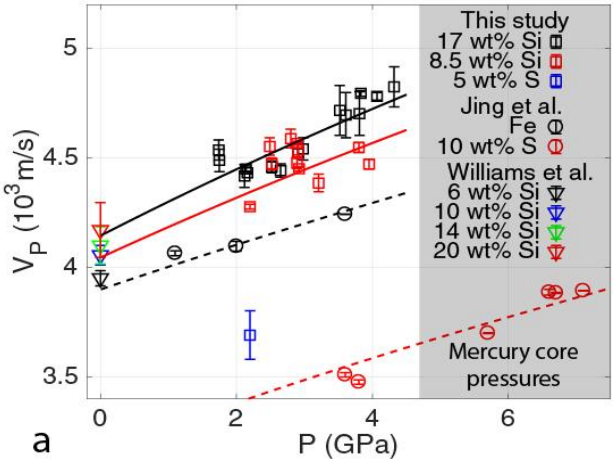

Figure 1: P-wave velocity (V_P) through Fe-rich metallic liquids measured by us (squares) and compared to literature data (other symbols) [15, 16].

References: [1] Urey, H. C. (1951) *GCA, 1*, 209-277. [2] Lewis, J. S. (1972), *EPSL, 15*, 286-290. [3] Lewis, J. S. (1988), *Mercury*, Univ. Arizona Press. [4] Weidenschilling, S. J. (1978), *Icarus*, *35*, 99-111. [5] Benz, W. et al. (2008), *SSSI, 26*, 7-20. [6] Cameron, A. G. W. (1985), *Icarus, 64*, 285-294. [7] Peplowski, P. N. et al. (2011), *Science, 333*, 1850-1852. [8] Wurm, G. et al. (2013), *ApJ, 769*, 1-7. [9] Asphaug, E. and A. Reufer (2014), *Nat. Geosci., 7*, 564-568. [10] Zolotov, M. Y. et al. (2013), *JGR Planets, 118*, 138-146. [11] Chabot N. L. (2014), *EPSL, 390*, 199-208. [12] Christensen, U. R. (2006), *Nature, 444*, 1056-1058. [13] Cao, H. et al. (2014), *GRL, 41*, 4127-4134. [14] Knibbe, J. S., and W. van Westrenen (2018), *EPSL, 482*, 147-159. [15] Jing, Z. et al. (2014), *EPSL, 396*, 78-87. [16] Williams, Q. et al. (2015), *JGR: Solid Earth, 120*, 6846-6855. [17] Lognonné, P. et al. (2003), EPSL, 211, 27-44.

DECAMETER-SCALE REGOLITH TEXTURES ON MERCURY. M. A Kreslavsky[1], A. Yu. Zharkova[2,3], and J. W. Head[4], [1]Earth and Planetary Sciences, University of California – Santa Cruz, Santa Cruz, CA, 95064, USA, mkreslav@ucsc.edu, [2]Moscow State University of Geodesy and Cartography (MIIGAiK), Moscow, Russia, [3]Sternberg Astronomical Institute, Moscow State University, Moscow, Russia, [4]Earth, Environmental and Planetary Sciences, Brown University, Providence RI 02912 USA.

Introduction: The surface of atmosphereless planetary bodies is covered with a layer of regolith, specific fragmental, highly heterogeneous material. Regolith "gardening" processes are responsible for formation of regolith textures seen in the high-resolution images. Here we report our results of the survey of regolith textures on Mercury and compare them to better-known lunar textures.

Survey. We surveyed the highest resolution images (0.7 – 2.5 m/pix sampling) obtained by MDIS NAC camera [2] onboard the MESSENGER orbiter toward the end of the mission (Feb. – Apr. 2015). Individual images are small, have a considerable amount of smear, low signal-to-noise ratio, and do not overlap (cannot be used to produce mosaics); in a sense, they are random samples of surface morphology. We selected and screened ~3000 best images of that data set. These images are scattered in a region delimited by 40 – 70°N and 210 – 320°E and occupied mostly by intercrater plains. To compare hermian and lunar regolith, we extracted similar random set of samples from LROC NAC images [3] and artificially degraded image quality to match MDIS images. Fig. 1 shows examples of MDIS (right) and degraded LROC (left) images.

Degradation of small impact craters: Generally, lunar and hermian surfaces are similar: they are dominated by small impact craters of different sizes (10s and 100s of meters) at different stages of degradation (Fig. 1). For the Moon small craters are thought to be in equilibrium: emplacement of new ones is balanced by obliteration of old ones by regolith gardening. The presence of the whole range of crater degradation stages in each image suggests that the same occurs on Mercury, as expected. The apparent density of discernable craters on Mercury varies from site to site to a great extent, probably, due to the presence of secondary clusters, at least, partly.

Elephant hide texture: It has long been known that on the Moon regolith-covered slopes, both steep and gentle, have a specific subtle dekameter-scale pattern dubbed "elephant hide" or "leathery" texture [e.g., 4-6]. Its origin is unknown; however, it is almost certainly related to regolith transport. On Mercury, such a pattern is typically not observed. On rare occasions we do observe a pattern similar to the lunar elephant hide texture (Fig. 2).

Young features: the majority of decameter-scale topographic features are smooth and subdued due to regolith gardening. Sharp slope breaks, "crisp" morphology and absence of superposed degraded craters indicate geologically young features. In addition to fresh craters, hollows on Mercury [7] are such young features. We see examples of decameter-scale hollows.

Finely-Textured Slope Patches (FTSP) (Fig. 3) are another type of apparently young fresh crisp morphology on Mercury with no, as far as we know, direct lunar analogs. We found a dozen of images with one or more FTSP. FTSP are patches of finely (meter-scale) textured slopes with sharp outlines. FTSP occur amid typical intercrater plains and old impact basins; there are no large young craters or hollows nearby; there are no resolvable albedo or color peculiarities close to FTSP locations. All FTSP examples found are in the southern half of the surveyed region; slopes bearing FTSP have different orientations; however, they avoid north-facing directions; this, however, could be coincidental. FTSP often occur in groups; in this case they occupy slopes of the same orientation. The mechanism of FTSP formation is not clear, it might be a form of regolith avalanches. New data from the upcoming BepiColombo Mission will provide insights into regolith features and processes on Mercury.

References: [1] McKay D. et al (1991) In: *Lunar Sourcebook*, 285. [2] Hawkins S. E. et al. (2007) *Space Sci. Rev. 131*, 247. [3] Robinson M. et al. (2010) *Space Sci. Rev. 150*, 81. [4] Howard K. & Larsen B. (1972) *Apollo 15 PSR*, 25-58 [5] Plescia J. & Robinson M. (2010) *EPSC 2010*, EPSC2010-731. [6] Antonenko I. (2002) *LPS XLIII*, 2581. [7] Blewett D. et al. (2013) *JGR 118*, 1013.

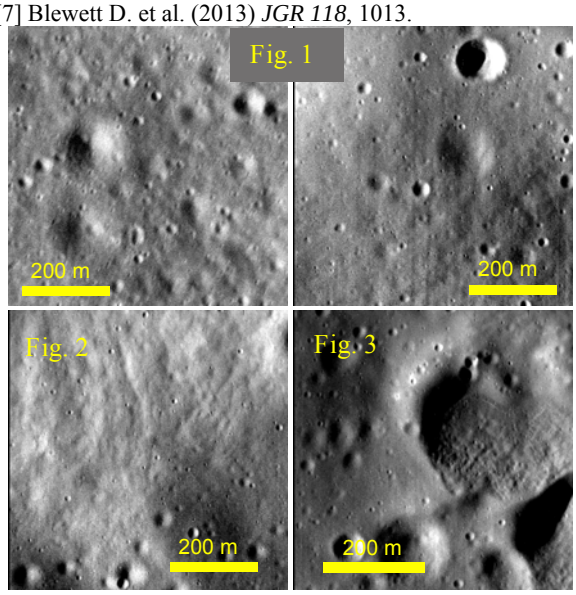

Mercury's exosphere: ground based observations as a support to the forthcoming Bepi-Colombo. F. Leblanc[1] and J. Y. Chaufray[2], [1]LATMOS/IPSL, UPMC Univ. Paris 06 Sorbonne Universités, UVSQ, CNRS, Paris, France (francois.leblanc@latmos.ipsl.fr), [2]LATMOS/IPSL, UVSQ Université Paris-Saclay, UPMC Univ. Paris 06, CNRS, Guyancourt, France (jean-yves.chaufray@latmos.ipsl.fr).

Ground based observations of Mercury's exosphere have provided a very complementary view with respect to satellite observations. As an example, MESSENGER MASCS observations of the sodium exospheric component showed a rather different portrait of this exosphere with respect to ground based observatories [1]. Indeed, a large set of observations of the high latitudes peak in the sodium exosphere have been reported from ground based observations [2] as well as observations of Mercury's sodium tail [3], whereas MESSENGER could not cover properly these regions because of its orbit and the field of view of MASCS [1]. On the other hand, MESSENGER observations reported the discovery of several new exospheric species [4, 5] and provided for the first time the annual variability of the sodium exosphere at the equator [1] highlighting in an unprecedented way its origins.

Whereas ground based observations can be performed regularly during decades [6, 7], they obviously suffer from limited instantaneous field of view and temporal window. However, ground based observations can obtain almost instantaneous 2D picture of Mercury's exosphere [8], perform very high spectrally resolved observations [9, 10], explore new types of observations [11] and might discover the emission from exospheric species not yet observed [12]. 2D imaging of Mercury's exosphere from ground based observations has been shown to be a very original way to map Mercury's exosphere relations with its magnetosphere [13], a technic that might considerably progress in spatial resolution thanks to a new generation of telescopes equipped with adaptive optics.

Both methods of observations of Mercury's exosphere will therefore continue to be very valuable in the forthcoming years. The ESA-JAXA Bepi-Colombo mission to be launched by the end of 2018 should be a renewed opportunity of coordinated ground-based and in situ observations. In particular, Bepi-Colombo will carry a large set of instruments dedicated to the observations of Mercury's exosphere and will be able to observe it from both MPO and MMO satellites with a more extended spectral range, sensibility and spatial coverage than MESSENGER instruments. A two points of view observation of Mercury's exosphere will also allow to better track any short time variability in Mercury's exosphere that might be induced by our Sun.

In this presentation, we will summarize what we believe are the still open questions regarding Mercury's exosphere, highlighting which new topics Bepi-Colombo set of instruments might be able to address with respect to MESSENGER. We will also underline how ground based observations should contribute to further improve our understanding and support MESSENGER and Bepi-Colombo observations.

References:

[1] Cassidy et al.. (2015) *Icarus, 248,* 547-559. [2] Potter et al. (2006) *Icarus, 181,* 1-12. [3] Schmidt et al. (2012) *J. Geophys. Res., 117,* 1-14. [4] Vervack et al. (2010) *Science, 329,* 672-675. [5] Vervack et al. (2016) *Geophys. Res. Lett., 43,* 11,545-11,551. [6] Potter et al. (2007) *Icarus, 186,* 571-580 [7] Leblanc et al. (2010) *Icarus, 209,* 280-300 [8] Baumgardner et al., (2008) *Geophys. Res. Lett., 35,* 1-5 [9] Potter et al. (2009) *Icarus, 204,* 355-367. [10] Leblanc et al., (2010) *Icarus, 223,* 963-974 [11] Lopez-Ariste et al. (2012) *Icarus, 220,* 1104-1111 [12] Bida and Killen (2017), *Icarus, 289,* 227-238 [13] Massetti et al. (2017) *Geophys. Res. Lett., 44,* 2970-2977.

SPECTRAL CLUSTERING AND GEOMORPHOLOGICAL ANALYSIS ON MERCURY HOLLOWS.

A. Lucchetti [1], M. Pajola[1], V. Galluzzi[2], L. Giacomini[2], C. Carli[2], G. Cremonese[1], G. A. Marzo[3], M. Massironi[4] and T. Roush[5]. [1]INAF-Astronomical Observatory of Padova, Vicolo dell'Osservatorio 5, 35131 Padova, Italy (alice.lucchetti@oapd.inaf.it); [2]INAF-IAPS Roma, Istituto di Astrofisica e Planetologia Spaziali di Roma, Rome, Italy; [3]ENEA Centro Ricerche Casaccia, Rome, Italy; [4]Dept. Of Geoscience, University of Padova, Italy, [5]NASA Ames Research Center, Moffett Field, CA 94035, USA.

Introduction: One of the most surprising discoveries revealed by MESSENGER (Mercury Surface, Space, Environment, Geochemistry, and Ranging, [1]) spacecraft was the presence of particular features, called hollows, on the surface of Mercury. These were revealed as shallow irregular and rimless flat-floored depressions with bright interiors and halos, often found on crater walls, rims, floors and central peak [2,3,4] and were named "hollows". These features are located everywhere on the surface of the planet [4] and since they are fresh in appearance, they may be actively forming today via a mechanism that could involve depletion of subsurface volatiles [2,5] whose nature is not known. [6] identified an absorption feature in the photometry of hollows located in center of the Dominici crater (1.38N, 323.5°E) extending from 559 nm to 828 nm and one centered at 629 nm in the south wall/rim hollows of the crater suggesting the presence of MgS or a combination of MgS and CaS. We already applied a spectral clustering technique to characterize in deeper detail the behavior of hollows located in three different craters [7,8]. Our aim is to understand whether there is a similar trend between hollows located in different areas of the planet, and whether a possible correlation exists between spectral behavior of hollows and geomorphological units.

Dataset: We chose three different craters hosting hollows: (i) the **Dominici crater** (1.38N, 323.5°E, Kuiper quadrangle) with a diameter of 20 km, selected due to previous different spectral detection [6]; (ii) an **unnamed crater** (25.62°N, -3.4°W, Victoria quadrangle) with a diameter of 25 km; (iii) the **Velazquez crater** (37.74°N, 304.77°E, Victoria quadrangle) with a diameter of 128 km. For each crater the following WAC dataset was used:

-Dominici crater: dataset with a scale of 935 m/px through eight filter ranging from 0.433 to 0.996 μm;

-Unnamed crater: dataset with a scale of 265 m/px through eleven filter ranging from 0.433 to 1.012μm.

-Velazquez carter: dataset with a scale of 260 m/px through eleven filter ranging from 0.433 to 1.012μm.

Methodology and Results: We applied a spectral clustering technique based on a K-mean algorithm that allow us to separate in clusters our studying area, and characterized each one by an average multi-color spectrum and its associated variability (Fig. 2). We applied radiometric and photometric correction to all images using the ISIS3 image processing package of the USGS. The spectral clustering method has been already reported in [7,8].

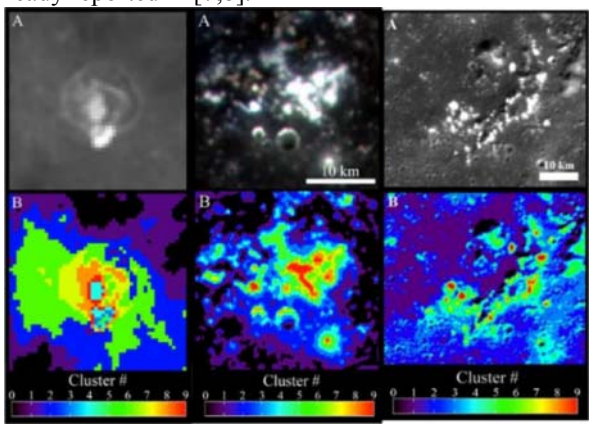

Fig. 2. *A:WAC reference images (EW0210848973D) (EW1017269227D) (EW1020781879D) for Dominici, unnamed and Velazquez crater respectively. B: The relative 10 clusters identified in the MDIS datasets.*

From clusters spectra [7,8] we discriminated areas with a possible diagnostic absorption indicative of sulfides in correspondence of hollows location in all craters (e.g. MgS as suggested by [6]).

In addition, in order to assess the powerful of our clustering method, we performed detailed geomorphological maps of the craters under study to make a comparison with the spectral clustering results. This strengthens the powerful of our method since the application of the clustering technique exhibits a spatially coherent distribution between clusters and the detailed geomorphology, as shown below for the Dominici crater case.

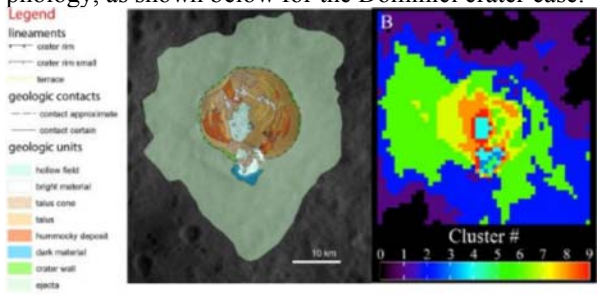

Acknowledgments: This activity has been realized under the BepiColombo ASI-INAF contract no.I/022/10/0.

References: [1] Hawkins, S. E. et al. (2007), *Space Sci. Rev.*, 131, 247-338 [2] Blewett D. T, et al. (2011) Science, 333, 1856–1859. [3] Blewett D. T. et al. (2013) JGR Planets, 118, 1013-1032. [4] Thomas R. J. et al. (2014), Icarus, 229, 221–235. [5] Vaughan W. M. et al. (2012) LPSC, 43, abstract 1187. [6] Vilas, F. et al. (2016), GRL, 43, 1450-1456. [7] Lucchetti, A. et al., (2017), LPSC 2017. [8] Lucchetti, A. et al., (2017), EPSC 2017.

POTENTIAL IDENTIFICATION OF SUBLIMATION-DRIVEN DOWNSLOPE MASS MOVEMENT ON MERCURY. C.C. Malliband[1], S.J. Conway*[2], D.A. Rothery[1], and M.R. Balme[1], [1]School of Physical Sciences, The Open University, Milton Keynes, MK7 6AA, UK (chris.malliband@open.ac.uk), [2]CNRS, LPG, Université de Nantes, France (susan.conway@univ-nantes.fr) *presenting author

Introduction: Mass movement has been recognised on many solar system bodies. Evidence of mass movement on Mercury has previously been limited to a single documented example, found in the pyroclastic vent NE of Rachmaninoff crater. Here we present the identification of a second example in a small, recent impact crater, ≈285 km north of Nabokov.

Mass movement at NE Rachmaninoff Vent: Attention was drawn to the slope features in the NE Rachmaninoff vent (Fig. 1) on the MESSENGER website, but so far as we are aware there has been no formal study. The features are downslope erosion-deposition systems with an alcove at the head, chute and a fan at the base. Feature heads appear to develop in a stratigraphic layer of brighter material (Fig. 1B). This brighter material appears to be related to hollows [1].

Slope features in unnamed crater (≈285 km N of Nabokov): The newly identified slope features are in a ≈12 km diameter simple impact crater. The crater is surrounded by low reflectance material and has an area of hollows on the NE crater rim. The slope features start just below the crater rim, in a bright stratigraphic layer. This may be similar to the hollow forming layer in NE Rachmaninoff.

Current work: We are examining other areas with steep slopes and catalogued hollows, and are performing a global survey to identify any further examples. We will compare the topography of these features to erosion-deposition systems on Mars [2,3] and Vesta [4]. Our working hypothesis is that these downslope movements are caused by sublimation.

References: [1] Blewett D.T. et al. (2011) *Science, 333*, 1856–1859. [2] Conway S.J. et al. (2015) *Icarus*, *253*, 189–204. [3] Brusnikin E.S. et al. (2016) *Icarus*, *278*, 52–61. [4] Scully J.E.C. et al. (2015) *EPSL*, *411*, 151–163.

Acknowledgements: This work is partially supported by the CNES, in preparation for BepiColombo.

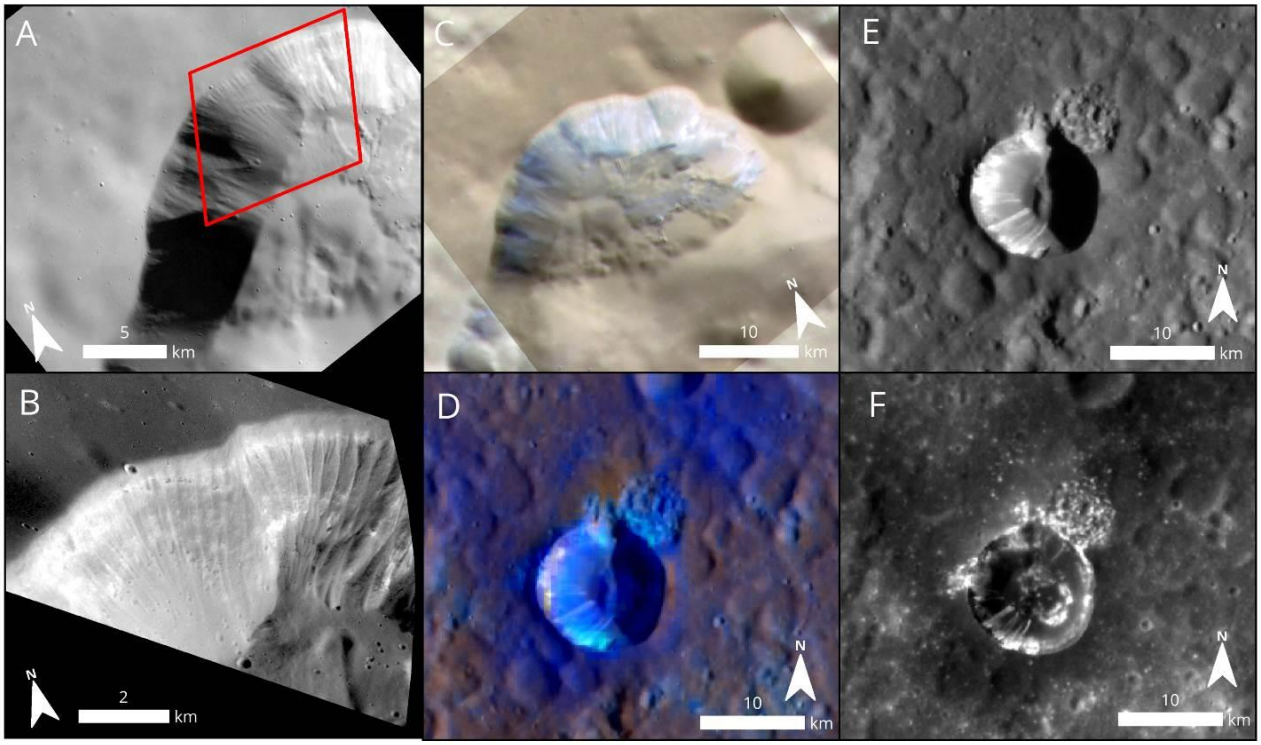

Fig. 1: A,B,C Gully-like slope features in vent NE of Rachmaninoff. A:Context image centered on 36°N, 63.8°E showing widespread slope features. Box shows location of B. (NAC: EN1003843866M) B: High resolution (6.4m/pixel) image showing source at bright layer (NAC: EN1028933034M) C: Enhanced color. D, E, F. Newly discovered slope features at 8°S, 55°E. D, enhanced color; E, high incidence angle (NAC: EN0252295266M) F, low incidence angle. Note bright, possibly hollow forming, material, high in crater wall (NAC: EN1028933034M).

1:3M GEOLOGICAL MAPPING OF THE DERAIN (H-10) QUADRANGLE OF MERCURY. C.C. Malliband[1], D.A. Rothery[1], M.R. Balme[1], and S.J. Conway[2], [1]School of Physical Sciences, The Open University, Milton Keynes, MK7 6AA, UK (chris.malliband@open.ac.uk), [2]CNRS, Laboratoire de Planétologie et Géodynamique, Université de Nantes, France

Introduction: We are currently undertaking detailed (1:3M) geological mapping of the Derain (H-10) quadrangle of Mercury. This is as part of a coordinated European project to produce a complete set of geological maps [e.g. 1,2,3,4,5] in advance of BepiColumbo's arrival at Mercury. This mapping will aid mission planning and provide scientific context for Bepi-Colombo observations.

Data and Methods: The map is being produced in ArcGIS 10.5 using data from NASA's MESSENGER mission. Mapping is being conducted principally using the 166 m/pixel (meters per pixel) BDR mosaic. This is complemented by a range of other MESSENGER products, in particular: Enhanced Colour (665 m/pixel), low incidence mosaics and the Global DEM (665 m/pixel). Features of particular interest are also investigated using individual frames from MESSENGER's Narrow Angle Camera. As the map is intended for publication at 1:3M, line work is being prepared principally at 1:300k in line with prior work [e.g. 1]. We are also mapping an extra 5° border beyond the Derain Quadrangle to allow better integration with adjoining maps.

Units: We aim to produce mapping that complements other geological mapping underway. This includes mapping crater degradation with both the 3-Class degradation scheme [1] (as shown in Figure 1) and the 5-Class degradation scheme [6].

Plains Units: The Derain quadrangle has a complex plains morphology, with numerous examples of small-scale smooth plains [7] and areas that do not easily classify as smooth or intercrater plains [8]. We are working to find a method to adequately display the visible geological relationships in these areas.

Progress and Ongoing Work: We have completed mapping large scale plains units and most crater ejecta in the north eastern portion of the quadrangle. Plains mapping will probably be updated to ensure the best representation of complex areas. We are continuing work to extend crater classification and ejecta mapping.

References: [1] Galluzzi V.et al, (2016), J. Maps, 12, Sup1, 227-238. [2] Mancinelli P. et al, (2016), J. Maps, 12, Sup1, 190-202. [3] Wright J.et.al, (2018) LPSC 49, #2164. [4] Guzzetta L. et al. (2017) J. Maps, 13.2, 227-238. [5] Pegg D. L. et al., this volume. [6] Kinczyk M. J. et al. (2016) LPS XLVII, #1573. [7] Malliband C.C., this volume. [8] Galluzzi V. et al., this volume.

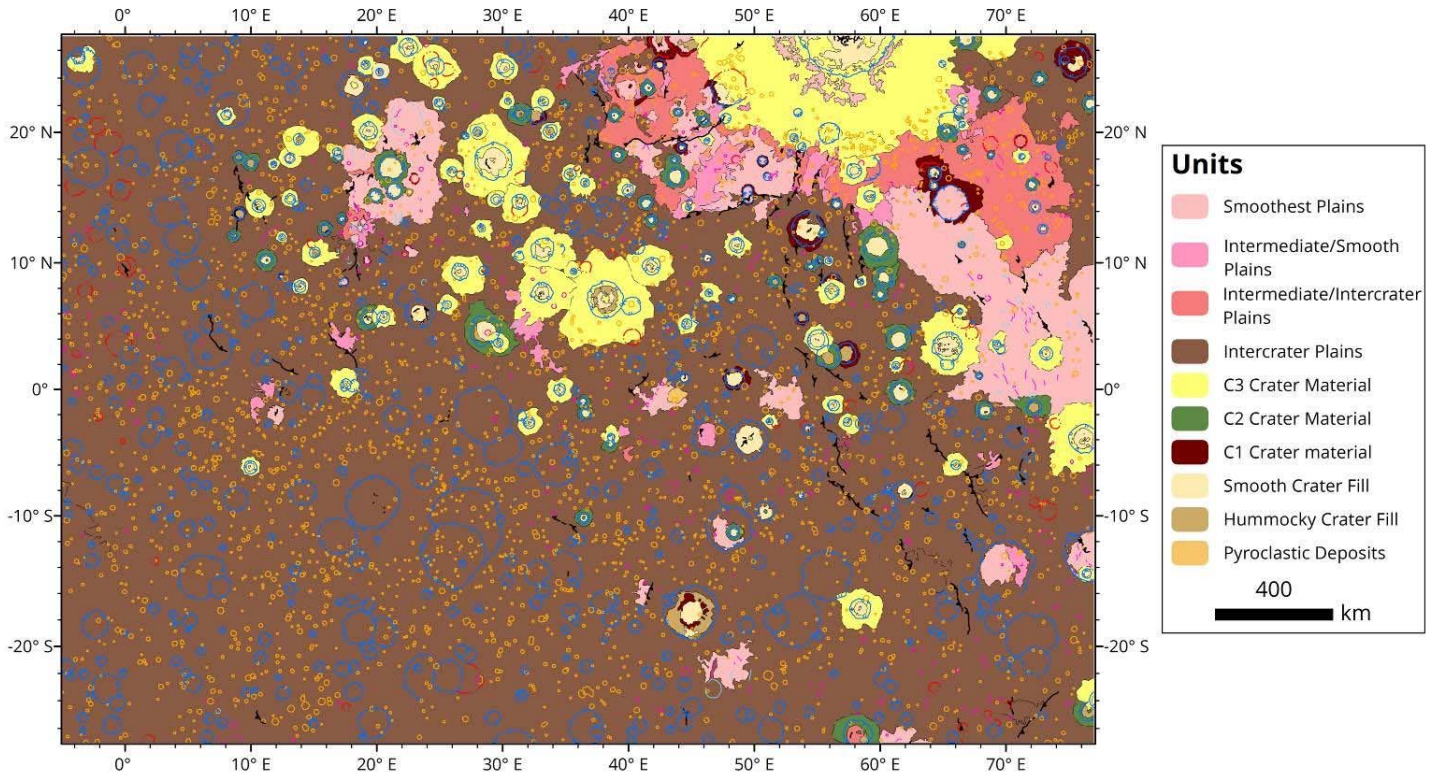

Fig 1. Working map (incomplete) of Derain quadrangle showing 3 class crater degradation scheme

SMALL SMOOTH UNITS ('YOUNG' LAVAS?) **ABUTTING LOBATE SCARPS ON MERCURY.**
C.C. Malliband[1], D.A. Rothery[1], M.R. Balme[1], and S.J. Conway[2], [1]The Open University, Milton Keynes, UK (chris.malliband@open.ac.uk), [2]CNRS, LPG, Université de Nantes, France

Overview: Elaborating the history of magmatism and tectonism at the surface of Mercury is vital to fully understand the planet's geological history. Current thinking has linked the end of large scale magmatism to global cooling and contraction. In the process of mapping the Derain (H-10) quadrangle of Mercury we have found small (<15000 km^2) patches of smooth plains units, often abutting against contractional tectonic features. This suggests some magmatism was not solely limited to impact basin interiors after the onset of global contraction.

Background: Magmatically derived units on Mercury are typically classified principally on the basis of their geomorphology [1,2]. Younger units are generally smooth and relatively uncratered, whereas more ancient units are more heavily cratered and textured. Lobate scarps and wrinkle ridges are widely recognized to be surface expressions of contraction faults linked to Mercury's global contraction [3].

Mercury has many large areas of smooth plains, thought to have been emplaced at around 3.7–3.9 Ga [2]. A contractional stress regime makes it hard for eruption pathways to remain open, inhibiting prolonged large-scale eruptions. Current thinking suggests large scale effusive volcanism ceased at around 3.5 Ga [4] at the start of global contraction. Previously the only younger smooth units identified have been restricted to medium-small impact basins [5] and impact melt [2]. This work is the first to document units outside impact basins that clearly postdate global contraction.

Examples found: We have found multiple examples of ponding at lobate scarps, and these examples outcrop with a small number of styles. The clearest examples are those that show deep ponding, evidenced by very smooth topography with little or no trace of the underlying landscape, directly abutting against a lobate scarp and superposing terrain with a notably more cratered texture. This is illustrated in Figure 1 which shows the example at Calypso Rupes. This is the most common type we have so far identified. Other examples do not show such deep magma flooding but show subdued, 'ghost-craters', indicating a thinner layer of lava (10-100s m vs many 100s m of flooding). Other examples show 'humpbacks' of cratered areas of higher topography caused by lobate scarps with smoother plains occurring on either side. Very few topography-forming processes occur on Mercury and elevated ridges are almost all fault controlled, suggesting these units formed after the onset of global contraction. The ponding examples found are geographically widespread and do not show any clear pattern of distribution. All are small in area (<15 000 km^2).

Other small scale smooth patches were noted by [1], but were not studied in detail. Our mapping has identified more than 5 examples of isolated smooth patches, remote from any identified fault features. We are studying these to complement studies of smooth patches abutting faulting.

Emplacement: We aim to examine how emplacement of these smooth patches occurred. As ponding examples are found abutting against fault scarps, it is possible that faults may have provided pathways for magma movement. It is also possible that temporary stress relief after fault movement allowed reactivation of existing magma pathways

References: [1] Whitten J. L. et. al. 2014 Icarus 241, 97–113 [2] Denevi B. W. et al. 2013. JGR-Planets. 118, 891–907. [3] Byrne P. K. et. al. 2014. Nature Geosci. 7, 301–307 [4] Byrne P. K. et. al. 2016. GRL, 2016GL069412 [5] Wright J. et. al. 2017. 48th LPSC, #2239

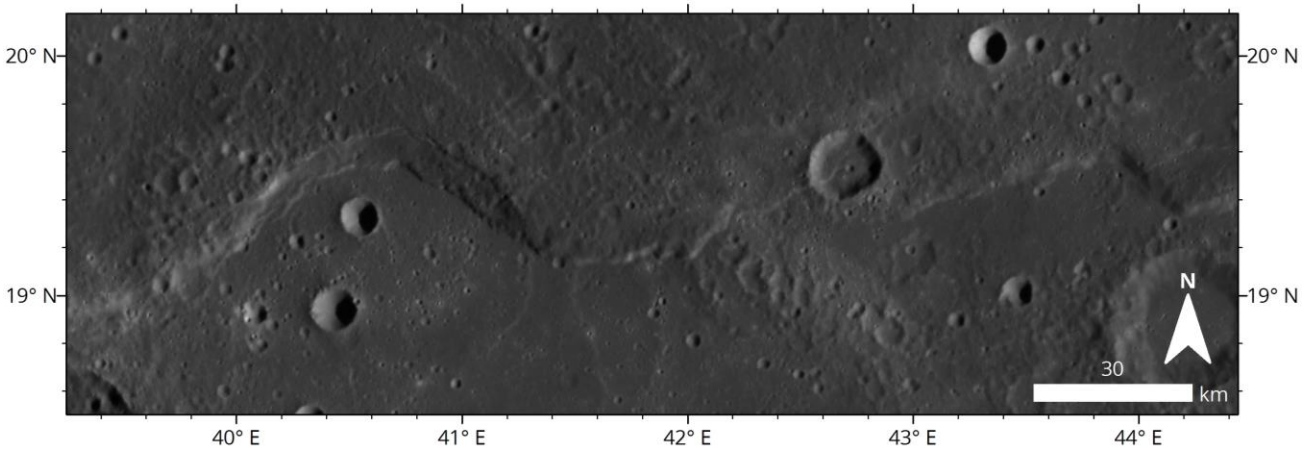

Fig 1: Calypso Rupes. Note the more heavily cratered surface on the hanging wall (north) and smooth plains abutting against the scarp.

A SPECTRAL LIBRARY OF EMISSIVITY SPECTRA FOR MERTIS ON BEPICOLOMBO. A. Maturilli[1], J. Helbert[1], I. Varatharajan[1], M. D'Amore[1], H. Hiesinger[2] [1]Institute for Planetary Research, German Aerospace Center DLR, Rutherfordstr. 2, 12489 Berlin, Germany – alessandro.maturilli@dlr.de, [2]University of Münster, Germany.

Introduction: MERTIS (MErcury Radiometer and Thermal infrared Imaging Spectrometer) onboard the ESA/JAXA BepiColombo mission is designed to identify rock-forming minerals, and to study the surface temperature variations in the hot environment of Mercury. At Planetary Spectroscopy Laboratory (PSL) we are building a spectral library of emissivity measurements for a large range of Mercury surface analogues in the MERTIS spectral range (7-14 µm) for temperatures from 100°C to >400°C.

PSL Set-up: A vacuum Fourier-Spectrometer featuring gold-coated mirrors is attached to an external vacuum chamber to measure the emissivity of solid and granular samples. Sample targets are heated using an induction system and stainless steel cups to reach temperatures from 320K up to 900K. Temperature sensors and a webcam allow monitoring the sample and its surroundings [1,2,3,4].

Mercury analogues collection: MESSENGER's X-Ray, Gamma-Ray, and Neutron Spectrometers [5] show that average surface composition falls close to the komatiite–boninite boundary. Mercury surface seems to be mainly composed of Mg-rich orthopyroxene and plagioclase, with lesser amounts of clinopyroxene, sulfides, olivine, and silica. Our current collection of analogues contains olivine, enstatite, labradorite, augite, komatiite (see [6]), tektite, anorthoclase, bytownite, L-chondrite, albite, hypersthene, diopside, quartz, nepheline, graphite, lunar simulant JSC-1A, and many sulfides (described in [7]).

Emissivity Measurements: Mercury's regolith is mostly composed of very fine particles, therefore we selected the <25µm fraction for our samples. Temperature sensors are put in contact with the sample cup and surface, to monitor its heating. Each sample is slowly heated under vacuum to reach 100°C, 200°C, 300°C, and 400°C, simulating different insulation properties (time of day and/or latitude) on Mercury's surface.

Spectral Collection: In the MERTIS spectral range many diagnostic features can be identified. Their evolution with temperature was already described in previous publications [3,8,9,10,12]. Here we show the emissivity spectra for 2 samples of our collection: komatiite (Fig.1), and olivine (Fig. 2), both in the size fraction <25µm. We notice variations in the position and shape on the CF (emissivity maxima) below 9 µm, in the shape of the Reststrahlen band (9-11 µm), and in that of the Transparency region (around 12 µm) for the 2 samples, and the temperature dependence of some of them (olivine Reststrahlen bands [9,10]).

Conclusions: MERTIS is the first spectrometer to observe Mercury in the TIR range (7-14 µm). Here diagnostic spectral features are T-dependent to a varying degree, therefore influenced by local insolation.

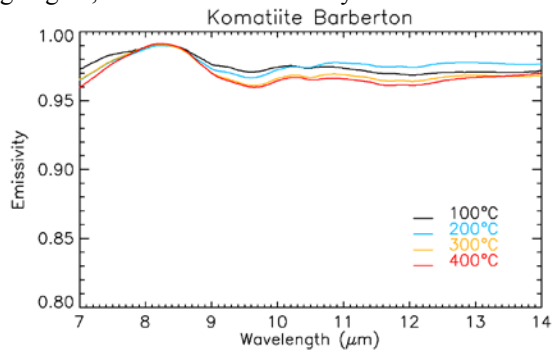

Figure 1. Emissivity spectra for a Barberton komatiite.

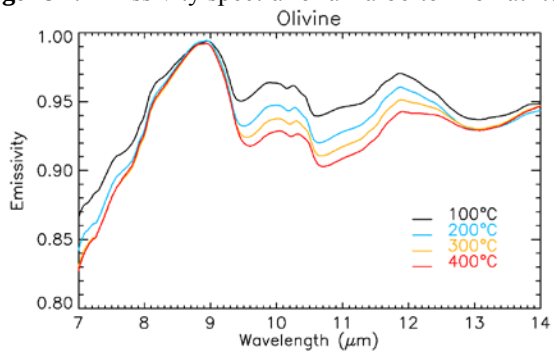

Figure 2. Emissivity spectra for an olivine ($Fo_{\#89}$).

At PSL we measured emissivity spectra in vacuum for a suite of Mercury surface analogues for temperatures from 100°C to >400°C. The spectral library is completed by reflectance measurements on samples fresh and post-heating (0.2 to 200 µm spectral range).

References: [1] Maturilli A. and Helbert J. (2006) PSS 54, 1057-1064. [2] Maturilli A. Helbert J. and Moroz L. (2008) PSS 56, 420-425. [3] Helbert J. and Maturilli A. (2009) EPSL 285, 347-354. [4] Maturilli A and Helbert J. (2014) JARS 8. [5] Vander Kaaden K. et al. (2016) doi: 10.1016/j.icarus.2016.11.041 [6] Maturilli A. et al. (2014) EPSL 398, 58-65. [7] Varatharajan I. et al. (2018) this meeting. [8] Logan L. M. and Hunt G. R. Hunt (1970), JGR 75, 6539-6548. [9] Henderson B. G. and Jakosky B. M. (1997) doi:10.1029/96JE03781. [10] Helbert J. et al. (2013) doi:10.1016/j.epsl.2013.03.038. [11] Helbert et al. (2018) this meeting. [12] Ferrari, S. et al. (2014) American Mineralogist 99(4), 786-792.

THE CRUST OF MERCURY AFTER THE MESSENGER GRAVITY INVESTIGATION. E. Mazarico[1], A. Genova[2], S. Goossens[3], G. Neumann[1], D. E. Smith[2] and M. T. Zuber[2], [1]NASA Goddard Space Flight Center, Code 698, Greenbelt, MD 20771, USA (email: erwan.m.mazarico@nasa.gov), [2] Department of Earth, Atmospheric and Planetary Sciences, Massachusetts Institute of Technology, Cambridge, MA 02139-4307, USA, [3]Center for Research and Exploration in Space Science and Technology, University of Maryland Baltimore County, Baltimore MD, USA.

Introduction: One of the main objectives of the NASA MErcury Surface, Space ENvironment, GEochemistry, and Ranging (MESSENGER) mission [1] was to better understand the interior structure of Mercury from core to crust, through geophysical measurements of the gravity field [2] and planetary shape [3-4]. Prior to its arrival at Mercury, ground-based radar measurements of a large longitudinal libration amplitude [5] revealed the decoupling between the crust and the innermost layers, indicative of a molten core [6]. Analysis of the radio tracking data acquired by MESSENGER in orbit constrained the long-wavelength gravity field [7] and helped improve our knowledge of the interior structure [8]. We recently analyzed the entire radio tracking dataset (including the last year with periapsis altitudes down to ~25 km) using a new methodology that co-integrates and co-estimates the orbits of Mercury around the Sun and MESSENGER around Mercury [9]. This work led to important advances in heliophysics and fundamental physics [9], and also showed the first evidence for an inner solid core [10]. Here, we present the measured gravity field (HgM008) and the resulting crustal thickness model.

Gravity Field: The gravity field was represented with spherical harmonics up to degree and order 100. We used the NASA GSFC GEODYN II orbit determination and geodetic parameter estimation software [11] to iteratively integrate the equations of motion and process the radio tracking data so as to minimize the residuals between observed and modeled observations. The ~4 years of orbital data were split into ~1500 arcs, each converged separately but combined for the final inversion of the gravity parameters. The outcome is higher-fidelity than previous solutions thanks to the better-determined Mercury ephemeris, in particular showing almost none of the 'striping' which characterized previous solutions that made use of the end-of-mission low-altitude passes. The free-air anomalies computed from the gravity field are shown in Figure 1. The resolution over the southern hemisphere is limited by the highly elliptical MESSENGER orbit with northern latitude periapses, but the long-wavelength features associated with topographic structures (e.g., Debussy near 20-70°E and Tolstoj near 210-240°E) appear as free-air anomalies. In the north, many small-scale craters are clearly resolved, such as Strindberg, Ahmad Bada, Verdi, and Brahms which stand out as negative anomalies surrounded by positive anomalies. We find gravity-topography correlations markedly improved in many regions compared to our previous solution (HgM007B, on the PDS Geosciences node).

Crustal Thickness: Following recent results at the Moon [12-13] and Mars [14], we computed the gravity expected from the topographic relief assuming a crustal density of 2800 kg/m^3. After subtracting this Bouguer correction from the measured free-air signal, we obtain the Bouguer anomalies which we can interpret via an Airy model as crustal thickness variations, assuming a crust-mantle density contrast (400 kg/m^3) and an average crustal thickness (35 km) [15-16].

Conclusions: A new analysis of the MESSENGER radio tracking data yielded an improved gravity solution with implications for the structure of Mercury's crust. We will present and interpret these results.

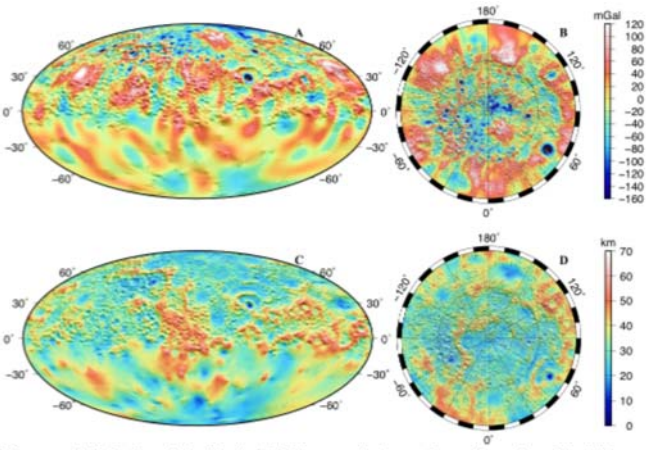

Figure 1. Mollweide (left, 0°E in center) and north polar (right) projections of free-air gravity anomalies (top, in mGal) and crustal thickness (bottom, in km) derived from our new gravity field solution, HgM008.

References: [1] Solomon et al. (2007), SSR, 131, 3. [2] Smith et al. (2012), Science, 336, 6078. [3] Perry et al. (2015), GRL, 42, 6951. [4] Philips et al. (2018), chapter in Mercury book, Cambridge University Press. [5] Margot et al. (2007), Science 316, 710. [6] Margot et al. (2012), JGR, 117. [7] Mazarico et al. (2014), JGR, 119, 2417. [8] Hauck et al. (2013), JGR, 118, 1204. [9] Genova et al. (2018), Nature Comm., 9, 289. [10] Genova et al. (2018), submitted. [11] Pavlis et al. (2013), SGT Inc. report. [12] Zuber et al. (2012), Science, 339, 668. [13] Wieczorek et al. (2012), Science, 339, 671. [14] Goossens et al. (2017), GRL, 44, 15. [15] Padovan et al. (2015), GRL, 42 . [16] James et al. (2015), JGR, 120.

GRAIL AT MERCURY: COHERENT LASER TRACKING FOR GEOPHYSICS. E. Mazarico[1] , S. Goossens[2], A. Genova[3], X. Sun[1], and G. Yang[1], [1]NASA Goddard Space Flight Center, Greenbelt, MD (erwan.m.mazarico@nasa.gov); [2]Center for Research and Exploration in Space Science and Technology, University of Maryland Baltimore County, Baltimore MD, USA; [3]Department of Earth, Atmospheric and Planetary Sciences, Massachusetts Institute of Technology, Cambridge, MA.

Introduction: Knowledge of the interior structure of planets is important to study the formation and evolution of the solar system, and recent developments in SmallSat technology are opening up opportunities to study various planetary bodies. While the GRAIL mission [1], a unique dedicated planetary gravity mission, was very successful and revolutionized lunar science, it cannot easily be replicated at other bodies due to size, mass, and cost. We are developing a Compact Coherent Laser Ranging (CCLR) technology to enable high-accuracy gravity mapping with SmallSats at other planetary bodies, in particular the planet Mercury.

Mercury plays a key role as an end member of terrestrial planet formation which was emphasized in the NRC Planetary Science Decadal Survey [2]. Indeed, although the gravity field of Mercury was observed from radio tracking of the MESSENGER spacecraft during its orbital mission between 2011 and 2015 [3-5], the low spatial resolution is not sufficient to answer many key questions about the planet's thermal and tectonic history, the impact formation processes, and the state of the crust. The joint ESA-JAXA Bepi-Colombo mission due for launch in late 2018 will strive to address these. However, measurements that would significantly improve gravity field resolution will not be possible with BepiColombo [6].

Optical Tracking: Our technology enables similar satellite-to-satellite tracking (SST) gravity missions similar to GRAIL (Figure 1), but at optical wavelength, with better precision and significantly smaller resources required [7]. As demonstrated at Earth and the Moon, SST can provide global, near-uniform coverage, well suited to further geophysical and geological studies, and our compact innovative technology will enable such a mission to be undertaken at Mercury, and beyond. We are currently developing CCLR, taking advantage of the technological progress in the telecommunication industry, and leveraged internal funding to demonstrate our approach's feasibility in the lab.

Objectives: More accurate gravity data are needed to advance our understanding of Mercury's internal structure on a par with the Moon after GRAIL, and thus better gauge the influence of key parameters in planetary evolution. As such, our science objectives, enabled by CCLR, are to: (1) Determine the thermal evolution of Mercury's lithosphere and crust; (2) Understand impact formation and subsequent modification; (3) Characterize the deep interior.

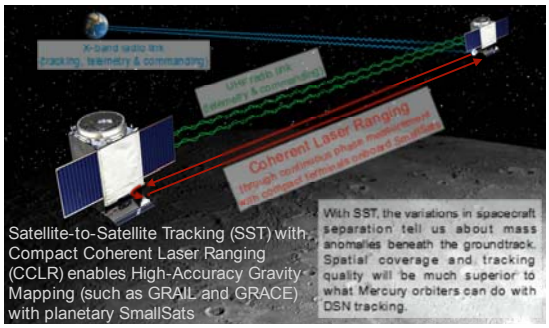

Fig. 1. Illustration of SST measurement concept.

Mission Concept: Two SmallSat will be placed in a stable 200-km orbit. The master spacecraft will be tracked from Earth and CCLR terminals onboard each will provide the science measurements. To achieve these goals, a range-rate accuracy of 0.03 μm/s is required (Fig. 2), vs. the CCLR accuracy (0.014 μm/s).

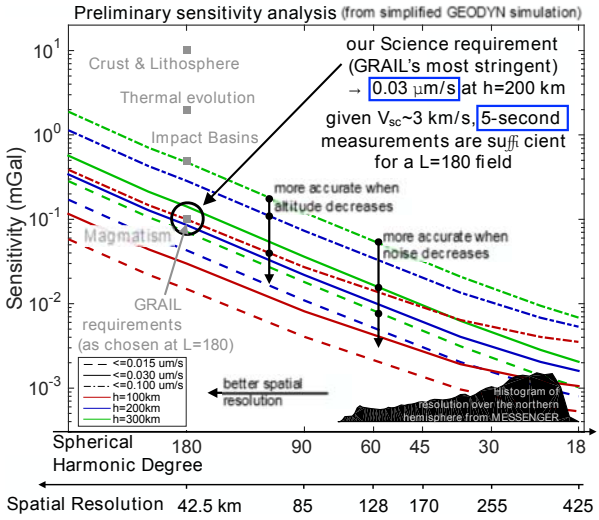

Fig. 2. Simulated gravity recovery vs resolution.

Summary: Some important questions are left unanswered after MESSENGER, and new ones are raised given our deeper knowledge of Mercury. Better gravity is a critical dataset for such future studies, and CCLR is an optical SST transponder technology that will allow SmallSats to execute such a mission at lower cost.

References: [1] Zuber et al. (2012), SSR, 178. [2] Squyres et al. (2011), NRC. [3] Smith et al. (2012), Science, 335. [4] Mazarico et al. (2014), JGR, 119. [5] Verma and Margot (2016), JGR, 121. [6] Iess et al. (2009), Acta Astron., 65. [7] Yang et al. (2016), 2016 IEEE Aerospace Conference.

First evidence connecting Mercury's magnesium exosphere to the regional composition of Mercury's surface from MESSENGER observations. A. W. Merkel[1], R. J. Vervack Jr.[2], T. A. Cassidy[1], R. M. Killen[3], W. E. McClintock[1], L. R. Nittler[4], and M. H. Burger[5], [1]Laboratory for Atmospheric and Space Physics, University of Colorado, 3665 Discovery Dr., Boulder, CO 80303, USA (aimee.merkel@colorado.edu); [2]The Johns Hopkins University Applied Physics Laboratory, Laurel, MD 20723, USA; [3]NASA Goddard Space Flight Center, Code 695, Greenbelt, MD 20771, USA; [4]Department of Terrestrial Magnetism, Carnegie Institution of Washington, Washington, DC, USA; [5]Space Telescope Science Institute, Baltimore, MD 21218, USA

Introduction: Mercury's near-surface exosphere is comprised of volatile and refractory species that are released from Mercury's surface through several production mechanisms. As magnetospheric and solar wind ions, dust particles, and photons impact the surface of Mercury, atoms and molecules are released into the exosphere, implying a link between the exospheric composition and surface geochemistry. However, observational evidence demonstrating a direct link between the exosphere and the underlying surface composition has been elusive. We have conducted a search for such a link by comparing magnesium (Mg) exosphere observations from MESSENGER's MASCS-UVVS instrument to Mg/Si composition maps from XRS. Our results reveal a direct connection between the distribution of Mg in the exosphere and the regional distribution of Mg on Mercury's surface.

Overview: Although it is understood that Mercury's surface supplies neutral atoms to the exosphere, there has been no evidence showing that the spatial variability of the surface composition is an important driver in the distribution of a species in the exosphere. However, the revelation from XRS measurements of a large geochemical terrane in the northern hemisphere that is rich in Mg [1] motivated a search to determine if there is a link between the Mg surface distribution to the distribution of Mg in the exosphere.

Merkel et al. [2] described the spatial and temporal variations of Mercury's dayside Mg exosphere. Mg is highly seasonal with a predominant enhancement of emission, and thus production, in the morning near perihelion. The characteristic temperature of ~6000 K (inferred from the dayside limb scans), along with a morning enhancement, points to a predominant ejection process characteristic of micrometeoroid impact vaporization. We therefore focused our study on the dawn Mg observations where the production is highest.

Because of Mercury's 3:2 spin-orbit resonance, dawn has an equatorial hot pole at 90º and 270º longitude that rotates 180º with respect to the Sun every other year. This has the effect that the UVVS observes over the same geological features every other year. After careful screening and characterization of the Mg observations it was revealed that the dawn Mg emission is enhanced every other Mercury year, implying that the enhancement could be connected to surface variability. By mapping the location of UVVS measurements onto the XRS Mg/Si composition map, it was further revealed that Mg emission is enhanced up to 30-40% when observed over the Mg-rich terrane. The production rate is also enhanced by 30-40% near the Mg surface reservoir; however, the characteristic temperatures remain near 6000 K with little year-to-year variation. Because the production rate variations are linked to the surface composition and a single source temperature is indicated regardless of geographic location, the Mg distribution appears to be controlled by a single dominant source process: micrometoroid impact vaporization. This result shows for the first time that the surface composition is directly related to the spatial distribution of the Mg exosphere.

Acknowledgements: This work is supported by NASA's Discovery Data Analysis Program.

References: [1] Weider S. Z. et al. (2015) Earth Planet. Sci. Lett., 416, 109-120. [2] Merkel A. W. et al. (2017) Icarus, 281, 46.

RADON OUTGASSING FROM THE SURFACE OF MERCURY EVIDENCED BY ITS LOW TH/U RATIO.

P.-Y. Meslin[1], P. Peplowski[2], G. Deprez[1], [1]Institut de Recherche en Astrophysique et Planétologie (IRAP), UPS/CNRS/CNES, Toulouse, France (pmeslin@irap.omp.eu); [2]Johns Hopkins University, APL, Laurel, MD, USA.

Introduction: After preliminary measurements acquired during its three flybys of the planet [1], the MESSENGER spacecraft has made the first measurement of the Th and U content of the surface of Mercury with its Gamma-Ray Spectrometer (GRS) [2]. Surprisingly, it measured a Th/U ratio of 2.5 ± 0.9 [2], which is significantly lower than its chondritic value, whose estimates vary between 3.53 ± 0.10 [3] and 3.9 ± 0.2 [4]. The bulk Th/U ratio of terrestrial planets is expected to be close to the chondritic value, or slightly larger as uranium can behave as a moderately volatile element [3], and the crustal Th/U ratio of terrestrial planets does not deviate much from this value (e.g., Th/U~3.9 in the Earth's crust, ~3.7 in lunar rocks [5], ~3.75 to 4.4 in SNC meteorites [6,7]). A large scale process that could have led to a fractionation of these two lithophile, incompatible elements, and which was proposed for Mercury, is the depletion of the relatively more volatile UO_3 species upon formation and evolution of this planet at high temperatures, or preferential incorporation of U in the core. However, these processes would lead to an increase of the Th/U ratio, contrary to what is observed. Therefore, the strongly subchondritic Th/U ratio characteristic of the Hermean surface remains to be explained. We propose hereafter that it actually reflects a relatively strong outgassing of radon from the regolith, and we show that the mobility of radon should be considered to derive accurate uranium concentrations of Mercury's crust.

Influence of radon exhalation on the Th/U ratio: The measurement of ^{238}U by gamma-ray spectroscopy is actually made through the analysis of two of its decay products, ^{214}Bi and ^{214}Pb, assuming secular equilibrium between these species in the regolith. These two radionuclides are decay products of ^{222}Rn, a radioactive gas (with 3.8 days half-life) that can escape from its mineral host by recoil and then diffuse to the surface and migrate through the exosphere, leading to an excess of ^{214}Bi and ^{214}Pb in the upper few centimeters of the regolith. If radon migration to the surface is efficient enough, the presence of these unsupported radionuclides can significantly increase the apparent uranium content and strongly bias the Th/U ratio. The very same process was proposed to explain the abnormally low Th/U ratio measured on Mars by Mars Odyssey GRS [8], and was confirmed by a refined analysis of uranium lines at several energies [9], which revealed a characteristic decrease of the apparent U/Th ratio with gamma-ray energy.

Modeling of radon transport: In order to simulate this effect, we have developed a 3D thermal model of the subsurface of Mercury (based on [10]), coupled to an adsorption-diffusion gas transport model. It uses as inputs the radon emanation factor of lunar samples (< 1%) [11] and the adsorption coefficient measured by [12], which is strongly dependent on temperature. Its output (a time-variable map of the exhalation rate) is injected into a Monte-Carlo code simulating the exospheric transport of radon (incl. surface adsorption) and the escape or implantation of its decay products into the surface. One of the outputs of the model is a prediction of the apparent U/Th ratio as a function of ray energy (i.e., the ratio that would be measured by a spacecraft after correcting for the attenuation of rays through the upper cm of the regolith).

Preliminary results and comparison to the lunar case: When running the model with typical lunar values for the emanation factor, regolith specific surface area and regolith thickness (~5m), we find an increase of the apparent U/Th ratio, which is larger at lower energies, but not to the same extent as that observed by MESSENGER (Fig. 1). However, the high temperatures of the Hermean surface may lead to a larger emanation factor of radon: an emanation factor of ~3% accounts well for the observed U/Th ratio. Alternatively, since the diffusion length of radon can probably reach ~10m at ~300 K [12], the high apparent U/Th can also be explained by the presence of a thicker regolith, which would be consistent with the analysis of the topographic roughness of Mercury, which indicates that the regolith of Mercury may be 3 times thicker than the lunar one [13].

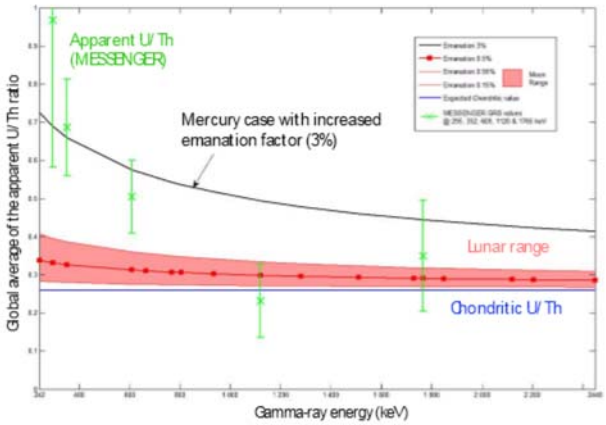

Fig. 1: Apparent U/Th vs. ray energy (revised values from [2]): comparison between MESSENGER values and outputs of the model for the lunar case and for a case with a larger emanation factor.

References: [1] Rhodes E. et al. (2011), PSS, 59. [2] Peplowski P. et al. (2011) Science 333, 1850. [3] Goreva, J.S. and Burnett, D.S. (2001), Meteoritics & Planet. Sci., 36. [4] Rocholl, A. and Jochum, K.P. (1993), EPSL, 117. [5] Korotev, R.L. (1998), JGR, 103. [6] Chen, J.H. and Wasserburg, G.J. (1985), LPS, 24. [7] Chen, J.H., et al. (1993), LPS, 24. [8] Meslin, P.Y. (2008), PhD Thesis, UPMC. [9] Meslin, P.Y. et al. (2012), 43rd LPSC. [10] Yan N. et al. (2006), ASR, 38. [11] Adams et al. (1973), 4th LSC. [12] Meslin et al. (2011), GCA, 75. [13] Kreslavsky et al. (2012), GRL, 41.

BEPICOLOMBO MPO-MMO COORDINATED OBSERVATIONS FOR THE STUDY OF THE ENVIRONMENT OF MERCURY. A Milillo[1], G. Murakami[2], J. Zender[3] and HEWG, [1]INAF/IAPS (via del Fosso del Cavaliere, 00133 Rome, Italy, anna.milillo@iaps.inaf.it), [2]JAXA (Tokyo, Japan, go@stp.isas.jaxa.jp), [3] ESA, ESTEC, (Noordwijk, The Nederlands, joe.zender@esa.int)

Introduction: The proximity of Mercury to the Sun makes its environment particularly extreme. Mercury's weak intrinsic global magnetic field supports a small, but dynamic, magnetosphere. The plasma in Mercury's space environment coexists with the planet's exosphere and strongly interacts with the surface. In fact, Mercury's environment is a complex and tightly-coupled system where the magnetosphere, exosphere, and surface experience temporal and spatial variations linked to each other. For this reason, having the possibility of simultaneous information on the external conditions and the close-to-planet environment would greatly help in the definition of the active processes. Performing simultaneous two-point measurements from two satellites, ESA-JAXA BepiColombo mission will offer an unprecedented opportunity to investigate magnetospheric and exospheric dynamics at Mercury as well as their interactions with solar radiation and interplanetary dust [1]. Many scientific instruments onboard the two spacecraft will be completely, or partially, devoted to study the environment of Mercury as well as the complex processes that govern it. The specific orbits of the two spacecraft and the comprehensive scientific payload will make this mission a great improvement with respect to the successful mission MESSENGER that ended in 2015.

HEWG activities. Coordinated measurements by different onboard instruments will permit a wider range of scientific questions to be addressed than those that could be achieved by the individual instruments acting alone. The Hermean Environment working group is actively involved in coordinating the modeling development for simulating of the expected signal and in the optimization of the coordinated science operation planning and eventually of the science return. Examples of possible coordinated observations are described by analyzing the required geometrical conditions, pointing, modes and timing.

References:

[1] Milillo, A.. et al. (2010) BepiColombo Special Issue on Planet. and Sp. Sci., 58, 40–60.

SPECTROSCOPY OF SYNTHETIC PLANETARY ANALOGS FOR MERTIS ON THE BEPICOLOMBO MISSION. Andreas Morlok[1], Bernard Charlier[2], Stephan Klemme[3], Olivier Namur[4], Martin Sohn[5], Iris Weber[1], Aleksandra Stojic[1], Harald Hiesinger[1], Joern Helbert[6] [1]Institut für Planetologie, Wilhelm-Klemm Strasse 10, 48149, Germany, morlokan@uni-muenster.de [2]University of Liege, Department of Geology, 4000 Sart-Tilman, Belgium, [3]Institut für Mineralogie, Corrensstrasse 24, 48149 Münster, [4]Department of Earth and Environmental Sciences, KU Leuven, 3001 Leuven, Belgium, [5]Hochschule Emden/Leer, Constantiaplatz 4, 26723 Emden, Germany 6Institute for Planetary Research, DLR, Rutherfordstrasse 2, 12489 Berlin, Germany.

Introduction: The IRIS (Infrared and Raman for Interplanetary Spectroscopy) laboratory generates spectra for a database [1] for the ESA/JAXA BepiColombo mission to Mercury. Onboard is a mid-infrared spectrometer (MERTIS-Mercury Radiometer and Thermal Infrared Spectrometer). This unique device allows to map spectral features and thus the mineralogy in the 7-14 μm range, with a spatial resolution of about 500 meters [2-5].

Heavy impact cratering played an important part in the formation of the surface regolith of Mercury [5]. Glass, which can arise through such impacts and in volcanic processes, lacks an ordered microstructure and represents the most amorphous phase of a material, typical for events involving high shock pressures and temperatures [6,7]. Using synthetic materials allows us to produce infrared spectra of analogue materials based on the observed chemical composition of planetary bodies, from which no meteorites are available so far [8]. Here, we present mid-infrared spectra of such synthetic analogue materials for surface regions of Mercury.

Samples and Techniques: Bulk glasses were synthesized based on the chemical composition for surface areas on Mercury, based on MESSENGER X-ray spectrometer data [9], following a procedure described in [8].

Furthermore, analogue material was produced in petrological experiments simulating the petrologic evolution of early Mercurian magmas under controlled temperatures, pressures and oxidation states [10-12]. Here we present data from two analogue samples: the high-Mg NVP (Northern Volcanic Plains) region, produced at 0.1 GPa and 1210°C, and material based on the composition of the Inter Crater Plains (ICP), which were equilibrated at 0.1 GPa and 1320°C) [10-12].

Bulk Spectroscopy: For the diffuse reflectance analyses, four powder size fractions were measured. For analyses from 2-20 μm we used a Bruker Vertex 70 infrared system with a MCT detector under low pressure (3 mbar).

In-situ Analyses: We analysed polished thin sections with a Bruker Hyperion 1000/2000 System at the Hochschule Emden/Leer. We used a 1000×1000 μm sized aperture, for each spectrum; 128 scans were added.

Results: The spectra of the surface regolith exhibit a single band at 9.8 μm, typical for glassy material [8]. Two additional characteristic features for remote sensing, the Christiansen feature (CF; the position of lowest reflectance), and the Transparency Feature (TF; characteristic of the finest grain size fraction) are located at 8.0 μm and at 11.9 μm, respectively.

The micro-FTIR analyses of the experimental sample analogs for the NVP show strong crystalline features at 9.3 μm, 9.9 μm, 10.4 μm and 11.6 μm, with minor features at 13.8 μm and 14.7 μm. The CF is at 8.1 μm, enstatite features mixed with diopside bands [13]. The spectrum of glassy material is similar to the regolith analog (single strong band at 9.7 μm and a CF at 7.9 μm). The analyses of the ICP analog material show crystalline bands at 9.6 μm, 10.2 μm, 10.7 μm and 11.9 μm; typical olivine bands [14]. The spectrum of a glassy spot on the same sample is also similar to the regolith-analog, with a strong band at 9.8 μm and a CF at 8.0 μm.

Conclusions: Future analyses will cover a wider range of bulk samples for the surface of the planet, as well as more detailed in situ studies of the phases formed in the petrological experiments under various temperature and pressure regimes.

References: [1] Weber I. et al. (2018) 49th LPSC Abstract #1430 [2] Maturili A. (2006) Planetary and Space Science 54, 1057–1064 [3] Helbert J. and Maturilli A. (2009) Earth and Planetary Science Letters 285, 347-354 [4] Benkhoff J. et al. (2010) Planetary and Space Science 58, 2-20 [5] Hiesinger H. et al. (2010) Planetary and Space Science 58, 144–165 [6] Johnson (2012) Icarus 221, 359–364 [7] Lee et al. (2010) Journal of Geophysical Research 115, 1-9 [8] Morlok A.et al. (2017) Icarus 296, 123-138 [9] Weider S.Z. et al. Earth and Planetary Science Letters 416, 109-120 [10] Namur and Charlier (2017) Nature Geoscience 10, 9-15 [11] Namur O. et al. (2016) Earth and Planetary Science Letters 448, 102-114 [12] Namur O. et al. (2016) Earth and Planetary Science Letters 439, 117-128 [13] Hamilton V. (2000) Journal of Geophysical Research, 105, 9701-9715 [14] Hamilton V. (2010) Chemie der Erde 70, 7-33.

Acknowledgements: This work was partly supported by DLR grant 50 QW 1302 in the framework of the BepiColombo mission.

Overview of Mercury Magnetospheric Orbiter (MMO) for BepiColombo

Go Murakami[1], Hajime Hayakawa[1], Masaki Fujimoto[1], and BepiColombo project team
[1]Institute of Space and Astronautical Science , Japan Aerospace Exploration Agency (3-1-1 Yoshinodai, Chuo, Sagamihara, Kanagawa 252-5210, Japan, E-mail: go@stp.isas.jaxa.jp)

Introduction: Mercury has the weak planetary magnetic field stands against the intense solar wind in the close proximity of the Sun. Mercury's plasma environment is quite different in the parameters from the well-studied terrestrial magnetosphere. Thus Mercury's magnetosphere is one of the best targets to study planetary environments. In addition, recently many Earth-type exoplanets orbiting in habitable zones very close to cool stars (M-dwarfs). Such exoplanets are exposed to extreme stellar winds and ultraviolet radiations. Exploring Mercury which is the innermost planet in the solar system plays a key role to understand such extreme environment.

The first Mercury orbiter MESSENGER explored this region and discovered a wide variety of phenomena. For example, Mercury's magnetosphere is much more dynamic than one had predicted and substorm-like events with the time scale of minutes were observed. In addition, magnetic field measurements by MESSENGER suggests the existence of field aligned currents even though Mercury has no ionosphere. However, due to the highly ecliptic orbit with north-south asymmetry and limited capability for plasma measurements, many science topics still remain unsolved.

The next Mercury exploration mission BepiColombo, which is the international joint project between ESA and JAXA, will be launched in October 2018 and will arrive at Mercury in December 2025. The JAXA's spacecraft for BepiColombo, Mercury Magnetospheric Orbiter (MMO), is spin-stabilized with a rotation rate of 15 rpm and is equipped to study the space environment of Mercury. MMO is mainly designed for plasma observations with the complete package of plasma instruments consortium and is expected to extract essential elements of space plasma physics that become visible in the Hermean environment. In addition, ESA's Mercury Planetary Orbiter (MPO) also has several instruments for plasma measurements, so we can investigate Mercury's environment with two points measurements.

Here we present how BepiColombo will contribute to deepen our understanding Mercury's environment by addressing the puzzles raised by MESSEGNER.

BepiColombo/MMO: The MMO spacecraft will have a ecliptic polar orbit with a period of 9.3 hours, a periapsis of 590 km, and a apoapsis of 11640 km. The orbital plane is same as that of MPO. The MMO will be spin-stabilized with a rotation rate of 15 rpm and a spin axis almost perpendicular to the orbital plane of Mercury around the Sun.

MMO has a complete package of plasma environment measurements: Magnetic Field measurement (MGF), Plasma Wave Instrument (PWI), and Mercury Plasma Particle Experiment (MPPE). These instrument will be operated as a plasma measurement consortium. In addition, two more instruments are installed onboard MMO to investigate Mercury's exosphere and dust environment: Mercury Sodium Atmospheric Spectral Imager (MSASI) and Mercury Dust Monitor (MDM).

Almost all of tests in ESA's test center (ESTEC) have successfully finished and soon the spacecraft will be shipped to the launch site in French Guiana. So now we can focus on science observation planning.

MMO has large constraints on science operations, such as thermal issue and limited telemetry rate. Due to the thermal issue each science instrument cannot always be turned on. In addition, due to the low telemetry rate in average, only a part (~20-30%) of science mission data with high resolution can be downlinked. Therefore, in order to maximize the scientific results and outcomes to be achieved by MMO, we are now working to optimize the science observation and downlink plans in detail.

REFLECTANCE OF MERCURY'S POLAR REGIONS: CALIBRATION AND IMPLICATIONS FOR MERCURY'S VOLATILES. G. A. Neumann[1], X. Sun[1], A. Cao[2], A. N. Deutsch[3], and J. W. Head[3], [1]NASA Goddard Space Flight Center, Greenbelt, MD 20771, USA (email: gregory.a.neumann@nasa.gov), [2]University of Washington, Seattle WA 98195, USA, [3]Department of Earth, Environmental and Planetary Sciences, Brown University, Providence, RI 02912, USA. [4]Department of Earth, Atmospheric and Planetary Sciences, Massachusetts Institute of Technology, Cambridge, Massachusetts 02139-4307, USA.

Introduction: The Mercury Laser Altimeter (MLA) [1] on board the MESSENGER spacecraft measured the outgoing and returned energy of 1064-nm-wavelength laser pulses reflected from the surface, as well as precise time-of-flight ranges. These ancillary measurements were interpreted via a link equation [2] as reflectances relative to Lambertian. The measurement precision of ~25% was best in a nadir geometry, where the height of pulses could be sensed at two separate threshold voltages, however most observations in the polar regions were necessarily oblique to the surface normal. Understanding the interaction of the laser beam at zero phase angle (the angle between incident and emitted light) is critical for understanding the composition and properties of the regolith on airless bodies, e.g., [3], and for characterizing volatile processes in permanently shadowed regions [4-9]. The energy in obliquely incident returns is dispersed over a greater interval of time than the incident pulse [10], with reduced amplitude. This poses a challenge to accurate calibration of data acquired over the course of 4+ years of operation at distances varying by orders of magnitude. As well, the systematic changes in the laser beam itself must be considered in the link equation.

Implications for Mercury's Volatiles: The importance of this work to understanding the distribution and emplacement history of volatiles warrants further attention to the calibration of reflectance under varying conditions. In the cold traps on Mercury, the distribution of both bright and dark materials has been obtained from scattered light images within persistently shadowed regions [11] but the images are highly stretched and not calibrated to reflectance. Distinct margins between regolith and lag deposits are resolved by images, and a few images also see the margins between regolith and bright deposits, but the stratigraphy of both types of volatiles is not resolved within the same image. Poleward darkening of the regolith can be interpreted as increasing population of sublimation lag deposits [12], while brightening poleward, even excluding well-resolved craters, has been attributed to patches of ice exposed at the kilometer scale resolution of the MLA data [13]. However the MLA dataset archived in the PDS [14] has systematic biases northward of the 84° orbital inclination of MESSENGER.

An engineering model of the MLA instrument (delivered in 2003) still operates as a test bed for calibrations (Fig. 1). Signals from a laser diode can be controlled digitally with arbitrary waveforms fed into a flight-like avalanche photodiode detector. The timing circuitry is also identical that used to measure the pulse energy on MLA [8]. We have examined the range precision and differential pulse widths obtained over 40 dB of signal attenuation from saturation to extinction and can now assess the factors that account for systematic biases (Fig. 2). Further work using this system and calibration progress will be presented.

References:

[1] Cavanaugh J. F. et al. (2007) Space Sci. Rev., 131, 451-479. [2] Sun X. and Neumann G. A. (2015) IEEE Trans. Geosci. Rem. Sens., 53, 2860–2874. [3] Barker M. K. et al. (2015) Icarus, 273, 96–113. [4] Zuber M. T. et al. (2012) Nature, 486, 378–381. [5] Lucey P. G. et al. (2014) JGR Planets, 119, 1665–1679 [6] Lemelin, M. et al. (2016) Icarus 273, 315–328. [7] Fisher E. et al. (2017) Icarus, 292, 74–85. [8] Neumann G. A. et al. (2013) Science, 339, 296–300. [9] Deutsch A. N. et al. (2017) Icarus, 280, 158–171. [10] Gardner C. S. (1992) IEEE Trans. Geosci. Rem. Sens. 30, 1061-1072. [11] Chabot N. L. et al. (2014) Geology, 42, 1051-1054. [12] Rubanenko L. et al. (2018) this meeting. [13] Chabot N. L. et al. (2018) this meeting. [13] Deutsch A. N. et al. (2017) GRL 44, 9233-9241. [14] Dataset mess-e_v_h-mla-3_4-cdr_rdr-data-v1 at pds-geosciences.wustl.edu/messenger/.

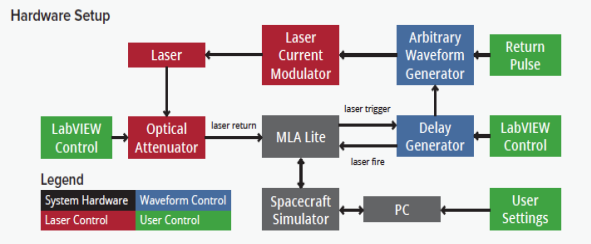

Figure 1: Instrument test setup block diagram.

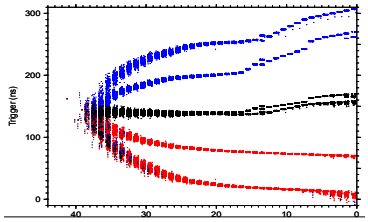

Figure 2: Leading and trailing edge pulse timings vs. attenuation at dual thresholds, used to infer energy.

MERCURY LASER ALTIMETER: HIGHLIGHTS FROM 10 YEARS IN SPACE. G. A. Neumann[1], X. Sun[1], E. Mazarico[1], M. K. Barker[1], D. E. Smith[2], M. T. Zuber[2], and J. W. Head[3], [1]NASA Goddard Space Flight Center, Greenbelt, MD 20771, USA. (email: gregory.a.neumann@nasa.gov), [2]Department of Earth, Atmospheric and Planetary Sciences, Massachusetts Institute of Technology, Cambridge, Massachusetts 02139-4307, USA, [3]Department of Earth, Environmental and Planetary Sciences, Brown University, Providence, RI 02912, USA.

Introduction: The Mercury Laser Altimeter (MLA), launched Aug. 3, 2004 on board the MErcury Surface, Space ENvironment, GEochemistry, and Ranging (MESSENGER) spacecraft, performed in-flight calibrations following an Earth gravity assist flyby in 2005, sent laser pulses to Venus to measure backscattering from atmosphere, and obtained its first Mercury data in during its first flyby in January 2008, at altitudes from 200 to 1460 km. Thereafter the altimeter made discoveries contributing to our knowledge of the surface environment, geology, tectonics, impact history, volcanism, and interior structure.

Measurement of surface topography at 2× the range of any previous planetary laser altimeter: The Mars Orbiter Laser Altimeter reached a maxiumm range of 750 km using far greater laser pulse energy and receiver aperture diameter. MLA routinely ranged in nadir geometry up to 1500 km distance [1].

First laser to operate in space for 10 years: The MLA laser operated through the end of the MESSENGER mission until the moment when spacecraft impacted the Mercury surface on April 30, 2015.

First two-way range at 24,000,000 km: Several dozen laser pulses from MLA were detected on the ground and uniquely identified by their digitized waveforms and relative timing pattern [2]. Modeling of these, together with 90 uplink pulses detected, provided clock correlation, range, range rate and acceleration with 20-cm overall precision and 27 meter accuracy after correction for the solar Shapiro time delay.

Determination of the global figure of Mercury in a center-of-mass frame, and its anomalous, non-hydrostatic degree-2 shape and flattening: The degree 2 shape [3] was found to be oblate and elongated, 10× more than its geoid, with its long axis rotated ~15° westward from the dynamically defined principal axis. Unlike the case of the Moon and Mars, the center of figure lies within 140 m of the center of mass.

First observation of Mercury rotational state and librations from orbital altimetry: The rotational axis of Mercury and libration amplitudes were obtained in part from altimetric measurements [4], with implications for the internal structure and size of core.

Discovery of the "northern rise": MLA identified this enigmatic 1000-km-diameter domical topographic swell, uplifted 1.5 km [5] at some point after the emplacement of the Northern Smooth Plains [6, 7]. Its origin, as well as that of similar long-wavelength features, continues to be debated [8, 9].

Detection of sublimation lags overlying radar-bright water ice deposits: While reflectance anomalies were expected in regions of permanent shadow, believed from Earth-based radar observations to contain substantial thicknesses of water ice, the entire first year of operations was limited by the 84° orbital inclination and showed only unusually dark or absent returns in such areas (Fig. 1). Subsequent obliquely targeted measurements northward of 85°N found surface exposures of water ice [10] in permanently-shadowed regions, where maximum surface temperatures inferred from thermal models [11] based on high-resolution topography had not exceeded ~100 K over geological time. The near-zero obliquity of Mercury and lack of atmosphere provides many such cold traps.

The extent and thickness of polar ice deposits has now been inferred from a combination of MLA, Earth-based radar and orbital imagery [12] yielding estimates of the quantity and distribution of ice that indicate an origin from a relatively recent cometary impact [13].

References: [1] Zuber M. T. et al. (2008) Science, 321, 77–79. [2] Smith D. E. et al. (2006) Science, 311, 53-53. [3] Perry M. E. et al. (2015) GRL, 42, 6951–6958. [4] Stark A. et al. (2015) GRL 42, 7881–7889. [5] Zuber M. T. et al. (2012) Science, 386, 217–220. [6] Denevi B. W. et al. (2013) JGR Planets, 118, 891–907. [7] James P. B. et al. (2015) JGR Planets, 120, 287–310 [8] Phillips R. J. et al. (2018) In "Mercury: The View after MESSENGER", Cambridge. [9] Head III J. W. et al. (2011) Science, 333, 1853-1856. [10] Neumann G. A. et al. (2013) Science, 339, 296–300. [11] Paige D. A. et al. (2013) Science, 339, 300–303. [12] Deutsch et al. (2017) GRL 44, 9233-9241. [13] Chabot N. L. et al. (2018) In "Mercury", ibid., in press.

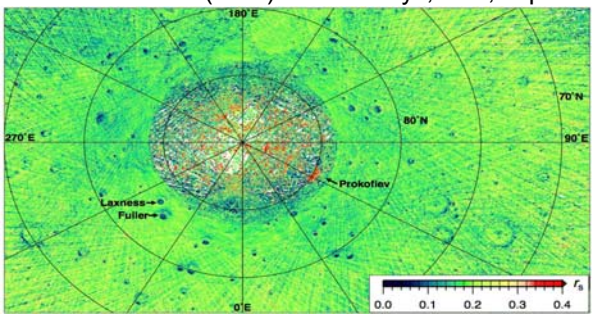

Figure 1: Normal albedo (reflectance) at 1064-nm wavelength measured by MLA [from 13] showing dark lag deposits covering water ice, with bright ice deposits exposed in e.g., Prokofiev crater.

HETEROGENEOUS DISTRIBUTION OF CHROMIUM ON MERCURY. L. R. Nittler[1,*], A. Boujibar[2], E. Crapster-Pregont[3], E. A. Frank[1], T. J. McCoy[4], F. M. McCubbin[5], Richard D. Starr[6,7], K. E. Vander Kaaden[8], A.Vorburger[2,9], S. Z. Weider[1], [1]Department of Terrestrial Magnetism, Carnegie Institution of Washington, Washington, DC 20015, USA, [2]Geophysical Laboratory, Carnegie Institution of Washington, Washington, DC 20015, USA,[3]Department of Earth and Planetary Sciences, American Museum of Natural History, New York, NY 10024, USA, [4]National Museum of Natural History, Smithsonian Institution, Washington, DC 20013, USA, [5]NASA Johnson Space Center, Houston, TX 77058, USA, [6]Physics Department, The Catholic University of America, Washington, DC 20064, USA, [7]Solar System Exploration Division, NASA Goddard Space Flight Center, Greenbelt, MD 20771, USA, [8]Jacobs, NASA JSC, Houston, TX 77058, USA, [9]Physics Institute, University of Bern, Bern, Switzerland. *E-mail: lnittler@ciw.edu.

Introduction: Measurements made with geochemical instruments on the MESSENGER spacecraft revealed that Mercury's crust is surprisingly rich in volatile elements, including S, Na, K, Cl, and C, and that it is enriched in Mg and depleted in Al, Ca, and Fe, relative to other terrestrial planets [1–5]. Geochemical maps also indicated the presence of a number of distinct geochemical terranes [6, 7]. The MESSENGER X-ray Spectrometer (XRS) detected X-ray fluorescence, induced by incident solar X-rays, from the top ~10s of μm of Mercury's surface. Like Fe, Cr was only detectable by XRS during large solar flares [5]. However, accurate Cr measurements are more susceptible to systematic errors than other elements measured by the XRS [3, 5]. Therefore, to date, Cr data have been published for only 11 XRS measurements [5], but we have recently [8] derived a map of Cr/Si across Mercury's surface. This map is based on data acquired through the complete MESSENGER mission and reveals clear spatial heterogeneity in Cr.

Methods: Following previous methods [5,9], we combined analyses of 133 XRS spectra, selected because they had non-zero derived Cr abundances and did not exhibit anomalously high detector backgrounds at high energy, to produce our Cr/Si map [8]. Data were empirically corrected for a phase-angle effect [5,8]. Following this correction, we calculate the global average Cr/Si as 0.003 (~800 ppm Cr), but there is at least a factor of two systematic uncertainty in absolute Cr/Si values. Relative differences between mapped Cr/Si values are much more robust.

Results and Discussion: Our Cr/Si map is compared to an XRS-derived Mg/Al ratio map [5] in the Figure. Coverage in the northern hemisphere is sparse for Cr/Si and spatial resolution is poor in the south, but the map includes multiple resolved measurements across the High-Magnesium Region (HMR) and Caloris Basin (CB) geochemical terranes. The HMR, which is also enriched in Mg, S, Ca, and Fe, and depleted in Al, has a clear enrichment in Cr compared with the global average (Cr/Si~0.0054, 1.8±0.4×average). Conversely, the CB interior plains, which exhibit the lowest Mg/Al on the planet, have a low Cr/Si ratio, with an average value of 0.0016, 0.54±0.11 times the average. Thus, Cr on Mercury correlates with Mg, S, Ca, and Fe, and anti-correlates with Al, at least in large geochemical terranes.

Based on its surface Fe and S composition, Mercury is inferred to have formed under highly reducing conditions, e.g., oxygen fugacity (fO_2) of 3 to 7 log units below the iron-wüstite buffer [10-12]. Under these conditions, Cr is expected to be present primarily in sulfides. Moreover, because the valence state of Cr depends on fO_2 [13], the new Cr data may provide additional constraints on Mercury's oxidation state [8, 14].

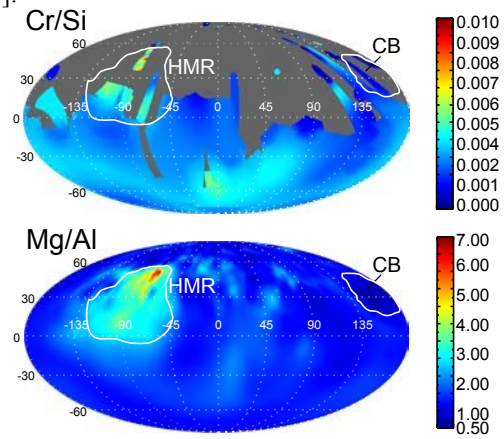

References: [1] Nittler L. R., et al. (in press) in: Mercury: The view after MESSENGER, Cambridge University Press, Cambridge. [2] Peplowski P. N., et al. (2011) *Science, 333,* 1850–1852. [3] Nittler L. R., et al. (2011) *Science, 333,* 1847–1850. [4] Peplowski P. N., et al. (2014) *Icarus, 228,* 86–95. [5] Weider S. Z., et al. (2014) *Icarus, 235,* 170–186. [6] Peplowski P. N., et al. (2015) *Icarus, 253,* 346–363. [7] Weider S. Z., et al. (2015) *EPSL, 416,* 109–120. [8] Nittler L. R., et al. (2018) *LPS 49,* Abstract #2070. [9] Nittler L. R., et al. (2016) *LPS, 47,* Abstract #1237. [10] McCubbin F. M., et al. (2012) *GRL*, 39, L09202. [11] Zolotov M. Y., et al. (2013) *JGR (Plan.)* 118, 138–146. [12] Namur O., et al. (2016) *EPSL*, 448, 102–114. [13] Bell A. S., et al. (2014) *Am. Min., 99,* 1404-1412. [14] Boujibar, A., et al. (2018), this meeting.

UNVEILING THE EARLY HISTORY OF MERCURY BY STUDYING ITS CRUSTAL MAGNETIC FIELD.

J. S. Oliveira[1,2] and L. L. Hood[3], [1]ESA/ESTEC, SCI-S, Keplerlaan 1, 2200 AG Noordwijk, Netherlands; [2]CITEUC, Geophysical & Astronomical Observatory, University of Coimbra, Coimbra, Portugal (joliveira@cosmos.esa.int); [3]Lunar & Planetary Lab, 1629 E. University Blvd., Univ. of Arizona, Tucson, AZ 85721, USA (lon@lpl.arizona.edu).

Introduction: Low altitude MESSENGER MAG data, obtained during the last months of the mission, allow the identification of crustal magnetic field anomalies in the northern hemisphere [1, 2, 3]. Though some of the anomalies are related to the Hermean topography structures, others are not. Therefore, the relationship of the anomalies to impact related events is not clear. Moreover, the measured crustal field can be explained through or by a combination of various sources such as thermoremanent magnetization, shock remanent magnetization or even induced fields. Distinguishing among those different sources that are contributing to a given anomaly is an extremely difficult task.

Here, we study the different anomalies that are found on Mercury, with special focus on those that are clearly related with craters or basins whose interior subsurfaces cooled very slowly and therefore were very likely thermoremanently magnetized. We use a unidirectional magnetization model, the so called Parker method [4], which assumes that the melt impact sheet recorded the constant core magnetic field present when the crater was formed. The most important property of this technique is that no assumption about the source geometry is required. Not only will the results help to look for true polar wander events on Mercury, but they also could serve as a proof that some anomalies, are not, at least, entirely induced in origin.

Results: We report results for the two main magnetic anomalies related to the craters Rustaveli (200 km in diameter, centered at 83°E, 52°N), and Vyasa (300 km in diameter, centered at 275°E, 50°N).
For the Rustaveli anomaly, we find the best paleopole position at 74ºE , 52ºS, with a misfit value of 0.83 nT (see Figure 1). Considering the uncertainties on the paleopole position, this anomaly is well constrained, i.e. it has a small area of possible paleopole solutions. Also, the solution includes the actual South pole, where the actual magnetic North pole is believed to be located. This could be explained by an ancient core field with same characteristics of today's field, but also by an induced field due to a permeability enhancement beneath the crater's interior surface.

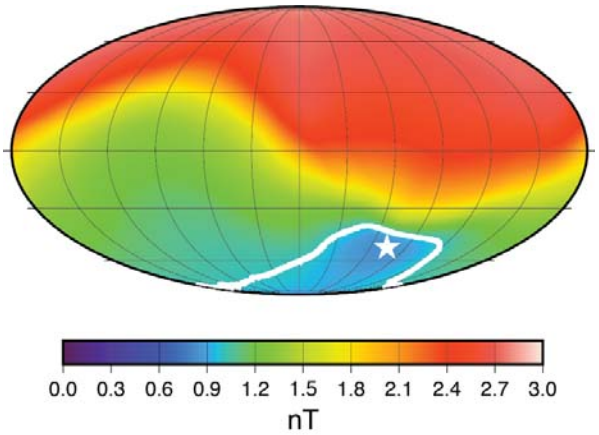

Figure 1: Misfit as a function of north paleomagnetic pole position with the corresponding uncertainty denoted by a white solid line. The best paleopole solution is denoted by a star.

For the Vyasa anomaly, we find the best paleopole at 145ºE, 2ºS, with a misfit of 1.4 nT. However, the possible paleopole position solutions are covering the entire southern hemisphere. This result, even showing an equatorial best solution, does not allow one to argue for a thermoremanent source, as the uncertainty also includes the present magnetic North pole.

Further investigation on other crater related anomalies are needed to look for undoubtedly thermoremanent crustal field anomalies and therefore provide constrains on the planet's early history, such as true polar wander events and the early history (e.g., reversals) of Mercury's dynamo.

Acknowledgment : Supported at the Univ. of Arizona by the NASA DDAP.

References: [1] Johnson C. et al. (2015) Science, 348, 892-895. [2] Hood L. (2015) GRL, 42, 10565-10572. [3] Hood L. (2016) JGR Planets, 121, 1016-1025. [4] Parker (1991) JGR, 96, 16101–16112.

MERCURY SODIUM EXOSPHERIC EMISSION AS A PROXY FOR SOLAR PERTURBATIONS TRANSIT

Stefano Orsini[1*], Valeria Mangano[1], Anna Milillo[1], Christina Plainaki[2], Alessandro Mura[1], Jim M. Raines[3], Monica Laurenza[1], Elisabetta De Angelis[1], Rosanna Rispoli[1], Francesco Lazzarotto[1], Alessandro Aronica[1] ([1]) INAF-IAPS, Roma, Italy ([*]stefano.orsini@iaps.inaf.it), ([2]) ASI, Roma, Italy, ([3]) University of Michigan, Ann Arbor, MI USA

Introduction: We report here about recently published results [1] on the first evidence at Mercury of direct relation between ICME transit and Na exosphere dynamics, suggesting that Na emission, observed from ground, could be a proxy of planetary space weather at Mercury. The link between the dayside exosphere Na patterns and the solar wind-magnetosphere-surface interactions is investigated. This goal is pursued by analyzing the Na intensity hourly images, as observed by the ground-based THEMIS solar telescope during 10 selected periods between 2012 and 2013 (with seeing, σ <= 2"), compared to MESSENGER data.

Frequently, two-peak patterns of variable intensity are observed, located at high latitudes in both hemispheres. Occasionally, Na signal is instead diffused above the sub-solar region. We compare these different patterns with the in-situ time profiles of proton fluxes and magnetic field data from MESSENGER. Among these 10 cases, only in one occasion the Na signal is diffused above the subsolar region, when the MESSENGER data detect the transit of two ICMEs. These cases suggest that the Na emission patterns are well related to the solar wind conditions at Mercury, yo be be considered as a 'natural monitor' of solar disturbances when transiting near Mercury.

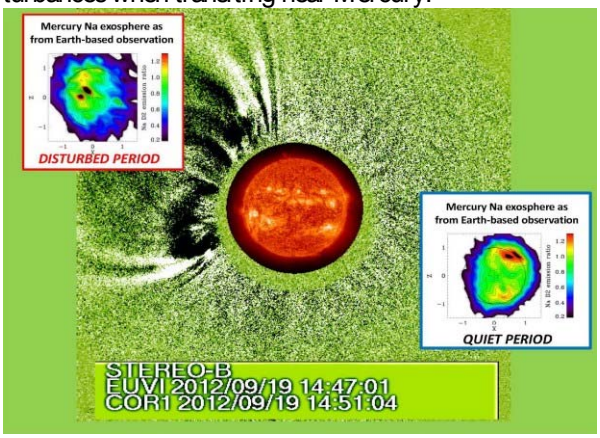

The possibility to use Mercury exosphere as a monitor would be of great profit for ICME modeling efforts. It follows that a continuous ground-observation of the planet would be desirable. Jointly with the Sun ICME emission monitoring, by allocating time and resources to the available solar telescopes.

Conclusions: In summary, the Na exospheric emission observed in the analyzed 10 sequences database (with average seeing <= 2") leads to two alternative scenarios of particle precipitations:

1. Open field lines plasma precipitation, which originates high-latitude two-peak Na emission. This is a frequent condition induced by significant reconnection rate at Mercury (low plasma β). At ICME transits, they cause thick, low-β plasma depletion layers and even higher reconnection rates, so that the cusps extend to lower latitudes, causing open field lines broad plasma precipitation areas [2], with the two-peak Na patterns still existing, but hardly distinguishable.
2. Occasionally, at the ICME transit, the magnetopause itself approaches the planet surface. We see evidence that such a distance may be small; lower than particle gyroradii, i.e., a few hundred km, so that magnetosheath plasma may precipitate on the planet's dayside [3] [4]. Although increases in the planetary field from core induction offset the effects of compression, they do not rule out compression of the magnetopause to near the surface at low dayside latitudes (48 – 320 km, near the subsolar point and closer in the southern hemisphere [2]). Near the subsolar point hot protons would have gyroradii of a few hundred km [5], allowing them to impact the surface at low latitudes via gyration.
3. Particle precipitation is the major driver of Na surface release, so that the observations of Na emission evidence planetary space weather features at Mercury. We have noticed that IMF components do not play a significant role with respect to the IMF magnitude itself, when IMF exceeds ~25 nT. The shown observations do not allow identification of the surface release process responsible for exospheric Na refilling. Ion sputtering yields are generally not sufficient for sustaining the observed release, but plasma impact on the surface would drive enhanced diffusion, which should be able to provide free Na atoms, then released in a short while through PSD process [6].

References: [1] Orsini, S. et al. (2018) Scientific Reports, 8:928, DOI: 10.1038/s41598-018-19163-x [2] Slavin, J. A., et al. (2014) J. Geophys. Res. Space Physics, 119, 8087. [3] Kallio, E., Janhunen (2003) Geophys. Res. Lett., 30, 17, 1877. [4] Winslow, R. M., et al. (2017) J. Geophys. Res. Space Physics, 122, 23548. [5] Raines, Jim M. et al. (2014) J. Geoph. Res. Space Phys, 119, 8, 6587. [6] Mura, A. et al. (2009) Icarus, 200, 1–11.

Experimental Study of Hollow Formation. S. W. Parman[1], T.M. Orlando[2], R. E. Milliken[1], J. W. Head[1], B. M. Jones[2], B. A. Anzures[1], [1]DEEPS, Brown University, 324 Brook St, Providence, RI 02912, stephen_parman@brown.edu, [2]Center for Space Technology and Research, Georgia Institute of Technology, 311 Ferst Dr., Atlanta, GA 30332

Introduction: Hollows are rimless, flat-bottomed pits on the surface of Mercury. Astonishingly, they appear to be produced by some form of sublimation and/or desorption of a layer of solid igneous rock [1,2]. Identifying the mineralogy and composition of the hollows forming material should provide constraints on the composition of Mercury's crust, the origin of Mercury's exosphere and even melting conditions within the mantle (Figure 1). A missing link in our understanding is that few studies have been conducted on how the relevant minerals (and their mixtures) behave under the extreme space weathering conditions found on Mercury.

Composition of Hollows: MESSENGER observations point to sulfides and graphite being components of hollows [1,2,3]. While graphite has essentially no compositional variability, highly reduced conditions can produce a myriad of exotic sulfides, many of which are found in the highly reduced enstatite chondrites. These include MgS (niningerite), CaS (oldhamite), djfisherite (K and Na bearing), $NaCrS_2$ (caswellsilverite), amongst others. An important point is that such sulfides in the crust of Mercury are unlikely to be pure, end-member compositions, and are likely to be mixed with other, equally complex sulfides, as well as other phases like graphite and silicate.

Experimental Approach: We are conducting a comprehensive study of the interaction of solar wind with potential hollow forming materials. Our approach is to start with pure minerals, then move to complex mineral compositions, and finally to mixtures of minerals. The mineral compositions are chosen to be consistent with phase equilibria studies of melts at low fO_2 [4,5].

A number of processes may be involved in hollows formation: thermally-induced sublimation, meteorite impact-induced vaporization, photon-stimulated desorption (PSD), ion-stimulated desorption (ISD) and electron-stimulated desorption (ESD) and evaporation [6,7]. Except for meteorite impact, all of these can be simulated at the EPICS lab at Georgia Tech [6]. Both the composition of released atoms, and their energies can be measured in-situ, and compared with observations on the composition of the exosphere [6]. Solid products of the experiments will be measured by VNIR spectroscopy and can be compared to hollows observations, such as the bright halo material and the darkening of the hollow floors [1,2,3]. Ideally, by combining constraints from the exosphere composition, the spectroscopy of hollows and phase equilibria of reduced materials, better constraints will be placed on what material makes up the hollows and what processes are producing them.

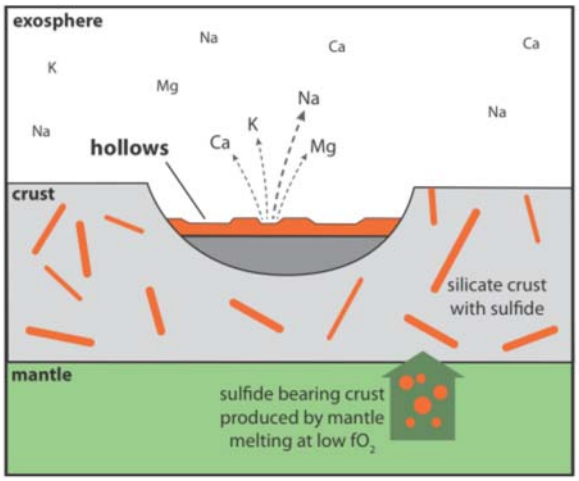

Figure 1. Hollows link the exosphere to the crust to the mantle. The hollows forming material (red) is located in the crust, highly associated with LRM [2]. The crust was produced by mantle melting, and so understanding the composition of the crust yields clues to mantle melting conditions. Whatever elements are sublimating from the hollows must contribute to the composition of the exosphere.

Preliminary data on CaS and MgS, suggest desorption under normal solar conditions is too slow to produce the topography of hollows, suggesting that if these are the hollows forming material, either sublimation or desorption under flare-conditions are responsible.

References: [1] Blewett D.T. et al (2016) JGR, 121, 1798–1813. [2] Thomas R.J. et al. (2014) Icarus 229, 455-465. [3] Vilas F. et al (2016) GRL, 43, 1450–1456. [4] Namur et al (2016) EPSL, 448, 102-114. [5] Vander Kaaden K.E. and McCubbin F.M. (2016) GCA 173, 246-263. [6] McLain J.L. et al (2011) JGR 116 [7] Bennet C.J. et al (2016) JGR 121, 137-146.

GEOLOGICAL MAPPING OF THE DEBUSSY QUADRANGLE (H-14) PRELIMINARY RESULTS

D. L. Pegg[1], D. A. Rothery[1], M. R. Balme[1], and S. J. Conway[2]. [1]The Open University, Milton Keynes, MK7 6AA, UK david.pegg@open.ac.uk. [2]LPG Nantes – UMR CNRS 6112, Université de Nantes, France.

Introduction: Geological mapping of Mercury is crucial to build an understanding of the history of the planet and to set the context for BepiColombo's observations [1]. Geological mapping of the Debussy quadrangle (H-14) is now underway as part of a program to map the entire planet at a scale of 1:3M using MESSENGER data [2]. The quadrangle is located in the southern hemisphere of Mercury at 0° – 90° E and 22.5° – 65° S. This will be the first high resolution map of the quadrangle as it was not imaged by Mariner 10.

Data and Methods: Mapping began in October 2017 using the MESSENGER 166 mpp mosaic as a base map supplemented with additional images from MESSENGER's Mercury Dual Imaging System.

Line work is currently underway. Craters larger than 5 km have been outlined. Ejecta, where observed, is being traced for craters larger than 20 km. Craters are classified based on crater degradation on both 3 class [3] and a 5 class [4] schemes. Tectonic features are shown by linework and extensive plains are being mapped as Intercrater or Smooth plains.

Features of Debussy Quadrangle: There are several large-scale features within the Debussy quadrangle that are of particular interest during mapping:

Rembrandt Basin: This 720 km diameter impact crater is the largest well-preserved basin in Mercury's southern hemisphere [5]. Smooth volcanic plains (lavas), which postdate the impact, partially fill the basin. Rembrandt hosts many of the features characteristic of large basins including wrinkle ridges, grabens, and ghost craters[6].

Enterprise Rupes: The cooling and contraction of Mercury has led to the formation of thrust faults [7]. Enterprise Rupes cuts across Rembrandt basin. It can thus play an important part in building understanding of the tectonic history of the planet [5]. The interaction of the lobate scarps with other landforms illustrates the structural controls that pre-existing landforms can have on the morphology of scarps [8]. Other rupes in the quadrangle include the east-west trending Belgica Rupes and the north-south Nautilus Rupes.

References: [1] Benkhoff J. et al. 2010 *Planet. Space Sci.* 58:2-20 [2] Galluzzi V. and BC Mapping team. 2017. 5th BepiColombo SWT Meeting. [3] Kinczyk M.J. et al. 2016. *LPSC*. 47: 1573. [4] Galluzzi V. et al. 2016. *J. Maps*, 12: 227-238. [5] Ferrari S. et al. 2015. *GSL Special Publications*. 401: 159-172. [6] Whitten J.L. et al. 2015. *Icarus*. 258: 350-365. [7] Watters T.R. et al. 2004. *GRL*. 31: L04701. [8] Ruiz J. et al. 2012. *Icarus*. 219: 511-514.

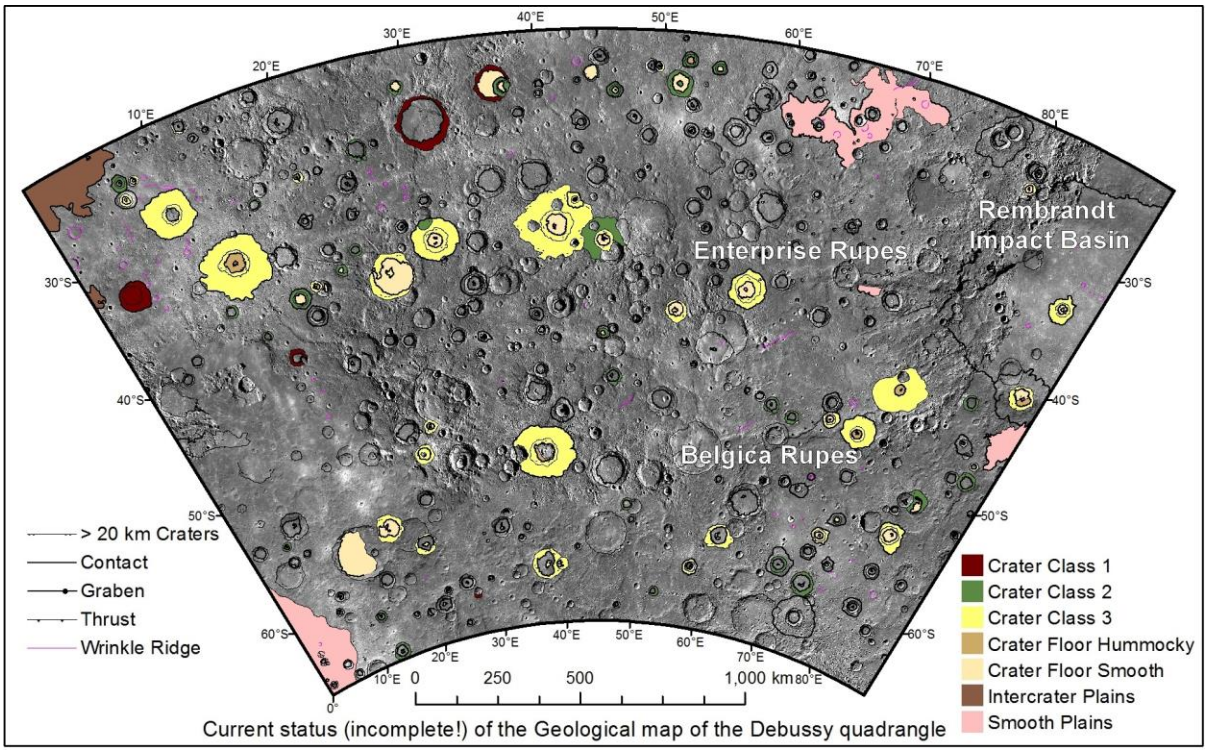

Current status (incomplete!) of the Geological map of the Debussy quadrangle

MERCURY'S GEOCHEMICAL TERRANES REVISITED. P.N. Peplowski[1*], K. R. Stockstill-Cahill[2], [1]Johns Hopkins Applied Physics Laboratory, 11100 Johns Hopkins Road, Laurel, MD 20723 USA; 2 Planetary Science Institute, Tucson AZ USA; [*]Patrick.Peplowski@jhuapl.edu.

Introduction: Prior efforts [1, 2] to map geochemical terranes on Mercury: 1) used limited inputs, 2) classified the surface into nonphysical "binary" terranes, 3) used subjective chemical definitions for terranes, and, in the case of [1], 4) a priori adopted geomorphological boundaries for some terranes. We resolve these issues with a new terrane mapping process that uses a robust analytical methodology for terrane identification.

Geochemical terranes were identified from a principle component analysis (PCA) of Mg/Si, Al/Si, [1] and K [3] elemental composition maps, produced from MESSENGER XRS and GRS data. These maps were chosen due to their complete northern hemisphere coverage. Mapping was restricted to the northern hemisphere due to poor or absent coverage of the southern hemisphere.

Results: The results of the PCA are shown in Fig. 1. PC1 (green) corresponds to low-Mg, low-Al, high-K materials, PC2 (red) corresponds to high-Mg, low-Al materials, and PC4 (blue) is low-Mg, high-Al materials. PC3 was not used. PC1, 2, 3, and 4, contain 60%, 24%, 11%, and 5% of the total variability on the surface, respectively. Scatter plots of the Mercury geochemical data, color-coded by geochemical terrane, are shown in Fig. 2. A more extensive set of scatterplots can be found in [6], including S/Si, Ca/Si, Fe/Si, and neutron data.

Discussion: These results are consistent with prior geochemical terrane mapping [1,3]. However, unlike [1], our terrane boundaries are derived entirely from elemental data and it is apparent that there is not a one-to-one relationship between geochemical and geomorphological units (Fig. 1). This undermines a key assumption of prior geochemical modeling efforts [7, 8] that assumed an equivalence between the northern volcanic plains and the northern geochemical terranes.

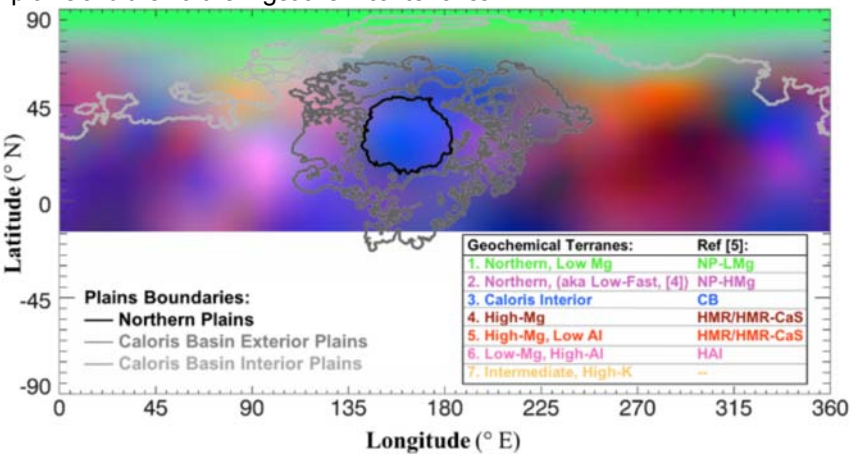

Figure 1. PCA of Mercury chemical maps, used to define geochemical terranes.

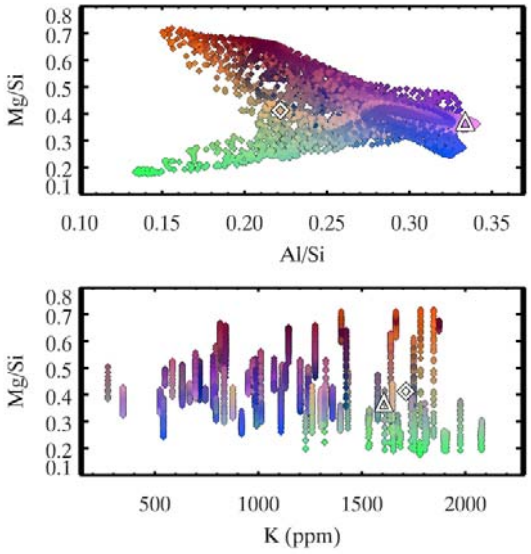

Figure 2. Element scatter plots, color-coded by PC (see Fig. 1). The mean values for the IHK and HAl terranes are marked as a diamond and triangle, respectively.

We classify a previously unrecognized terrane, the Intermediate, High-K (IHK) terrane, which is associated with the ejecta of the ~180-km-diameter Rustavelli basin. Its location suggests that it excavated HMR-like materials from beneath overlying northern-terrane-like materials, however it is mixed with higher K than is observed in HMR. Additionally, we note that the previously identified Low-Mg, High-Al (HAl) terrane appears as an end-member in the Mg/Si vs. Al/Si phase-space (Fig. 2), suggesting an important role in Mercury's petrology.

References: [1] Weider, S.Z. et al. (2015), EPSL 416, 109. [2] Peplowski, P.N. et al. (2015), Icarus 253, 346. [3] Peplowski, P.N. et al. (2012), JGR Planets 117, E00L04. [4] Lawrence, D.J. et al. (2017), Icarus 281, 195. [5] Vander Kaaden, K. E. et al. (2017), Icarus 285, 155-168. [6] Peplowski and Gleyzer (2017), 48th LPSC, abstract 1592. [7] Namur, O. et al. (2016), EPSL 439, 117. [8] Vander Kaaden and McCubbin (2016), Geochimica et Cosmochimica Acta 173.

DISTRIBUTION OF AREAL STRAIN ON MERCURY: INSIGHTS INTO THE INTERACTION OF VOLCANISM AND GLOBAL CONTRACTION. G. A. Peterson[1], C. L. Johnson[1,2], P. K. Byrne[3], and R. J. Phillips[4], [1]Department of Earth, Ocean and Atmospheric Sciences, University of British Columbia, Vancouver, BC, V6T 1Z4 (gpeterso@eoas.ubc.ca), Canada, [2]Planetary Science Institute, Tucson, AZ 85719, USA, [3]Planetary Research Group, Department of Marine, Earth, and Atmospheric Sciences, North Carolina State University, Raleigh, NC 27695, USA, [4]Dept. of Earth and Planetary Sciences and McDonnell Center for the Space Sciences, Washington University, St. Louis, USA.

Introduction: Deformation on Mercury is dominated by thrust faults, which vary in relief, length, and areal density. [1,2,3]. Cooling of Mercury's interior is thought to have decreased the planet's radius by 5–10 km [1,4]. Thrust fault-related landforms (i.e., lobate scarps and high-relief ridges) within the "intercrater plains" (ICP) reflect this large crustal shortening [1,2,3] and have maximum relief of 1–3 km and lengths of up to 500 km. The ICP is the oldest (~4.1 Ga) and most extensive geological unit exposed at the surface. In contrast, smaller-scale wrinkle ridges mainly occur in areas of volcanic smooth plains (SP). Wrinkle ridges on average have relief of 400 m and lengths of 50 km, and are thought to be shallowly-rooted thrust faults exploiting mechanical detachments within the volcanic strata [1,2,3]. At least some wrinkle ridges have resulted from flexure of the lithosphere due to volcanic loading, and likely accommodated little strain compared to the ICP, specifically that arising from global contraction [1,2,3].

However, recent mapping with MESSENGER data have shown that the SP hosts more faults per unit area than the ICP [1]. Approximately 63% of the mapped shortening structures and 50% of the total mapped fault length are within the SP, although the SP occupies only 27% of the planetary surface area [1].

Here, we analyze relative areal strain distributions among the ICP, SP, and the northern smooth plains (NSP) alone, which is the largest single SP deposit, to assess whether stresses from global contraction contributed to the formation of SP and/or NSP landforms.

Areal Strain Study: Strain estimates follow methods documented previously [1,5]. We assessed the relief of 25% of Mercury's total mapped fault population [1]. The maximum relief was used to estimate the maximum displacement (D_{max}) assuming dip values of 25°, 30°, and 35°. The total fault strain can be found by summing the horizontal shortening (D_{max} times the fault length) for each fault in the SP, NSP, and ICP and then dividing by the respective surface area of each region [1,5]. In cases where the relief of the landform could not be estimated, D_{max} was calculated from a scaling relation (γ), determined from those faults where the relief was characterized [5]. Results for γ and strain are given in Table 1 as a function of fault dip.

Results and Discussion: Areal strain results show that the SP overall, and the NSP specifically, host more shortening strain per area than the ICP, suggesting that the SP has been substantially deformed by global contraction.

Furthermore, in the ICP strain is localized to the largest faults: 50% of the strain is accommodated by the 15% of the fault population that has lengths greater than 150 km. This could help explain the contrast in relief, length, and areal density observed between the SP and ICP. If the lithosphere in the SP is mechanically weaker, perhaps because of décollements within the lava deposits [1], this would promote the formation of many small landforms (i.e., strain would be evenly distributed among many faults). In contrast, shortening strains might concentrate into fewer, larger structures in crust that apparently lacks such distinct strata, such as in the ICP units. Additionally, the ICP has relatively large spatial gradients in crustal thickness not seen in the SP. These variations may localize shortening strains, creating faults with large reliefs and lengths where thick and thin crust are proximal [1].

Finally, initial results from dislocation modelling suggest that thrust faults in the SP could penetrate to depths of 25 km—inconsistent with the wrinkle ridge structures being thin-skinned but consistent with having accumulated a large amount of strain. [6].

Fault dip angle	25°	30°	35°
γ_{SP}	0.0087	0.0074	0.0064
γ_{ICP}	0.0010	0.0084	0.0074
Compressional Strain			
SP	0.0070 (-0.0008,+0.0023)	0.0056 (-0.0006,+0.0019)	0.0046 (-0.0005,+0.0015)
NSP	0.0065 (-0.0007,+0.0020)	0.0053 (-0.0006,+0.0016)	0.0043 (-0.0005,+0.0013)
ICP	0.0042 (-0.0003,+0.0009)	0.0034 (-0.0003,+0.0007)	0.0028 (-0.0002,+0.0006)

Table 1: Derived γ and strain estimates for the SP and ICP for θ of 25°, 30°, and 35°.

References: [1] Byrne et al. (2014) Nature Geosci., 7, 301-307 [2] Melosh, H. J. & McKinnon, W. B. (1988) Univ. Arizona Press., 374–400 [3] Watters and Nimmo (2010)., Cambridge Univ. Press [4] Tosi et al. (2015) Geophys. Res. Lett., 42, 7327-7335 [5] Cowie et al., (1993) Geophys. Res. Lett., 98, 17911- 17920 [6] Peterson et al., (2017) LPS XLVIII Abstract # 2315

THE SHAPE OF MERCURY'S MAGNETOPAUSE: WHAT CAN BEPICOLOMBO TELL US?. L. C. Philpott[1], C. L. Johnson[1,2], B. J. Anderson[3], and R. M. Winslow[4], [1]Department of Earth, Ocean and Atmospheric Sciences, University of British Columbia, Vancouver, BC, Canada V6T 1Z4, lphilpott@eoas.ubc.ca, [2]Planetary Science Institute, Tucson, AZ, USA, [3]The Johns Hopkins University Applied Physics Laboratory, Laurel, MD, USA, [4]Institute for the Study of Earth, Oceans, and Space, University of New Hampshire, Durham, NH, USA,.

Introduction: The MErcury Surface, Space ENvironment, GEochemistry, and Ranging (MESSENGER) mission enabled global observations of Mercury's magnetosphere. In particular, the time-averaged two-dimensional geometry of Mercury's magnetopause, as well as temporal variations in the overall shape have been mapped and described via empirical models [1, 2, 3, 4]. Three-dimensional (3-D) models of the magnetopause shape have been attempted [5], that include dawn-dusk asymmetries and a northern cusp indentation. However, such asymmetries and any other 3-D structure are more difficult to establish because of coverage limitations of the MESSENGER data. Here we quantify the extent to which MESSENGER observations can establish departures of Mercury's magnetopause from axisymmetry and we examine how BepiColombo observations will further improve our understanding of the magnetopause shape.

MESSENGER Data: Analyses and Results: Using magnetic field data from the onboard Magnetometer (MAG), we update the list of MESSENGER magnetopause crossings [1], to cover the entire orbital mission, and find best-fit axisymmetric [6] and 3-D [5] models (Fig. 1). Although a 3-D model provides a lower misfit to the data, some parameters are not well constrained. To understand MESSENGER data limitations in the cusp region we consider all MAG data in the region $-0.5R_M \leq Y_{MSM} \leq -0.5R_M$, where MSM denotes Mercury Solar Magnetospheric coordinates [see e.g., 1] and R_M denotes 1 Mercury radius. We calculate the probability of being inside the magnetopause in 0.01 R_M bins in the X-Z plane, using observed innermost magnetopause crossings on each orbit. Figure 1 shows that MESSENGER observations are consistent with an axisymmetric magnetopause and that data is lacking in the region that constrains a cusp indentation.

BepiColombo Data Coverage Simulations: With two spacecraft, the Mercury Planetary Orbiter (MPO) and Mercury Magnetospheric Orbiter (MMO), in magnetopause crossing orbits, BepiColombo will provide data in areas not covered by MESSENGER (notably the southern hemisphere), as well as simultaneous measurements in different regions. Using pre-operational spice kernels [7] we simulate where MPO and MMO will cross the magnetopause for axisymmetric and 3-D model magnetopause shapes. Model parameters from best-fits to MESSENGER data are used,

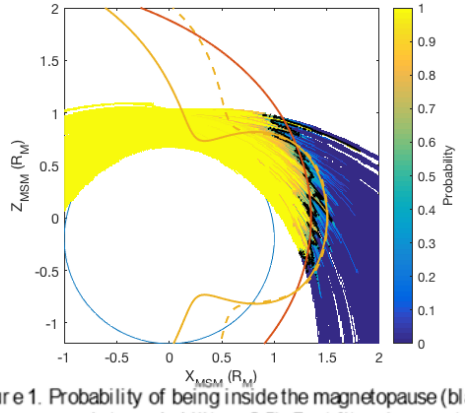

Figure 1. Probability of being inside the magnetopause (black contour corresponds to probability = 0.5). Best fit axisymmetric (orange) and 3-D (yellow, solid) magnetopause shapes are shown. For reference, the best fit magnetopause shape found by [2] using a smaller data set is shown in yellow (dashed).

including variation of the magnetopause standoff distance with Mercury heliocentric distance (see e.g., [4]), and simulations include random noise. The probability of being inside the magnetopause is calculated. Figure 2 shows that BepiColombo may allow us to constrain a cusp indentation, while also providing key information about the southern hemisphere magnetopause.

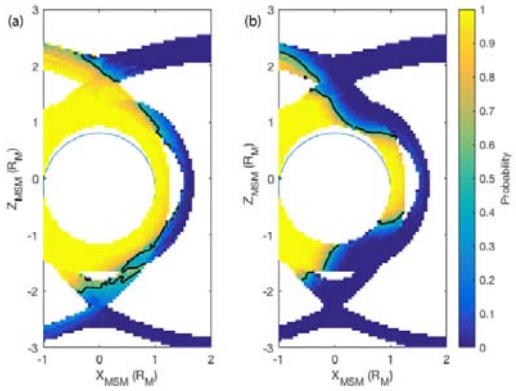

Figure 2. Probability of being inside the magnetopause, based on simulated magnetopause crossings for MMO and MPO, assuming (a) axisymmetric and (b) 3-D magnetopause shapes.

References: [1] Winslow R. M. et al. (2013) JGR: Space Physics, 118, 2213-2227. [2] Johnson C. L. et al. (2016) GRL, 43, 2436-2444. [3] Korth H. et al. (2015) JGR: Space Physics, 120, 4503-4518. [4] Korth H. et al. (2017) GRL, 44. [5] Zhong J. et al. (2015) JGR: Space Physics, 120, 7658-7671. [6] Shue J.-H. et al. (1997) JGR, 102, 9497-9511. [7] ftp://spiftp.esac.esa.int/data/SPICE/BEPICOLOMBO/kernels.

REGIONAL MODELING AND POWER SPECTRA OF MERCURY'S CRUSTAL MAGNETIC FIELD. A. M. Plattner[1] and C. L. Johnson[2, 3], [1]Dept. of Earth and Environmental Sciences, California State University, Fresno, CA 93740, USA. aplattner@csufresno.edu, [2]Dept.of Earth, Ocean and Atmospheric Sciences, University of British Columbia, Vancouver, BC, V6T 1Z4, Canada. [3]Planetary Science Institute, Tucson, AZ 85719, USA.

Overview: Mercury's magnetic field recorded by the MErcury Surface, Space ENvironment, GEochemistry, and Ranging (MESSENGER) satellite mission contains a crustal component first described by [1]. Data at sufficiently low altitudes to successfully measure the weak crustal field are only available for latitudes north of ~30°N because of MESSENGER's highly eccentric orbit. As a consequence, regional methods are required to invert for crustal magnetic field models. Here we present models obtained using two different approaches: altitude-cognizant gradient vector Slepian functions (AC-GVSF) as described by [2] using the software available from [3], and equivalent-source dipoles (ESD) [4]. The two models shown in Fig. 1 differ in their fine-detail structure but reveal the same large- and medium-scale patterns. For each of the models, we calculated a regional Mauersberger-Lowes power spectrum using the method of [5] for latitudes 45° N to 72° N and for three spherical caps, each covering a distinct region (Fig. 2).

Crustal Magnetic Field Modeling: Mercury's magnetic field is dominated by contributions from the core dynamo and from magnetospheric current systems. We remove these by subtracting the magnetospheric model of [6] and then using an orbit-by-orbit along-track filter [1]. The data cover our modeling region unevenly as the track-to-track distance at lower latitudes is substantially greater than that near the poles. To avoid model artifacts from uneven sampling, we randomly subsampled the data 200 times using an equal-area approach. For each of the 200 data sets, we calculated, and then averaged, individual AC-GVSF models for latitudes 45° N to 72° N (Fig. 1, left). We used the same approach to obtain a mean ESD model for the region north of 38° N (Fig. 1, right).

Regional Power Spectra: For both the AC-GVSF model and the ESD model, we calculated regional power spectra using the approach described by [5]. Fig. 2 shows the spectra for the area between latitudes 45° N to 72° N ("ring") and for the spherical caps indicated in Fig. 1. The AC-GVSF model (solid) focuses on the spherical-harmonic degrees up to 110 and minimizes contributions from the more noise-sensitive higher degrees, whereas the ESD model (dashed) evenly distributes the model energy over the higher degrees. The "meridian" region is weakly magnetized. The "Rustaveli" region is similar but with more energy at the wavelengths associated with the Rustaveli Basin. Decorrelation depths [7] are consistent with crustal sources in these regions. The "Caloris" region, north of the Caloris Basin, contains more energy in the low spherical-harmonic degrees, indicating that the magnetic sources are either at greater depths, or are spatially correlated over large areas, e.g., Caloris impact melt or ejecta. The "ring" spectrum is a superposition of the spectra for the distinct regions.

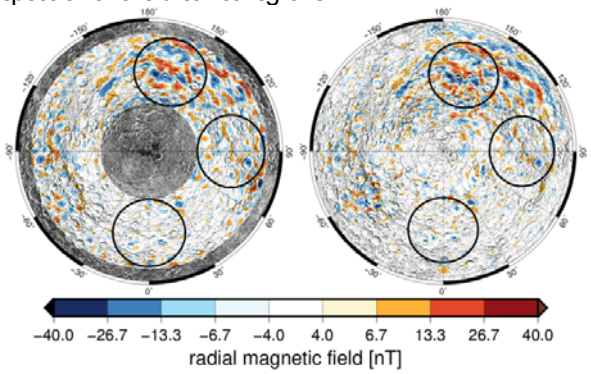

Figure 1. Left: Mean AC-GVSF model, right: mean ESD model. Both radial crustal magnetic field models are projected onto the planet's surface approximated by a sphere of radius 2440 km. Black circles denote the regions for the power spectra in Fig. 2: "Caloris" (165° E), "Rustaveli" (90° E), "meridian" (0° E).

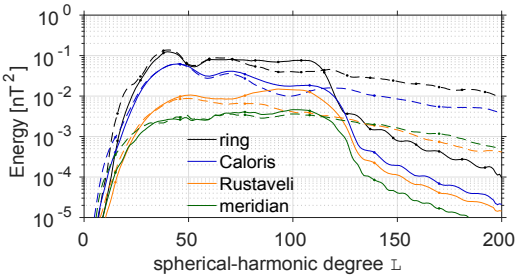

Figure 2. Regional power spectra for latitudes 45° N to 72° N ("ring") and the 13° spherical caps shown in Fig. 1. Solid lines are for the AC-GVFS model (Fig. 1, left), dashed lines for the ESD model (Fig. 1, right).

References: [1] Johnson C. L. et al. (2015) Science, 348, 892. [2] Plattner A. and Simons F. J. (2017) GJI, 211, 207-238. [3] Plattner A. (2017), doi: 10.5281/zenodo.583624. [4] Langel R. A. and Hinze W. J. (1998). [5] Wieczorek M. A. and Simons F. J. (2005) GJI, 162, 655-675. [6] Korth H. et al. (2017) GRL, 44, 10147-10154. [7] Voorhies C. V. et al. (2002), JGR, 107, E6, 5034.

A COMPREHENSIVE MODEL OF THE METEOROID ENVIRONMENT AROUND MERCURY

P. Pokorny[1,3], M. Sarantos[2] and D. Janches[3], [1]Department of Physics, The Catholic University of America, Washington, DC 20064, USA (petr.pokorny@nasa.gov), [2]Geospace Physics Laboratory, Code 673, NASA Goddard Space Flight Center, Greenbelt, MD 20771, [3]Space Weather Laboratory, Code 674, NASA Goddard Space Flight Center, Greenbelt, MD 20771

We present our latest model for the meteoroid environment surrounding the orbit of our innermost solar system planet, Mercury. Our model takes on where our preliminary model [1] finished. We combine contributions of four distinctive sources of meteoroids in the solar system: main-belt asteroids, Jupiter family comets, Halley-type comets, and Oort Cloud comets. All meteoroid populations are described by currently available dynamical models that have been thoroughly tested and applied to explain various phenomena in the inner solar system [2],[3],[4],[5]. In this contribution we will show unique characteristics of individual meteoroid populations surrounding Mercury. We present vastly different distributions of orbital elements, impact velocities and directions for all four meteoroid populations and their variations with different scenarios for size-frequency distributions and collisional grooming. Furthermore, we use a recent calibration of meteoroid influx onto Earth [3] as a pivot for the combined population model on Mercury. Due to a large degree of free parameters in our models we explore the robustness of our solution for a suite of models. Our preferred solution provides a good agreement with previously reported Mercury's exosphere observations by the MESSENGER spacecraft and is not highly sensitive to variations of model free parameters.

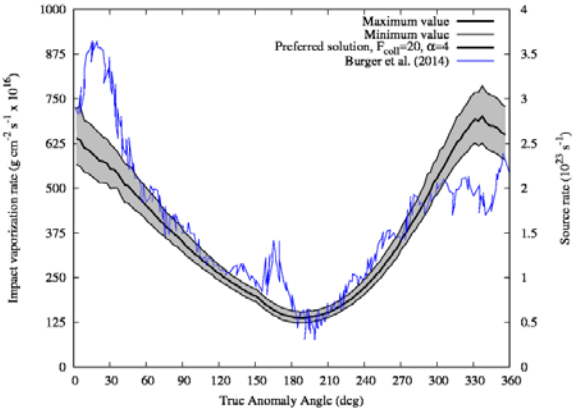

Figure 1. The impact vaporization rate in absolute units with respect to the true anomaly angle of our preferred solution (solid thick black line), the confidence interval (gray area and thin black lines representing interval boundaries), and the source rate from [6] (blue solid line using the secondary y-axis).

We provide a fully calibrated model with the high-resolution maps of flux and vaporization rates for different values of the true anomaly angle (Figure 1).

References:

[1] Pokorny P., et al. (2017), ApJL, 842L, 17, [2] Janches D. et al. (2018), GRL, accepted, [3] Carrillo-Sanchez J. D. et al. (2016), GRL, 43, 23, 11979, [4] Nesvorny D. et al. (2011), ApJ, 743, 129, [5] Pokorny P. et al. (2014), ApJ, 789, 25, [6] Burger M. H. et al. (2014), Icarus, 238, 51

HIGH-RESOLUTION TOPOGRAPHY FROM MESSENGER ORBITAL STEREO IMAGING – THE SOUTHERN HEMISPHERE. F. Preusker[1], A. Stark[1], J. Oberst[1,2], K.-D. Matz[1], T. Roatsch[1], S. Burmeister[2], and K. Gwinner[1], [1]German Aerospace Center, Institute of Planetary Research, D-12489 Berlin, Germany, [2]Technical University Berlin, Institute for Geodesy and Geoinformation Sciences, Berlin, Germany.

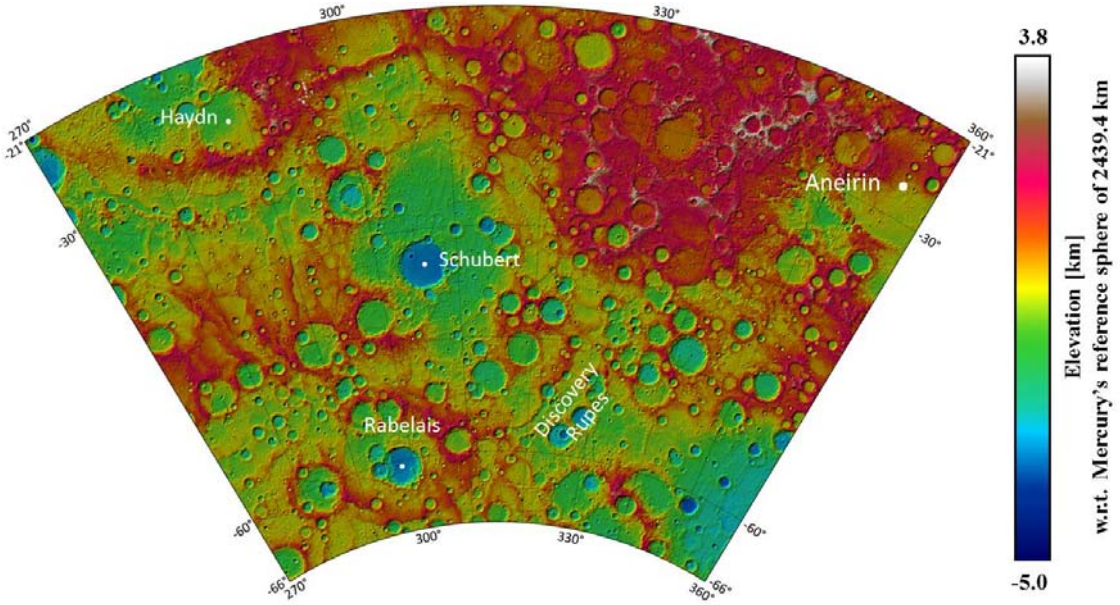

Fig. 1. H11 ("Discovery") DTM (hill-shaded color-coded heights) in Lambert two-parallel (conformal) projection.

Introduction: The MErcury Surface, Space ENviorment, GEochemistry, and Ranging (MESSENGER) spacecraft entered orbit about Mercury in March 2011 [1] to carry out a comprehensive topographic mapping of Mercury. Measurements of Mercury's topography have been made using stereo imaging [2], laser altimetry [3], limb profiling [4], and radio occultation [5]. We describe the production of a high-resolution digital terrain models (DTM) of Mercury's Southern hemisphere quadrangles using stereo photogrammetry.

Data: The Mercury Dual Imaging System (MDIS) onboard MESSENGER spacecraft consists of a wide-angle camera (WAC) and a narrow-angle camera (NAC) co-aligned on a pivot platform. In almost 4 years of mapping MDIS has acquired more than 200,000 images. Owing to MESSENGER's highly eccentric orbit, associated with a pericenter near the North Pole, the WAC is primarily used to cover the northern hemisphere and the NAC to cover the southern hemisphere, respectively. Approximately 125,000 images with a mean image scale of about 160 m/pixel have been used to date.

Method: The stereo-photogrammetric processing is based on a proven software suite, which comprises photogrammetric block adjustment, multi-image matching, surface point triangulation, DTM generation, and base map production [2,6]. In order to manage the complexity and challenges of the global surface reconstruction, we chose to derive individual terrain models following a scheme of 15 quadrangles proposed for Mercury.

Results: Each quadrangle tile contains between 10,000 and 15,000 individual images, among which we typically identify about 30,000 to 50,000 stereo image combinations consisting of at least three images each. We first corrected for errors in the nominal pointing and position data using a photogrammetric block adjustment, which improved the three-dimensional (3D) point accuracy in all tiles from about ±800 m to about ±50 m. Next, individual image matching runs were carried out to yield two to seven billion surface points. Finally, we generated a DTM for each tile with a lateral spacing of 192 pixel/degree (~222 m/pixel) and a vertical accuracy of about 30 m (Fig. 1.). While we previously reported on the map quadrangles H3, H5, H6, and H7 [6-9], we will report about progress in the processing of the southern Quadrangles H11 - H15 at the time of this meeting.

References: [1] Solomon et al. (2011), EPSC-DPS, Abstract #430. [2] Preusker et al. (2011), PSS, 59, 1910–1917. [3] Zuber et al. (2012), Science, 336, 217-220. [4] Elgner et al. (2014), PSS, 103, 299-308. [5] Perry et al. (2011), PSS, 59, 1925-1931. [6] Preusker et al. (2017), PSS., 142, 26-37. [7] Oberst et al. (2017), LPSC, Abstract #1442. [8] Stark et al. (2017), LPSC, Abstract #2287. [9] Preusker et al. (2017), LPSC, Abstract #1441.

PHOTOMETRY ESTIMATION OF THE STRUCTURE OF THE SURFASE LAYER OF MERCURY SOUTH POLE RELIEF.

S. G. Pugacheva[1], E. A. Feoktistova[1], V. V. Shevchenko[1], [1]Sternberg Astronomical Institute, Moscow State University, Universitetsky 13, Moscow 119992, Russia, pugach@sai.msu.ru.

Introduction: The paper reveals results of Mercury South pole surface relief research by photometry methods. The photometry method searches out the intensity of reflectivity of planet's surface and provides studying of ground fine texture. Main materials of the research are photographic images of Mercury surface transferred by "Messenger" interplanetary station during its passing near Mercury. For Mercury surface relief structure evaluation the images of Mercury Southern hemisphere have been used. The photographic images of Mercury surface transferred by "Messenger" have high spatial resolution of 2 km/pixel, while the accuracy of Southern hemisphere altitudes evaluation makes at average 1.5 m.

Features of Mercury surface relief: According to its photometric features Mercury resembles the Moon, however the planet has its unique physical characteristics. Surface of Mercury is the combination of craters, worn-down plains, saw-edged cliffs (escarps) and ray patterns. The relief of Mercury surface differs with numerous escarps hundreds kilometers long, formation of which is linked with compression processes in crust taken place during cooling of mantle and partial consolidation of planet's core. During its passing near Mercury "Messenger" had transferred photographs of Mercury surface with earlier unknown formations represented with immensely long rays that look like meridians emerging from recent craters located near north limb.

Photometric evaluation of Mercury surface relief: Main types of Mercury surface are: cratered terrain and intercrater plains that had demolished craters with low diameter. We have selected several photographs of Mercury Southern hemisphere made by "Messenger". Each image has reference data and a calibration scale for translating the image density into relative brightness values [1]. The photographs have been processed by pixel scanning system for definition of surfaces with equal brightness [3]. At the same time, using MultiSpecWin32 system we have defined areas with different reflectivity. Thus, we have evaluated surface roughness and relative number of impact craters on it. As a result, three main morphological units have been obtained: the surface with low reflection coefficient characterized by high roughness and high density of impact craters; the surface of linear form characterized by extra low reflection coefficient; and even surface characterized by less density of craters and median reflectivity, which is typical for relatively recent formations. Photometric processing of space photographs made by Mariner-10 and "Messenger" space vehicles allowed us to evaluate various type of Mercury surface reflectivity and define its soil structure. In general the surface of Mercury is being more homogeneous and monotonous by its photometric parameters [2]. Radar researches of circumpolar areas reveal presence of ice in shadow points of craters in polar areas of Mercury. The result of modeling the surface structure of the Mercurian regolith layer using the photometric properties shown that the lunar regolith upper layer is more rough than the modeled surface layer of the Mercury regolith.

Conclusion: Photographic images transferred to Earth helped to determine that in the past on Mercury quite intense tectonic activity had place. Its traces can be found in the Eastern and Western hemispheres of the planet in the form of large even plains. "Messenger" discovered new earlier unknown craters within the area of Mercury South pole. During its passing near the planet "Messenger" made carried out research of Mercurian atmosphere and revealed traces of recent volcanic eruptions. Thus, as of today about 98% of Mercury surface is explored.

References: [1]. Hapke B. (2005) *Cambridge university press*. 455 p. [2] Head J. et al. (2008) *Science*. V. 321. P. 69-72. [3] Shevchenko V. V. (2004) *Astron. Vestn*. V. 38. №6. P. 504-512.

Planetary ions at Mercury: Unanswered questions after MESSENGER

Jim M. Raines

MESSENGER made the first ever measurements of ions at Mercury during its 2008 flyby. These observations continued through the four years in orbit around Mercury, 2011-2015, producing hundreds of thousands of ion spectra. Studies of this data have revealed a tremendous amount about Mercury's magnetosphere. Measurements of ions from Mercury itself, planetary ions, have been shown to be ubiquitous in its space environment, present on every orbit and in every region around the planet. Besides serving as additional tracers of magnetospheric physics, studies of these planetary ions have begun to show connections to Mercury's exosphere and even its surface. However, there is still much more to learn, both from further analysis of MESSENGER data and from measurements to be made by the upcoming BepiColombo mission. We will discuss the key open questions relating to planetary ions, including the behavior of recently created photoions, the near absence of Ca+ / K+ in MESSENGER ion measurements, and the role of ion sputtering in the system.

First in-situ observations of exospheric response to CME impact at Mercury

Jim M. Raines, Kathryn L. Wallace, Menelaos Sarantos, Jamie M. Jasinski, Patrick J. Tracy, Ryan M. Dewey, Micah J. Weberg, and James A. Slavin

We present the first in-situ observations of enhancements to Mercury's He exosphere generated by CME impact. We analyzed both plasma and magnetic field measurements from the Mercury Surface Space Environment, Geochemistry and Mapping (MESSENGER) spacecraft over a 60-hour period as a coronal mass ejection (CME) passed by the planet. We identified the shock, magnetic cloud and cavity regions of the moderate intensity CME while MESSENGER was in the solar wind. Inside the magnetosphere just after the CME shock passage, we observed a very active dayside magnetosphere, as evident from the high flux plasma parcels passing through the dayside and a broad northern magnetospheric cusp with exceptionally high planetary ion content. All of these signatures indicate substantial reconnection at the dayside magnetopause, making conditions that were excellent for solar wind access to Mercury's surface. The CME appeared to have been particularly enriched in He2+, causing the observed density of solar wind He2+ in the cusp to rise above 0.1 cm^{-3} and putting it in the top 1% of the over 3200 cusps analyzed. As the low-density CME cavity passed over the planet on the next orbit, the magnetosphere appeared much quieter, with smoother magnetic fields and a smaller, less intense northern cusp but with greatly enhanced He+ content. The elevated He+ observed density continued to increase on subsequent cusp crossings, peaking at 0.1 cm^{-3} 36 hours after CME impact, the highest observed throughout the entire MESSENGER mission. We suggest that the enhancement in He+ indicates an increase to the neutral He exosphere density from the He-enriched CME, a phenomenon observed at the moon, possibly acting as follows: Increased access to the surface from CME-enhanced reconnection, combined with high He2+ flux, enhanced surface implantation. Neutral He atoms were then liberated at an increased rate by surface processes supplying the exosphere, causing a gradual increase in He exosphere density. This led to an increase in He+ abundance through photoionization and charge exchange, which, after acceleration on the dayside, was measured by MESSENGER. These first in-situ observations of exospheric response to CME impact at Mercury have implications for understanding exosphere generation and loss processes, as well space weathering of the planet's surface.

Thermochemical Evolution of Mercury's Mantle and the Formation of the Volcanic Plains. J. H. Roberts[1], P.N. Peplowski[1], A. M. Stickle[1], K. R. Stockstill-Cahill[2], B. W. Denevi[1], D. L. Buczkowski[1], and O. S. Barnouin[1]. [1]Johns Hopkins Applied Physics Laboratory, 11100 Johns Hopkins Road, Laurel, MD, 20724 (James.Roberts@jhuapl.edu), [2]Planetary Science Institute, 1600 E Fort Lowell Road, Tucson, AZ.

Introduction: Large portions of Mercury's surface are covered by smooth plains, which are interpreted to be volcanic in origin [1]. Extensive volcanism implies an era of convection in the Mercurian mantle, and widespread partial melting and secondary crustal production [2]. Gravity observations from MESSENGER suggest that the mantle of Mercury may be quite thin (< 400 km) [4], limiting the degree of crustal production that is possible before mantle convection shuts down [7]. Volcanic plains are also associated with impact basins (e.g., Caloris), which exhibit compositional and age differences from other plains units [5, 8–9].

Here we discuss analysis of MESSENGER Dual Imaging Spectrometer [1], Gamma-Ray and Neutron Spectrometer [10] and X-Ray Spectrometer (XRS) data [11] which could reconcile four independent observations and constraints related to the formation of volcanic plains on Mercury: 1) The longevity of volcanism [13–14]; 2) The low volume available for processing into secondary crust [4]; 3) The amount of internal heating available in the mantle (a function of partitioning of radioactive elements into the crust); and 4) Global contraction severely inhibiting subsequent melt production and magma ascent [5–7].

Constraining Crustal Production: The Mg/Si map shown in Figure 1 is interpreted [11, 14] to reflect underlying heterogeneities in the mantle, although the Mg map does not strongly correlate with the plains boundaries for reasons that are not yet understood. Although the Mg/Si content is similar in the northern plains and Caloris (right-hand edge of Fig. 1), Al/Si is higher in Caloris, and neutron absorption is also different for these regions, suggesting that they have sampled different mantle compositions. In order to fully interpret these data, it is necessary to model thermochemical evolution in the Mercurian mantle. We extend previous analyses [e.g., 15–17], using thermochemical convection models [18–19] to account for compositional evolution, using more recent estimates for the internal structure of Mercury to address challenges in sustaining convection [17], and a 3D geometry to more accurately estimate melt volumes [16] and lateral variations in magma distribution.

Sources of Volcanic Plains Material: Plains material can be produced through convective processes as described above. Impact melting is also a possibility, particularly at the high impact velocities expected at Mercury [20]. Heating from basin-forming impacts may significantly increase the temperature in pre-existing

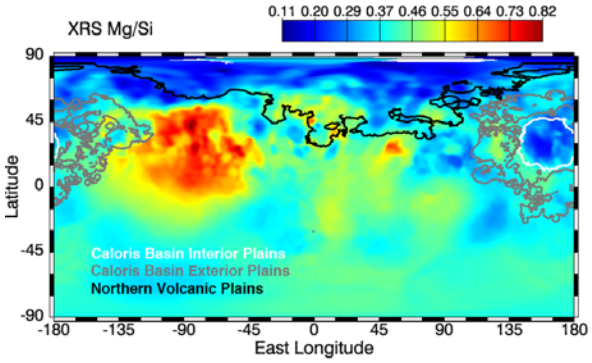

Figure 1: Map of Mg/Si derived from XRS data [12] with outlines of the plains units [1] superposed on it.

mantle upwellings adjacent to the impact site, but outside the present-day basin rim [18]. These upwellings would be much deeper than the surface rocks supplying the direct impact melt. Melt formed in these upwellings could be the source for the volcanic plains surrounding Caloris, which have a different age and spectral signature than the interior Caloris plains [5, 21]. The different melting processes may thus sample different depths in the mantle, and different residual compositions, and the volcanic plains may reveal pre-existing compositional stratification [5, 22]. Early impact melting may suppress later volcanism by prematurely using up the more easily melted components.

References: [1] Denevi, B. W. et al. (2013), JGR 118, 891–907. [2] Nittler, L. R. et al. (2011), Science 333, 1847–1850. [3] Hauck, S. A. et al. (2013), JGR 118, 1204–1220. [4] Knibbe, J. S. and van Westrenen, W. (2015), JGR 120, 1904–1923. [5] Denevi, B. W. et al. (2009), Science 324, 613–618. [7] Byrne et al. (2016), GRL 43, 7408–7416. [8] Murchie, S. L. et al. (2008), Science 321, 73–76. [9] Whitten, J. L. and Head, J. W. (2015), Icarus 258, 350–365. [10] Peplowski, P. N.. et al. (2012), JGR 117, E00L04. [11] Weider S. Z. et al., (2015), EPSL 416, 109–120. [12] Prockter, L. M. et al. (2010), Science 329, 668–671. [13] Ostrach, L. R. et al. (2015), Icarus 250, 602–622. [14] Peplowski, P. N.. et al. (2015), Icarus 253, 346–363. [15] Tosi et al. (2014), JGR 118, 2474–2587. [16] Roberts, J. H. and Barnouin, O.S. (2012), JGR 117, E02007. [17] Michel, N. C. et al. (2013), JGR 118, 1033–1044. [18] Zhong, S. et al. (2000), JGR 105, 11063–11082. [19] Tan et al. (2006), G3 7, Q06001. [20] Le Feuvre, M. and Wieczorek, M. A. (2008), Icarus 197, 291–306. [21] Fassett, C. I. et al. (2009), EPSL 285, 297–308. [22] Ernst, C. M. et al. (2015), Icarus 250, 413–429.

THE CHAOTIC TERRAINS OF MERCURY: A HISTORY OF LARGE-SCALE CRUSTAL DEVOLATILIZATION. J. A. P. Rodriguez[1], D. L. Domingue[1], D. C. Berman[1], J. S. Kargel[1], V. R. Baker[2], L. F. Teodoro[3], M. Banks[4], and G. Leonard[5], [1]Planetary Science Institute (1700 E Fort Lowell Road, Suite 106, Tucson, AZ 85719, USA, alexis@psi.edu), [2]Department of Hydrology and Atmospheric Sciences, University of Arizona, Tucson, AZ, USA, [3]NASA Ames Research Center, Moffett Field, CA, USA, [4]NASA Goddard Space Flight Center, Goddard, MD, USA, [5]Catalina Sky Survey, University of Arizona, Tucson, AZ,USA.

Introduction: The finding of abundant volatile-bearing outcrops on Mercury's surface comprises one of the critical discoveries by MESSENGER (Mercury Surface Space Environment Geochemistry and Ranging) [1-7]. The role of devolatilization in the planet's landscape evolution remains uncertain. The current state of knowledge documents the presence of small, shallow hollows as potential sublimation byproducts [8-12]. Mass losses due to sublimation, however, were minor and resulted only in local landscape modifications. The key observation is that the hollows indicate a significant volatile content. We propose that devolatilization of Mercury's buried volatile-rich materials generated the planet's chaotic terrains. These terrains consist of vast fields of ridges, mesas, and knobs made up of degraded rims of craters and a ruptured landscape of intercrater plains.

Reassessing the Origin of Mercury's Chaotic Terrains: The 1974 Mariner 10 flybys of Mercury discovered some of the Solar System's largest and oldest chaotic terrains [13]. Schultz and Gault [14] proposed an origin by seismically-induced landsliding and impact by ejecta fallout related to the formation of the antipodal Caloris Basin. The lengths of Mercury's chaotic-terrain-forming promontories conform to NE- and NW- trending alignments across a broad region. These alignments are traceable over hundreds of kilometers and interconnect areas that exhibit varying degrees of chaotic terrain development. Schultz and Gault [14] hypothesized that repositioning of impact crater rim materials due to severe seismicity implies that the outlines of larger impact crater populations dominated the chaotic terrain patterns. Our geologic characterization of these terrains reveals that, in addition to the linear terrain arrangements, there is retention in the circularity of most impact crater outlines, which is independent of their diameters. An exception is the presence of tectonically aligned rims, which alters the circularity of some small craters. We find that chaotic terrains exhibit varying degrees of landscape modification. Some terrains show lineations that mark but do not significantly disturb, the pre-existing cratered landscapes. On the other hand, there are other areas characterized by the presence of promontories arranged in circular and linear patterns, which reflect the distribution of pre-existing faults and crater rims. Local variations in the magnitudes of resurfacing include the sharp boundaries. Our impact crater counts indicate that the chaotic terrains formed ~400 Ma after the Caloris Basin impact. The chaotic terrains include numerous lava channels throughout their inter-crater regions as well as crater interior lava plains. The terrain post-date the major phases of regional collapse.

Volcanically-induced Tectonic Collapse as a Primary Chaotic Terrain Forming mechanism: These observations rule out the catastrophic seismic rupturing of crater rims as the origin of Mercury's chaotic terrains. We propose that ~400 million years after the Caloris basin impact basin formed, extensive collapse generated the planet's chaotic terrains. The primary types of geologic processes leading to collapse likely combined regionally elevated volcanic heat flow and its induced devolatilization of large volumes of crustal materials. Collapse along NE- and NW-trending extensional faults was dominant, which resulted in widespread chaotic terrain interior pattern retention. These patterns reflect the pre-existing tectonized landscapes, and therefore, while highly disruptive, the collapse was not sufficient to eliminate most pre-existing landforms. We propose that large-scale upper crustal devolatilization produced a multi-meter deep lag of volatile-depleted materials, which effectively reduced the devolatilization rates. Later volcanic eruptions might have reduced the volume of underlying magma, decreasing regional heat flow.

References: [1] Nittler, L. R., et al. (2011), Science, 333, 1847–1850. [2] Evans, L. G., et al. (2015), Icarus, 257, 417–427. [3] Murchie, S. L., et al. (2015), Icarus, 254, 287–305. [4] Weider, S. Z., et al. (2015), Earth Planet. Sci. Lett., 416, 109–120. [5] Peplowski, P. N., et al. (2012), J. Geophys. Res., 117, E00L04. [6] Peplowski, P. N., et al. (2014), Icarus, 228, 86–95. [7] Peplowski, P. N., et al. (2016), Nat. Geosci., 9, 273–276. [8] Blewett, D. T., et al. (2011), Science, 333, 1856–1859. [9] Blewett, D. T., et al. (2013), J. Geophys. Res. Planets, 118, 1013–1032. [10] Vaughan, W. M., et al. (2012), Lunar Planet. Sci., 43, Abstract 1187. [11] Helbert, J., et al. (2013), Planet. Sci. Lett., 369–370, 233–238. [12] Blewett, D. T., et al. (2016), J. Geophys. Res. Planets, 121, 1798–1813. [13] Murray, B. C., et al. (1974) Science 185, 169. [14] Schultz, P.H., and Gault D. E. (1975), The Moon, 12, 159-177.

THE DEPTH OF ICE INSIDE THE COLD TRAPS ON MERCURY: IMPLICATIONS ON AGE AND DEPOSITION

GIN L. Rubanenko[1], E. Mazarico[2], G. A. Neumann[2] and D. A. Paige[1], [1]Department of Earth, Planetary and Space Sciences, UCLA, LA, CA 90095, [2]NASA Goddard Space Flight Center, Greenbelt, MD, USA (liorr@ucla.edu)

Introduction: Volatiles may be trapped inside permanently shadowed regions (PSRs) cast by topographic features near the poles of Mercury [1, 14, 20]. Evidence for the presence of water ice inside these cold-traps was remotely sensed in RADAR [9], reflectance [12] and visible imagery [3]. More recently, evidence for the presence of ice inside smaller craters ($\sim$ 1 km) and micro cold-traps (1 $-$ 10 m) was found using data obtained by the Mercury Laser Altimeter (MLA) [6, 16]. Here we constrain the thickness of these small deposits in order to learn about their age and deposition method. We consider two types of topographic features: small craters (3 $-$ 15 km) and micro cold-traps (1 $-$ 10 m) cast by the unresolved topography.

Measuring the Ice Depth Inside Small Craters: We begin by identifying small, simple craters on the Mercury Dual Imaging System (MDIS) global basemap. Then, we measure the crater elevation along a south-north profile on the gridded MLA polar map. Overall we measured 1003 craters between latitudes 75° $-$ 86°, where the most reliable MLA data is found. Figure 1 shows the craters depth/diameter (d/D) distribution on Mercury decreases between latitudes 75° $-$ 78° (where ice should not accumulate according to thermal models) and latitudes 83° $-$ 86° (where ice should accumulate), as shallower craters replace deeper craters. The mean d/D decreases from 0.106$\pm$ 0.036 in latitudes 75° $-$ 78° to 0.086$\pm$ 0.034 in latitudes 83° $-$ 86°. As the mean crater depth in low latitudes is $\sim$ 400 m, this decrease implies a mean infill of order 10 $-$ 100 m.

Constraining the Ice Depth Inside Micro Cold-Traps: Micro cold-traps form in permanent shadows cast by small, often unresolved, topographic features. A common way to describe the topography at these scales is to use random Gaussian surfaces [e.g. 2, 5, 8, 10, 19]. This artificial realization has a Gaussian slope distribution and a power-law power spectrum. The degree of roughness is given by the slope RMS at the slope scale, σ_s. Higher σ_s corresponds to smaller lateral scales; the slope distribution on scales > 1 km has $\sigma_s \sim 5^\circ$, while the slope distribution on scales $\sim$ 1 $-$ 100 m has a higher $\sigma_s \sim 20^\circ - 10^\circ$ [2, 15]. To first order, the thickness of ice inside a cold-trap is limited by the depth of the permanent shadow volume (PSV) it occupies. To calculate the PSV depth we employ a 3-D illumination model [17]. First, we find the transient shadow depth; the vertical distance between the surface and the shadow that covers it. Then, we calculate the depth of the permanent shadow by finding the temporal minimum of this shadow. We demonstrate the shape of these PSVs in Figure 2 (a), which shows a cross section through the topography (black line) along with the modeled maximum possible ice depth (blue line). Models predict the scale of ice deposits in micro cold-traps on Mercury is 1 $-$ 10 m (σ_s = 20 $-$ 15°) [16, 18]. As an example, we show the shadow depth CDF of a random surface with σ_s = 20° (Figure 2). We find the maximum median ice thickness covering this surface to be a few decimeters.

Discussion: Above we showed small craters near the pole of Mercury become shallower with latitude. If this infill is due to accumulation of ice, we estimate its thickness to be 10 $-$ 100 m. This implies a net delivery rate of a few meters per Ga, in accord with previous theoretical [11, 13] and observational [7] estimates. Recently it was shown ice may be

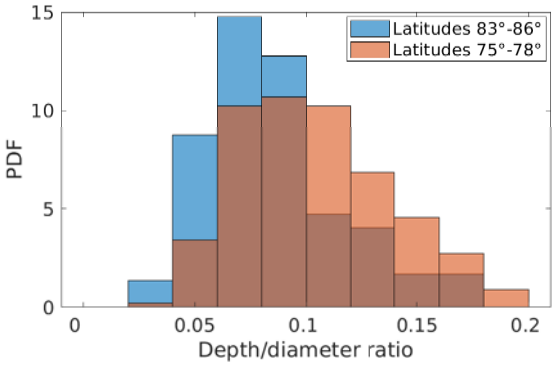

Figure 1: The d/D distribution in two latitude rings. Craters become shallower in high latitudes, where ice is expected.

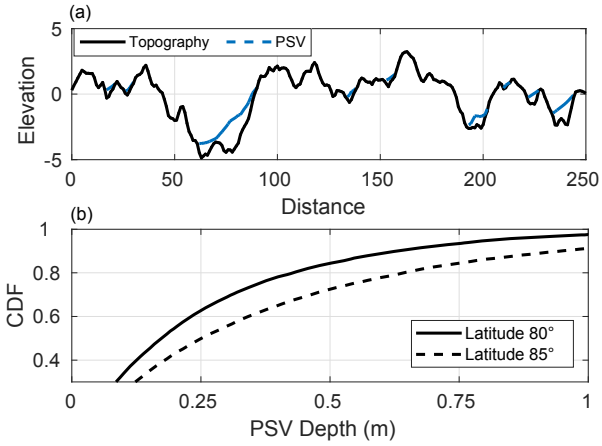

Figure 2: The maximum possible ice thickness inside micro cold-traps on Mercury modeled on a rough random surface with σ_s = 20° (lateral scale $\sim$ 1 m).

trapped inside micro cold-traps on scales 1 $-$ 10 m [16]. We may constrain the maximum thickness of these deposits to be a few decimeters. At these scales, impact erosion is expected to dominate over accumulation [4]. However, the fact these deposits are still present leads us to believe they were latterly emplaced. Recent impact models suggest the turnover rate in the first few decimeters is $10^{-6} - 10^{-7}$ yr^{-1} [4]. If these models are correct, we can constrain the age of these deposits to be $\sim 10^7$ years, comparable to modeled comet impact rate [11].

References: [1] JR Arnold. JGR (1979). [2] JL Bandfield et al. Icarus (2015). [3] NL Chabot et al. Geology (2014). [4] E Costello et al. AGU Fall Meeting (2017). [5] BJR Davidsson et al. Icarus 243 (2014), 58–77. [6] AN Deutsch et al. GRL (2017). [7] AN Deutsch et al. (2017). [8] T Hagfors. JGR (1964). [9] JK Harmon et al. Icarus 149 (2001). [10] S Jamsa et al. A&A 271 (1993), 319. [11] JI Moses et al. Icarus (1999). [12] GA Neumann et al. Science (2013). [13] L Ong et al. Icarus (2010). [14] DA Paige et al. Science 258 (1992). [15] MA Rosenburg et al. JGR: Planets (1991-2012) 116 (2011). [16] L Rubanenko et al. GRL (in review) (2018). [17] L Rubanenko et al. Icarus (2017). [18] L Rubanenko et al. (2017). [19] B Smith. IEEE TAP (1967). [20] K Watson et al. JGR (1961).

THE MIA (MERCURY ION ANALYZER) INSTRUMENT ONBOARD BEPI COLOMBO MMO (MERCURY MAGNETOSPHERIC ORBITER).

Y. Saito[1], W. Miyake[2], S. Yokota[3], A. Coates[4], A. Fazakery[4], H. Hasegawa[1], A. Ieda[5], S. Machida[5], T. Nagai[6], T. Nagatsuma[7], C. Owen[4], K. Seki[8], I. Shinohara[1], and T. Terasawa[9], [1]Institute of Space and Astronautical Science, [2]Tokai University, [3]Osaka University, [4]MSSL, University College London, [5]ISEE, Nagoya University, [6]Tokyo Institute of Technology, [7]NICT, , [8]University of Tokyo, [9]RIKEN, (Y. Saito: 3-1-1 Yoshinodai, Chuo, Sagamihara, Kanagawa 252-5210, JAPAN, saito@stp.isas.jaxa.jp).

Introduction: Mercury's plasma/particle environment has gradually become clear thanks to the new observations made by MESSENGER spacecraft orbited around Mercury. However, it is also true that many questions are left unsolved. In order to elucidate the detailed plasma structure and dynamics around Mercury, an orbiter BepiColombo MMO (Mercury Magnetospheric Orbiter) is going to be launched in 2018 as a joint mission between ESA and ISAS/JAXA. Mercury Plasma/Particle Experiment (MPPE) is a comprehensive instrument package for plasma, high-energy particle and energetic neutral atom measurements[1]. It consists of 7 sensors: two Mercury Electron Analyzers (MEA1 and MEA2), Mercury Ion Analyzer (MIA), Mass Spectrum Analyzer (MSA), High Energy Particle instrument for electron (HEP-ele), High Energy Particle instrument for ion (HEP-ion), and Energetic Neutrals Analyzer (ENA). Currently, the MPPE sensors are on the MMO spacecraft waiting for the launch scheduled in October 2018.

Mercury Ion Analyzer (MIA): The scientific objectives of low energy ion measurement on Mercury orbit are to understand: (1) structure of the Mercury magnetosphere, (2) plasma dynamics of the Mercury magnetosphere, (3) Mercury–solar wind interaction, (4) atmospheric abundances, structure, and generation/loss process, and (5) solar wind between 0.3 and 0.47 AU. In order to realize the required measurements, MIA should measure three-dimensional distribution function of solar wind ions around Mercury (0.3–0.47 AU), and Mercury magnetospheric ions simultaneously.

MIA is a top-hat type electrostatic analyzer with toroidal deflectors. With the spin motion of spacecraft, three-dimensional ion distribution function is observed. The inner toroidal electrode is supplied with high voltage swept between 0V and -5 kV. Ions coming through the collimator are attracted down toward the inner electrode by the applied potential. Only the ions with specific energy range can further travel down to the exit of the electrodes. The ions passing through the toroidal deflectors enter to Z-stack MCP and are intensified to detectable charge pulses. Finally, the charge pulses are received by 63-channel discrete anode. The positions where the charge pulses are detected correspond to the incident azimuthal directions of the ions. MIA uses a newly developed ASIC (application specific integrated circuit) that is installed on the MCP anode. The ASIC consists of 64-chanel discriminators, 64-channel fast preamplifiers, and 64-chanel counters[2]. The estimated dynamic range of the low-energy ion flux around Mercury including both intense solar wind ions and weak magnetospheric ions is as wide as 10^6[3]. In order to measure both solar wind ions without saturation and Mercury magnetospheric ions with enough counting statistics, MIA has a function to change g-factor electrically. Sensitivity of the analyzer is controlled by changing the high voltage applied to the ''top-hat'' part. The center of the ''top-hat'' part is insulated from the surrounding structures. By applying high voltage between 0V and -5 kV, g-factor can be reduced down to 1/50. In addition to the electrical g-factor control, attenuation grid (10% transmission) is placed at limited sector of the entrance part of the analyzer in order to further reduce geometrical factor for solar wind ion measurement[4].

The energy range of MIA is 5 eV/q to 30 keV/q. The maximum number of energy step is 128 that are necessary for distinguishing solar wind alpha particles from solar wind protons. The angular resolution for measuring solar wind ions is 5.625deg., while the angular resolution for measuring Mercury magnetospheric ions is 11.25deg. or 22.5deg., depending on the allocated capacity of the telemetry data. MIA will provide three-dimensional distribution functions of low energy ions in half a spin period (nominal spin period: 4 s) of MMO. According to our knowledge of the Earth's magnetosphere, full three-dimensional measurements of low-energy ions with high time resolution are indispensable for understanding the structure and dynamics of the magnetosphere. Since no full three-dimensional low-energy ion data have been obtained around Mercury, low-energy ion data obtained by MIA together with MSA on MMO will provide us with unique opportunity to understand detailed structure and dynamics of the Mercury magnetosphere.

References: [1] Saito Y. et al. (2010) PSS, 58, 182–200. [2] Saito Y. et al. (2017) JGR, 122, 1816-1830. [3] Mukai T. et al. (2004) ASR, 33, 2166-2171. [4] Miyake W. et al. (2009) ASR, 43, 1986-1992.

CORRELATION OF MERCURY'S MAGNESIUM EXOSPHERE WITH MICROMETEOROIDS FROM JUPITER FAMILY COMETS. M. Sarantos[1](menelaos.sarantos-1@nasa.gov), P. Pokorny[1,2], D. Janches[1], and the MESSENGER *UVVS* Team, [1]Heliophysics Science Division, NASA Goddard Space Flight Center, Greenbelt, MD 20771,USA [2]Department of Physics, The Catholic University of America, Washington, DC 20064, USA.

Introduction: New observations from the MESSENGER mission enable us to constrain the physical processes that contribute to the Hermean exosphere. By understanding the processes that promote and deplete Mercury's exosphere, we learn about other objects in the solar system where similar conditions exist. Such objects include asteroids and the moons of Earth, Mars, Jupiter and Saturn.

Measurements by MESSENGER of key exospheric constituents in Mercury's atmosphere have suggested that meteoroid impact vaporization may be an important source process for these gases as altitude profiles are consistent with temperatures expected from meteoroid impacts [1, 2]. However, several features of these measurements remain unexplained. For instance, Ca, the most refractory of these elements, appears to have a peak in gas density almost always at dawn, but Mg, a chemically related species, appears to peak around mid-morning. We wish to understand what processes are responsible for these differences.

Methods: We analyzed measurements of Mg in Mercury's dayside and nightside exosphere obtained by the UltraViolet and Visible Spectrometer (UVVS) on MESSENGER. The key improvements over the state-of-the art come from 1) the availability for the first time of a dynamical model of the zodiacal cloud, which includes meteoroids from Jupiter Family, Halley Type and Oort Cloud Comets, and which predict where meteoroids arrive at Mercury [3], with what velocity distribution, with what distribution in latitude and local time, and how this changes with Mercury's True Anomaly Angle (TAA); and 2) the application of a unique physics-based tomography technique [4] which enables us to derive the spatial dependence and magnitude of the number flux of neutral Mg leaving Mercury's surface from UVVS sightlines.

Results: Meteoroids from long-period comets (*Halley-type and Oort Cloud Comets)* arrive at the apex of Mercury's motion, whereas meteoroids from short-period comets (*Jupiter Family Comets, or JFCs)* arrive at different local times during different Mercury TAAs. When Mercury is heading towards the Sun (TAA>180°) most *JFC* meteoroids impact the dayside near the subsolar point. During this leg we find that the Mg exosphere peaks well sunwards of its usual 8 AM peak, and the local time of the peak Mg density varies with TAA in the same way as the modeled vapor from JFC meteoroids [Fig. 1]. This result suggests that measurements of Mercury's exosphere may be used to probe meteoroid populations in the inner Solar System.

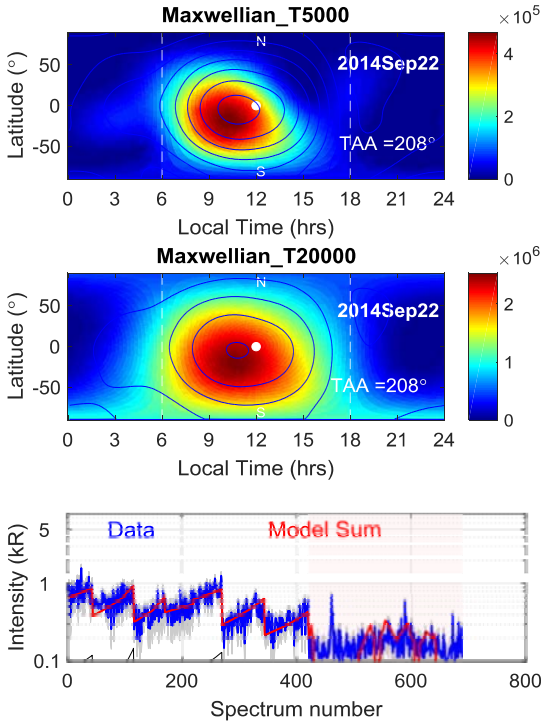

Fig 1: Model-predicted micrometeoroid arrival directions from Jupiter Family Comets (vapor shown in blue contours) agree with Mg atom efflux derived from UVVS data (color-coded flux as a function of latitude and local time). Units indicate the number flux (Mg atoms/cm^2/s) leaving the surface and with what temperature.

References: [1] Burger, M. H. et al (2014) *Icarus*, *238*, 51-58. [2] Merkel et al. (2017) *Icarus*, *281*, 46-54. [3] Pokorny P. et al. (2017) *ApJLett*, *842*(2), L17. [4] Sarantos M. et al. (2012) *EPSC Abstracts Vol. 7*, Abstract # EPSC2012-707-1.

WHEN MERCURY SMASHED: DYNAMICS AND COMPOSITION THROUGH A GRAZING COLLISION WITH A LARGER PLANET.

G. Sarid, University of Central Florida, Florida Space Institute, 12354 Research Parkway, Orlando, FL 32826, U.S.A (gal.sarid@ucf.edu).

Introduction: We present an erosive Hit-and-Run (H&R) impact analysis for the origin of Mercury's mass and compositional distribution, as inferred from the MESSENGER mission and previous observations [1].

In this scheme, proto-Mercury is the projectile body in a similar-sized collision event (SSC), where it becomes disrupted and can lose significant amounts of rocky mantle material [2, 3, 4]. The larger target body plays an advantageous role in removal of subsequent debris. The mantle composition is preserved due to the rapid re-accumulation of the remnant projectile body. This body is now composed of the surviving (iron) core and gravitationally bound rock fragments [3, 4]

We explore here the projectile H&R collision origin approach and present the following arguments:

- Are there events that produce a "Mercury"? – Plausible in the context of classical and dynamically excited terrestrial planet formation, in terms of impact velocities and planetary mass spectrum [5, 6].
- How to get rid of ejecta? – A larger body (nominal "target") is advantageous for debris removal but would still require a dynamical separation mechanism (interaction with environment) to control the ejecta mass in the system and prevent the remnant projectile from being re-accreted [7, 8].
- How to preserve mantle composition? – The gravitationally bound mantle fragments re-accrete and the vapor parcels from these fragments re-condense in the same potential [9, 10].

Modeling: We performed a large set of simulations of SSC events, covering a range of mass ratios (1-0.2), impact parameters (0.25-0.96, for near head-on to barely grazing) and impact velocities (~1.5-5 X mutual escape velocity). We used the SPH code GADGET2, which was modified to handle ANEOS-style equations of state (parameters used for SiO2 and iron) and has been used previously in simulating giant planetary impacts [3, 11]. The initial proto-Mercury mass (as the projectile) was set to ~2.25 times its current mass, which is the minimum mass needed to comply with a composition of roughly chondritic abundance (70:30 silicate-to-iron ratio). Total number of SPH particles implemented in each setup was > 10^5 and they were tracked through 24-48 hrs of simulated post-impact time.

Results: Fig. 1 shows all the results of our simulations, in terms of the final projectile body mass fraction as a function of the impact velocity, normalized by the mutual impact velocity of the system. We show results for all of the projectile-to-target mass ratios examined (from 1 to 0.2) and for a range of impact parameters that correspond to a grazing impact, for each of the mass ratios. Acceptable ''Mercurys" (dashed gray box) encompass a range of collision conditions, but favor higher mass ratios and intermediate impact angles (~2/3 of the cases). Colors denote the impact parameters and symbols represent the initial mass ratios, with the value of the mutual escape velocity in parentheses.

Fig. 2 is a visualization of a specific collision setup, with colored circles representing subsequent times. It shows the thermodynamic phase space for the remnant projectile silicate material that remains bound throughout the post-impact re-accumulation. The conditions are such that volatile elements do not have a chance to outgas completely and escape the gravity well. The volatile element reservoir (related to the rocky mantle) goes through melting and vaporization, but envisioned global magma ocean and puffed atmosphere are bound and eventually crystallize and collapse.

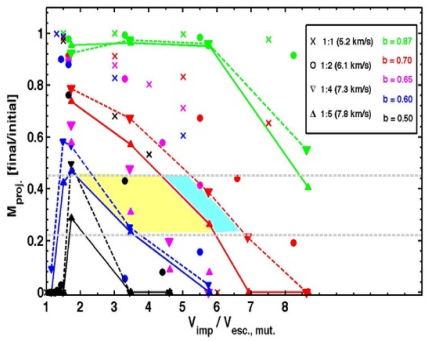

Fig. 1: Mass fraction of remnant projectile body as a function of normalized impact velocity.

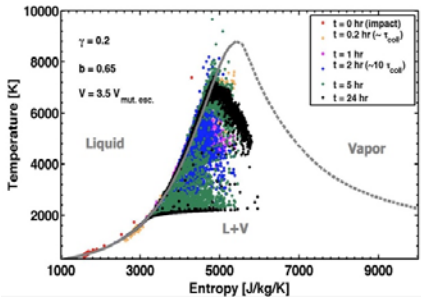

Fig. 2: Thermodynamic phase space for the projectile silicate material that ends-up bound in the final "Mercury"

References: [1] Hauck, S. A. et al. 2013. JGR 118, 1204. [2] Asphaug, E. 2010. ChEG 70, 199. [3] Sarid, G. et al. 2014. LPI Tech. Rep. 45, #2723. [4] Asphaug, E. & Reufer, A. 2014. Nature Geosci. 7, 564. [5] Raymond, S. N. et al. 2009. Icarus 203, 644. [6] Walsh, K. J. et al. 2011. Nature 475, 206. [7] Carter, P. J. et al. 2015. ApJ 813, 72. [8] Jackson, A. P. & Wyatt, M. C. 2012. MNRAS 425, 657. [9] Stewart, S. T. et al. 2013. LPI Tech. Rep. 44, #2306. [10] Stewart, S. T. et al. 2016. LPI Tech. Rep. 47, #2954. [11] Cuk, M. & Stewart, S. T. 2012. Nature, 338, 1047.

A COMBINED EXPERIMENTAL AND MODELING PROGRAM TO STUDY THE IMPACT OF SOLAR WIND IONS ON THE SURFACE AND EXOSPHERE OF MERCURY. D. W. Savin[1], B. C. Bostick[1], D. L. Domingue[2], D. S. Ebel[3], G. E. Harlow[3], and R. M. Killen[4], [1]Columbia University, New York, NY 10027 (savin@astro.columbia.edu), [2]Planetary Science Institute, Tucson AZ, 85719, [3]American Museum of Natural History, New York, NY, 10024, [4]NASA Goddard Space Flight Center, Greenbelt, MD, 20771.

Introduction: Our objective is to improve the interpretation of in-situ and remote-sensing data of Mercury. We will use updated exosphere and spectrophotometric models that incorporate new data from our planned laboratory simulations of solar wind ion irradiation of Mercury's regolith surface.

Current exosphere and spectrophotometric surface models, make simplified assumptions about the sputter yield and spectral changes from ion irradiation. This is due in large part to the lack of experimental data for regolith-like loose powders. Our laboratory studies will be the most realistic simulations to date of the effects of ion irradiation on regolith-like loose powders and will provide quantitative data for the corresponding sputter yield and spectral changes. We will incorporate these data into our exosphere and spectrophotometric models and reinterpret the archival data of Mercury (e.g., Fig. 1).

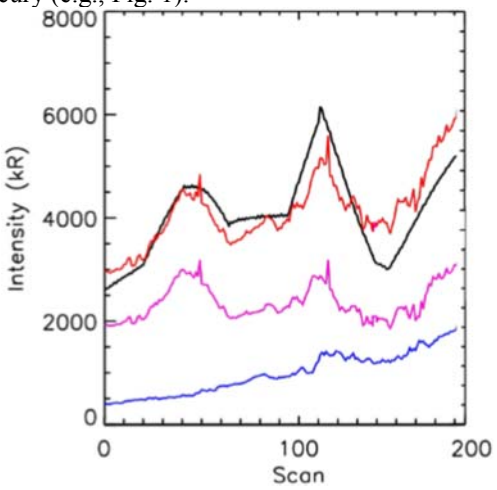

Figure 1: Na intensity in kiloRayleighs for the high-latitude Mercury Atmospheric and Surface Composition Spectrometer (MASCS) scans from MESSENGER orbit 936. The measured intensity is in black. Using our exosphere model [1,2], the predicted intensity due to solar wind ion sputtering is shown in magenta, that due to photon-stimulated desorption (PSD) in blue, and the sum in red.

Planetary science: Specific planetary science questions that we will address include: (1) What fraction of the Na exosphere of Mercury is formed by solar wind ions? (2) Is there a systematic difference between sputtering in Mercury's Northern and Southern cusps due to the offset of its dipole magnetic field? (3) Can ion sputtering explain all or only part of the Na loss from the planet? (4) How are Mercury's spectrophotometric properties altered by solar wind ions? and (5) Is there a correlation between sputtering yields and changes in the spectrophotometric surface properties?

Laboratory work: For the laboratory portion of our work, we will construct a novel beam-line configuration to irradiate regolith-like loose powders from above at zenith angles of 15°, 45°, and 75°. We will irradiate the samples with ion beams of H and He at typical solar wind energies of 1 keV/amu, where amu is atomic mass unit. These elements make up on average ~95% and ~5% of the solar wind, respectively. Sputter yields will be measured catcher foils, which will be analyzed ex-situ using synchrotron-based X-ray photoelectron spectroscopy (XPS). We will perform in-situ 350-2500 nm spectroscopic analyses for incident and emergent angles of 0°, ±15°, ±30°, and ±45°, covering phase angles from 15° to 90°. The spectral analysis will be in vacuo, thereby avoiding atmospheric contamination of the irradiated samples. Samples will be prepared in an inert environment to further minimize surface contamination by atmosphere.

We know of no other laboratory with all of the above capabilities. State-of-the-art ion irradiation studies have used flat surfaces (i.e., slabs) or powders which have either been highly compressed or epoxied. None of these are reliable simulants for the loose powders expected to comprise the regoliths of airless bodies. Most previous irradiation studies with H^+ and He^+ have used energies 10-1000 times higher. Other have used ions of C, N, O, Ne, and Ar at excessively high energies. These elements comprise <0.1% of the solar wind, and it is unclear whether the results can be reliably scaled to H and He at the relevant energies.

For our studies, samples will be derived from feldspars, expected to be common on the surface of Mercury. Both crystalline and glass powders will be used, the latter to account for surface vitrification by micrometeorite impact vaporization. Slabs will be used for comparison reference measurements.

Acknowledgements: This work is supported in part by the NASA Solar System Workings and Planetary Major Equipment programs.

References: [1] Killen, R. M. et al. (2007), *Space Sci. Rev.*, *132*, 433-509. [2] Burger, M. H. et al. (2010), *Icarus*, *209*, 63-74.

Absorption Spectroscopy of Mercury's Exosphere During the 2016 Solar Transit. C. A. Schmidt[1,2], F. Leblanc[2], K. Reardon[3], R. M. Killen[4], D. E. Gary[5], K. Ahn[6], [1]Boston University, [2]LATMOS Laboratoire Atmosphères, Milieux, Observations Spatiales / CNRS, [3]National Solar Observatory, [4]NASA Goddard Space Flight Center, [5]New Jersey Institute of Technology, [6]Big Bear Solar Observatory

Introduction: Sodium is the most studied species in Mercury's exosphere and its bright resonant transitions offer a wealth of information. A consistent portrait of the sodium exosphere has been nearly 30 years in development. Due to the planet's proximity to the Sun, much of the ground-based work has been done in daylight using solar telescopes, and despite the higher background noise levels compared to traditional astronomical observations, exospheric sodium emissions are sufficiently bright to be measured by specialized instrumentation. On rare occasions, the exosphere can also be measured in *absorption* as Mercury transits between Earth and the Sun. Such observations can provide excellent spectral, spatial and temporal coverage of an otherwise elusive target, since more than ample photons are available with a modern telescope pointed at the Sun.

2016 Solar Transit: Transit observations have the unique property that line absorption can effectively provide an image of the exosphere's column density at all points above the terminator. We observed Mercury during the 9 May 2016 transit with the 1.6m Goode Solar Telescope at Big Bear Solar Observatory using the Fast Imaging Solar Spectrograph. Its adaptive optics system locked onto the solar granulation structure, permitting sub-arcsecond spatial resolutions. The spectrograph slit scanned over the planet's disk in 130 steps every 16 seconds. This technique produced nearly 500 "data cubes," each with a high resolution spectra as its 3rd dimension.

Shown in the upper panel of the figure, line profiles at every spatial bin (black) are divided by a shifted-and-scaled reference spectrum (red) in order to isolate the exosphere's absorption (blue) from line absorption in the solar atmosphere and structures inherent to granulation. Equivalent widths shown in the lower panel are directly proportional to the exosphere's column density, $\sim 10^{11}$ cm^{-2}. The densest column of sodium appears near the poles and at dawn, whereas the dusk-side column is very tenuous.

This sodium distribution is strikingly similar to 2003 transit results taken at the same 150° true anomaly angle [1], confirming MASCS-UVVS evidence that the atmosphere is seasonally predictable [2]. However, the data quality and volumes herein permit a more in-depth study than previous transit measurements. This presentation will describe the atmospheric scale heights, the Doppler shifts due to the bulk motion of the atmosphere and an investigation of potential temporal variability within the 2.5 hours of observation.

2019 Solar Transit: The entire 5.5 hour transit on 11 November, 2019 will be optimally visible from European solar telescopes like THEMIS and GREGOR. This event will provide an excellent opportunity to characterize the sodium exosphere in the opposite Mercury season and better study its time-dependence.

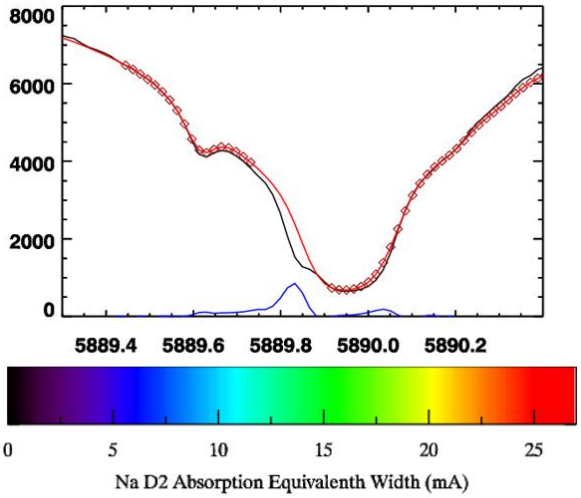

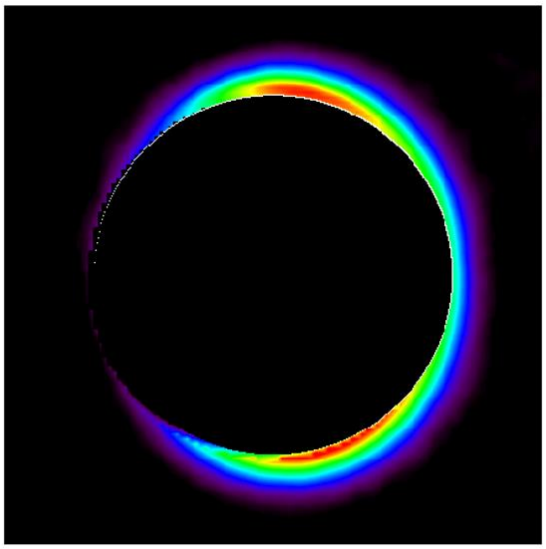

References: [1] Schleicher, H et al., 2004, Detection of neutral sodium above Mercury during the transit on 2003 May 7, Astronomy & Astrophysics, v.425 [2], Cassidy et al., 2015, Mercury's seasonal sodium exosphere: MESSENGER orbital observations, Icarus, v.248.

WIDEBAND PHOTOMETRY OF MERCURY IN THE U, B, V, R, I, J AND H FILTERS: A REVIEW. R. W. Schmude, Jr., Gordon State College, 419 College Dr., Barnesville, GA 30204, (Schmude@gordonstate.edu).

Introduction: Harris [1] reviews early photometric work of Mercury. He also reports B – V, V – R and R – I values of 0.93, 0.85 and 0.52, respectively based on unpublished work of Hardie. He does not indicate the date or phase information of when these measurements were taken. Irvine et al. [2] published over 300 brightness measurements made through 13 different filters covering wavelengths of between 314.7 and 1,063.5 nm. Some of their measurements were made through the U, B and V filters. Schmude [3, 4] published a few B, V and R measurements. Mallama et al. [5] report both Earth-based measurements and measurements made from LASCO images. Their V filter measurements cover solar phase angles between 2° and 170°. They report a 7th degree polynomial which fits their data. Warell and Bergfors [6] report B, V, R and I measurements covering solar phase angles of between 22° and 152°. They also report that Mercury may undergo phase reddening. Schmude [7] reports J and H filter brightness measurements. The J filter measurements cover phase angles of 52° – 125° and the H filter measurements cover the corresponding range 39° – 133°. Photometric systems were transformed to the Johnson UBVRI or the Mauna Kea JH systems. Filter characteristics for the two most recent studies are summarized in Table 1.

Table 1: Characteristics of Wideband filters

Filter	Peak wavelength (nm)	Full-width at half maximum (nm)
U	384	51 [6]
B	427	97 [6]
V	524	95 [6]
R	613	147 [6]
I	768	267 [6]
J	1,250	200 [7]
H	1,650	300 [7]

Analysis of Previous Data: Data from [2] through [7] were analyzed. The data for [2], and [6] were fit to equations and the standard errors was computed. This is the square root of the sum of the deviations squared divided by n – 2 where n is the number of measurements. It gives an idea of how well the data fit the derived equation. Schmude already reports his standard error of estimate. The resulting standard errors of estimate are summarized in Table 2.

The color indexes of Mercury were also examined. The U – B and B – V values are computed from [2] whereas the V – R and R – I values are from [6]. The V – J value is computed from the predicted V filter value for a solar phase angle of 90° is from [5] and the J filter result in [7]. The J – H value is from [7]. The color indexes are compared to the Moon at first quarter which is from [8]. The color indexes for the Moon and Mercury are within the standard errors.

Table 2: Standard errors of estimate for photometric studies of Mercury

Filter	Equation	Standard error magnitudes	Source
U	Linear	0.10	[2]
B	Cubic	0.08	[2]
B	Cubic	0.11[a]	[6]
R	Cubic	0.34	[6]
I	Cubic	0.36	[6]
V	7th order	0.08	[5]
J	Cubic	0.12	[7]
H	Cubic	0.09	[7]

[a]One bad point was excluded.

Table 3: Color index values for Mercury and the first quarter Moon

Color index	Mercury	Moon [8]
U – B	0.45	0.50
B – V	0.91	0.92
V – R	0.67	0.91
R – I	0.48	0.46
B – R	1.58	1.83
V – J	1.90	---
J – H	0.63	---

Acknowledgements: The writer thanks Gordon State College for a Faculty Development Grant which enabled him to purchase the SSP-4 photometer needed to make J and H filter measurements of Mercury.

References: Harris D. (1961) *Planets & Satellites*, Univ. of Chicago Press, pp. 272–342. [2] Irvine, W. M. et al. *AJ*, 73, 807–828. [3] Schmude, R. W. Jr. (1993) *JRASC*, 87, pp. 133–139. [4] Schmude, R. W. Jr. (1995) *IAPPP* Comm. 61, pp. 45–47. [5] Mallama, A. et al. (2002) *Icarus* 155, 253–264. [6] Warell, J. and Bergfors, C. (2008) Plan. & Space Sci, 56, 1939–1948. [7] Schmude, R. W. Jr. (2018) accepted by Ga. J. Sci. [8] Schmude, R. W. Jr. (2017) Encyclopedia of Lunar Science, Springer International Publishing.

INVESTIGATING MERCURY'S SOUTH POLAR DEPOSITS WITH HIGH-RESOLUTION DETERMINATION OF ILLUMINATION CONDITIONS. Evangela E. Shread[1] and Nancy L. Chabot[1], [1]Johns Hopkins Applied Physics Laboratory, 11100 Johns Hopkins Rd., Laurel, MD, 20723.

Introduction: Over two decades ago, Earth-based radar observations of Mercury's poles revealed radar-bright features supposed to be water ice [1-3]. The MErcury Surface, Space ENvironment, GEochemistry, and Ranging (MESSENGER) mission provided subsequent evidence to support the hypothesis that a significant amount of water ice exists in areas of permanent shadow in the north and south polar regions [4-9]. This study uses data acquired by the high-resolution narrow-angle camera (NAC) of the Mercury Dual Imaging System (MDIS) to map the permanent shadow in Mercury's south polar region, which has been less studied than the north polar region due to the high eccentricity of MESSENGER's orbit.

Illumination Conditions: In previous work, wide-angle camera (WAC) images acquired during MESSENGER's first year of orbital operations were used to map the average illumination of the south polar region over one Mercury solar day [4]. In this study, 1,094 NAC images from MESSENGER's full orbital mission of just over four years were used to create an average illumination map spanning the region from 80 to 90° S, with a pixel resolution of 200 m [Fig. 1]. The NAC-based illumination map is consistent with the WAC-based map, but can better enable discernment of small-scale features since the NAC has a spatial resolution seven times greater than that of the WAC.

Long-exposure NAC Imaging: A series of long-exposure NAC images (250-9989 ms), focusing mainly on the 180-km-diameter crater Chao Meng-Fu (Fig. 1), were acquired in the south polar region as part of a campaign to image within areas of permanent shadow. Adjusting the brightness and contrast of many of these images revealed features within Chao Meng-Fu that were not visible in the standard exposure (<40 ms) images used in the base map. We find that the long-exposure images did not reveal features within Chao Meng-Fu that are in areas of permanent shadow, but rather exposed areas on the crater floor that are directly sunlit but are too dimly lit to be detected by standard-exposure imaging. Four of these images were incorporated, along with the illumination map in Fig. 1, to produce a map of the regions of permanent shadow for Mercury's south pole. Overall, including the long-exposure NAC images reduced the shadowed area within Chao Meng-Fu by 28%.

Implications: We compared our NAC-based permanent shadow map with a radar image of Mercury's south polar region that was produced from combined Arecibo observations in 2005 and 2012 [10,11]. The result was that 77% of radar-bright features overlapped with or were located within 1.5 km of the permanently shadowed area. We conclude that the distribution of permanent shadow is consistent with the distribution of radar-bright areas, supporting the hypothesis that water ice on Mercury must be located within areas of permanent shadow to be thermally stable for geologically long periods of time.

About half of the shadowed terrain in the south polar region is not radar-bright. These shadowed areas that do not directly correspond to radar-bright features are distributed non-uniformly across the region, with the majority of these features confined extensively within 80 to 85° S and closer to 0° E. Since a similar trend was noted in the north polar region [9], the observed uneven distribution of water ice may be evidence for the hypothesis that a recent, large impact event caused the placement of ice on Mercury.

References: [1] Slade, M. A. et al. (1992) *Sci., 258,* 635-640. [2] Harmon, J. K. and Slade, M. A. (1992) *Sci., 258,* 640-643. [3] Butler, B. J. et al. (1993) *JGR, 98,* 15,003-15,023. [4] Chabot, N. L. et al. (2012) *GRL, 39,* L09204. [5] Lawrence D. J. et al. (2013) *Sci., 339,* 292-296. [6] Neumann G. A. et al. (2013) *Sci., 339,* 296-300. [7] Paige D. A. et al. (2013) *Sci., 229.* 300-303. [8] Chabot N. L. et al. (2014) *Geology, 42,* 1051-1054. [9] Deutsch et al. (2016) *Icarus, 280,* 158-171. [10] Harmon J. K. et al. (2011) *Icarus, 211,* 37-50. [11] Chabot N. L. et al. (2018) *JGR,* in revision.

Acknowledgements: NASA DDAP grant NNX15AK89G to N.L.C; APL ASPIRE and NASA/APL intern programs for E.E.S to do this work.

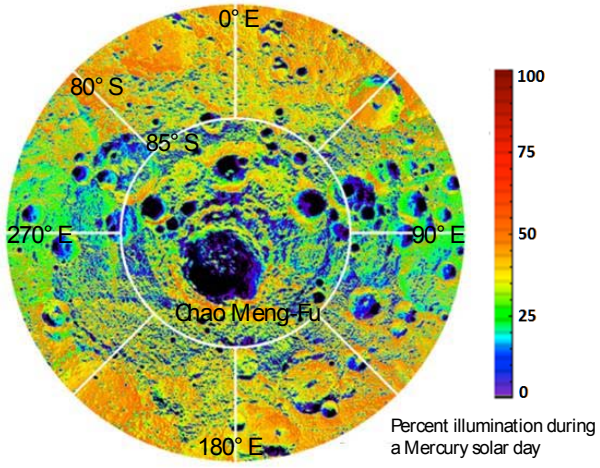

Figure 1*. NAC-based average illumination map of Mercury's south polar region (80-90 °S) over one Mercury solar day.*

MERCURY'S SOLAR WIND INTERACTION: THE VIEW FROM MESSENGER

James A. Slavin

Department of Climate and Space Science & Engineering, University of Michigan, Ann Arbor, USA

MESSENGER's three close fly-bys and 4 years of observations from orbit have revealed that Mercury possesses a highly dynamic and complex magnetic field and plasma environment. A magnetosphere is formed by the interaction of the solar wind with its modest, ~ 200 nT – R_M^3, intrinsic magnetic field. Despite the low altitude of its magnetopause, ~ 0.5 R_M, the dayside magnetosphere resists compression of by the solar wind, e.g. during coronal mass ejection impacts, by driving induction currents in Mercury's highly conducting iron core. Magnetic reconnection at the magnetopause is far more frequent and intense than at Earth. Indeed, the dayside magnetosphere is sometimes observed to disappear during periods of extremely intense southward interplanetary magnetic fields. Mercury's surface-bounded exosphere is maintained by sputtering and other surface interactions that eject neutrals from the regolith. In fact, a plasma mantle composed of H^+ and Na^+ is observed in the high-latitude magnetotail emanating from the magnetospheric cusps. These ions feed a plasma sheet largely of solar wind origin, but with ~ 1 to 10% Na^+ by number density. Future prospects for understanding Mercury's coupled magnetosphere – exosphere – solid planet as a system with the measurements to be returned by ESA's BepiColombo mission in 2025 will be discussed.

MERCURY'S REFERENCE FRAMES AFTER THE MESSENGER MISSION. A. Stark [1], J. Oberst [1,2], F. Preusker [1], S. Burmeister [2], G. Steinbrügge [1], H. Hussmann [1]. [1] DLR, Institute of Planetary Research, Rutherfordstr. 2, 12489 Berlin, Germany, alexander.stark@dlr.de, [2] Technische Universität Berlin, Institute of Geodesy and Geoinformation Sciences, Berlin, Germany

Introduction: The Mercury Surface, Space ENvironment, GEochemisty, and Ranging (MESSENGER) spacecraft has provided many new insights about the innermost planet. With the detailed information about shape [1,2], gravity field [3,4], and rotation state [3,4,5] of Mercury, it is advisable to verify the validity of Mercury's reference frames. Thus, we discuss the dynamical, the principal-axes, the ellipsoid, as well as the cartographic reference frames. We also describe the reference frame adopted by the MESSENGER science team for the release of their cartographic products and we provide expressions for transformations from this frame to the other reference frames. We summarize the performed measurements of Mercury's rotation based on terrestrial radar observations [6] as well as data from the Mariner 10 [7] and the MESSENGER missions [3,4,5].

MESSENGER reference frame: This cartographic frame is currently used for all data products from the MESSENGER mission. The rotation parameters are based on Earth-based radar [6] and MESSENGER radio science measurements [3]. Since the analysis of MESSENGER data revealed Mercury's rotation rate to be significantly different [3,5] from the previously assumed rotation rate [8], the prime meridian constant W_0 was revised [9]. The prime meridian of Mercury is defined by assigning the longitude 340° E (20° W) to the center of the small crater Hun Kal. The previous rotation rate, based on the assumption of a 3:2 spin-orbit resonance, dates back to pre-Mariner 10 time and leads to a longitudinal offset of 0.0519° (2.2 km) in Hun Kal's position in MESSENGER images. Recent photogrammetric analysis of more than 10,000 MESSENGER images in the H-6 (Kuiper) quadrangle of Mercury [10,11] confirmed the adopted prime meridian constant within 220 m.

Dynamical frame: Mercury's rotation state is tied to its orbital motion through a 3:2 spin-orbit resonance. This property allows to define a dynamical reference system, which can be realized by accurate analysis of Mercury's ephemeris [12]. Within the dynamical frame the prime meridian is defined as the mean location of the sub-Solar point at every second pericenter passage of Mercury. Interestingly, the cartographic frame defined by the crater Hun Kal and the dynamical frame do not coincide. The difference amounts to 0.12° (5.12 km) in longitude at the midterm of the orbital phase of the MESSENGER mission.

Principal-axes frame: The principal-axes reference system is defined by the principal components of Mercury's moment of inertia. The low-degree gravity field coefficients reflect the mass distribution within the planet and can be used to derive the orientation of the principal axes. Considering Mercury's gravity field estimates based on MESSENGER radio science data [3,4] we derived the transformation from the MESSENGER to the principal-axes reference frame. We further found that the principal-axes frame coincides with the dynamical frame within the measurement accuracy.

Ellipsoid frame: Due to the strong tidal force from the Sun Mercury's global shape can be characterized by a tri-axial ellipsoid and allows a definition of an ellipsoid reference system. Contrary to the cartographic, dynamical and principal-axes reference systems which have their origin at the center of mass, the ellipsoid reference system is related to the center of figure. The ellipsoid frame can be obtained from any kind of topographic measurements including radar ranging [13], limb profiles [2], laser altimetry [14], radio link occultation [1], and stereo images [15]. While there are hints at an offset between the center of mass and the center of figure in the order of 100 m, the orientation of the long axis of the ellipsoid frame is consistently offset from the axis of smallest inertia through all available data sets. The weighted average of estimates from all available studies suggests a longitudinal offset of 16.7°±1.7° between these two reference frames.

References: [1] Perry et al. (2015), GRL, 42, 6951. [2] Elgner et al. (2014), PSS, 103, 299. [3] Mazarico et al. (2014), JGR-Planets, 119, 2417. [4] Verma and Margot (2016), JGR-Planets, 121, 1627. [5] Stark et al. (2015), GRL, 42, 7881. [6] Margot et al. (2012), JGR-Planets, 117, E00L09. [7] Klaasen (1976), Icarus, 28, 469. [8] Archinal et al. (2011), CMDA, 109, 101. [9] Stark (2015), MESSENGER PDS Release (21 December 2015) available as ftp://naif.jpl.nasa.gov/pub/naif/pds/data/mess-e_v_h-spice-6-v1.0/messsp_1000/document/stark_prime_meridian.pdf [10] Preusker et al. (2017), PSS, 142, 26 [11] Preusker et al. (2018), this conference [12] Stark et al. (2015), CMDA, 123, 263. [13] Anderson et al. (1996), Icarus, 124, 690. [14] Neumann et al. (2016), LPSC, Abstract number #2087. [15] Becker et al. (2016), LPSC, Abstract number #2959.

AREAS FOR COMFORTABLE HUMAN HABITATION ON THE MERCURY. A.F. Steklov[1,2] and Vidmachenko[2,3]. [1]Interregional Academy of Personnel Management, Str. Frometivska, 2, Kyiv, 03039, [2]Main Astronomical Observatory of National Academy of Sciences of Ukraine, Str. Ak. Zabolotnogo, 27, Kyiv, 03143, [3]National University of Life and Environmental Sciences of Ukraine, Str. Heroyiv Oborony, 12, Kyiv, 03041. vida@mao.kiev.ua.

On its form, Mercury is close to a ball with a radius of R≈2440 km. The gravitational acceleration near the surface (g≈3,7 m/s^2) is 0.378 of Earth. Mercury is nearest to the Sun and revolves around it in an elliptical orbit with an eccentricity of 0.2056 [5, 6]. This leads to a change in distance to the Sun from 0.31 AU in perihelion to 0.47 AU in aphelion. For this reason temperature in the sunflower point of Mercury is +410°C and +480°C, respectively, for aphelion and perihelion. Before sunrise, the temperature at the equator decreases to -180°C [9]. Axis of planet's rotation on 7 differs from the normal to the plane of ecliptic. Therefore, Mercury has no seasons in sense that is usually for Earth or other planets [2-4, 7, 10]. So in the Polar Regions there are areas to which the sun's rays never reach. Results obtained in November 2012 by "Messenger" confirmed the presence of a significant amount of ice in several deep craters in areas near of North and South Pole, where to sunlight never hits [8].

Due to the very high daily temperatures at the equator, for a long time there was an opinion that people generally cannot live on Mercury. But can there be regions on Mercury, with a comfortable temperature for possible human habitation? And if there are no such regions on the surface, then, probably, such areas can are under its surface. And it is quite possible to build space settlements there [11].

It is known that the soil is a good heat insulator. Therefore, the temperature fluctuations on the surface of planet very slowly propagate in to depth of the soil. As evidenced by measurements on Earth, the highest temperature in the warmest season of the year comes to a depth of 3 meters with a delay of 76 days; in the coldest time of the year - with a delay of 108 days. With a deepening into the ground, the temperature fluctuations penetrate later, and significantly weaken. At some depth, such variations completely disappear, and for a given place there is the same average annual temperature. This phenomenon was discovered by the french scientist Lavoisier. In 1790, on the territory of the Paris Observatory, he dug a mine 28 m deep; the temperature there has not changed for more than 227 years and is +12°C. For Kiev – such a constant temperature is +9°C. In the early 20th century the problem of mathematical physics for the thermal conductivity of a semi-infinite rod was solved by academician Steklov V.A. This decision could explain such planetological phenomena. Solving a similar problem for Mercury, giving a difference in temperature on the surface at the equator in the range from +425°C to -170°C, we obtained a temperature difference on the surface for latitude |80 in the range from +150°C to -190°C.

But on latitudes |70 the temperature under the surface at depths of 3-30 meters will be guaranteed constant. And depending on the latitude, the range of changes in the values of this "constant temperature" will be within +5 C. At the same time, the regions on the planet, with the most suitable temperature for biological life (in the range of +15 C) are in the sub-polar areas below the surface, and occupy an area of more than 3 million square kilometers! According to the area – it's 5 of Ukraine! Thus, under the sub-face of Mercury at a depth of 3-30 meters, thousands of endo - settlements can be accommodated. It remains only to provide them with water and symbiotic spacesuits for long-term human habitation there, and for obtaining resources on the planet Mercury [1].

Let's remind that in the near-polar regions of the planet, constantly shaded from solar craters, there are huge quantities of water ice. Therefore, now it is necessary to work on the creation of special symbiotic "Cocoons", which can themselves burrow into the ground, for the creation of long-term endoplanet's settlements. And also to build for these settlements a ring of closed circumpolar solar power stations.

References: [1] Steklov A.F., et al. (2017) *17IAGamowConf: ACGCRaA*, 41-42. [2] Vid'Machenko A.P. (1999) *KPCB, 15(5),* 320 – 331. [3] Vidmachenko A.P. (1985) *KPCB, 1(5),* 101-102. [4] Vidmachenko A.P. (1987) *KPCB. 3(6),* 9-12. [5] Vidmachenko A.P. (2007) *AstAlm, 54,* 185-207. [6] Vidmachenko A.P. (2012) *AScR, 8(2),* 136-148. [7] Vidmachenko A.P. (2016) *LPS XXXXVII, Abstract* #1092. [8] Vidmachenko A.P. and Morozhenko O.V. (2014) *MAO NASU, NULESU. Kyiv, PH Profi.* 388 p. [9] Vidmachenko A.P. and Morozhenko O.V. (2014) *AScR, 10(1),* 6-19. [10] Vidmachenko A.P., et al. (1984) *SALet, 10(5),* 289-290. [11] Vidmachenko A.P., et al. (2000) *NEA SRWorksh*, 50.

GEOCHEMICAL CONSTRAINTS FOR MERCURY'S PCA-DERIVED GEOCHEMICAL TERRANES. K. R. Stockstill-Cahill[1] and P. N. Peplowski[2], [1]Planetary Science Institute, 1700 E. Fort Lowell, Tucson, AZ, 85719, [2]Johns Hopkins Applied Physics Laboratory, 11100 Johns Hopkins Road, Laurel, MD 20723; cahill@psi.edu

Introduction: Previous efforts to define geochemical terranes on Mercury were provisional due to the nature of how the terranes were defined [1]. Namely, these efforts [2-3] commonly used limited compositional information and/or defined some terrane boundaries to match geomorphic features despite a lack of evidence that the two are correlated. In an effort to resolve these issues and provide a more robust, analytical definition of terranes that include all available datasets, Peplowski and Gleyzer [1] utilized a principal components analysis (PCA) of elemental composition maps and neutron maps. Geochemical terranes were identified from a PCA of Mg/Si, Al/Si, [2] and K [4] and GRS/ACS neutron [3] maps. These maps provide complete northern hemisphere coverage, but lack coverage in the southern hemisphere; so the PCA maps are also limited to the northern hemisphere (Fig. 1).

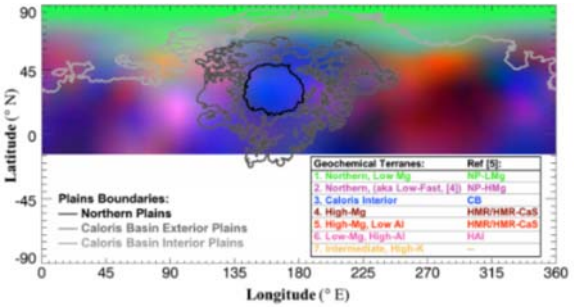

Figure 1. PCA map of [1] showing geochemical terranes defined using various geochemical inputs.

Principle component (PC) 1 (green) is low-Mg, low-Al, high-K materials; PC2 (red) is high-Mg, low-Al materials; and PC4 (blue) is low-Mg, high-Al materials. (PC3 was not used.) Scatter plots (e.g., Fig. 2) of the Mercury geochemical data, color-coded by geochemical terranes, were then used to identify the compositional characteristics of the terranes [1].

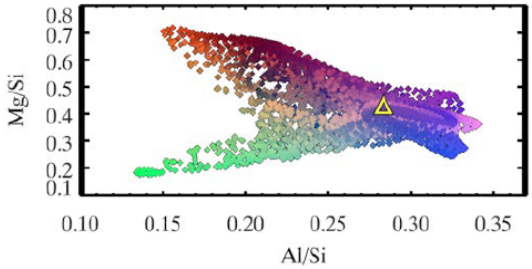

Figure 2. Scatter plot with data color-coded to geochemical terranes from [1].

Methods: Using the compositional characteristics of the terranes derived by [1], we are evaluating the petrologic history and geochemical implications for the various geochemical terranes. Specifically, we are using a CIPW normative analysis [5] and IUGS petrologic classification diagrams [6,7]. We are also using petrologic modeling to understand Mercury's mantle evolution. We used the methods of [8] to derive oxide abundances from the elemental ratios produced by MESSENGER XRS and GRS.

Results: An example of initial mineralogical results from the CIPW norm and MELTS models for PC1 end member (low-Mg, low-Al materials) are shown in Table 1 and Figure 3. Relative to the northern plains units of [8], this composition is significantly lower in MgO (8.3 vs. 12.50-20.28) and lower in S (0.55 vs. 1.8-1.88). It also plots at higher SiO_2 and lower total alkalis than previous work has shown. We will discuss the results for all terranes in greater detail.

Table 1. Derived oxide abundances and CIPW norm for PC1 (low-Mg, low-Al materials)

SiO_2	62.3
Al_2O_3	13.8
FeO	2.17
MgO	8.30
CaO	6.77
Na_2O	5.60
K_2O	0.50
S	0.55

CIPW Norm	
Plagioclase	60
Diopside	17
Hypersthene	12
Quartz	7
Orthoclase	3

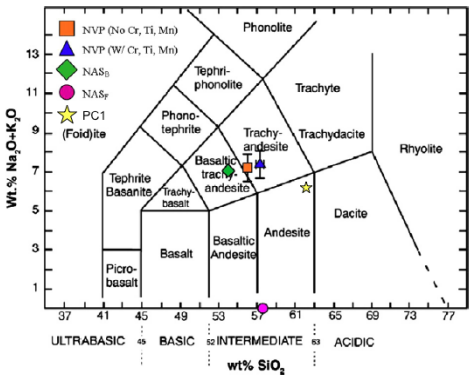

Figure 3. Total-alkali diagram with various compositions for northern plains plotted [after 8].

References: [1] Peplowski, P.N. & Gleyzer (2017), 48th LPSC, abst. #1592. [2] Weider, S.Z. et al. (2015), EPSL 416, 109. [3] Peplowski, P.N. et al. (2015), Icarus 253, 346. [4] Peplowski, P.N. et al. (2012), JGR Planets 117, E00L04. [5] Cross et al. (1903), Quantitative Classification of Igneous Rocks, Univ. Chicago Press. [6] Le Bas, M. J. (2000) J. Petrol. 41, 1467–1470. [7] Le Bas, M. J. & Streckeisen, A. L. (1991) J. Geol. Soc., Lond. 148, 825–833. [8] Vander Kaaden & McCubbin (2016), GCA, 173, 246-263.

MEASURING THE THICKNESS OF RADAR-BRIGHT DEPOSITS ON MERCURY USING INDIVIDUAL MERCURY LASER ALTIMETER (MLA) TRACKS.

H.C.M. Susorney[1,2], P. B. James[3], C. L. Johnson[1,2], N. L. Chabot[4], C. M. Ernst[4], E. M. Mazarico[5], O.S. Barnouin[4] and G. A. Neumann[5], [1] University of British Columbia, Vancouver BC V6T 1Z4 (hsusorney@eoas.ubc.ca), [2]Planetary Science Institute, Tucson, AZ 85719, [3]Baylor University, Waco TX 76798, [4]The Johns Hopkins University Applied Physics Laboratory, Laurel, MD 20723, and [5]Goddard Space Flight Center, Greenbelt, MD 20771

Introduction: The discovery of Mercury's radar-bright deposits [e.g., 1] and subsequent studies [e.g., 2,3] have expanded our understanding of volatiles in the solar system. Key to deciphering the history and origin of the radar-bright deposits is an estimate of the volume of radar-bright material that in turn requires a measure of the average thickness of the deposits.

Several studies have placed bounds on the thickness, h_{rb}, of radar-bright deposits at the north pole. Previous studies have measured surface roughness and inferred an upper limit on h_{rb} of 170 m [4]; used a catalog of craters and MLA derived topography to estimate h_{rb} = 50 ± 35 m [5]; and recently estimated a maximum h_{rb} of 41^{+30}_{-14} m based on the depth/diameter of small craters on the deposits [6]. In this study we investigate changes in topography across radar-bright deposits hosted in flat-floored complex craters, using individual Mercury Laser Altimetry (MLA) tracks.

Method: We identified twelve craters in Mercury's north polar region that host radar-bright deposits and are larger than 30 km. MLA tracks crossed the floor and the radar-bright region of four of these craters. We hand-filtered each track (using all the tracks that crossed the radar-bright deposit and crater floor) to remove the topography associated with superposed craters and central peaks. The difference in height, Dh, between radar-bright and non-radar-bright regions on a crater floor provides an estimate of h_{rb}.

Results: The four radar-bright craters have a mean Dh values and a 1 sigma error bar of 33 ± 60 m, 44 ± 38 m, -22 ± 27 m, and 42 ± 35 m respectively. We compared our results with changes in floor height for two large fresh craters on Mercury to see if our observed Dh can be attributed to natural variations in the height of the crater floor (particularly because radar-bright deposits in the observed craters are concentrated near the edges of the crater floors). We found that the craters Abedin and Grotell have mean Dh of -12 ± 55 m and -76 ± 73 m, respectively, measured in an arbitrary region near the edge of the crater floor with similar size to the measured radar-bright deposits. The mean difference in floor height for the non-radar-bright craters is lower than the mean difference in height of the radar-bright craters, but the one-sigma error bars overlap.

Conclusions: Although we do not find a statistically significant difference in the height between radar-bright and non-radar-bright regions of complex crater floors, we can constrain an upper limit on h_{rb} within these craters. At the 1 sigma level, the maximum h_{rb} is 93 m and the average h_{rb} for radar-bright deposits within the four craters examined is 24 m, within the uncertainties of previous estimates [5,6]. Taken together, this and other studies suggest h_{rb} is on the order of tens of meters or less. Taking our mean h_{rb} = 24 m as the thickness of all radar-bright deposits and the area of radar-bright material [7], we calculate a total volume of radar-bright material for both poles of ~600 km^3, consistent with previous studies [5,6]. Future missions to Mercury with high-resolution laser altimeters could further constrain estimates for the thickness of radar-bright deposits or, depending on the orbit of the spacecraft, provide complimentary thickness estimates of the south pole radar-bright deposits.

References: [1] Harmon J. K. and Slade M. A. (1992) Science, 258, 640-643. [2] Chabot N. L. et al (2014) Geology, 42, 1051-1054. [3] Lawrence D. J. et al (2013) Science, 339, 292-296. [4] Talpe M. J. et al (2012) JGR, 117, E00L13. [5] Eke V. R. (2017) Icarus, 284, 407-415. [6] Deutsch A. N. et al (2018) Icarus. doi:10.1016/j.icarus.2018.01.013. [7] Harmon J. K. et al (2011) Icarus, 211, 37-50.

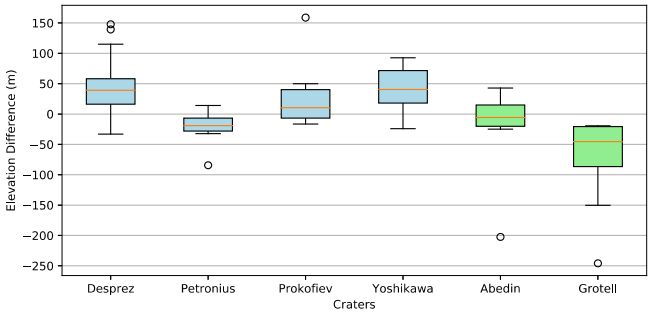

Figure 1. Boxplots of the difference in height along individual hand-filtered MLA tracks of four radar-bright craters (blue) and two non-radar-bright craters (green). For each data point, the orange line represents the median value and the box is the first to third quartile. The black circles are outliers and the bars represent the full range of measured values excluding the outliers.

PLACING TIGHTER CONSTRAINTS ON MERCURIAN SURFACE Fe ABUNDANCES THROUGH THE SYNTHESIS AND CHARACTERIZATION OF Fe-POOR SILICATES. K. E. Vander Kaaden[1], F. M. McCubbin[2], R. L. Rowland II[1], R. V. Morris[2], J. J. Reppart[1,3], and R. L. Klima[4]. [1]Jacobs, NASA Johnson Space Center, Mail Code XI3, Houston, TX 77058, [2]ARES NASA Johnson Space Center, 2101 NASA Parkway, Houston, TX 77058, [3]Department of Geoscience, University of Las Vegas, 4505 Maryland Parkway, Las Vegas, Nevada 89154, [5]The Johns Hopkins University Applied Physics Laboratory, Laurel, Maryland. Corresponding Author E-mail: Kathleen.e.vanderkaaden@nasa.gov

Introduction: Ferromagnesian silicates like olivine and pyroxene display a diagnostic FeO absorption feature near 1-μm that is caused by crystal field transitions in Fe^{2+} in the crystal structure [1]. The pure Mg endmember (e.g., forsterite) does not display a 1-μm absorption feature due to the absence of Fe in the crystalline structure. However, very little is known about exactly how much FeO is needed before the FeO band is detected in olivine. Spectral behavior near the Mg endmember changes rapidly and is not a linear function of X_{FeO} up to the point of 1-μm band saturation [2]. Furthermore, little is known about what concentration of FeO is needed to saturate the FeO band feature. Many planetary bodies in the Solar System that are analyzed in the ultraviolet and visible wavelengths have enough FeO in the ferromagnesian silicates such that the FeO band is detected; however, a 1-μm absorption feature has yet to be observed on the surface of Mercury, despite the presence of wt% levels of Fe on the surface detected by X-Ray Spectroscopy (XRS) [e.g., 3]. Obtaining a quantitative understanding of the detection limit for a 1-μm absorption feature could substantially improve our understanding of Mercury. In the present study, we set out to synthesize a series of low-FeO ferromagnesian minerals to place better constraints on the spectral properties of low-FeO planetary crusts like that observed on Mercury by MESSENGER [3].

Methods: All minerals have been synthesized and characterized at NASA's Johnson Space Center. Additional characterizations are underway at the Applied Physics Lab and the KECK/NASA RELAB.

Mineral Synthesis. Every mineral in this study was synthesized at 1 atm pressure. Starting materials consisted of some combination of reagent grade oxides (e.g., MgO, SiO_2, Fe_2O_3), reagent grade talc, natural talc, and natural San Carlos olivine crystals. Starting forsterite powdered mixes were produced by combining MgO with the respective amount of either SiO_2 or talc and mixing them under ethanol until homogeneous. For all forsterite mixes, the starting materials were loaded into either a $Pt_{95}Au_5$ crucible or an Al_2O_3 crucible and placed in a Lindberg oven. The sample was then heated to 1500–1600 °C over the course of ~5 hours and held there for a minimum of 8 hours. The power to the furnace was then shut off and the sample was left in the furnace to cool. Once cool to the touch, the crucible was removed from the furnace and the sample was reground by hand in an Fe-free mortar and pestle. The sample was then returned to the crucible, and this process was repeated up to 2 more times.

Analytical Methods: Each sample was hand ground in a mortar and pestle and analyzed via 1) powder X-ray diffraction (XRD) in a PANalytical X'Pert Pro MPD diffractometer, 2) electron probe microanalysis in a JEOL 8530F, and 3) reflectance spectroscopy utilizing an Analytical Spectral Devices FieldSpec-3 VNIR spectrometer.

Results: All XRD analyses of the synthetic forsterites produced a 100% semi-quantitative match to the referenced forsterite in the ICDD PDF database. Electron microprobe analyses indicate FeO abundances from below detection of the instrument to 0.53 wt%. The higher amounts of FeO were from the forsteritic samples synthesized in a $Pt_{95}Au_5$ crucible, which was likely the source of Fe-contamination. Assuming all Fe is present as ferrous Fe, we synthesized forsteritic olivine with Mg#'s of 99.48, 99.61, 99.96, and 100. VNIRS analyses are in agreement with the microprobe data where the sample with below detection Fe does not display a 1-μm absorption band and all samples with detectable Fe do exhibit a 1-μm band.

Discussion: Although our preliminary results have considered only small variations across the olivine solid-solution series from $Fo_{99.48}$ to Fo_{100}, we can see the presence of a 1-μm absorption band with as little as 0.04 wt% FeO (i.e., $Fo_{99.96}$). Future work will involve synthesis and characterization of olivine with FeO abundances between $Fo_{99.96}$ and Fo_{100}. In addition, we will synthesize and characterize various Mg-rich pyroxene compositions for better applicability to low-FeO planetary bodies like Mercury.

Conclusion: With well crystallized and carefully characterized synthetic minerals, we aim to make advancements towards reconciling the discrepancy between the lack of a 1-μm absorption band observed on the surface of Mercury, despite wt% levels of Fe observed by XRS.

References: [1] Burns, R.G., (1993), New York: Cambridge University Press. 551. [2] Klima, R.L., et al. (2007) Meteoritics & Planetary Science. **42**(2): p. 235-253. [3] Nittler, L.R., et al., (2011) Science. **333**(6051): p. 1847-1850.

EMISSIVITY OF Ca-SULFIDE IN MID-INFRARED UNDER SIMULATED EXTREME THERMAL ENVIRONMENT OF MERCURY. I. Varatharajan[1], A. Maturilli[1], J. Helbert[1] and H. Hiesinger[2], [1]Institute for Planetary Research, German Aerospace Center DLR, Rutherfordstrasse 2, 12489 Berlin, Germany (indhu.varatharajan@dlr.de), [2] Wilhelms Universität Münster, Germany

Introduction: Understanding the distribution and abundance of volatiles in the planet's surface helps to understand the thermal evolution of the planet itself. There are multiple lines of evidence suggesting the presence of sulfide minerals on the surface of Mercury such as FeS, CaS, MnS, FeS, CrS, and TiS [1-2]. CaS and MgS are spectrally detected in the hollows using MESSENGER MDIS datasets [3]. This October, the ESA-JAXA BepiColombo mission will carry the MERTIS instrument to Mercury which will map the surface mineralogy at 7-14µm and 500m/pixel resolution [4,5]. Studying the emissivity of possible Mercury analogues including sulfides at varying daytime surface temperatures upto 450°C will therefore be an important addition to the standard spectral library for MERTIS [6]. We have measured the mid-infrared (MIR) emissivity spectra at 7-14µm for a wide range of sulfides in simulated Mercury conditions and obtained the corresponding reflectance spectra of both fresh and thermally weathered sulfides in 0.2-100µm at various phase angles [7].

Calcium sulfides: Among the emissivity of sulfides studied, CaS showed strong emissivity features while heating from room temperature to 500°C and showed less susceptibility to thermal weathering while heating for one Mercury day (Fig. 1a). In this study, we conducted emissvity of CaS for a total of four simulated Mercury days to study the nature of its thermal weathering under repeated temperature cycles. Fine-grained synthetic CaS of 99% purity obtained from the certified industrial suppliers are used for this study.

Planetary Spectroscopy Laboratory (PSL): A Bruker Vertex 80V instrument with a MCT HgCdTe detector and KBr beamsplitter at PSL is used to measure thermal emissivity spectra. This spectrometer is attached to an external emissivity chamber where CaS are placed in steel cups which are then heated to Mercury's daytime temperatures via induction technique under vacuum.

Methods and Results: Emissivity of CaS samples are obtained while heating the sample to temperatures from 100° to 500°C (step 100°C) at vacuum. Radiance from the heated samples is collected by a gold (Au) coated parabolic at 90° off-axis mirror which is then reflected to the spectrometer which obtains the thermal emission spectra of the samples at wavelength intervals of 7-14 µm at spectral resolution of 4 cm^{-1}. The emissivity measurements are therefore taken at temperatures of 100°C, 200°C, 300°C, 400°C, and 500° C (Fig. 1a). The sample is then cooled down in vacuum. This is the standard procedure followed for subsequent days of emissivity measurements of CaS.

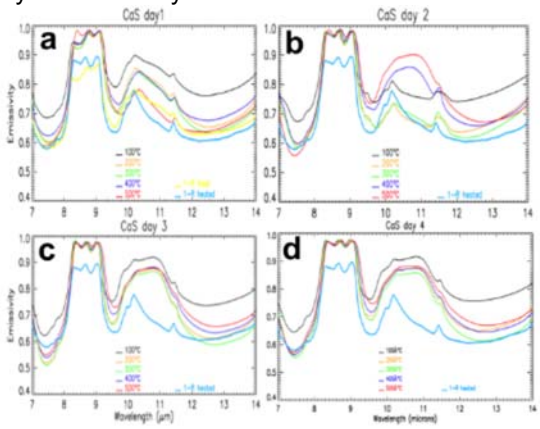

Figure 1. Thermal weathering of CaS and their effect in emissivity under four Mercury Days. (a,b,c,d).

Fig 1a shows that CaS did not undergo significant changes in its spectral behavior while heating through one Mercury day except for ~8.4µm at 500°C. While repeating the standard procedure for day 2 (Fig 1b) the emissvity between 9.5–12µm varies with temperature due to thermal weathering; however, the spectral morphology between 8–9.5µm was undisturbed. The procedure is again repeated for day 3 (Fig 1c), where the emissivity CaS almost maintains its spectral behavior comparable to peak emissivity spectra of day 2 (Fig. 1b; red spectra). Repeating the standard procedure for day 4 (Fig. 1d), the emissivity spectra remains unchanged wrt Day 3. The study shows that reliable representative emissvity spectra of CaS on Mercury is Fig. 1d and neither Fig. 1a nor 1-reflectance of fresh CaS.

Conclusions: The study therefore shows the importance in experimental study of thermal behavior of CaS under repeated Mercury conditions. Though CaS was thermally stable during one Mercury day thermal exposure, the spectral behavior evolves with repeated heating. This is important to address while looking for CaS on Mercury's surface which has undergone long exposure of thermal weathering conditions.

References: [1] Helbert, J. et al (2013). EPSL, 369–370: p. 233-238. [2] E. Vander Kaaden, K., et al. (2017). Icarus, 285: p. 155-168. [3] Vilas, F., et al. (2016). GRL, 43(4): p. 1450-1456. [4] Hiesinger, H. and J. Helbert (2010) PSS, 58,144-165. [5] Helbert, J et al. (2018) at this meeting, [6] Maturilli, A., et al. (2017) 48th LPSC, p. 1427. [7] Varatharajan, I et al (2017) 48th LPSC, p. 1398.

NANO-FTIR SPECTROSCOPY TO INVESTIGATE THE SILICATE MINERALOGY OF MERCURY ANALOGUES: SUPPORTING MERTIS ONBOARD BEPICOLOMBO MISSION. I. Varatharajan[1], A. Maturilli[1], J. Helbert[1], G. Ulrich[2], K. Born[3], O. Namur[4], B. Kästner[2], L. Hecht[3], B. Charlier[5], H. Hiesinger[6] [1]Institute of Planetary Research, German Aerospace Center (DLR), Rutherfordstr 2, 12489 Berlin, Germany; indhu.varatharajan@dlr.de, [2]Physikalisch-Technische Bundesanstalt (PTB), Abbestr. 2-12, 12489 Berlin, Germany, [3]Museum für Naturkunde (MfN), Invalidenstr 43, 10115 Berlin, Germany, [4]Department of Earth and Environmental Sciences, KU Leuven, 3001 Leuven, Belgium, [5]University of Liege, Department of Geology, 4000 Sart-Tilman, Belgium, [6]Institut für Planetologie, Wilhelm-Klemm Strasse 10, 48149 Münster, Germany.

Introduction: Spectroscopy is a powerful technique allowing to study the surface mineralogy of any (airless) planetary body from orbit. Different spectral ranges give details on different chemical and physical aspects of the surface, e.g. VIS-IR spectroscopy of terrestrial planet gives details about distribution of Fe- and Ti- rich silicates minerals whereas Thermal IR spectroscopy gives details on Si-O abundance of the bulk silicate mineralogy. Though the geochemical suite on the NASA MESSENGER spacecraft to Mercury revealed compositionally diverse crustal materials, the spectrometer suite (MASCS; VIS-IR) could not reveal the silicate mineralogy of crustal materials due to Fe^{2+}-poor nature of silicate minerals. The Mercury Radiometer and Thermal Imaging Spectrometer (MERTIS) payload of ESA/JAXA BepiColombo mission will therefore map the surface mineralogy at thermal IR wavelength range (7-14 µm at spatial resolution of 500 m/pixel) [1,2].

The Study: In this study, we used the experimental products by [3] representing the low-Mg Northern Volcanic Plains (NVP), Intercrater Plains (ICP), and High-Mg Province (HMg) terrains of Mercury. These experimental products are 5 x 5 mm^2 in area containing major minerals including forsterite, diopside, enstatite, plagioclase, and locally FeSi. Therefore, studying the spectra of bulk sample and the spectra of each mineral phases in these samples will cast a new light on understanding the spectral behavior of the silicate mineralogy of Mercury.

The study consists of three parts in which we obtain; 1. bulk spectra of the samples, 2. high resolution elemental composition image of the samples for all terrains, 3. nano-FTIR spectra of each mineral units.

Facilities and Methods: The bulk reflectance spectra of these experimental products representing Mercury terrains (NVP, ICP, HMg) in both VIS-IR (0.4-1 µm; Si diode detector) and Thermal IR spectra (1-25 µm; MCT detector) are measured using a Bruker Vertex 80V at the Planetary Spectroscopy Laboratory (PSL), DLR at the spectral resolution of 4 cm^{-1} with the smallest aperture of 0.25 mm diameter [4-5].

In order to navigate the very high resolution (nano-FTIR) spectroscopy, we first obtained the high resolution elemental composition map (Fig. 1a) of all the samples using the Secondary Electron Microscope (SEM) facility at Museum für Naturkunde (MfN).

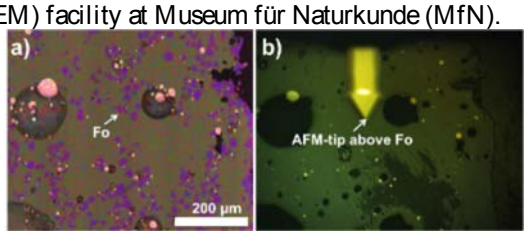

Figure 1. Sample Y0128-HMg containing 32% Forsterite (Fo). a) SEM image where pink units are Fo; b) nano-FTIR setup where cantilever tip pointing to Fo.

The use of broadband synchrotron radiation from IR-beamline of the electron storage ring (Metrology Light Source; MLS) at Physikalisch-Technische Bundesanstalt (PTB), Berlin allows us to perform nano-FTIR (nanoscale) spectroscopy on these experimental products using a Neaspec scattering-type scanning near-field optical microscope (s-SNOM) [6-7]. This is a non-destructive and surface sensitive optical technique based on atomic force microscopy (AFM), where the broadband synchrotron IR light source is utilized to illuminate the cantilever with a gold coated silicon probe-tip (Fig. 1b). This metallic probe acts as an antenna which confines the incident electric field around the tip-apex thus providing a nanoscale light source for very high-resolution imaging. Using this facility, we obtained the spectra of each mineral units guided by SEM images of the samples at the spatial resolution of <40nm for the spectral range of 5-12µm with the spectral resolution of 6.25cm^{-1}.

Ongoing work: Nano-FTIR spectra obtained for all terrain samples are currently being analyzed for its silicates. The spectral deconvolution algorithm will be tested on bulk spectra obtained at PSL using the endmember nano-FTIR silicate spectra. All the results will be presented at the conference.

References: [1] Hiesinger, H. and Helbert, J. (2010) PSS, 58, 144-165. [2] Helbert, J et al. (2018) at this conference, [3] Namur, O. and Charlier, B. (2017) NatGeo, 10, 9–13. [4] Maturilli, A et al. (2017) LPSC, #1427. [5] Maturilli, A et al. (2018) at this conference, [6] Hermann, P. et al. (2013) Optic Express, 21, p.2913 [7] Hermann, P. et al. (2017) Optic Express, 25, 16574-16587.

MESSENGER Orbital Observations of Mercury's Hydrogen Exosphere. R. J. Vervack, Jr.[1], D. M. Hurley[1], W. Pryor[2], and R. M. Killen[3], [1]Johns Hopkins Applied Physics Laboratory, 11100 Johns Hopkins Rd., Laurel MD 20723, USA (ron.vervack@jhuapl.edu), [2]Central Arizona College, Coolidge AZ 85128, USA, [3]NASA Goddard Space Flight Center, Greenbelt MD 20771, USA.

Introduction: Because of the difficulty of remotely observing H Lyman α emission at Mercury, the MESSENGER mission afforded the first chance since Mariner 10 to investigate in detail the hydrogen exosphere of Mercury. Mariner 10 discovered H at Mercury [1-2], but raised questions about the puzzling temperature and density distributions seen in the data. In particular, altitude profiles revealed a two-component distribution for H, with a 420 K "warm" component at high altitudes and a 110 K "cold" component dominating below 300 km [2]. Because Mariner 10 data were limited to flyby observations, an understanding of this distribution, including the mechanism of release for the two components, has remained a mystery.

Observations: Dayside limb observations during the MESSENGER flybys of Mercury suggested that the H exosphere was grossly similar to what was observed by Mariner 10, but with higher overall emission levels [1]. A more complete set of observations of H Lyman α emission was obtained during the orbital phase of MESSENGER, which spanned nearly 17 Mercury years. The Ultraviolet and Visible Spectrometer (UVVS) [4] onboard MESSENGER regularly conducted observations of the H Lyman α emission. It is important to note, however, that H Lyman α can come from three sources at Mercury: exospheric emission, scattered solar H Lyman α from the dayside surface, and background interplanetary H Lyman α (IPH). Accounting for these effects is crucial to proper interpretation of the exospheric signal.

To mitigate the effects of the IPH background, this analysis focuses on observations for which the pointing was inertially fixed. In these cases, the IPH is essentially constant during the observation, allowing determination of an IPH level far from the planet that can be subtracted from all of the measurements to yield an altitude profile.

Altitude profiles determined in this manner have been summed over the entire orbital phase and binned by local time to give a global picture of the H exosphere, as illustrated in Figure 1. Each point shown represents the average of at least 100 individual measurements. H Lyman α is brightest at morning local times, with slightly lower emission intensities in the evening and much lower emission levels on the nightside.

Figure 2 shows the altitude profile of emission integrated along the lines of sight for one set of observations. A Chamberlain model (green) is fitted to the data using two components with temperatures of 400 K (red) and 100 K (blue), chosen to approximate the Mariner 10 temperatures. Clearly, this model is a good match to the MESSENGER profile. The altitude profile shown in Figure 2 is representative of the MESSENGER observations, indicating that the two temperature populations are a persistent, real feature of Mercury's H exosphere.

We will present a complete analysis of the H altitude profiles, with an emphasis on changes in the two components on both local-time and seasonal timescales.

Acknowledgements: We are grateful for support from the NASA Discovery Data Analysis Program.

References: [1] Broadfoot A. L. et al. (1974) Science 185, 166-169. [2] Broadfoot A. L. et al. (1976) Geophys. Res. Lett. 3, 577-580. [3] McClintock et al. (2008), Science 321, 92-94. [4] McClintock W, E. and Lankton M. R. (2007) Space Sci Rev 131, 481-521.

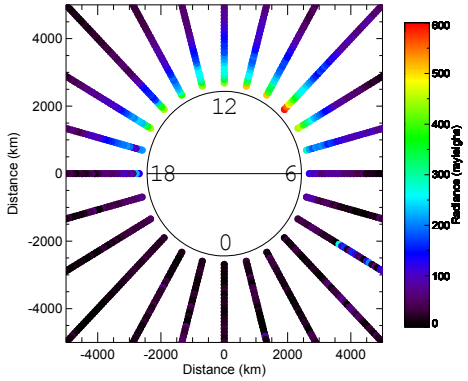

Figure 1. Average H Lyman a brightness as a function of local time at Mercury. The bright points at 4 am local time are likely a star in the UVVS slit.

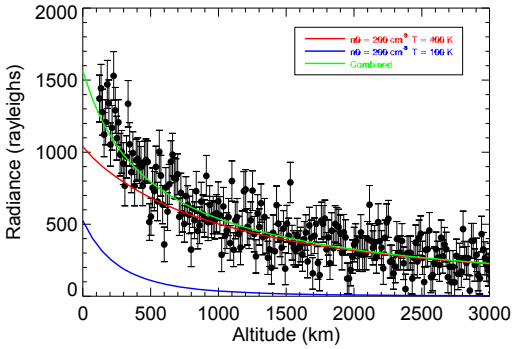

Figure 2. Typical H Lyman a altitude profile measured by MESSENGER. Chamberlain model profiles are superimposed on the data for comparison.

CORRELATED TIME-VARYING MAGNETIC FIELDS AT MERCURY. I. Wardinski, B. Langlais, E. Thébault, Laboratoire de Planétologie et Géodynamique, CNRS & Université de Nantes, France.

Introduction: The planet Mercury is characterized by a peculiar internal magnetic field. Although it has a deep origin as for the Earth, it is much weaker, strongly axisymmetric, and has a much larger quadrupole-to-dipole ratio at its surface than on the Earth [1-4]. The current data coverage (by MESSENGER, between March 2011 and April 2015) is too limited to derive a global model with a high spatial resolution. However, the duration of the mission, in excess of 16 Hermean years, makes it possible to study if there are any temporal changes on the global scale. We investigate these variations of internal and external origin, as modeled from the measurements once a mean magnetic field model has been subtracted. In this study we analyze these variations and correlate them with the orbital parameters.

MESSENGER data and mean model: MESSENGER orbited around Mercury During this interval it flew at low altitude (below 1000 km) mainly over the northern hemisphere. This led to an uneven distribution for topics related to the description and understanding of the Hermean magnetic field. Due to this data distribution it is only possible to compute low degree and order spherical harmonic global models (e.g., [1-2]), or local models (over the northern hemisphere) with a better resolution (e.g., [3-4]). All these models are temporally averaged, and describe the mean magnetic field of Mercury.

For self-consistency we start with the raw magnetic field measurements and compute a mean magnetic field model up to degree and order 3. We consider only night-side measurements below 1000-km altitude. The derived model is very similar to that of [4]. We then subtract the measurements from this model in order to focus on the time-varying residuals.

Time-varying model: Measurements are sorted into temporal bins so that each contains 8 consecutive orbits (provided that there are no significant gaps between orbits). For each subset, a SH degree and order 1 internal and external magnetic field model is computed. The misfit of each subset significantly improves, going from about 26 nT (after removal of a mean global magnetic field) to less than 10 and as low as 4 nT (after modeling of the considered subset), depending in the subset..

Results: The results consist in a time series of 6 times 450 coefficients, for the internal (g_1^0, g_1^1, and h_1^1) and external (q_1^0, q_1^1, and s_1^1) parts. We show on Fig. 1 the time series for the external and internal axial dipole terms.

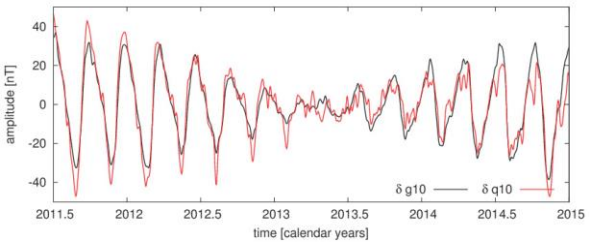

Fig.1 Time series of Gauss coefficients g_1^0 (black) and q_1^0 (red) over the duration of the MESSENGER mission.

Both terms are highly correlated and present a periodic temporal variability. Their main period is 88 days; i.e., the duration of one Hermean revolution around the Sun. This periodic variation seems to be modulated by an additional term, which cancels out in the beginning during the first half of 2013. This corresponds to the time when MESSENGER's periapsis was the closest to the pole.

Similar observations are made for the equatorial dipole terms, although the main periods are different, with two overlapping ones at 58 and 176 days (i.e., one day and two years or one solar day).

In this paper we will show several statistical analyses, which all confirm these figures. These correlated time variations of internal and external origin are very intriguing and their exact origin is under investigation. The fact that most periods are associated with the orbital parameters of Mercury make an external origin more likely, with possibly different source regions.

References: [1] Anderson B. J. et al. (2012) *J. Geophys. Res. 117*. [2] Johnson C. J. et al. (2012) *J. Geophys. Res. 117*. [3] Oliveira J. S. et al. (2015) *J. Geophys. Res. 120*. [4] Thébault E. et al. (2018) *Phys. Earth Plan. Int. 276.*

Additional Information: This work is supported by a grant of the Agence Nationale de la Recherche, ANR-13-BS05-0012, and by CNES in the frame of the BepiColombo project.

ANALYSIS OF LARGE-SCALE RESURFACING PROCESSES ON MERCURY: MAPPING THE DERAIN (H-10) QUADRANGLE.

J. L. Whitten[1], L. R. Ostrach[2], C. I. Fassett[3], [1]Center for Earth and Planetary Studies, Smithsonian Institution, MRC 315, PO Box 37012, Washington, DC 20013 (whittenj@si.edu), [2]U.S. Geological Survey, Astrogeology Science Center, 2255 N. Gemini Dr., Flagstaff, AZ 86001 (lostrach@usgs.gov), [3]NASA Marshall Space Flight Center, Huntsville, AL 35805 (caleb.i.fassett@nasa.gov).

Introduction: The surface of Mercury is dominated by three major geologic units: the smooth plains, the intercrater plains, and crater materials [e.g., 1]. Of these units, the intercrater plains are the oldest and most areally extensive deposit, defined as level to gently rolling plains with a high density of secondary craters <10 m in diameter [1]. Both the distribution and cratering statistics of the intercrater plains argue for large-scale ancient resurfacing across the surface of Mercury [2, 3]. This ancient resurfacing can be accomplished by either volcanic or impact-related processes.

Smooth plains have largely been interpreted as volcanic [e.g., 4–6]. However, there are several, large circum-basin plains (10^5–10^6 km^2) with an uncertain origin, including the smooth plains around Caloris [6, 7] and Rembrandt [6, 8] basins. The high average impact velocity (~42 km/s) expected for Mercury [9] should result in large volumes of impact melt across the planet's surface. We will assess this potential importance of impact melt and other ejecta deposits on resurfacing Mercury by creating a 1:5M map of the deposits contained within the Derain (H-10) Quadrangle (Fig. 1).

Data: MESSENGER datasets provide the opportunity to produce USGS geologic maps of those regions of Mercury that were not visible in the Mariner 10 datasets. H-10 represents "average" ancient Mercury crust because it is unaffected by more recent geologic processes (e.g., smooth plains volcanism, basin ejecta) and contains a large fraction of intercrater plains. Mapping is being completed at the 1:1.25M scale on the MDIS 166 m/pixel basemap. The results of previous mapping efforts [2, 6, 10] will be used to assist with unit and landform mapping. All craters >8 km will be mapped to determine the N(10) and N(20) areal crater density values (the number of craters >D per 10^6 km^2 [11]) and derive a relative stratigraphy of the units in H-10.

Current results: A subset of the H-10 quadrangle is being mapped (Fig. 1 red box, Fig. 2). This sub-region contains gradational boundaries between all of the units (crater ejecta blends into the intercrater plains, smooth plains and intercrater plains gradually transition) that will be useful in resolving early in the map process to clearly defining identification criteria for the rest of H-10. Smooth plains and crater rim/wall/floor materials are the most easily identifiable geologic units thus far. Several major lobate scarps are also identified, as are impact craters and partially buried impact craters.

References: [1] Trask N.J. & Guest J.E. (1975) JGR, 80, 2461–2477. [2] Fassett C.I. et al. (2011) GRL, 38, L10202. [3] Marchi S. et al. (2013) Nature, 499, 59–61. [4] Strom R.G. et al. (1975) JGR, 80, 2478–2507. [5] Head J.W. et al. (2011) Science, 333, 1853–1856. [6] Denevi B.W. et al. (2013) JGR, 118. [7] Fassett C.I. et al. (2009) EPSL, 285, 297–308. [8] Whitten J.L. & Head J.W. (2015) Icarus, 258, 350–365. [9] LeFeuvre M. & Wieczorek M.A. (2008) Icarus, 197, 291–306. [10] Herrick R.R. et al. (2011) Icarus, 215, 452–454. [11] Crater Analysis Techniques Working Group (1979) Icarus, 37, 467–474.

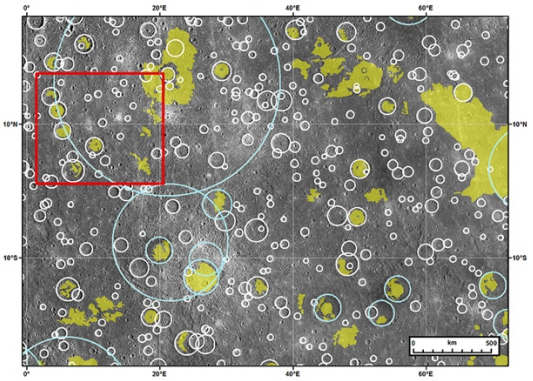

Figure 1. The Derain (H-10) Quadrangle on Mercury (25°N to 25°S and 360°W to 288°W). Red box denotes extent of subregion currently being mapped. Smooth plains [6] are shown as yellow polygons and impact craters ≥30 [2] are displayed in white circles. Craters outlined in blue are >150 km in diameter. MDIS 750 nm moderate-incidence angle 166 m/pixel mosaic.

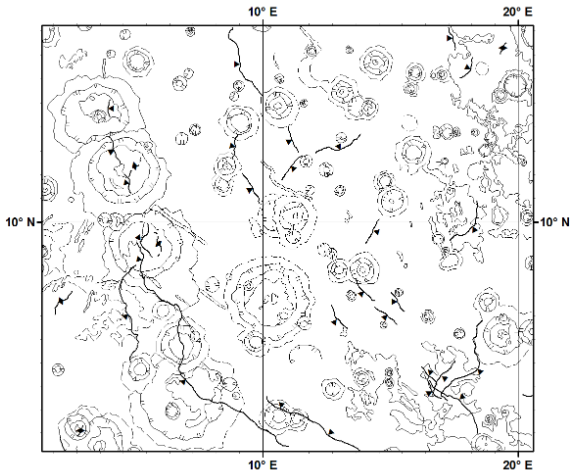

Figure 2. Geologic mapping completed in the sub-region (Fig. 1, red box) of H-10, including geologic units and linear features, such as lobate scarps.

AUBRITE AND ENSTATITE CHONDRITE IMPACT MELT METEORITES: ANALOGS TO MERCURY? Z. E. Wilbur[1,2], A. Udry[1], F. M. McCubbin[3], K. E. Vander Kaaden[2,], R. R. Rahib[1], and T. J. McCoy[4]. [1] Department of Geoscience, University of Nevada, Las Vegas, Las Vegas, NV 89154, USA (wilbur@unlv.nevada.edu), [2]Jacobs, NASA Johnson Space Center, Mail Code XI3, Houston, TX 77058, [3]ARES, NASA Johnson Space Center, 2101 NASA Parkway, Houston, TX 77058, [4]Natural Museum of History, Smithsonian Institution, Washington, D.C., USA.

Introduction: New data obtained during the MESSENGER mission has allowed us to better contrain the composition and mineralogy of the mercurian surface [e.g., 1-3]. One unique feature of Mercury is its extremely low oxygen fugacity (fO_2) (Iron Wustite (IW) -7.3 to IW-2.6) [4–6]. At such extreme conditions, elements that exhibit lithophile behavior on Earth can exhibit chalcophile or siderophile behavior, leading to the formation of exotic sulfides and metals [5,7–9].

As no samples have been returned from Mercury, it is critical to study meteorite analogs to better understand the formation conditions of the minerals present at the mercurian surface, as well as mercurian magmatic processes. Given the low fO_2 on Mercury, we have selected to investigate potential meteoritic analogs for Mercury among the most reduced meteorite types, including the aubrites and enstatite chondrite impact melts. The aubrites are differentiated meteorites that show varying degrees of brecciation, have a similar fO_2 to the mercurian surface and interior, and contain exotic sulfides that have been inferred to be present on the mercurian surface [13–15]. The enstatite chondrite impact melts are from undifferentiated parent bodies, have a similar fO_2 to the mercurian surface and interior, and contain exotic sulfides that have been inferred to be present on the mercurian surface [13–15].

In this study, we present a comprehensive analysis of a representative suite of aubrites and enstatite chondrite impact melts and assess their relevance to understanding magmatic processes on Mercury.

Samples: We have gathered 14 aubrites: Allan Hills (ALH) 78113, ALH 84007, Bishopville, Cumberland Falls, Khor Temiki, LaPaz Icefield (LAP) 02233, Larkman Nunatak (LAR) 04316, Miller Range (MIL) 07008, MIL 13004, Mount Egerton, Northwest Africa (NWA) 9396, Norton County, Peña Blanca Spring, and Shallowater; and 4 enstatite chondrite impact melts (NWA 4799, NWA 7214, NWA 7809 and NWA 11071).

Preliminary results:

Aubrites: The aubrites are composed of FeO-poor enstatite, forsterite, diopside, plagioclase, metal, and exotic sulfides. Miller Range 13004, Bishopville, Cumberland Falls, and Mount Egerton contain Ti-bearing troilite, Mg-bearing daubréelite, Mn-bearing oldhamite, ferroan alabandite, schreibersite and perryite within Si-bearing Fe, Ni kamacite, caswellsilverite, brezinaite, and djerfisherite.

Enstatite Chondrite Impact Melts: These meteorites are composed of FeO-poor enstatite, interstitial plagioclase, metal, graphite, and exotic sulfides. Wilbur et al. [13] show that these samples contain Ti-bearing troilite, niningerite, possibly indicating an EH parent body origin; Mn-bearing daubréelite, Mg-bearing oldhamite, caswellsilverite, and schreibersite present within Si-bearing Fe, Ni kamacite.

Implications for Mercurian Mineralogy: The mineralogy of the mercurian surface is complex [1–13], and MESSENGER data and meteorite analogs will help us better understand elemental partitioning at extremely reducing conditions. The aubrites and enstatite chondrite impact melts in this study contain similar sulfide mineralogies inferred to be on the mercurian surface (FeS, MgS, and CaS) [5,12]. However, the meteorite samples have a lower sulfide vol.% compared to most mercurian terrains (1.23–6.3% normative sulfides) [5,12]. The enstatite chondrite impact melts have higher abundances of albitic plagioclase than aubrites and higher abundances of Na_2O than aubrites, which may make them a better match for a mercurian analog than aubrites.

Conclusions: Neither the aubrite meteorites nor impact melts from enstatite chondrites represent perfect analogs for mercurian rocks; however, both provide valuable insights into the distribution and geochemical behavior of natural systems under highly reducing conditions. The bulk compositions of the enstatite chondrite impact melts are a better match to the mercurian surface than aubrites [15–18]. However, unlike Mercury, the enstatite chondrite impact melts are from undifferentiated parent bodies.

References: [1] Nittler et al. (2011) *Science*, *333*, 1847-1850. [2] Evans et al. (2012) *JGR*, *117*, E00L07. [3] Starr et al. (2012) *JGR, 117*, E12. [4] McCubbin et al. (2012) *GRL, 39*, L09202. [5] McCubbin et al. (2017) *JGR, 122*,. [6] Zolotov et al. (2013) *JGR, 118*, 138-146. [7] Weider et al. (2012) JGR 117, E00L05. [8] Charlier et al. (2013) *EPSL, 363*, 50-60. [9] Vander Kaaden & McCubbin (2016) *GCA, 83*, 272-291. [10] Peplowski et al. (2014) *Icarus*, 228, 86-95. [11] Namur & Charlier (2017) *Nat. Geo., 10*, 9-13. [12] Vander Kaaden et al. (2017) *Icarus, 285*, 155-168. [13] Wilbur et al. (2018) *LPS XLIX, Abstract #1355* [14] Keil (2010) *Chem. Erde*, *70*, 295-317. [15] Rubin (2015) *Chem. Erde*, *75*, 1-28. [16] McCoy et al (1995) *GCA, 59*, 161–175. [17] Wasson et al. (1994) *Meteoritics, 29,* 658-662. [18] Lodders and Fegley (1998) Planetary Scientists companion.

POST-DEPOSITION (AND ONGOING?) MODIFICATION OF CALORIS EJECTA BLOCKS. J. Wright[1], S. J. Conway[2], D. A. Rothery[1] and M. R. Balme[1], [1]School of Physical Sciences, The Open University, Milton Keynes, MK7 6AA, UK, [2]CNRS, Laboratoire de Planétologie et Géodynamic, Université de Nantes, France.

Introduction: Mercury's circum-Caloris region hosts numerous kilometer-scale knobs [1]. If these landforms, peculiar to Caloris, are its ejecta, then they can provide insight into the deep materials of the planet.

Observations: Circum-Caloris knobs are found up to ~1000 km from Caloris, but they are more densely distributed near the rim [2] (Fig 1a). They are up to ~10 km in diameter and are domal to conical in shape. They can be discrete or coalescent, and exist in isolation, clusters or, importantly, chains radiating from Caloris. This suggests the knobs are ejecta blocks.

Most knobs host few resolvable superposing impact craters, even at MESSENGER's NAC [3] resolution, on their steep (~20°) upper flank slopes (Fig. 1b). They often have lower-angle basal slopes that grade into the surroundings. Some seem to bury nearby craters (Fig. 1c). These observations suggest mass-wasting modification.

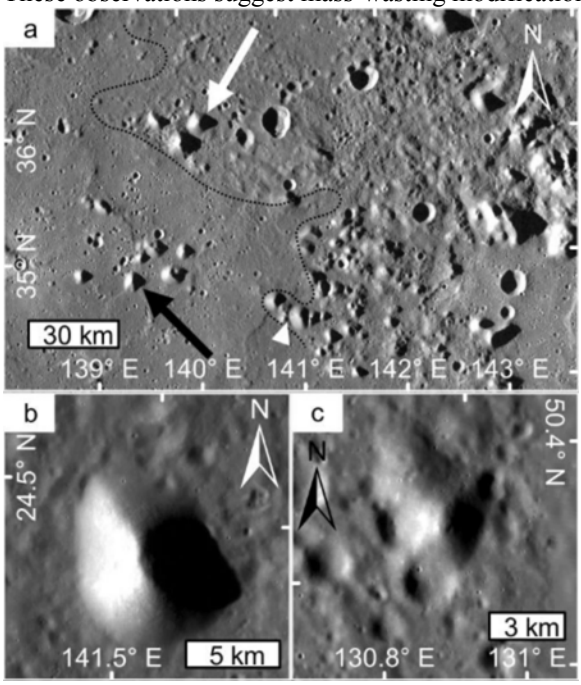

Fig. 1. *Circum-Caloris knobs.* ***(a)*** *Examples of knobs west of the Caloris rim. Discrete knobs within smooth plains (black arrow) and the Odin Formation (white arrow). Coalesced knobs (white triangle). Dotted line is approximate contact between smooth plains and Odin Formation. (b) A fresh, isolated knob (~36 m/pixel). (c) A degraded knob with flank material infilling an impact crater.*

Block modification may have taken place long after their formation, and is possibly ongoing. Knob material abuts a lobate scarp that deforms the Caloris plains, which resolvably post-date the Caloris impact [1]. Hollows (geologically young landforms believed to form by the sublimation of a crustal volatile [4]) are found on knob material, suggesting this Caloris ejecta has a volatile component. We hypothesize that volatile loss plays a role in the ongoing modification of the conical knobs. Thus, their geomorphology may help constrain the enigmatic volatile content of Mercury's deep interior.

Acknowledgements: This work is supported in part by the CNES, in preparation for BepiColombo.

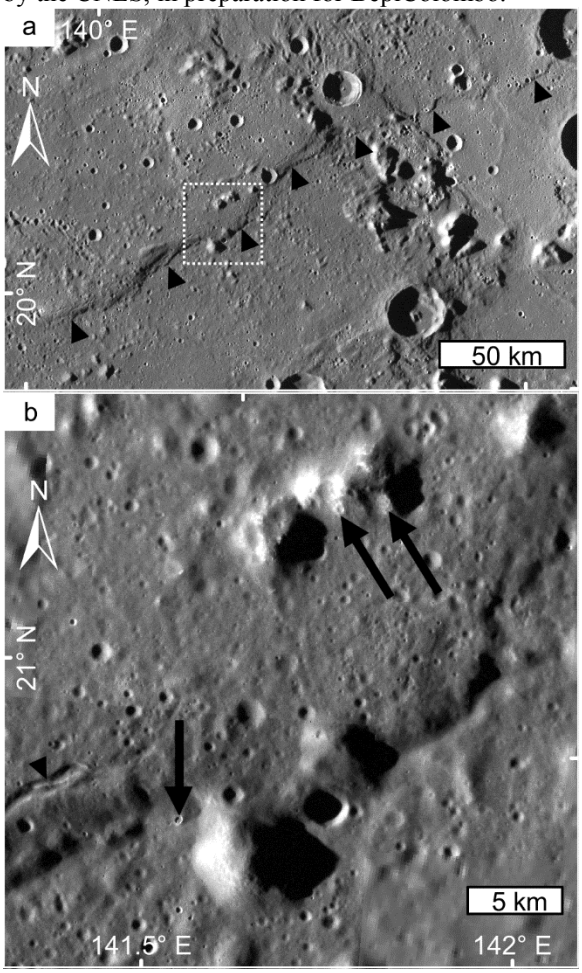

Fig. 2. ***(a)*** *Lobate scarp (triangles) cutting Caloris plains and rim. Extent of (b) (box).* ***(b)*** *Knobs abutting scarp. Hollows in knob material (arrows). Back-scarp graben indicating young fault movement (triangle).*

References: [1] Fassett C. I. et al. (2009) *Earth Planet. Sci. Lett., 285,* 297–308. [2] Wright J. et al. (2018) *LPS XLIX*, Abstract #2133. [3] Hawkins S. E. et al. (2007) *Space Sci. Rev., 131,* 247–338. [4] Blewett D. T. et al. (2013) *Science, 333,* 1856–1859.

CANDIDATE CONSTRUCTIONAL VOLCANIC EDIFICES ON MERCURY. J. Wright[1], D. A. Rothery[1], M. R. Balme[1] and S. J. Conway[2], [1]School of Physical Sciences, The Open University, Milton Keynes, MK7 6AA, UK (jack.wright@open.ac.uk), [2]CNRS, Laboratoire de Planétologie et Géodynamic, Université de Nantes, France.

Introduction: Studies using MESSENGER data suggest that Mercury's crust is predominantly a product of effusive volcanism [1,2] that occurred in the first billion years following the planet's formation [3,4]. Despite this planet-wide effusive volcanism, no constructional volcanic edifices, characterized by a topographic rise, have hitherto been robustly identified on Mercury [5,6], whereas constructional volcanoes are common on other planetary bodies in the solar system with volcanic histories [e.g. 7].

Here, we describe two candidate constructional volcanic edifices we have found on Mercury and discuss how these edifices may have formed [8].

Candidate volcanic edifice #1 (CV1): CV1 is a topographic prominence 6.1 km across and ~530 m high in Heaney crater (Fig. 1). It has flank slopes of ~10° and a summit depression 1.7 km across that is shallower than impact craters of similar size. CV1 is surrounded by smooth plains that cover the floor of Heaney. No kipukas or wrinkle ridges indicative of a former peak-ring, which otherwise might explain CV1, are observed within Heaney. CV1 is coincident with a red color anomaly consistent with others elsewhere on Mercury that are interpreted as pyroclastic deposits [9].

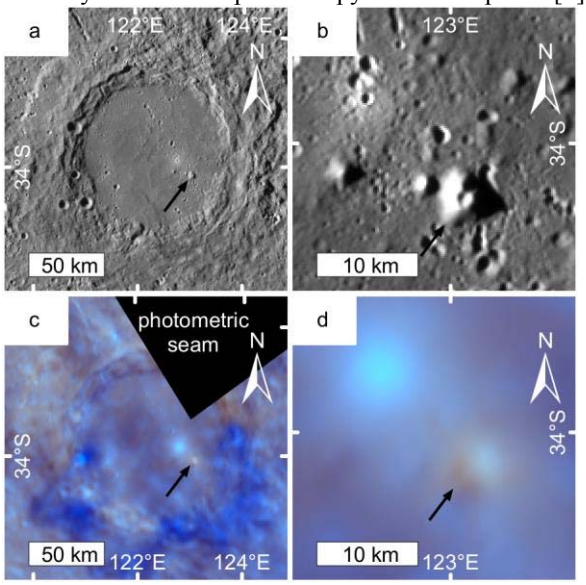

Fig. 1. *CV1 indicated by black arrow in all panes.* ***(a)*** *Heaney crater.* ***(b)*** *Detail of CV1. Two smaller knobs to the west may also be volcanic. A fresh impact crater lies ~10 km NW of CV1.* ***(c)*** *Enhanced color view of Heaney. Low-reflectance material is exhumed in the southern rim and ejecta. CV1 is coincident with a red color anomaly.* ***(d)*** *Detail of CV1 red color anomaly. The blue anomaly to the NW is due to fresh ejecta from the young impact crater in (b).*

We suggest that CV1 formed towards the end of small-volume, post-impact effusive volcanism that occurred within Heaney. As the effusion rate dropped, flows shortened and stacked to form an edifice. A terminal explosive eruption, facilitated by volatiles derived from subsurface low-reflectance material [10], may have created the red color anomaly.

Candidate volcanic edifice #2 (CV2):

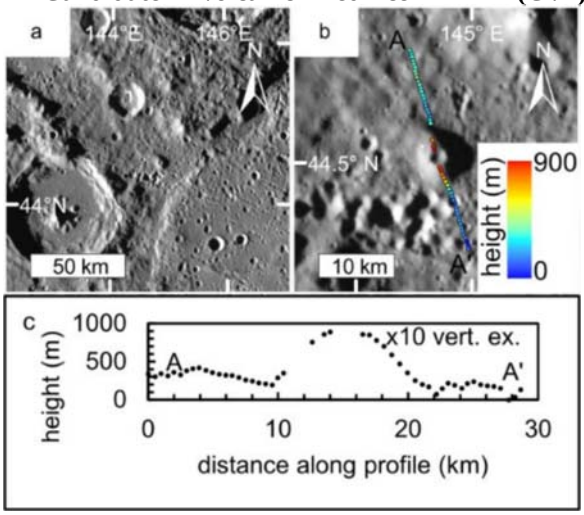

Fig. 2. ***(a)*** *Setting of CV2 in NW of Caloris rim.* ***(b)*** *Detail of CV2 and locations of elevation data. A and A' mark the ends of the topographic profile shown in (c).* ***(c)*** *Topographic profile of CV2.*

CV2 resembles CV1. It is 12.1 km across, ~700 m high and has an average flank slope of 7–8° (from Mercury Laser Altimeter (MLA) [11] data). It also has a shallow summit depression but lacks a red color anomaly similar to that of CV1. CV2 may have formed as the eruptions that formed Caloris Planitia waned.

References: [1] Denevi B. W. et al. (2013) *J. Geophys. Res. Planets, 118*, 891–907. [2] Whitten J. L. et al. (2014) *Icarus, 241*, 97–113. [3] Byrne P. K. et al. (2016) *Geophys. Res. Lett., 43*, 7408–7416. [4] Marchi S. et al. (2013) *Nature, 499*, 59–61. [5] Head J. W. et al. (2008) *Science, 321*, 69–72. [6] Rothery D. A. et al. (2014) *Earth Planet. Sci. Lett., 385*, 59–67. [7] Sigurdsson H. et al. (2000) *Encyclopedia of volcanoes.* [8] Wright J. et al. (in rev.) *J. Geophys. Res. Planets.* [9] Thomas et al. (2014) *J. Geophys. Res. Planets, 119*, 2239–2254. [10] Weider S. Z. et al. (2016) *Geophys. Res. Lett., 43*, (3653–3661). [11] Cavanaugh J. F. et al. (2007) *Space Sci, Rev., 131*, 451–479.

GEOLOGICAL MAPPING OF THE HOKUSAI (H05) QUADRANGLE OF MERCURY: STATUS UPDATE.

J. Wright[1], D. A. Rothery[1], M. R. Balme[1] and S. J. Conway[2], [1]School of Physical Sciences, The Open University, Milton Keynes, MK7 6AA, UK (jack.wright@open.ac.uk), [2]CNRS, Laboratoire de Planétologie et Géodynamic, Université de Nantes, France.

Introduction: MESSENGER data are being used to construct ~1:3M scale quadrangle geological maps of Mercury [1–6]. Here, we present our progress mapping the Hokusai (H05) quadrangle (Fig. 1). A more complete update on this work can be found in [4].

Data and Methods: Since H05 is a mid-northern latitude quadrangle (0–90° E; 22.5–66° N), its map is in a Lambert Conformable Conic projection. Linework is drawn at the 1:400k scale, using ArcGIS, for publication at the 1:3M scale, per USGS recommendations [7]. Thus, this map will be compatible with the other new quadrangle maps of Mercury [8].

The basemap is constructed from the MESSENGER MDIS basemap tiles, with an average ground resolution of 166 m/pixel. Ancillary mapping data products include global topography [9], mosaics with high- and low-incidence illumination from both east and west [10], and an enhanced color mosaic [11].

Future Work: The smooth plains within H05 are fully mapped. We are now mapping the cratered plains. Some plains are not easily mapped as smooth or intercrater plains, likely requiring a new unit on the map.

References: [1] Galluzzi V. et al. (2016) *J. Maps*, *12*, 227-238. [2] Mancinelli P. et al. (2016) *J. Maps*, *12*, 190-202. [3] Guzzetta L. et al. (2016) *J. Maps, 13,* 227–238. [4] Wright J. et al. (2018) *LPS XLIX*, #2164. [5] Malliband C. et al. (2017) *LPS XLVIII,* #1476. [6] Pegg D. L. et al. (2017) 15th Early Career Planetary Scientists' Meeting, UKPF. [7] Tanaka K. L. et al. (2010) *Planetary Geologic Mapping Handbook – 2011*, *USGS*. [8] Galluzzi V. et al. (2017) *11th EPSC*, EPSC2017-1005.

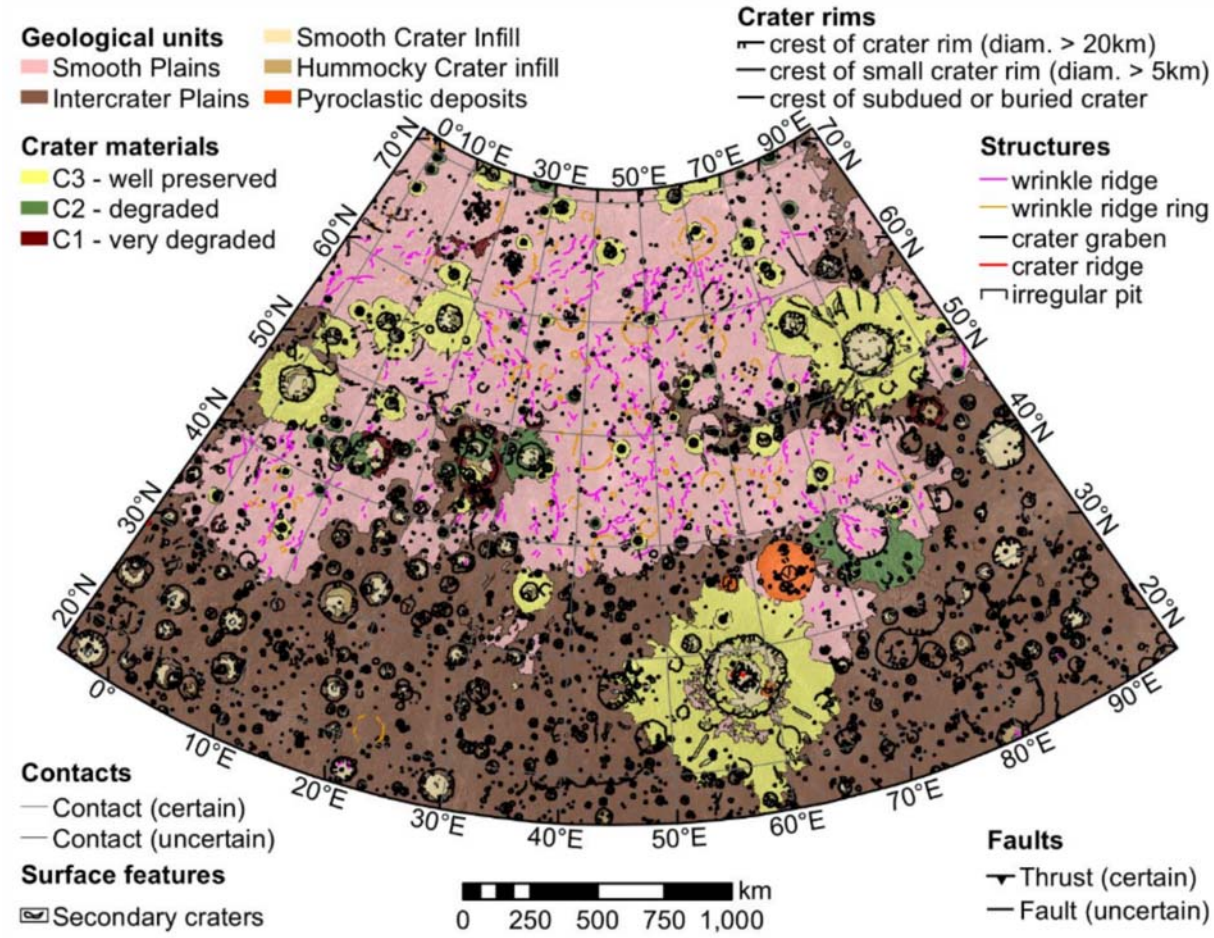

Fig. 1. *Our current working geological map of the Hokusai quadrangle of Mercury. 5° of overlap is shown with the surrounding quadrangles.*